AN EXPERIMENTAL STUDY OF THE STRESS INTENSITY FACTORS OF SEMI-ELLIPTICAL & CRESCENT MOON SURFACE FATIGUE CRACKS IN ROUND BARS.

by

Odesh Sharma Rambocus B.Sc. Eng. (Electro-Mechanical)

A Dissertation Submitted in Partial Fulfilment of the Academic Requirements for the Degree Master of Science in Engineering.

University of Cape Town
Department of Mechanical Engineering

May 2005

ABSTRACT

In mechanical engineering, rotating round and cylindrical components, such as power transmission shafts, screw drives, and shafts with variable cross-section are extremely common and find wide application. Despite good design for such components, surface fatigue cracks still frequently initiate at stress concentration locations, associated with changes in section, due to cyclic stresses to which the component is exposed in service, and this can lead to fracture and often catastrophic collapse. For such shafts and similar rotating components, which may exhibit fatigue crack development, a "fitness for purpose" methodology is required, to assess the safety performance of the component. The fracture mechanics discipline most appropriately addresses this requirement, as it relates the strength of a structure (containing a defect) to the material's intrinsic fracture toughness, as well as to the crack size, (shape and location), and the effective stress in the vicinity of the flaw. The so-called stress intensity, K_I provides a relationship between the flaw size, a, and effective stress, σ. When this stress intensity, K_I, exceeds the local material toughness, K_{IC}(under linear elastic conditions) failure ensues. The relationship between the above parameters is linked by the geometry compliance factor, Y.

The Y compliance functions have largely been developed theoretically, but very little experimental data is available. This is particularly the case for so called "crescent moon" and "thumbnail" shaped cracks in round bars, even though these shapes are frequently encountered in practice. Several authors have studied this question for semi elliptical cracks in round and cylindrical sections, as well as in rectangular bars, by using finite element methods and have produced meaningful computational results for semi-elliptical cracks, for tension, bending and even torsion. All these stress intensity factor studies were undertaken from a computational point of view, making various assumptions for constitutive equations and boundary conditions. The number of reported experimental studies on the fracture behaviour of semi elliptical, "thumbnail" or "crescent moon" shaped surface fatigue cracks, of variable aspect ratio, is, however, very limited.

This thesis attempts to address this shortcoming by generating experimental data for Y compliance at fracture, in bending as well as tension, which can be compared to the published literature on computational data for round bars. The Y compliance values were assessed for various aspect ratios (a/2c) as well as relative depth (a/d). The materials used were 7075-T6 and 2030-T3 aluminium alloys, which exhibit relatively high strength but with a comparatively low toughness, thus still tractable within the linear elastic fracture mechanics (LEFM) regime.

Fatigue cracks were developed in the shape of 'crescent moon' and 'thumbnail', shapes with different aspect ratios, crack depths and surface lengths, as well for a range of diameters from 12 to 20mm. Crescent moon fatigue crack shapes were obtained by rotational fatigue of a specimen, which contained a substantial stress concentration around part of its circumference, at which the fatigue crack readily initiated. Since the stress concentration was achieved by prior specimen machining, it was possible to effectively pre-determine the subsequent crescent moon fatigue crack shape and aspect ratio. After fatigue pre-cracking to the requisite size and shape, the specimens were loaded to failure in either tension or bending, and the load recorded.

This failure load and crack size, as well as the previously determined LEFM material fracture toughness, measured conventionally, facilitated determination of the critical Y compliance value at failure.

There is a major concern about where on the crack front the fast failure initiates, as it is well known that there is a variation of stress intensity along the crack front. This is often greatest at the deepest point of the crack and less at the surface, but this does depend on relative aspect ratio and loading configuration (e.g. bending). In the present case the Y compliance values were determined from the load at failure, so the material and load conditions themselves had 'selected' the critical failure condition, so to speak, but this needs to be confirmed.

The present study yields Y compliance values as a function of aspect ratio (a/2c) and relative depth (a/d) for round bars in bending and tension, which are consistent with reported values for thumbnail cracking obtained by Carpinteri, and Fenner in the

range up to 0.4a/d. Y compliance stress intensity values for crescent moon type cracking do not appear to have been reported previously. The computational and present experimental curves provide a 'concave-up' relationship for Y versus a/d and a/2c, and the Y compliance appears higher in tension than in bending. In addition the Y values for fixed a/d, appear to increase as the flaw aspect ratio decreases (from thumbnail, through straight "chord" shapes to "crescent moon" shape). Through such improved and experimental Y compliance values, it is believed that a contribution can be made to the enhanced safety of round shafts exhibiting ***practically encountered*** *fatigue cracking situations.*

DECLARATION

I hereby declare that this dissertation contains only my own original work, except where reference is made with acknowledgement to others. I also declare that this material has not been submitted for any purpose or examination to any other Department or University.

Odesh Sharma Rambocus

Date:

Acknowledgements

I am indebted to a large number of people for their assistance, advice and support in preparing this thesis.

Firstly, I express my sincere gratitude to my parents, my brother Sheilesh (for his tremendous support) and the rest of my family for their constant encouragement, belief in me, and mostly for their love.

The academic staff in the Department of both Mechanical and Materials Engineering, in particular, my supervisor Prof. R.B. Tait for his invaluable assistance in being available to advise, to correct and discuss all aspects of this work and seeing to its completion. Thanks again for everything.

Glen Newins, Len Watkin, Horst Emrich, Martin Batho and Hubert Tomlinson for their constructive discussion on the designs of the test components as well as their expert machining of these components and test specimens and Peter Jacobs for his assistance in the workshop and Julian Meyer for his help in the setting up of the electrical circuit for the rotational bending machine.

My friends in the Mechanical Engineering Department: Dr. K. Marcus for his invaluable help, Mrs. Siphila Mumenya for her motivation and technical advice, Mr. A. Cousins for devoting his time to assist me on the E.S.H testing machine and Mrs. P. Park-Ross to assist me on the Zwick machine.

Special thanks to my family friends in Cape Town: Aunty Zaheida, Mumtaz, and Feroz Adam, Riaaz and Farhana Abdullah, Sheyn Latchmea, Avinash, Uncle Krish and Aunty Renita Andhee for their wonderful love, motivation and support throughout the course of my degree. Lastly, I would also like to thank my new flatmates- Jessen, Joy and Roy for their kind support and friendship during my write up.

Dedicated to my loving parents-

Surend and Meera Rambocus

Tables of Contents

List of Figures

List of Tables

1. Introduction.

1.1 Introduction to Fracture Mechanics

The catastrophic possibilities of sudden fracture in terms of financial loss, human life and even national prestige and security, have inspired many studies on fracture phenomena **[1]**. Many engineering designs employ the use of high strength, lightweight materials for the efficiency of the design. These structural materials are, however, prone to the development of cracks as a result of various stresses such as overloading, fatigue, corrosion-influenced fatigue, stress corrosion cracking (SCC) heat and wear. Propagation of such cracks may result in catastrophic failures of the engineering structures due to the complete fracture of the materials and components used. Presence of cracks can result in the fracture of materials below the material yield strength.

Failures of structural components as a result of cyclic loading have also been a major design problem and have resulted in numerous investigations into the growth of cracks by fatigue. The present approach, which has gained increasing recognition over the past few years, assumes that all materials may contain flaws of some magnitude.

These flaws exist due to

i) the metallurgical defects (as inclusions or porosity)

ii) microscopic crack like flaws (intrinsic or obtained during the operation) **[2]**.

Fracture mechanics is the science that relates the strength of a structure containing a crack or cracks to the material's fracture toughness, and to the crack size, shape, location, sharpness, and the stress that would lead to propagation of the flaw **[2]**. It may be regarded as the study of why structures fail, and perhaps best represented by the *'Triangle of Integrity'* as shown in Figure 1.1.

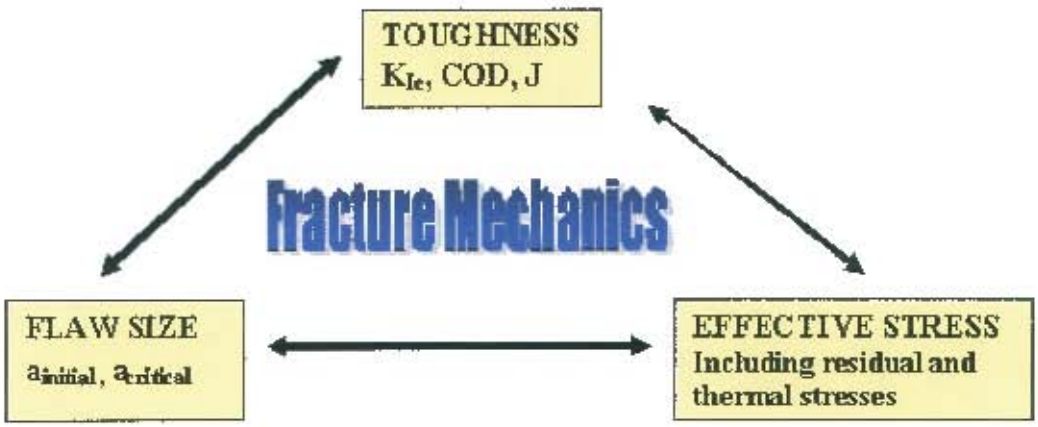

Figure 1.1: Triangle of Integrity

The fracture mechanics triangle of integrity approach can answer questions of structural integrity such as **[2]**:

- What load is safe for a given crack length?
- What is the residual structure strength as a function of crack size?
- How long might it take for a crack to grow from initial to critical size?
- What size of pre-existing flaw can be permitted? And
- How often a particular structure should be inspected?

This discipline of Fracture Mechanics is well established and of great value in assessing "fitness for purpose" in engineering applications. This is no less true for round or cylindrical shafts which find huge application in engineering, but which can still experience fatigue cracking under rotation conditions.

Round bars and cylindrical components have various types of application in mechanical design such as power transmission shafts, bolts, screws, tubes etc. Such structural components are often subjected to cyclic stresses, which can cause damage and premature failure by fatigue crack growth, often with assorted crack shapes as shown in Figure 1.2. Most of the mechanical failures by fatigue processes in rotor shafts have the crack origin on the surface and cracks grow with various

shapes, including semi-elliptical shape (or "thumbnail") as well as longer shallower crack shapes, rather like a "crescent moon".

These problems are frequently encountered in electric power plants, propeller shafts of screw driven ships or any other rotating load-transmission devices where systems run with a general nominal steady torsion combined with cyclic bending stress due to self-weight bending during rotation, or possible misalignment between journal bearings [3].

Figure 1.2: Failures of round components with formation of fatigue cracks of various shapes [4].

To assess the "fitness for purpose" of such cracked round shafts, and also in an attempt to lead to a greater understanding of their degradation, fracture mechanics methodologies may be employed. With reliable stress analysis, combined with appropriate and regular NDT inspection sudden catastrophic failure can largely be eliminated or minimised. Obtaining data in this manner allows fracture mechanics' specialists to predict when the sudden catastrophic failures are going to occur and in doing so can prevent these failures from occurring.

For the cases of linear elastic fracture mechanics, LEFM, the relationship with the triangle of integrity is based upon this equation

$$K = Y\sigma\sqrt{\pi a} \qquad 1.1$$

Where K is the stress intensity factor (MPa $\sqrt{m}$)

Y is the geometry compliance factor

σ is the total effective stress

a is the relevant flaw size.

The stress intensity factor is a scaling factor used to describe the intensity of applied stress at the tip of a crack of known size and shape. At the onset of rapid crack propagation in any structure containing a crack, the factor is called critical stress intensity factor or the fracture toughness for that particular material.

If the stress intensity factor K, is equal, or greater than the critical fracture toughness K_{IC} of the material, fracture is likely to occur. The so-called Y compliance factor, as shown in the equation 1.1, is linked by the fracture of toughness K_{IC}, the stress σ, and the flaw size, a. The intensity factor can be non-dimensionalised to determine the Y compliance function as shown by the equation 1.2,

$$Y = \frac{K_{IC}}{\sigma_{fail}\sqrt{\pi a_{crit}}} \qquad 1.2$$

The Y compliance functions, in this equation, have largely been developed theoretically and computationally, but relatively little experimental data is available **[5]**. This is particularly the case for so called "crescent moon" and "thumbnail" shaped cracks in round bars, even though these shapes are frequently encountered

in practice. Several authors have studied this question for semi elliptical cracks in round and cylindrical sections, as well as in rectangular bars. Using finite element methods, Newman and Raju **[6]**, Carpinteri **[7]**, Ng and Fenner **[8]**, have produced meaningful computational results for semi-elliptical cracks, for both tension and bending. Da Fonte and De Freitas **[3]** have similarly reported stress intensity factors for semi elliptical cracks in round bars under bending and torsion. Daoud and Cartwright **[9]** have considered straight cracks under tension and bending, and this has been extended by Erjian Si **[10]**, to include both straight front and semi elliptical cracks. All these stress intensity factor studies were undertaken from a computational point of view, making various assumptions for constitutive equations and boundary conditions. The number of reported *experimental* studies on the fracture behaviour of semi elliptical, "thumbnail" or "crescent moon" shaped surface cracks, of variable aspect ratio, is, however, somewhat limited **[5,11]**.

These computational solutions are dependent upon various assumptions of loading, boundary conditions and limitations of the experimental approach. The majority of computational work focuses on the determination of the relationship of Y v/s the crack aspect ratio (a/2c), and Y v/s (a/d), where a is the crack length, the term 2c refers to the circumferential length of the crack and d the diameter of the specimen as shown in Figure 1.3.

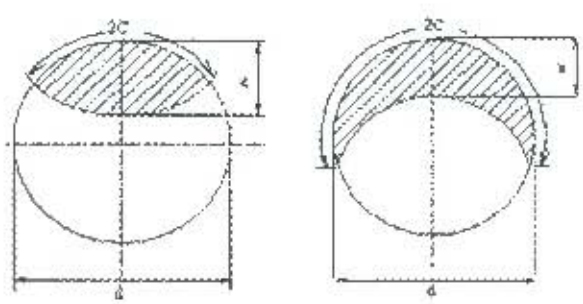

(a) (b)

Figure 1.3: (a) Thumbnail shape or almond shape cracks
(b) Crescent moon shape cracks

In view of this apparent paucity of experimental data on stress intensities for thumbnail and crescent moon shaped cracks, in particular in round bars, the present study was focussed specifically in this area. Experiments were conducted in particular on "crescent moon" shaped cracks. Surface fatigue cracks were forced to develop at specific points on round specimens of three different diameters (14mm, 17mm and 20mm) by creating a stress concentration effect. The specimens were fatigued through rotational bending conditions, and then loaded to failure in tension or bending. The data was then used to generate Y compliance values for a range of crack shapes and aspect ratios

1.2 Aim of the Project

The aim of the project was to develop quantitative estimates of the Y compliance function for various aspect ratio fatigue cracks using the following methology. The materials chosen for the project were Al7075 T6 and Al2030 T3 which were of high strength and low toughness. The approach of the project was firstly to determine the fracture toughness of these materials. Subsequently a variety of fatigue cracks of different circumferential lengths and depths were created in round bar specimens of different diameters. This led to a range of crack shapes from long shallow cracks known as 'crescent-moon' through to shorter, deeper "thumbnail" type crack shapes as shown in Figure 1.4.

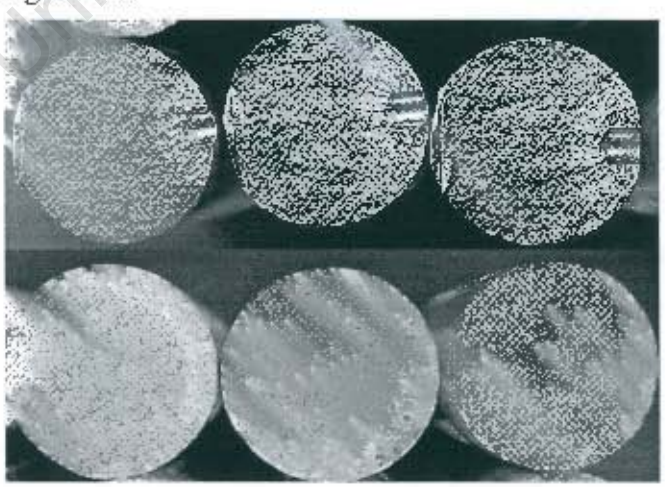

Figure 1.4: Thumbnail crack shapes and Crescent moon crack shapes.

Once the cracks were generated in the specimens they were loaded to failure either in bending or in tension. The Y-compliance was determined from the failure loads, known fracture toughness and measured crack depth a of respective specimens. In the experiment, the thumbnail specimens were broken in bending and the crescent moon specimens of different sizes were broken in tension as earlier tests in this laboratory have already partially considered crescent moon cracks in bending. The relationship between the normalised Y-compliance and the aspect ratios a/d and a/2c was investigated and compared to the available published data in the literature.

1.3 Scope and Limitations

Specimens were tested both in bending and tension. The sizes of the crescent moon specimens were designed according to the limitation of the rotational bending machine used. As for the thumbnail specimens, only relatively few were tested due to material limitations and time constraints and because the emphasis was on the crescent moon specimens.

1.4 Plan and Development

The thesis is structured into various sections. The first section covers the literature review relevant to this field. In particular discussion was on work covered mostly by different fracture mechanics specialists on round bars, and also some research done on fracture toughness and size effect.

The next section consists of the experimental methods and techniques of approach to perform particular experiments of this study, including fatigue testing of various shapes.

The thesis then presents the results obtained from the experiments, which were analysed and compared to the computational data from the literature and forms part

of the Discussion chapter. From these, conclusions and recommendations were made.

2. Literature Review.

2.1 Introduction

Many numerical analyses, theoretical studies and experimental investigations have been conducted to obtain stress intensity factors (SIFs) for three dimensional (3D) cracked round and cylindrical bodies. Empirical expressions and explicit solutions have also been obtained for surface and corner cracks on smooth strips or straight round bars at circular holes in finite thickness plates **[12-15].** This chapter considers research which has been undertaken, mostly computationally, by many fracture mechanics specialists, focussing on semi-elliptical cracks in round bars. It also provides a short review of the size effect on fracture toughness.

2.2 Computational Approach to the Problem of Stress Intensity Factors

There have been several studies to investigate stress intensity factors for semi elliptical cracks in both rectangular bars and round bars. The usual approach of the problem is computational, and experimental studies are limited **[5, 11]**. Numerical solutions such as finite element methods are being applied by using three-dimensional analysis techniques.

A short review of the authors who have undertaken successful researches in the fracture mechanics field for rectangular section on the stress intensity factors for semi elliptical crack are discussed.

Smith *et al* **[16,17, 18]** reported an increase in stress intensity at the junction of a semi elliptical crack with a free surface, as compared to the deepest part of a crack. Rice and Levy **[19]**, Nisantani and Murakami **[20]**, and Pickard **[21]** also successfully addressed the stress intensity problem, to semi circular cracks, from a

finite element point of view. Newman and Raju **[6]** and Newman **[22]** compared a range of solutions for the semi-elliptical surface cracks in plates under tension and bending and found that there was reasonably good agreement for shallow cracks but significant deviations for deep cracks (relative to the plate thickness). However, the accuracy of these methods varies significantly and appears to depend on the techniques used. The interpretation used by Newman and Raju **[6]** has been critically evaluated by Hosseini & Mahmoud **[23]** which were compared to the Society for Experimental Stress Analysis (SESA) recommendations (McGowan **[24]**), as well as crack shapes grown by fatigue and found to be generally acceptable.

Carpinteri **[25, 26]** used a model employing finite strips arranged in series and parallel to address the question of semi-elliptical surface cracks in plates, in tension and bending, where he obtained normalised stress intensity factor functions for a full range of aspect ratios and relative crack depth which were practical to use. More recently Tait, Herbert and Horn **[5]** and McKellar, Tait and Douglas **[11]**, at the University of Cape Town, provided some experimental stress intensity results which were consistent with their own computational results, as well as those of Carpinteri **[25, 26]** for thumbnail fatigue cracks for rectangular bars.

As for surface cracks in round bars, Raju and Newman **[6]**, Athanassiadis *et al* **[27]**, Nezu, Machida and Nakamura **[28]**, Forman and Shivakumar **[29]**, Daoud and Cartwright **[9]** approached the problem by also using a three dimensional finite element analysis.

Ng and Fenner **[8]** used an extrapolation method applied to the crack face displacement, for semi-elliptical cracks in round bars under tension and bending, taking account of the plane strain (internal) and plane stress (surface) conditions. His results were obtained from a three dimensional finite element analysis of the variation of the stress intensity factor K_I along the front of an edge crack in a circular bar having a length to diameter ratio of 3.

Cracks of various depths and with either straight or circular-arc fronts were modelled for the bar subjected to either tension or bending shown in Figure 2.1 (a) and (b).

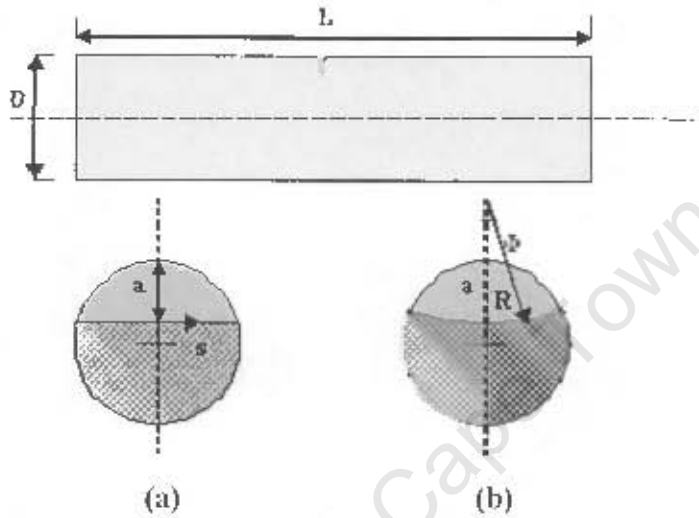

Figure 2.1: Edge crack in circular bar [8]: (a) Straight crack front, and (b) Circular-arc crack front

The circular arc radius R was assumed to be equal to (0.06D + a) with a crack centre of curvature at a distance of 0.56D from the bar surface. Layers of 20 node isoparametric brick elements were used as shown in Figure 2.2 where the thicknesses of successive layers were reduced towards the crack plane with an arithmetic progression ratio of 0.5. Side nodes adjacent to the crack front were shifted to quarter-point positions to induce the required $\sqrt{r}$ variation in the displacement functions for the crack front elements (where r is the distance from the front crack). To be able to generate the meshes efficiently, an interactive mesh generation program was developed.

The mesh used for curved-fronted cracks comprises 320 elements and 1687 nodes and for straight fronted cracks were 450 and 2319 nodes. For the curved front cracks a/D ratio in the range of 0.1 to 0.594 and 0.175 to 0.6 were analysed for

tension and bending respectively. The finite element method was also used to calculate the variation of the stress intensity factor along the straight crack fronts in grooved and ungrooved shafts and cracks with semi-circular fronts for both tension and bending **[30, 31]**. Figure 2.2 shows the finite element meshed shaft used by Ng and Fenner **[8]** for the curved fronted cracks.

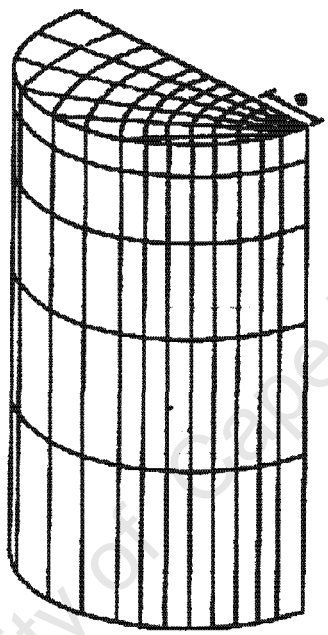

Figure 2.2: Finite element meshes for bar with curved fronted crack L/D=3, [8].

Ng and Fenner used a compliance Factor K^*_1 as calculated by the formula

$$K_I^* = \frac{K_1}{\sigma\sqrt{\pi a}} \qquad 2.1$$

Where K_1 is the fracture toughness of the material, σ is the effective stress for either tensile or bending and a is the crack depth.

The results for the stress intensity factors for both tension and bending, shown in Table 2.1 and Figures 2.3 and 2.4, indicate how the compliance factor varies with the relative depth a/D for both in tension and bending for angular position, $\phi = 0$.

a/d	K_I^* Tensile	K_I^* Bending
0.175	0.730	0.590
0.240	0.770	0.560
0.305	0.870	0.540
0.370	0.980	0.550
0.435	1.12	0.560
0.500	1.34	0.600
0.600	1.91	0.740

Table 2.1: Results of a/D vs. K_I^* ,[8].

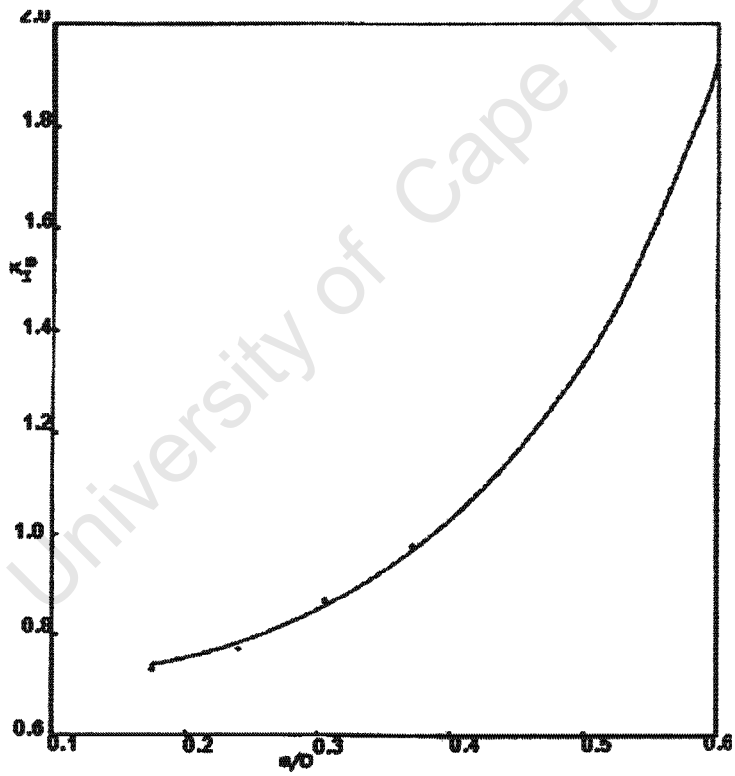

Figure 2.3: Graph of stress intensity factor $K_{I\,tensile}^*$ vs. a/D at the centre of a curved cracked front, [8].

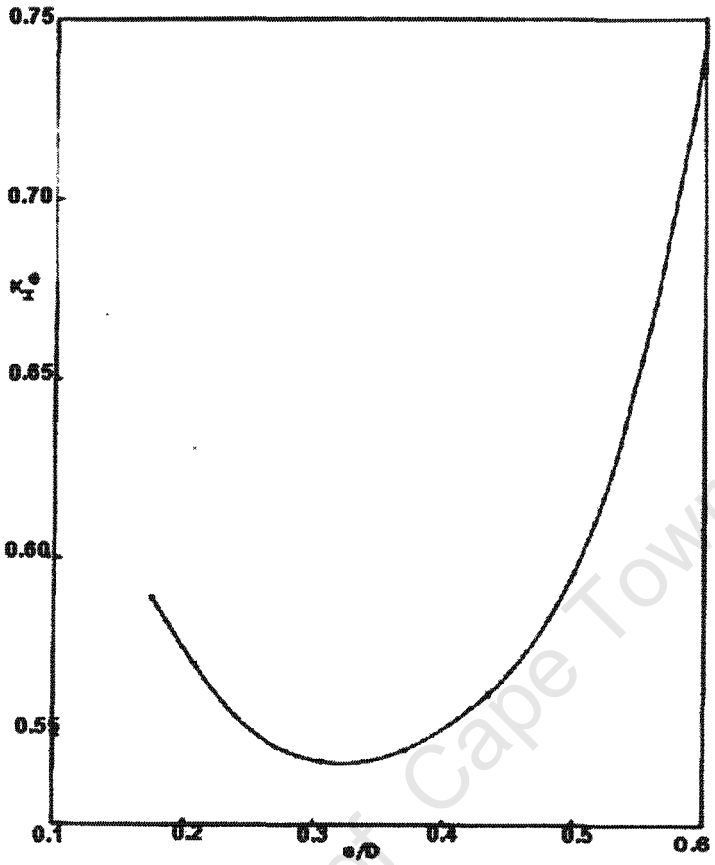

Figure 2.4: Graph of stress intensity factor $K_{I\ bending}^{*}$ vs. a/D at the centre of a curved cracked front, [8].

They found a maximum in the stress intensity factor at the centre of a straight crack front, but, when the crack was curved, the centre region has a minimum stress intensity factor for both tension and bending loading. The form of variation as a function of relative depth, however, was different for the tension and bending cases.

2.3 *A Proposed Normalised Stress Intensity Factor Curve*

Erjian Si **[10]** analyses results obtained from other authors **[9, 27-29, 31-35]**. Based on the analysed and comparison of those results, a normalized stress intensity factor as a function of crack depth was proposed.

The comparison of various results from the literature was difficult due to different definitions and measurements of crack shapes used by other authors as shown in Table 2.2.

Name of prime author	Analytical or experimental method	Assumed crack front configuration	Test results
Forman	Approximate equation	Circular arc crack front ⊥ cylinder surface	No
Newman	3-D Finite element	Semi-elliptical crack front ⊥ cylinder surface	No
Athanassiadis	Boundary integral equation	Semi-elliptical	No
Caspers	Weighted average function	Straight; semi-elliptical	No
Daoud	Strain energy release rate	Circular-arc; straight	Yes
Salah	3-D Finite element	Circular; straight	Yes
Nezu	Finite element	Circular	Yes
Bush	Experimental compliance measurements	Straight	Yes
Murakami (JSMS)	Body force method or approximate analysis	Semi-elliptical	No

Table 2.2: List showing Si's review of authors and their assumption of crack front shape, [10].

The stress intensity factor was expressed as

$$K_T = \sigma_T \sqrt{\pi a} F \quad \text{(Tension)} \qquad \textbf{2.2}$$

$$K_B = \sigma_B \sqrt{\pi a} F \quad \text{(Bending)} \quad \text{where,} \qquad \textbf{2.3}$$

$$\sigma_T = \frac{4P}{\pi d^2} \text{ (Uniform tension)} \qquad \textbf{2.4}$$

$$\sigma_B = \frac{32M}{\pi d^3} \text{ (Pure bending)} \qquad \textbf{2.5}$$

F is the dimensionless configuration factor (which is also known as the stress intensity factor), σ_T and σ_B which are the respective stresses for the tension and bending respectively.

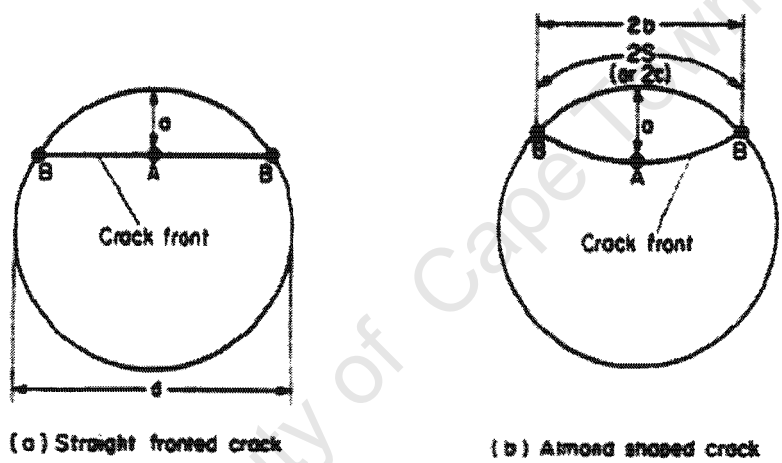

Figure 2.6: Crack configurations and definitions of crack parameters, [10].

Si **[10]** reviewed the literature pertaining to variable crack shapes in round bars and presents a synthesised and normalised stress intensity factor as a function of relative crack depth. The proposed solution for F- factors was obtained by combining selected solutions from Daoud and Cartwrigth **[9]**, Caspers and Mattheck **[32]**, Forman and Shivakumar **[29]**, Athanassiadis *et al.* **[27]**, Salah and Lovegrove **[31]** and Bush **[35]** for curved and straight fronted cracks and combining them together in the transition region.

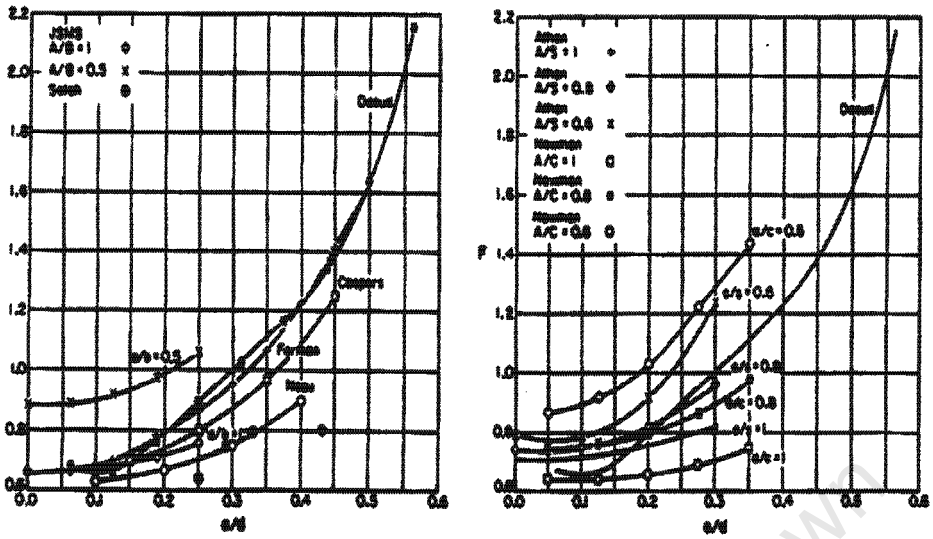

(a) (b)

Figure 2.7 (a) & (b) : Stress intensity F- factors at the centre of curved fronted edge cracks in round bars under tension as summaries by Si, [10].

Figure 2.7 illustrates the graphs from which his proposed solution was based. In Figure 2.7 (b), families of curves were obtained from specimens having similar aspect ratios of a/c or a/s which vary with different values of the relative depth, a/d and F the compliance factor. As the a/c value increases, the value of F factors decreases.

Si assumed that crack growth behaviour was formed as shown in Figure 2.8.

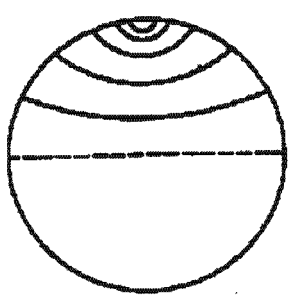

Figure 2.8: Assumed Crack behaviour, [10].

Si assumed that short cracks have curved fronts initially but gradually the cracks grow such that the front becomes straight by mid-thickness. The assumed crack configuration in Figure 2.8 was described as:

Curved fronted crack ($a/s \approx 0.78$), for $a<R$.

↓ In transition

Straight fronted crack ($a/s \rightarrow 0.64$), for $a \rightarrow R$.

- ***Comparing Results in Bending and Tension (Round Bar vs. Plates).***

The proposed data points for the compliance factors F_T (in tension) and F_B (in bending) with respect to the relative depth ratio a/d is shown in Table 2.3.

	Round bar				Plate		
	Tension	Bending			Tension	Bending	
a/d	F_T	F_B	F_T/F_B	t/W	F_T	F_B	F_T/F_B
0	0.74	0.74	1.0	0	1.12	1.12	1.0
0.1	0.75	0.65	1.15	0.1	1.2	1.04	1.154
0.2	0.92	0.61	1.51	0.2	1.375	1.05	1.31
0.3	1.18	0.707	1.67	0.3	1.67	1.12	1.491
0.4	1.663	0.9	1.85	0.4	2.12	1.26	1.683
0.5	2.425	1.15	2.11	0.5	2.825	1.49	1.896
0.6	3.691	1.5	2.46	0.6	3.05	1.9	2.132

Table 2.3: Proposed results for the comparison of the F- factors for curved front cracks, [10].

F_T values show much higher values than F_B values as a/d increases. Figure 2.9 and 2.10 illustrate the proposed results of the F-factors at the center of curved and straight fronted edge cracks in round bars under tension and bending respectively. The proposed results of the compliance factor for the round bars were also compared to that of a proposed solution of a rectangular plate as shown in Figure 2.11. It was interesting to note that results obtained in plate were much higher than that obtained for the round bar.

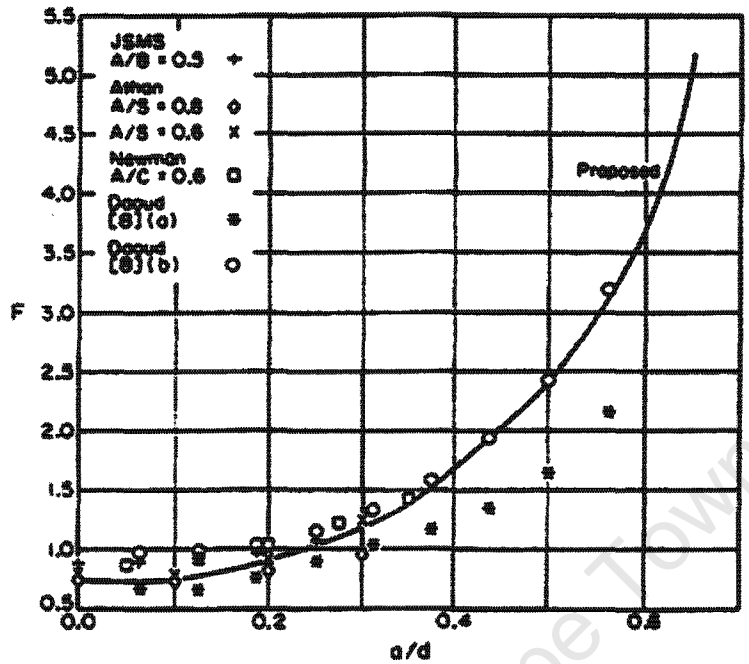

Figure 2.9: F compliance vs. a/d (in tension), [10].

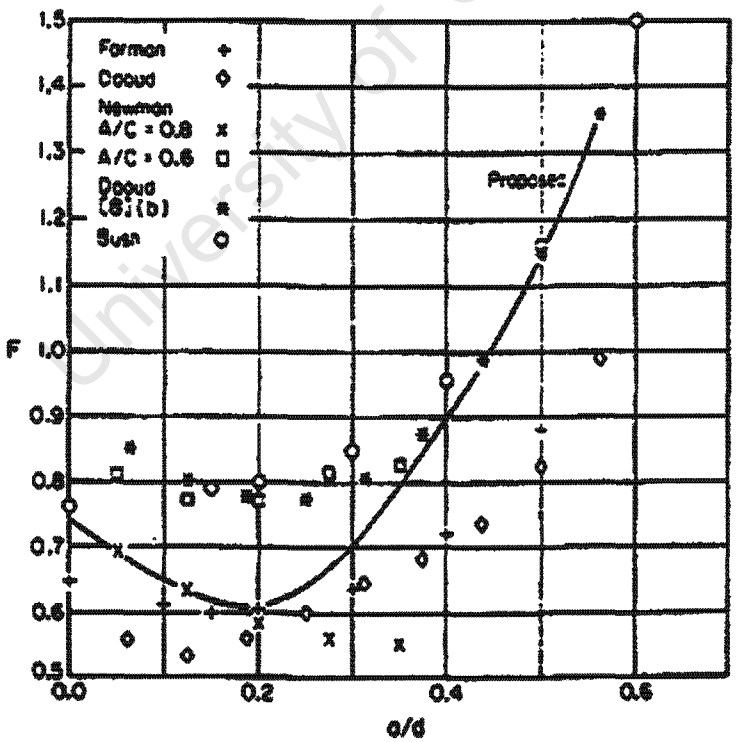

Figure 2.10: F compliance vs. a/d (in bending), [10].

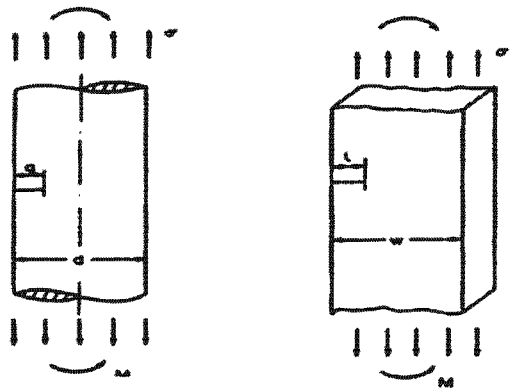

Figure 2.11: Round bar was compared to rectangular bar, [10].

Figure 2.12 shows the comparison of the proposed F-factors between the round bar solution and plate solution respectively. The intensity solution for both types indicates a similar tendency (as a function of crack length) in that stress intensity factors in rectangular plate are generally higher than that of round bars.

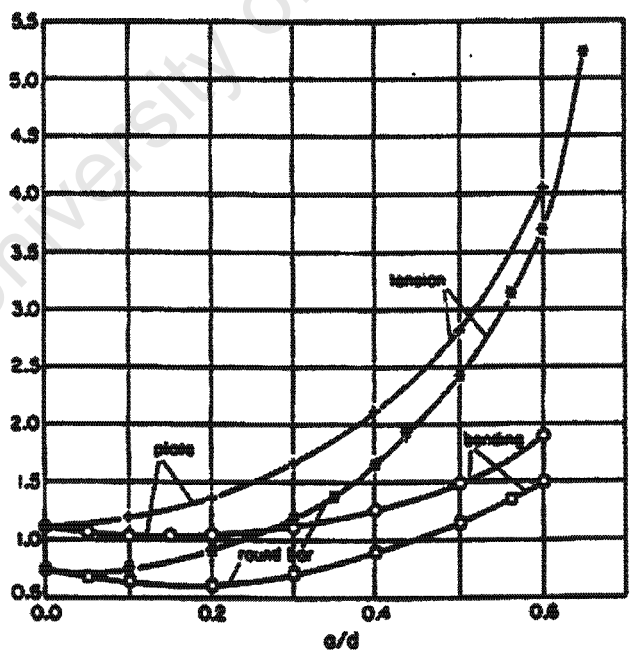

Figure 2.12: F compliance vs. a/d (in bending and tension), [10].

The range of interest for the aspect ratio *a*/2c interest was between 0.6 and 1.0 for a/d ≤ 0.5. The F factor is always higher for tension than for bending. The variation in stress intensity in both depth *a* and the surface length 2c of the crack was different.

From his results he pointed out that the intensity factor was always a maximum at the centre point A than the surface point B in Figure 2.6. Some of the authors **[27,32,33]** have pointed out that a/s tends to 1.0 for curved fronted cracks, the maximum SIF is at the surface i.e. at point B and as for straight fronted cracks as a/s tends to 0.6, the maximum SIF is at the centre i.e. point A.

2.4 The Stress Intensity Factor with Semi Elliptical Aspect Ratio

Carpinteri **[7,25]** has also made use of a three-dimensional finite element analysis for both straight fronted cracks and curved fronted cracks in round bars but using semi minor *a* and semi major axis *b* of an ellipse to characterise the crack as shown in Figure 2.13. Both of these types of cracks show a three dimensional nature **[8, 9, 31, 36-44]**. He investigated the influence of the crack with aspect ratio a/b on the stress intensity factor for the elliptical-arc surface cracks in round bars, which had not previously been extensively investigated **[27, 33, 34, 45, 46]**.

He assumes that an elliptical-arc surface could be used to characterise the crack. This was located in the centre-line cross section of a round bar with a diameter D and length 2l. The loading was either a tensile force F acting perpendicularly to the crack plane, or a bending moment M about an axis perpendicular to the crack depth *a*, so that the flaw was in the tension side of the bar, as shown in Figure 2.13. The relative crack depth $\xi = a/D$ ranged from 0.1 to 0.6, while the flaw aspect ratio a/b varied from 0.0 (straight crack front) to1.0 (circular-arc crack front). The generic point P along the crack front is identified by the normalised coordinate ζ / h.

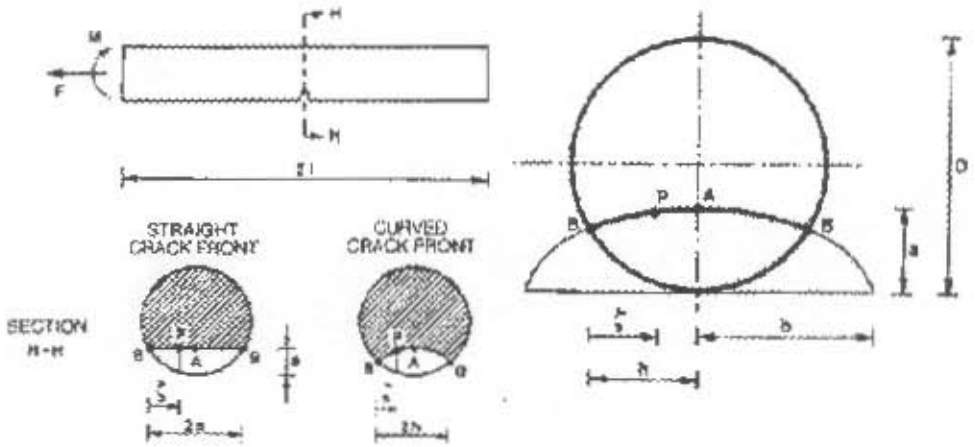

(a) (b)

Figure 2.13: (a) Cylindrical shaped structural component with straight front crack and curved fronted cracks.
(b) Elliptical-arc surface crack configuration, [7].

The maximum stress intensity factor is reached in correspondence to the deepest point on the crack front for a/b=0 and for a/b=1 it is attained near the external surface. Hence the straight front cracks tends to become curved where the flaw aspect ratio a/b increases while for a circular front tends to flatten that is a/b decreases.

2.4.1 Carpinteri's Stress Intensity Calculations

20 node isoparametric elements were used by Carpinteri to determine the stress intensity factor. The dimensionless stress intensity factor K^{*}_{IM} and K^{*}_{IF} were calculated.

K^{*}_{IM} - for the bending load

K^{*}_{IF} – for the tension load

$$K^{*}_{IF} = \frac{K_{I,F}}{\sigma_{F}(\pi a)^{\frac{1}{2}}} \qquad 2.6$$

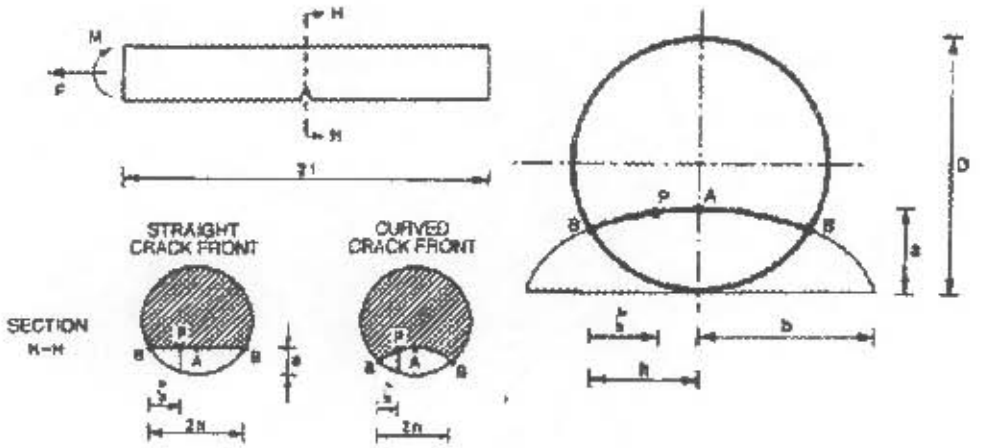

(a) (b)

Figure 2.13: (a) Cylindrical shaped structural component with straight front crack and curved fronted cracks.
(b) Elliptical-arc surface crack configuration, [7].

The maximum stress intensity factor is reached in correspondence to the deepest point on the crack front for a/b=0 and for a/b=1 it is attained near the external surface. Hence the straight front cracks tends to become curved where the flaw aspect ratio a/b increases while for a circular front tends to flatten that is a/b decreases.

2.4.1 Carpinteri's Stress Intensity Calculations

20 node isoparametric elements were used by Carpinteri to determine the stress intensity factor. The dimensionless stress intensity factor $K^{\sim}_{IM}$ and $K^{\sim}_{IF}$ were calculated.

$K^{\sim}_{IM}$ – for the bending load

$K^{\sim}_{IF}$ – for the tension load

$$K^{\sim}_{IF} = \frac{K_{I,F}}{\sigma_F (\pi a)^{\frac{1}{2}}} \qquad 2.6$$

$$K_{IM} = \frac{K_{I\text{-}M}}{\sigma_M (\pi a)^{\frac{1}{2}}} \qquad 2.7$$

Where σ_M and σ_F are the stresses for bending and tension respectively.

$$\sigma_F = \frac{F}{(\pi D^2/4)} \qquad 2.8$$

$$\sigma_M = \frac{M}{(\pi D^3/32)} \qquad 2.9$$

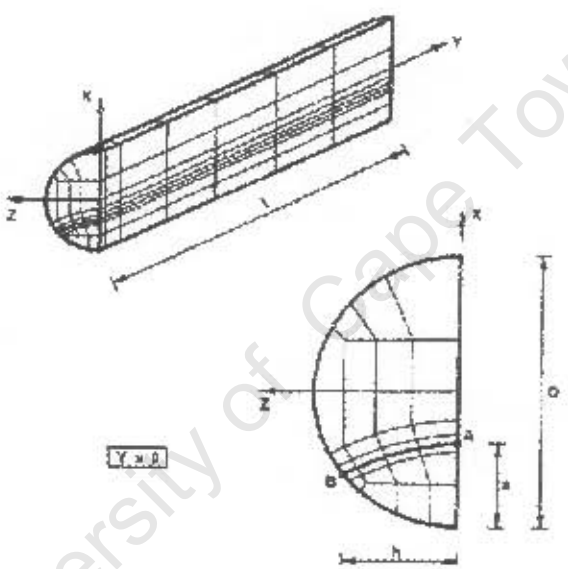

Figure 2.14: Finite element mesh for a round bar with an elliptical-arc surface crack [7].

Due to the cylindrical shape only one quarter of the bar was analysed as shown in Figure 2.14. The symmetry conditions have to be prescribed on the portions of the boundary defined by the two symmetry planes. A total of 210 finite elements and 1175 nodes were used in his model, shown in Figure 2.14. The ratio between quarter-point element size perpendicular to the crack front and maximum flaw depth a was assumed to be equal to 0.05/0.15 for the different values of ξ. The bar was considered to have a diameter of 50mm and a length of 200mm with elastic modulus of 206kNmm^2 and a Poisson ratio of 0.3.

2.4.2 Test Results Obtained for a/b Flaw Aspect Ratios

Carpinteri's theoretical results for SIF for various a/b aspect ratios are shown in Tables 2.4 and 2.5 for tension and bending. The range of a/b is from 0 to 1 which shows a transition from straight- fronted cracks to thumbnail shape cracks.

		$\xi = a/D$					
a/b	Point	0.1	0.2	0.3	0.4	0.5	0.6
0.0	A	1.05	1.23	1.49	1.92	2.70	3.81
	B	0.78	0.93	1.19	1.59	2.33	3.35
0.2	A	0.99	1.22	1.48	1.89	2.65	3.66
	B	0.72	0.92	1.18	1.58	2.32	3.34
0.4	A	0.95	1.15	1.39	1.77	2.46	3.50
	B	0.72	0.91	1.17	1.58	2.31	3.33
0.5	A	0.91	1.10	1.32	1.66	2.30	3.29
	B	0.72	0.91	1.17	1.57	2.31	3.32
0.6	A	0.87	1.04	1.25	1.56	2.14	3.00
	B	0.72	0.91	1.17	1.56	2.26	3.30
0.8	A	0.79	0.93	1.07	1.30	1.75	2.34
	B	0.72	0.90	1.13	1.46	2.12	3.02
1.0	A	0.71	0.82	0.93	1.08	1.35	1.67
	B	0.71	0.86	1.03	1.30	1.84	2.52

Table 2.4: Dimensionless stress intensity factor for different ξ and a/b values for the case of tensile loading, [7].

		$\xi = a/D$					
a/b	Point	0.1	0.2	0.3	0.4	0.5	0.6
0.0	A	0.86	0.87	0.89	0.96	1.19	1.47
	B	0.63	0.61	0.65	0.75	0.97	1.20
0.2	A	0.83	0.85	0.87	0.94	1.16	1.39
	B	0.62	0.61	0.66	0.76	0.97	1.20
0.4	A	0.78	0.80	0.82	0.91	1.08	1.36
	B	0.61	0.66	0.71	0.82	1.03	1.31
0.5	A	0.75	0.76	0.78	0.83	1.01	1.28
	B	0.64	0.68	0.74	0.83	1.05	1.40
0.6	A	0.71	0.72	0.73	0.78	0.92	1.14
	B	0.65	0.71	0.77	0.86	1.06	1.32
0.8	A	0.64	0.63	0.62	0.62	0.74	0.84
	B	0.64	0.72	0.77	0.86	1.07	1.27
1.0	A	0.58	0.55	0.50	0.50	0.52	0.55
	B	0.63	0.69	0.74	0.82	0.98	1.14

Table 2.5: Dimensionless stress intensity factor for different ξ and a/b values for the case of bending loading, [7].

Considering the case for tension loading, Figure 2.15 displays the dimensionless stress-intensity factor at the deepest point A (with continuous lines in Figure 2.15) and near point B (in dashed curves) against relative crack depth for different flaw aspect ratios a/b, in tension. It was noted that for a/b > 0.4, the two curves related to $\zeta/h = 1.0$ and $\zeta/h \cong 0.0$ intersect in a point, the abscissa of which defines the critical value ξ_{CR} for different a/b. It was found that K^{-}_{IF} is maximum at the point A for $\xi \leq \xi_{CR}$ and near point B for $\xi \geq \xi_{CR}$. It can be seen from the graph that the intersection point, that is ξ_{CR}, decreases as the value a/b increases. The maximum stress intensity factor was attained at point A where the parameter a/b and ξ tend to increase. When a/b reached a value for which the stress intensity is attained near point B, a/b tends to decrease in the following stages until the stress intensity factor shows the maximum at point A again [7].

For the case of bending, the trends of theses curves were similar to those described for the tension loading as shown in Figure 2.16. The value of the stress intensity K^{-}_{IM} at point A is greater than that near point B for $\xi < \xi_{CR}$, with ξ_{CR} decreasing as a/b increases.

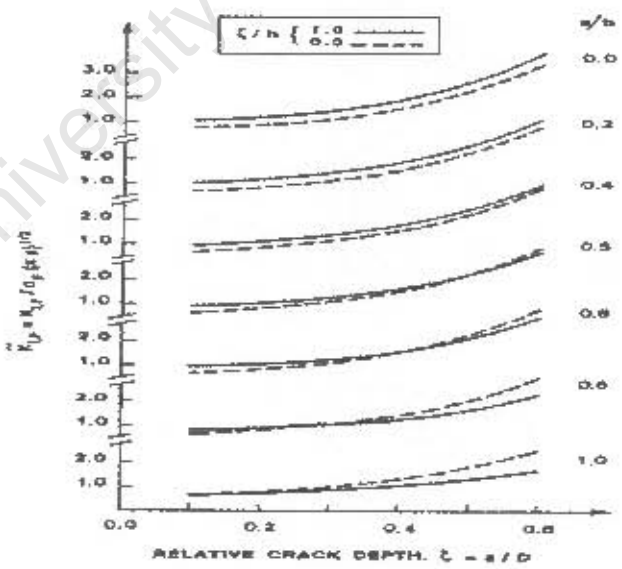

Figure 2.15: Dimensionless stress intensity K^{-}_{IF} (tension at point A ($\zeta/h = 1.0$) and near point B ($\zeta/h \cong 0.0$) against ξ, for different a/b, [7].

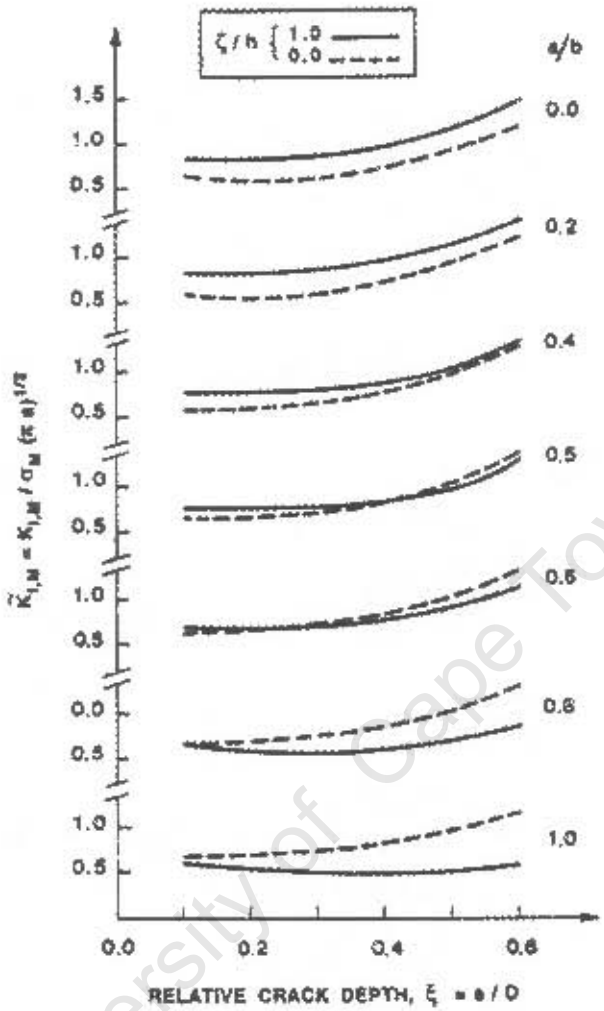

Figure 2.16: Dimensionless stress intensity K_{IM} (tension at point A ($\zeta / h = 1.0$) and near point B ($\zeta / h \cong 0.0$) against ξ, for different a/b, [7].

It was seen in both Figure 2.15 and 2.16, that the described crack growth stabilises for a/b equal to a value between 0.5 and 0.6 for 0.5<a/d<0.6 under tension and a/b equal to a value between 0.4 and 0.5 for 0.5<a/d<0.6 under bending respectively.

Carpinteri [7] pointed out that Caspers *et al.* [32, 47] have shown similar trends and indicated that the aspect ratio of an initially circular-arc tends to approach 0.78 in tension and 0.71 in bending. However, they did not specify at what relative depth,

a/d that occurred. Analogously, Athanassiadis *et al.* [27] have predicted stabilisation of crack front shape at the value of a/b =0.78 for both tension and bending loading.

Forman and Shivakumar **[29]** proposed an equation for both straight fronted cracks and curved fronted cracks and found that a/b ≅ 0.63 at a/b =0.5 for both bending and tension.

Carpinteri compared his results with available data from other authors **[27, 34, 45, and 46]** and his results were found to be consistent for both tension and bending with values within about 10-15% of those from others as shown in Figure 2.17.

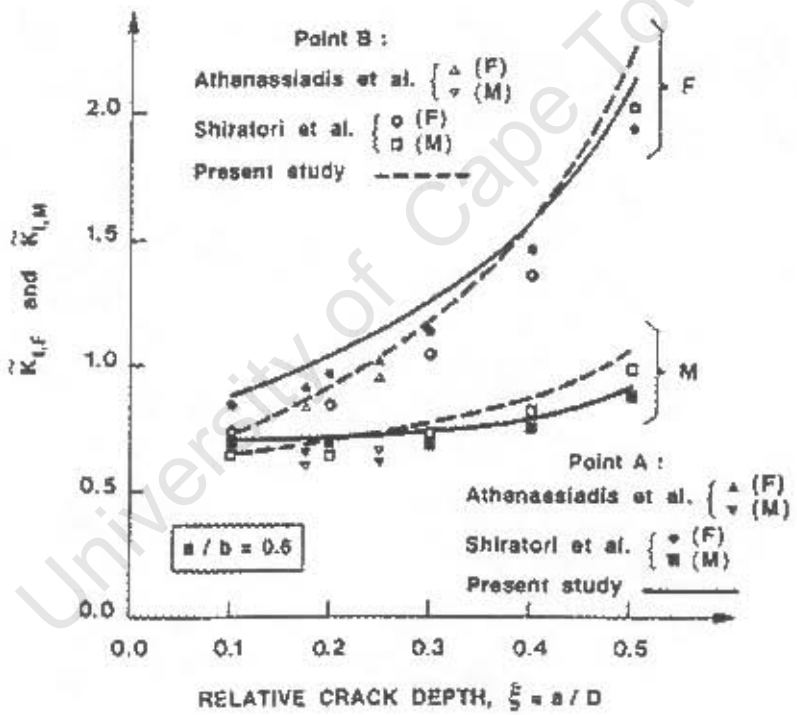

Figure 2.17: Dimensionless stress intensity factors for $\tilde{K}_{IF}$ and $\tilde{K}_{IM}$ at point A and B for an elliptical- arc surface crack with a/b =0.6, [7].

2.5 *SIFs for Semi-elliptical Surface cracks in Round Bars under Bending and Torsion*

The discussion of reported data has considered Cracks in round bars subject to tensile and bending stress. Da Fonte and De Freitas **[3]** have extended this to include torsion as well as bending. They presented stress intensity factors for semi-elliptical cracks in round bars subjected to bending and torsion using a three dimensional finite element model. SIF solutions for a wide range of geometries under Mode I loading are reported in literature but Mode III torsional loading of shafts with cracks solution are less common, due to difficulties in obtaining accurate analytical or numerical solutions.

The aim of their research was to obtain stress intensity factors (K_I, K_{II} and K_{III}) for semi elliptical cracks in round bars. Figure 2.18 shows the elliptical profile of a typical crack front. The elliptical crack front was assumed to present a constant crack length/crack depth ratio as experimentally obtained in previous studies **[48, 49]** and illustrated by equation 2.10. The geometric parameters for eight ellipses are presented in Table 2.6 and the semi-minor axis of the ellipse a is calculated according to equation 2.11.

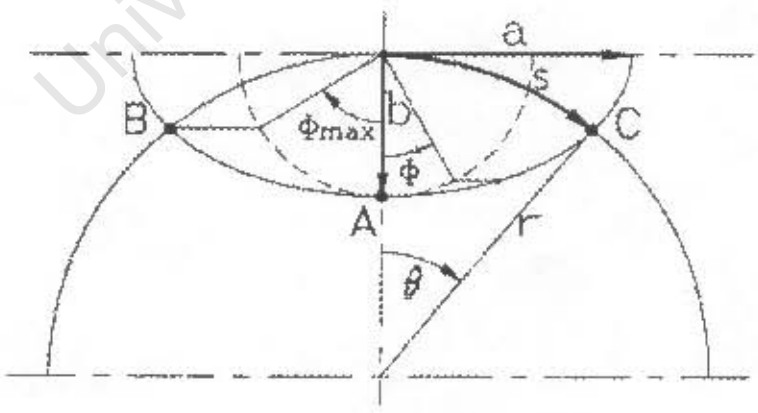

Figure 2.18: Geometry of semi-elliptical surface crack, [3].

$$b = \frac{2s}{\pi} \qquad 2.10$$

Ellipses	θ	b/r	b/a	b/s
1	10°	0.111	0.6338	0.6366
2	20°	0.222	0.6253	0.6366
3	30°	0.333	0.6104	0.6366
4	40°	0.444	0.5878	0.6366
5	50°	0.555	0.5555	0.6366
6	60°	0.666	0.5091	0.6366
7	70°	0.777	0.4413	0.6366
8	80°	0.888	0.3325	0.6366

Table 2.6: Geometric parameters of the eight ellipses studied by Da Fonte [3].

$$a = \frac{r.\sin 0}{\sqrt{1-\frac{r^2}{b^2}(1-\cos\theta)^2}} \qquad 2.11$$

2.5.1 *Da Fonte's 3-Dimension Finite Element Model*

Da Fonte **[3]** three-dimensional analysis was carried out by using 20-node isoparametric solid elements. The stress square-root singularity is modelled by shifting the finite element mid-side nodes near the crack front to quarter point position **[50, 51]**. The elastic modulus was assumed to be 207000 MPa and Poisson's ratio of 0.3. The finite element mesh consists of 3168 elements and about 15000 nodes depending on the type of ellipse which was being analysed. Figure 2.19 illustrates the finite element model. The code used to develop the solution was COSMOS/M.

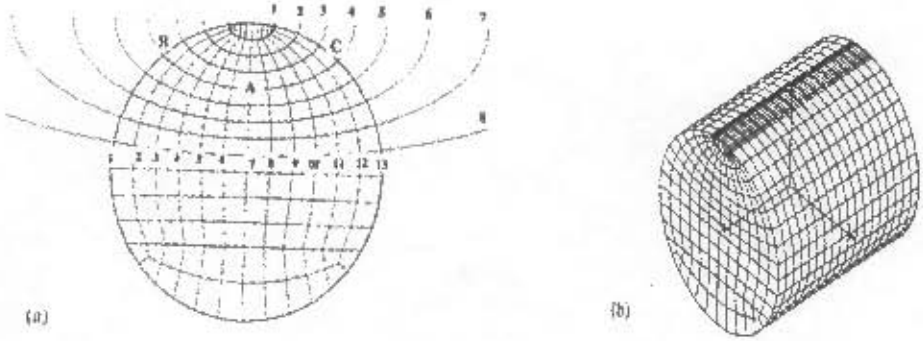

Figure 2.19: Finite element model: (a) Cross-section with eight semi-elliptical cracks. (b) Three-dimensional view round bar [3].

In order to be sure of the results obtained, Manuel da Fonte **[3]** performed a series of numerical tests subjecting the cracked geometry to pure bending. Several solutions are available in Raju and Newman **[33]**, Shiratori *et al.* **[45]**, Murakami **[34]** and Carpinteri **[7,52-54]**, where the SIFs were obtained by different techniques (finite element, body forces) and different parameters to define the crack geometry either by the crack depth *b* or half-crack length *s*. The arc crack length (2s), the parameter experimentally determined in fatigue crack growth tests **[48, 49, 55]** used by Shiratori **[45]** and Murakami **[34]** was chosen to compare results obtained by Da Fonte. Hence the Mode I stress intensity factor K_I for any point along the surface crack front was obtained from the equation 2.12.

$$K_I = F_I\left(\frac{b}{r}, \frac{b}{a}, \phi\right) B_S \sqrt{\pi s} \qquad \textbf{2.12}$$

Where B_S is the remote applied bending stress, s is the arc crack half-length and F_I is the boundary correction factor or the dimensionless Stress Intensity Factor for Mode I. This is itself a function of the elliptical crack shape- (b/a) flaw aspect ratio,

relative crack depth (b/r) and position along the crack front, which is defined by the parametric angle ϕ as shown in Figure 2.18.

2.5.2 Calculating Mode II and III by Da Fonte [3]

Da Fonte and De Freitas **[3]** also assumed that the crack always maintains an elliptical shape, and defined the point on the crack front at the deepest crack, A and the points where the crack intersect the external surface of the round bar B,C as being the most important. When analysing a crack in 3D geometry, problems frequently occur at free boundaries **[56]**.Theoretically **[57-59]**, from fracture energy considerations, the singularity power at the border (points B and C of the crack front) depends on the material Poisson ratio ν and on the intersection angle β between crack front and external surface. Manuel da Fonte used $\beta = 87^{\circ}$ which he assumed constant for each ellipse.

For Mode I loading **[54, 57-59]**, with a Poisson ratio of 0.3, a singularity of 1/2 is obtained for $\beta = 100.4^{\circ}$ and for Mode II and III loading $\beta = 67^{\circ}$. Hence the method of using quarter point finite element (square root singularity) does not produce reliable results in the boundary layer at points B and C. Since this effect is confined by a small zone **[54, 60]**, the nearest nodes in the mesh at points B and C were used to obtain the results for K_I, K_{II} and K_{III}.

The stress intensity factors K_{II} and K_{III} were presented by the same geometric parameters used for Mode I as shown by equations 2.13 and 2.14.

$$K_{II} = F_{II}\left(\frac{b}{r}, \frac{b}{a}, \phi\right) T_S \sqrt{\pi s} \qquad \textbf{2.13}$$

$$K_{III} = F_{III}\left(\frac{b}{r}, \frac{b}{a}, \phi\right) T_S \sqrt{\pi s} \qquad \textbf{2.14}$$

Where T_S is the remote applied torsional stress in the round bar and F_{II} and F_{III} are the boundary correction factors for Mode II and Mode III, respectively.

2.5.3 *Da Fontes' Results Compared to Available Literature*

- ***Bending Case***

Da Fonte's results as represented below were compared to authors as shown in Table 2.7. For the shorter crack depths, the relative difference obtained is between 2% and 5% with respect to the mean value of literature and for the larger cracks depths, the difference is between 12% and 15% which he regarded as reasonable.

ELLIPSES	points	present	Shiratori [3]	Newman [2]	Carpinteri [5]
ELLIPSE 1	A	0.602	0.603	0.627	
b/t=0.111	B*-C*	0.568	0.530	0.569	
ELLIPSE 2	A	0.599	0.577	0.601	
b/t=0.222	B*-C*	0.525	0.543	0.567	
ELLIPSE 3	A	0.564	0.562	0.590	
b/t=0.333	B*-C*	0.500	0.542	0.557	
ELLIPSE 4	A	0.546	0.559	0.593	
b/t=0.444	B*-C*	0.485	0.540	0.573	
ELLIPSE 5	A	0.555	0.575	0.611	0.596
b/t=0.555	B*-C*	0.484	0.552	0.579	0.598
ELLIPSE 6	A	0.564	0.613	0.615	0.635
b/t=0.666	B*-C*	0.500	0.551	0.561	0.613
ELLIPSE 7	A	0.611	0.676	0.626	0.691
b/t=0.777	B*-C*	0.524	0.559	0.551	0.648
ELLIPSE 8	A	0.681	0.767		0.799
b/t=0.888	B*-C*	0.568	0.615		0.713

Table 2.7: Normalised Stress intensity factors F_I at points A, B and C [3].

The correlation of Da Fontes' results with those of Murakami **[34]** is within less than 10%, while comparison with in Carpinteri **[7]** as mentioned have the accuracy within approximately 10% and 15%. The correlation with Raju and Newman **[33]** is also less than 10% and in Shiratori the accuracy is undefined. Da Fonte's **[3]** results were satisfactory in comparison with the other authors as shown in Figure 2.20 (a) and (b).

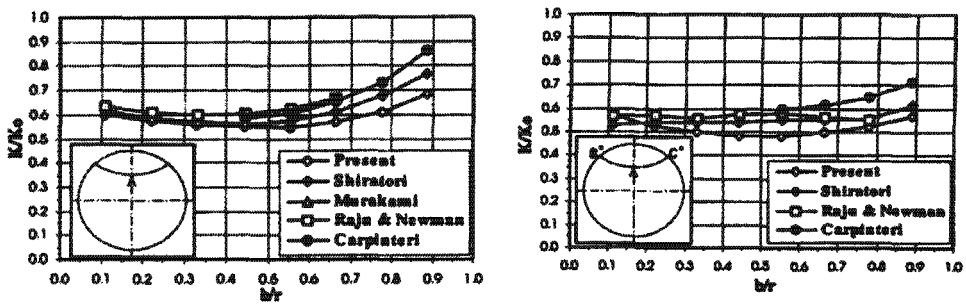

(a) (b)

Figure 2.20: Comparison of Da Fonte's study [3] with other author's work for
(a) Dimensionless K_I at point A for each crack front.
(b) Dimensionless K_I at points B and C for each crack front.

- ***Torsion Case***

The stress intensity factors for the torsional case were calculated in a similar way as the bending case, by replacing the bending stress with the torsional stress to the same eight semi- elliptical surface cracks. Da Fonte [3] found that point A exhibited a pure state of Mode III i.e. (K_I=K_{II}=0) and for points B and C, the numerical values for K_{III} obtained are consistent to each other, while asymmetrical values are shown by K_{II}. He indeed affirms that this behaviour confirms the lack of symmetry conditions for the case of torsion loading stress as shown in Figure 2.21 (a). For his experiment no comparisons can be performed since no available data exists in the literature, compared to the bending case. Table 2.6 shows the dimensionless stress intensity factors for F_I, F_{II} and F_{III} along the eight crack profile divided into 12 equal parts. A plot of the node displacements, obtained for crack front no.5 is shown in Figure 2.21(b).

Dimensionless Stress Intensity Factors along eight semi-elliptical front cracks in round bars

Points	BENDING F_I	TORSION F_{II}	TORSION F_{III}
Ellipse 1			
1B	0.498	−0.541	−0.232
2B*	0.415	0.026	−0.438
3	0.509	0.023	−0.633
4	0.566	0.022	−0.770
5	0.605	0.006	−0.856
6A	0.619	0.000	−0.884
7	0.605	−0.006	−0.855
8	0.566	−0.022	−0.770
9	0.509	−0.023	−0.633
10C*	0.415	−0.026	−0.438
11C	0.498	0.541	−0.232
Ellipse 2			
1B	0.603	−0.674	−0.269
2B*	0.525	−0.618	−0.272
3	0.532	−0.583	−0.334
4	0.549	−0.528	−0.437
5	0.570	−0.424	−0.564
6	0.590	−0.247	−0.680
7A	0.599	0.000	−0.732
8	0.590	0.247	−0.680
9	0.570	0.424	−0.564
10	0.549	0.528	−0.437
11	0.532	0.583	−0.334
12C*	0.525	0.618	−0.272
13C	0.603	0.674	−0.269
Ellipse 3			
1B	0.530	−0.717	−0.322
2B*	0.500	−0.615	−0.298
3	0.514	−0.563	−0.357
4	0.528	−0.493	−0.455
5	0.544	−0.380	−0.563
6	0.558	−0.213	−0.654
7A	0.565	0.000	−0.692
8	0.558	0.213	−0.654
9	0.544	0.380	−0.563
10	0.528	0.493	−0.455
11	0.514	0.563	−0.357
12C*	0.500	0.615	−0.298
13C	0.530	0.717	−0.322
Ellipse 4			
1B	0.479	−0.764	−0.374
2B*	0.485	−0.612	−0.342
3	0.502	−0.548	−0.401
4	0.516	−0.463	−0.490
5	0.530	−0.343	−0.577
6	0.541	−0.185	−0.644
7A	0.547	0.000	−0.669
8	0.541	0.185	−0.644
9	0.530	0.343	−0.577
10	0.516	0.463	−0.490
11	0.502	0.548	−0.401
12C*	0.485	0.612	−0.342
13C	0.479	0.764	−0.374

(continued in next column)

(continued)

Points	BENDING F_I	TORSION F_{II}	TORSION F_{III}
Ellipse 5			
1B	0.447	−0.816	−0.428
2B*	0.484	−0.613	−0.396
3	0.503	−0.533	−0.456
4	0.517	−0.431	−0.533
5	0.530	−0.307	−0.599
6	0.540	−0.161	−0.644
7A	0.544	0.000	−0.661
8	0.540	0.161	−0.644
9	0.530	0.307	−0.598
10	0.517	0.432	−0.533
11	0.503	0.533	−0.456
12C*	0.484	0.613	−0.396
13C	0.447	0.816	−0.428
Ellipse 6			
1B	0.436	−0.879	−0.491
2B*	0.500	−0.610	−0.461
3	0.524	−0.512	−0.520
4	0.540	−0.397	−0.582
5	0.554	−0.272	−0.627
6	0.563	−0.138	−0.655
7A	0.567	0.000	−0.664
8	0.563	0.138	−0.655
9	0.554	0.272	−0.627
10	0.540	0.397	−0.582
11	0.524	0.512	−0.520
12C*	0.500	0.610	−0.461
13C	0.436	0.879	−0.491
Ellipse 7			
1B	0.431	−0.959	−0.570
2B*	0.523	−0.608	−0.538
3	0.556	−0.489	−0.591
4	0.578	−0.362	−0.636
5	0.593	−0.239	−0.663
6	0.603	−0.117	−0.676
7A	0.607	0.000	−0.680
8	0.603	0.117	−0.676
9	0.593	0.239	−0.663
10	0.578	0.362	−0.636
11	0.556	0.489	−0.591
12C*	0.523	0.608	−0.538
13C	0.431	0.959	−0.570
Ellipse 8			
1B	0.438	−1.066	−0.675
2B*	0.568	−0.612	−0.627
3	0.616	−0.468	−0.670
4	0.647	−0.328	−0.698
5	0.667	−0.207	−0.708
6	0.679	−0.099	−0.711
7A	0.683	0.000	−0.710
8	0.679	0.099	−0.711
9	0.667	0.207	−0.708
10	0.647	0.328	−0.698
11	0.616	0.468	−0.670
12C*	0.568	0.612	−0.627
13C	0.438	1.066	−0.675

Table 2.6 : Dimensionless stress intensity factors for F_I, F_{II} and F_{III} along the eight crack profile divided into 12 equal parts due to Da Fonte [3].

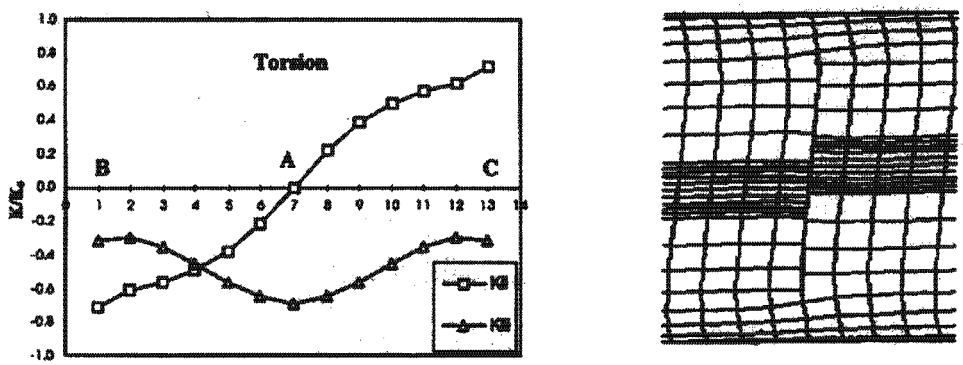

Figure 2.21 :(a) Dimensionless K_{II} and K_{III} along the crack front (for crack front no.3),
(b) Deformed mesh for Mode II with crack front no 5, [3].

2.6 *SIFs for Elliptical Surface Cracks in Round Bars with Different Stress Concentration Coefficients*

A further extension of the SIF concept for cracks in round bars was undertaken by Guo **[61]** on the effect of stress concentrations. Guo's research investigated the dependence of stress intensity factors of surface cracks in notched round bars upon stress concentration coefficient and notch geometry. He similarly used three–dimensional finite element models with 20-node singular elements, which were arranged round the tip of the crack. In his investigation, he considered a wide range of notch and crack geometry parameters and also compared available numerical data to experimental results to show effectiveness of his present results.

2.6.1 Crack Configuration, Notch Geometry and FE Model used by Guo

Before investigating the influence of notch geometry and theoretical stress concentration coefficient upon the SIFs of surface cracks at the root of the crack, Guo **[61]** analysed the influence on SIFs for round bar in various states:

(a) without notch,

(b) with semicircular annular notch,

(c) U-type annular notch and a

(d) V-type annular notch of 60° opening angle as shown in Figure 2.21.

Six cases of geometric parameters were assumed as listed in Table 2.9. Without a crack the stress concentration coefficients K_t was found to be 1, 2.5, 2.5, 2.5, 4 and 5 respectively **[62]**. The minimum diameter d chosen was 7.5 mm. Different notch geometries in cases 2,3 and 4 were given the same stress concentration coefficient, K_t = 2.5 to show the effect of the notch geometry on SIFs .The cracks had a semi elliptical shapes with semi-major axis *c* and semi minor axis *a* as shown in Figure 2.22 (c).

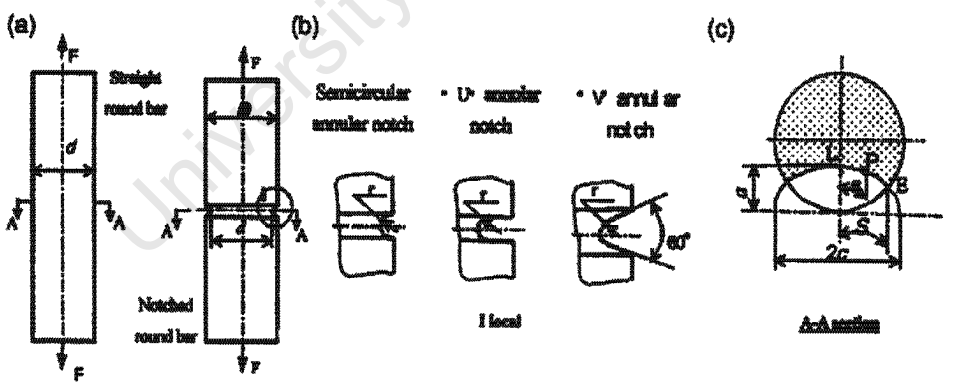

Figure 2.22: Guo's analysis cases [61]:
(a)Round bar without notch, (b) with semicircular annular notch, (c)U-type annular notch and V-type annular notch of 60° opening angle.

2.6.1 Crack Configuration, Notch Geometry and FE Model used by Guo

Before investigating the influence of notch geometry and theoretical stress concentration coefficient upon the SIFs of surface cracks at the root of the crack, Guo **[61]** analysed the influence on SIFs for round bar in various states:

(a) without notch,

(b) with semicircular annular notch,

(c) U-type annular notch and a

(d) V-type annular notch of 60° opening angle as shown in Figure 2.21.

Six cases of geometric parameters were assumed as listed in Table 2.9. Without a crack the stress concentration coefficients K_t was found to be 1, 2.5, 2.5, 2.5, 4 and 5 respectively **[62]**. The minimum diameter d chosen was 7.5 mm. Different notch geometries in cases 2,3 and 4 were given the same stress coefficient, $K_t = 2.5$ to show the effect of the notch geometry on SIFs .The cracks had a semi elliptical shapes with semi-major axis *c* and semi minor axis *a* as shown in Figure 2.22 (c).

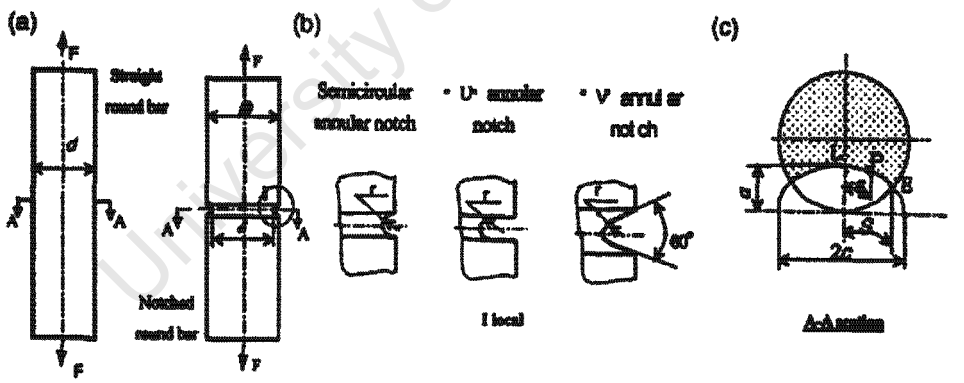

Figure 2.22: Guo's analysis cases [61]:
(a)Round bar without notch, (b) with semicircular annular notch, (c)U-type annular notch and V-type annular notch of 60° opening angle.

Specimen number	Notch type	Dimension of specimen (mm)			Stress concentration coefficient K_t
		D	d	r	
Case 1	Without notch	–	7.5	–	1
Case 2	Semi-circular annular notch	8.532	7.5	0.516	2.5
Case 3	'U' annular notch	12	7.5	0.79	2.5
Case 4	'V' annular notch	12	7.5	0.39	2.5
Case 5	'V' annular notch	12	7.5	0.26	4
Case 6	'V' annular notch	8.969	7.5	0.135	5

Table 2.9: Dimensions and theoretical stress concentration coefficients of specimens [61].

Figure 2.23 illustrates the finite element mesh model (FE) of the specimens analysed. Twenty node hexahedron elements have been used in the FE model to provide a high precision of the notch root radius and the crack shape. Elements were arranged to ¼ point position in order to simulate square root singularity of stress and strain near the crack border as shown in Figure 2.23.

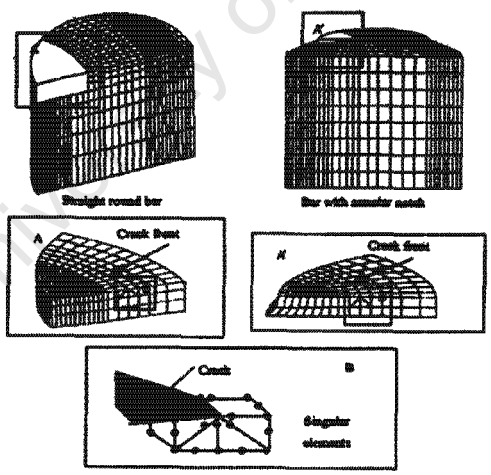

Figure 2.23: Finite element model and element mesh from Guo [61].

2.6.2 Guo's Stress Intensity Factors Calculations

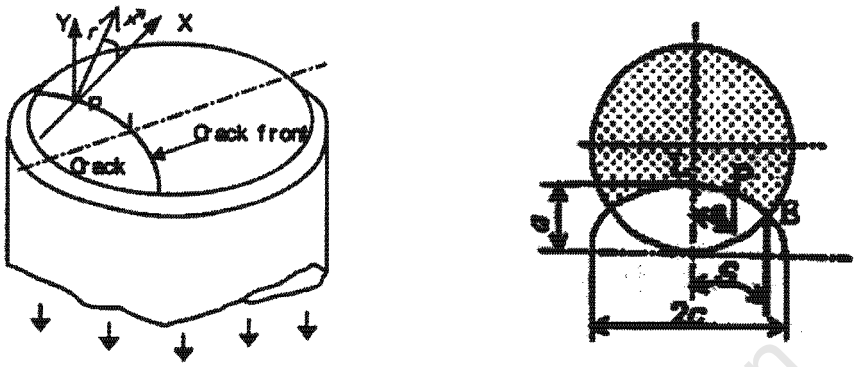

(a) (b)

Figure 2.24: (a) Local coordinates at elliptical crack front.
(b) Crack parameter measured, [61].

From Figure 2.24 (a), the coordinate set (X,Y) was defined at any position of point P along the crack front to calculate the SIF at that point. By using polar coordinate (r, ϕ) in the X-Y plane, P is perpendicular to both X and Y axis. Assuming that the crack opening displacement expression, which was given by the $r^{-1/2}$ singular solution, is valid for the surface crack **[61, 63, 64]**, the displacement perpendicular to the crack surface was written as

$$V = \frac{(1+\nu)K_I}{2E}\sqrt{\frac{r}{2\pi}}\left[(2\lambda+1)\sin\frac{\phi}{2} - \sin\frac{3\phi}{2}\right] \qquad \textbf{2.15}$$

where ν is the Poisson's ratio, E the Elastic modulus and K_I is the SIF at point P. λ is a function of Poisson's ratio and stress state which is reflected as E' in equation 2.17 **[61]**.

The opening displacement V under remote tensile stress σ can be obtained as

$$V_{\phi=180^o} = \frac{(1+\nu)(\lambda+1)K_I}{E}\sqrt{\frac{r}{2\pi}} \qquad \textbf{2.16}$$

and this equation leads to equation 2.17 **[61]**.

$$K_I = \frac{\sqrt{2\pi}E'V|_{\phi=180^\circ}}{4\sqrt{r}} \text{ as } r \to 0 \qquad \textbf{2.17}$$

where $E' = E$ in plane stress state and $E' = E/(1-\nu^2)$ in the plane strain state.

To verify the validity of the equation, Guo's results **[61]** were compared to those of Li and Chen **[65]** as shown in Figure 2.25 where γ is the relative location of the point of interest P on the crack front. Point P is expressed as the ratio of s to half of the length of the whole crack front S as shown in Figure 2.24(b) and Y is the normalised SIF which Guo defined in equation 2.18 (later). His results were found to be comparable with those of Chen **[65]**.

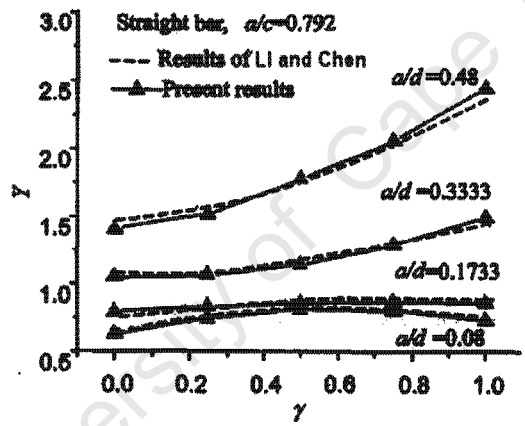

Figure 2.25: Comparison of Guo's [61] results with Chen [65] for normalised SIFs of surface crack of straight crack of straight bar.

2.6.3 Influence of Notch Geometry and K_t on SIFs of Surface Crack for Round Bar

By analysing the SIFs of the different notch geometries with similar K_t values, it was observed that although the notch geometry changes significantly, the corresponding change in SIFs is not that significant as shown in Figure 2.26. It was recorded that the change in SIF was less that 10%. However, the stress intensity

factor of surface cracks in notched bars was found to be largely dominated by the stress concentration coefficient K_t rather than the geometry of notches. The influence of K_t upon the SIFs for surface crack with different depth ratio a/d is shown in Figure 2.27 **[61]**. It can be seen that K_t has a strong influence for small surface cracks in Figure 2.27 (a) which becomes weaker as the crack grows Figure 2.27 (b)-(c). Figure 2.27(a) shows that the SIF increases in the whole crack border with increasing K_t but for crack a/d = 0.333, the influence of K_t is very weak in Figure 28(c). For larger cracks, the SIF in the interior crack showed a decreasing effect, with an increase in K_t value. The overall influence of K_t on the SIF decreases as crack grows. The influence of K_t on the average SIF along the whole crack front is illustrated in the bar chart in Figure 2.28.

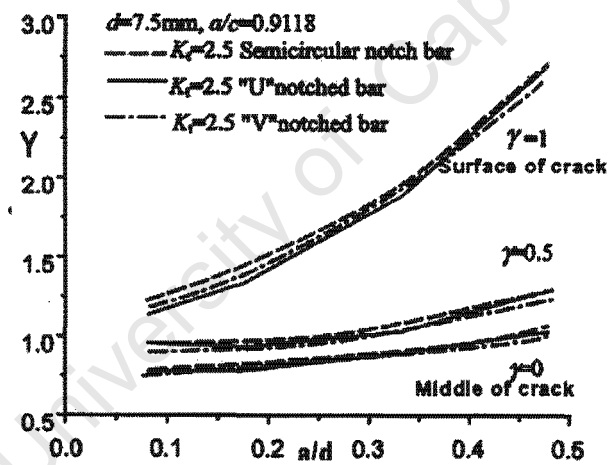

Figure 2.26: Influence of notch geometry on SIFs for K_t = 2.5, [61].

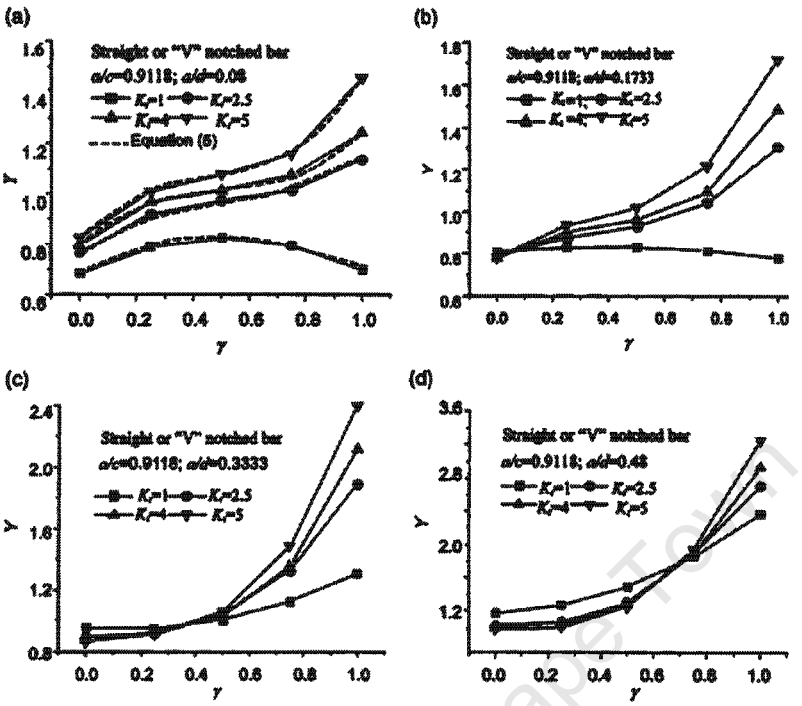

Figure 2.27: Influence of K_t on SIFs of notched round bars [61].

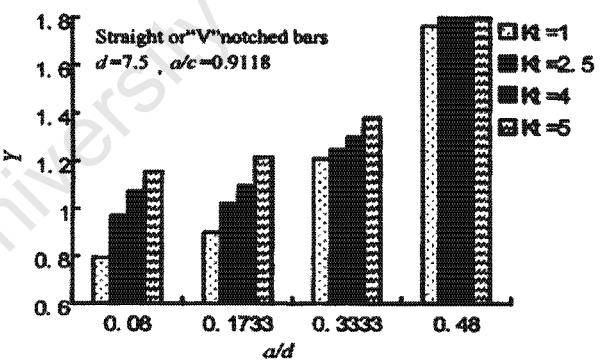

Figure 2.28: Influence of K_t on average SIFs along the surface crack front [61].

Guo found that for each of the cases 1, 4,5 and 6 in Table 2.9, four crack depths were adopted namely : $\alpha=a/d$ = 0.08, 0.1733, 0.3333 and 0.48 and for each a/d, three aspect ratios $\beta = a/c$ = 0.6114, 0.792 and 0.9118 were obtained from many experiments that yield these ratios within this range **[63,64]**.

Since the stress intensity factor is nearly independent of the notch geometry for a given Kt, Guo has provided an expression of SIF written as a function of K_t, crack geometry and size of crack **[61]** as shown in equation 2.18.

$$K_I(\alpha,\beta,\gamma,K_t) = Y(\alpha,\beta,\gamma,K_t)\sigma\sqrt{\pi a}/\sqrt{\Phi} \qquad \textbf{2.18}$$

where σ is the nominal stress on the minimum cross section of the bar without a crack and $\Phi = 1 + 1.464(a/c)^{1.65}$.

The derived expression from results obtained was then expressed when the K_t value was equal to 1.

The normalised stress intensity factor Y was then given as

$$Y(\alpha,\beta,\gamma) = A(K_t) - B(K_t)\alpha - C(K_t)\beta + D(K_t)\gamma + E(K_t)\alpha^2 - F(K_t)\beta^2 - G(K_t)\gamma^2 - H(K_t)\alpha\beta - I(K_t)\alpha\gamma + J(K_t)\beta\gamma - K(K_t)\alpha^2\beta + L(K_t)\alpha^2\gamma - M(K_t)\beta^2\alpha - N(K_t)\beta^2\gamma + O(K_t)\gamma^2\alpha - P(K_t)\gamma^2\beta + Q(K_t)\alpha^3 + R(K_t)\beta^3 + S(K_t)\gamma^3 \qquad \textbf{2.19}$$

When solving the coefficients from the FE equations **[61]**, equation 2.20 was obtained.

$$Y(\alpha,\beta,\gamma) = 2.8070 - 5.0233\alpha - 3.6777\beta + 0.3893\gamma + 0.6130\alpha^2 - 1.850\beta^2 - 0.7178\gamma^2 - 19.9930\alpha\beta - 7.3442\alpha\gamma + 2.3000\beta\gamma - 7.3193\alpha^2\beta + 11.1045\alpha^2\gamma - 12.964\beta^2\alpha - 1.6981\beta^2\gamma + 4.0786\gamma^2\alpha - 0.1928\gamma^2\beta + 7.8967\alpha^3 + 3.4425\beta^3 + 0.0246\gamma^3 \qquad \textbf{2.20}$$

This derived expression was tested with the FE result and the discrepancy between the FE results was less than 8%. The graphs in Figure 2.29 show the correlation between results of the FE codes and the derived equation.

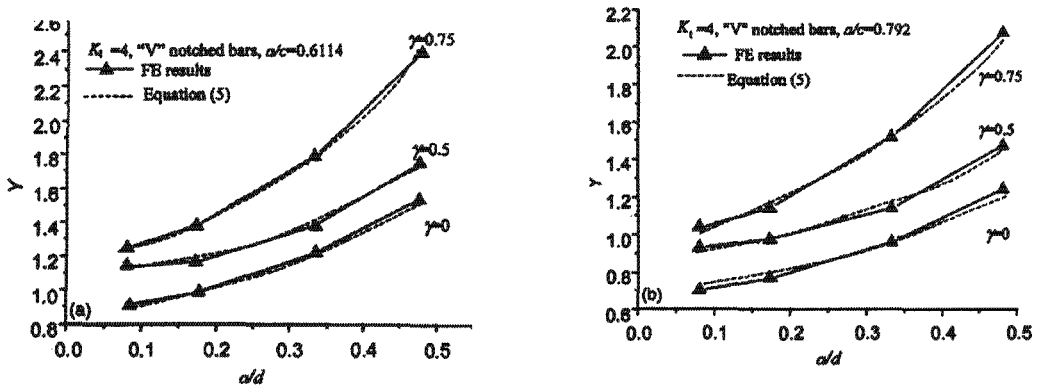

Figure 2.29: Graphs comparing equation results with computational FE results with different a/c [61].

Using this equation, Guo extended his experiments on tensile screw bolts. Wei and Zhong **[66]** did some investigations on M22 × 1.5 coarse plain thread bolts made of 20CrMo steel by using the James-Anderson method (JAM) to evaluate the stress intensity factor of the surface cracks in the bolts. A modified JAM was used by Shen and Guo **[67]** which has been proved by 3D numerical and experimental data of surface cracks in round bars and this is shown in Table 2.10 and illustrated by the graph in Figure 2.30. The discrepancies between data obtained by the modified JAM approach and experimental results at the centre of the crack were less than 9.7% and at the surface point were 22%. The large discrepancy at the surface point was because a/c has a non-linear decrease as a/d increases **[66]**.

SIFs of cracked screw thread bolt M22 × 1.5 under tension

a/d	a/c	Normalized SIFs at center ($\gamma = 0$)			Normalized SIFs at surface ($\gamma = 1$)		
		Experimental Y	Eq. (5)	Error (%)	Experimental Y	Eq. (5)	Error (%)
0.1675	0.764	0.836	0.817	2.3	1.345	1.494	11.1
0.2105	0.706	0.977	0.961	1.8	1.687	1.779	5.4
0.2505	0.688	1.094	1.045	4.5	1.911	1.983	3.7
0.251	0.712	1.064	1.009	5.2	1.583	1.934	22
0.293	0.687	1.214	1.117	7.9	2.056	2.19	6.5
0.3145	0.725	1.255	1.19	5.2	1.893	2.224	17
0.3245	0.687	1.301	1.175	9.7	2.223	2.361	6.2
0.362	0.669	1.394	1.274	8.6	2.306	2.617	13.4
0.3795	0.683	1.398	1.292	7.6	2.398	2.702	12.6
0.413	0.637	1.523	1.416	7.1	2.62	3.004	14.7

Table 2.10: SIFs of cracked screw thread bolt M22×1.5 under tension [61].

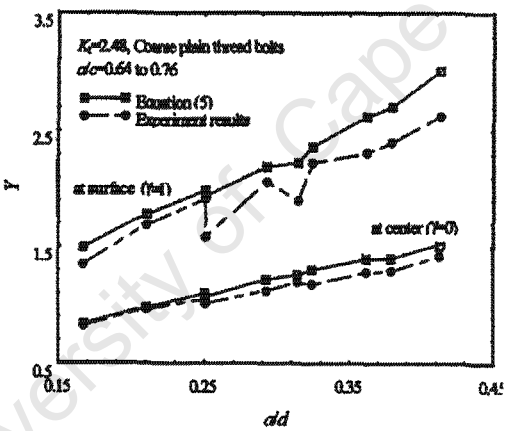

Figure 2.30: Comparison of results from equation 22 with experimental results yielded by modified JAM [61].

Thus Guo **[61]** proved that the empirical expression can be used conveniently in life prediction of notch bars with various geometry and stress concentration coefficient at least within the parameters of his work.

2.7 *Thumbnail Shape Cracks and Crescent-moon Shape Cracks in Bending*

So far, in the literature only Thumbnail or Almond crack shapes have been deeply studied. Crescent moon cracks as shown in Figure 1.3 and 2.31 (b) have not been substantially studied, despite being frequently encountered in fatigue in round bars in engineering practice.

Crescent moon crack shaped fatigue cracks have been the subject of experimental research at the University of Cape Town where cracks have been grown to different lengths and depths. This research was undertaken in such a way as to be able to determine how Y compliance varies with various aspect ratios and is described in greater detail elsewhere in this thesis. Preliminary studies by Radebe and Fleuriau have however been re-analysed and so are included here with suitable acknowledgement and referencing. Radebe **[68]**, Fleuriau **[69]** and Rambocus **[70]** under Tait's supervision of University of Cape Town, have undertaken some experimental research on semi elliptical cracks in 14mm round bars in bending and in tension. The experimental results obtained were consistent with the results of other authors **[3, 7, 8, 10, 45]** when the crack depths were small, but open up greater interpretation at larger crack sizes.

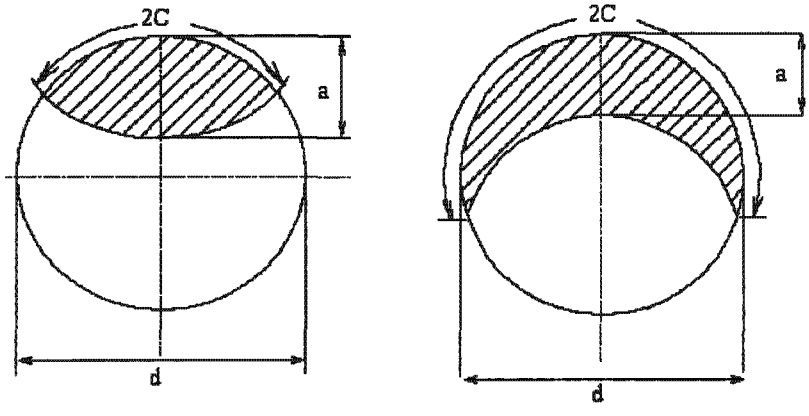

(a) (b)

Figure 2.31: (a) Thumbnail shape or almond shaped cracks
(b) Crescent moon shape cracks, showing nomenclature [70].

The measurements they recorded for each specimen were the maximum load at which it was broken in bending (or tension) the crack length dimensions (*a* and the crack length *2c*) as shown in Figure 2.31. From the known measured toughness, the Y compliance was then determined as a function of the relative depth and aspect ratio a/2c. These experimental results by Radebe **[68]** together with some computational studies by Fleuriau **[69]** are briefly discussed here and expanded upon in the Discussion Chapter 5 where they are combined with the authors' own results.

2.7.1 Radebes' Results

The aim of Radebe's experimental study was to investigate Y compliance vs. a/d and a/2c aspect ratios. In Radebe's experimental work, the new moment of area after fatigue and fracture for each specimen was recalculated by using an AutoCAD program. This was used to obtain the new section properties of the cracked component and hence a more precise value of the stress intensity factor Y, as shown in Table 2.11. Radebe's data, however, included mixed type information which contained both thumbnail cracks and crescent moon crack shapes. He combined both thumbnail shape data with crescent moon data in his analysis.

Crescent moon cracks

Thumbnail cracks

a/t	a/2c	Y AutoCAD	Y values
0.0535	0.0365	0.7958	0.8913
0.3928	0.2857	0.3618	0.7257
0.1964	0.1182	0.5098	0.796
0.2321	0.13	0.3074	0.7113
0.5178	0.2377	0.2706	1.5803
0.6071	0.2833	0.1959	2.2068
0.3036	0.2023	0.4913	0.8375
0.2678	0.1442	0.4427	0.7675
0.375	0.2234	0.3804	0.9005
0.1176	0.3809	0.6059	0.552
0.1617	0.4074	0.7031	0.6196
0.2205	0.4285	0.5814	0.5318
0.2362	0.4324	0.5478	0.5191
0.2647	0.375	0.5084	0.5671
0.2794	0.3958	0.5761	0.5641
0.3823	0.3823	0.5745	0.6472
0.3235	0.3728	0.514	0.6063
0.3529	0.25	0.4764	0.896

Table 2.11: Radebes' Y compliance data [68] obtained, showing both crescent moon and thumbnail cracks with the corrected Auto cad value of Y compliance.

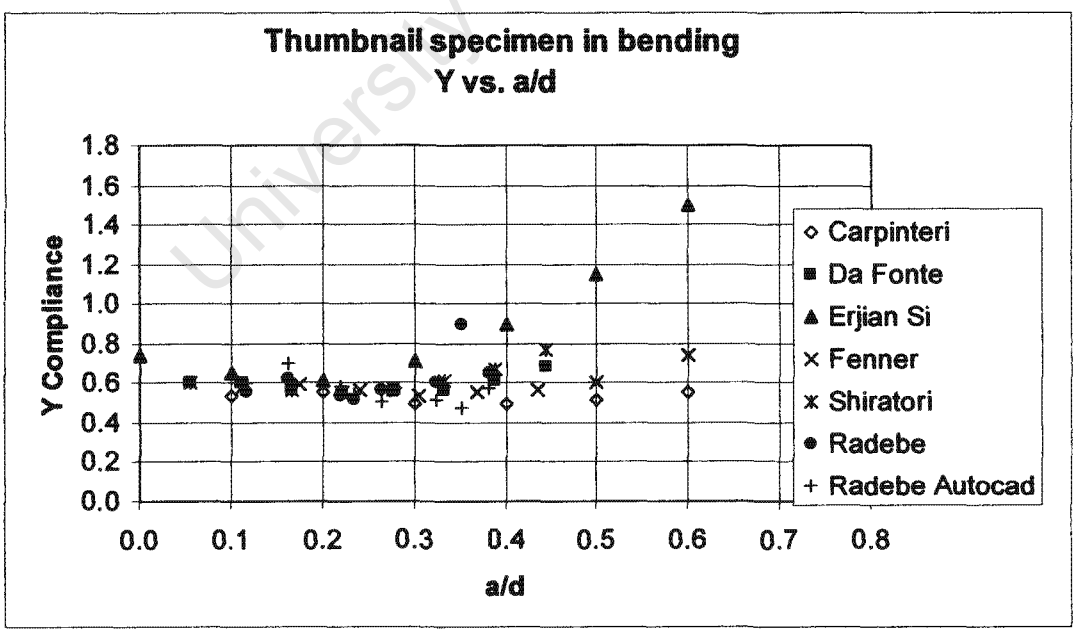

Figure 2.32(a): Radebes' Y compliance [68] for thumbnail cracks in bending compared to other authors [3, 7, 8, 10 and 45].

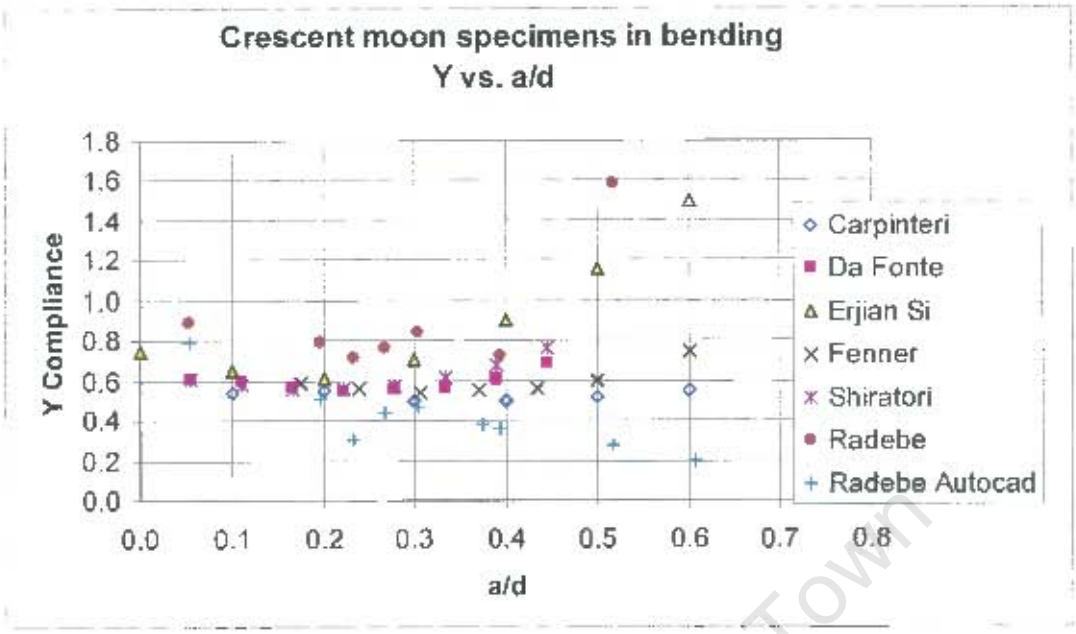

Figure 2.32(b): Radebes' Y compliance [68] for crescent moon cracks in bending compared to other authors.

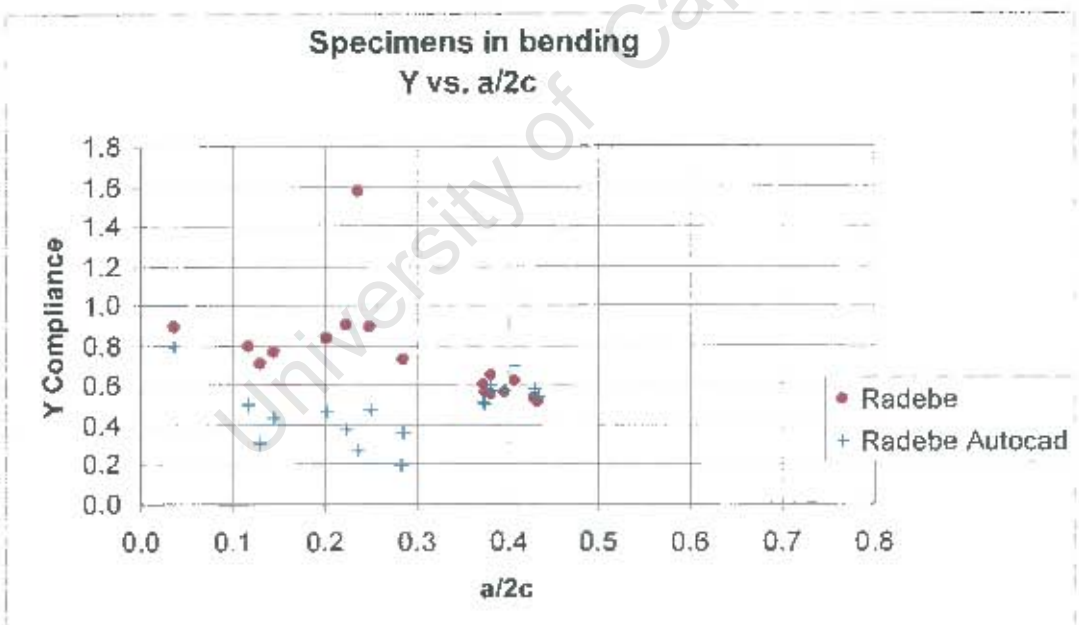

Figure 2.33: Y compliance vs. the aspect ratio a/2c using circular cross section area as the fast fractured region and using the actual fast fracture area (from AutoCAD) [68].

Other authors results also exhibit a "concave up" behaviour when plotting the Y compliance against both the relative depth ratio a/d (see Figure 2.32 (a) and (b)) and the aspect ratio a/2c as shown in Figure 2.33. The Y compliance data when using the true area instead of the circular area are much lower as shown by graphs in Figure 2.33. Y tends to increase with an increasing value of a/d when the fast fracture region is assumed to be circular in bending but shows a decreasing trend when the proper fracture region is considered. The observation made was that if the fast fracture region is assumed to be circular, the experimental data provides Y values that are higher than computational values. It is incorrect to assume the fast fracture region to be circular as this underestimates the stress concentration at the crack tip for deeper crack length a by more than 50% and eventually creates errors in the analysis.

2.7.2 *Fleuriau's Computational and Experimental Work on SIFs for semi Elliptical Cracks*

a/2c	a/d	Y	Y abaqus
0.08	0.39	1.15	1.42
0.145	0.34	0.95	1.05
0.18	0.45	0.9	1.12
0.23	0.33	0.82	0.925
0.3	0.27	0.63	0.71
0.33	0.31	0.66	0.76

Table 2.12: Fleuriaus' data [69] with a side photo of his broken specimens

Fleuriau's work **[69]** was both computational and experimental. The code used for his computational analysis was ABAQUS.

For a three-dimensional fracture mechanics model, ABAQUS requires the use of 20 nodes quadratic brick elements. This element has a specific node numbering sequence which must be adhered to in order for ABAQUS to generate a mesh of the model. For calculation involving the J integral, ABAQUS requires that the front face of the brick be collapsed so that it forms a wedge as shown in Figure 2.34.

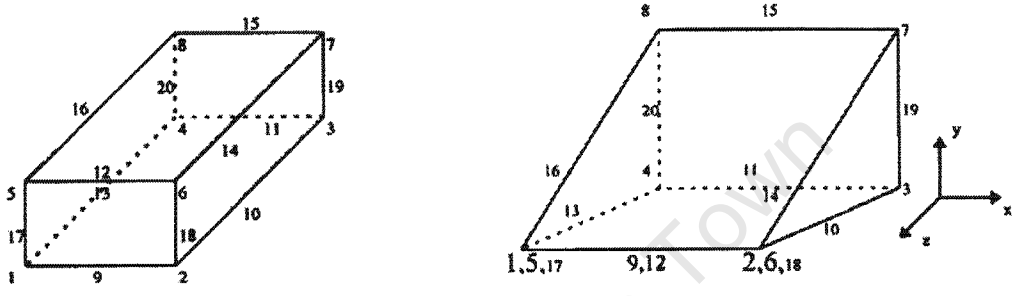

Figure 2.34: Original 20 node quadratic brick elements to collapsed 20 node quadratic elements [69].

As it can be seen the nodes (1,5,17), (9,12) and (2,6,18) would now lie on the crack front and this is known as a focused brick (crack tip) and due to this reason, nodes 10,12,14 and 16 have been moved to the quarter point position. All the nodes that have been collapsed on to the crack tip were tied to one node at the crack tip to eliminate the excessive degrees of freedom). The resulting concentration of nodes at the crack tip known as node cluster is shown in Figure 2.35. Due to the two planes of symmetry, only one quarter of the specimen was modelled as shown in Figure 2.36 for evaluating the J-intergral along the crack front, the direction of the crack growth for each point along the crack was required and it was obtained by calculating the average normal unit vector at each crack tip cluster as shown in Figure 2.37 from equations 2.21 and 2.22.

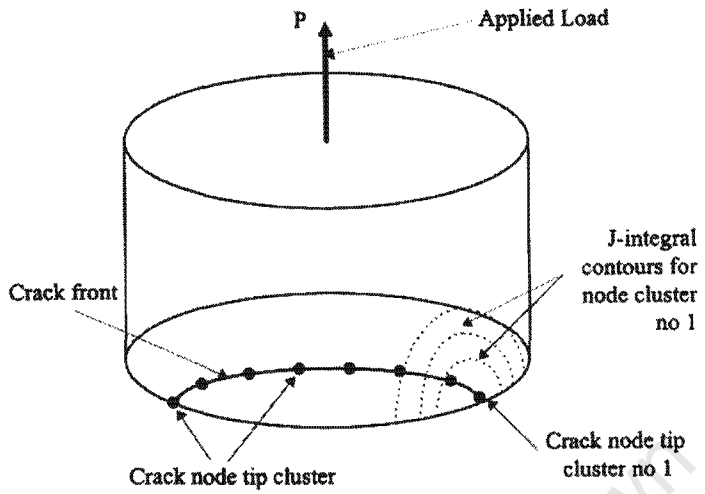

Figure 2.35: Focussed crack-tip cluster [69].

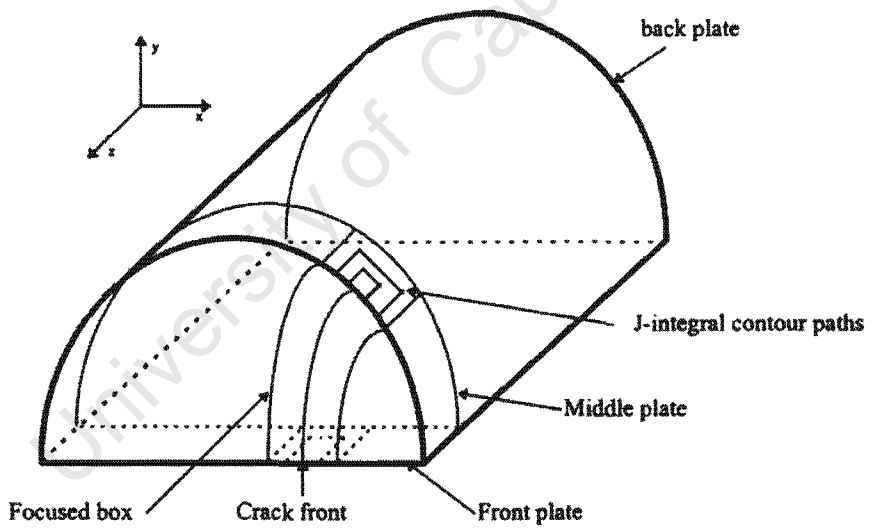

Figure 2.36: Specimen showing quarter block to be modelled [69].

$$n_x = \frac{1}{2}\left[\frac{y_3 - y_2}{\sqrt{(x_3 - x_2)^2 + (y_3 - y_2)^2}} + \frac{y_2 - y_1}{\sqrt{(x_2 - x_1)^2 + (y_2 - y_1)^2}}\right] \quad \textbf{2.21}$$

$$n_y = \frac{1}{2}\left[\frac{x_3 - x_2}{\sqrt{(x_3 - x_2)^2 + (y_3 - y_2)^2}} + \frac{x_2 - x_1}{\sqrt{(x_2 - x_1)^2 + (y_2 - y_1)^2}}\right] \quad \textbf{2.22}$$

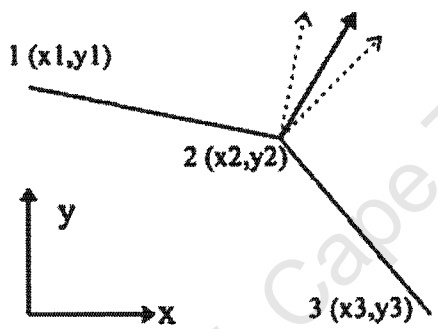

Figure 2.37: Normal vector [69].

The entire model was built by extruding the node set from the front plate to the middle and back plate. The mesh was generated by virtue of a spread sheet approach. The mesh contains 1320 finite elements and a total of 8890 nodes as shown by Figure 2.38 with the stress distribution.

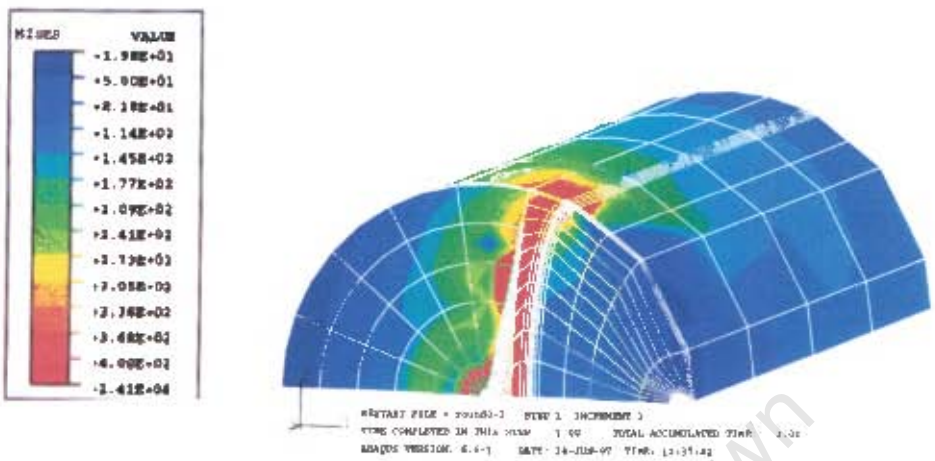

Figure 2.38: The stress distribution along the crack front [69].

He also produced consistent data set in tension which also could be compared to other authors **[7, 8, 10]** as shown in Figure 2.39.

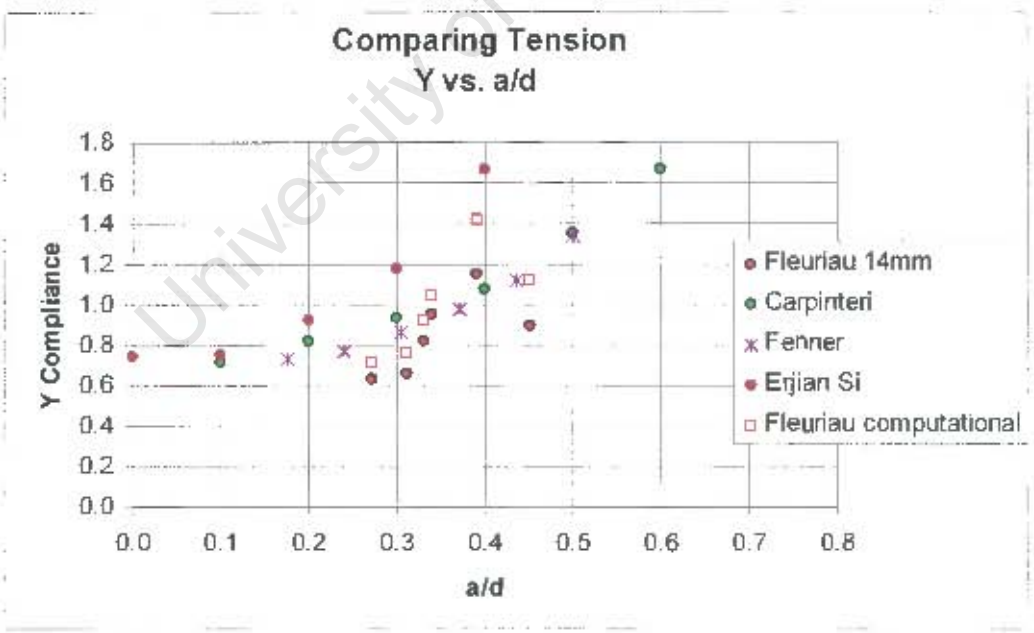

Figure 2.39: Fleuriaus' data [69] being compared to other authors.

2.8 *A Short Review of Size Effect on Fracture Toughness*

Since the present research also concerned an aspect of size effect on stress intensity factors, a short review on the size effect on fracture toughness is included here.

Fracture toughness may be regarded as a measure of the ability of a material to resist the growth of a pre-existing crack or flaw. It has been considered as a "material property", which implies it should be independent of size and geometry. Most of the current integrity analyses are based on this assumption. However, it has been found that fracture toughness does indeed depend on the specimen size, crack depth, geometry, and loading condition to some extent **[71]**.

These effects have been attributed to different crack-front constraints. As a result, it is questionable to apply the fracture toughness value determined from small laboratory specimens to integrity assessment of large structures which may contain defects. At low temperature, or elsewhere on the lower shelf of the brittle transition regime in metals, there appears to be more scatter of fracture toughness results **[72]**.

The size effects have the consequence that fracture toughness data obtained from small laboratory specimens do not necessarily directly describe the fracture behaviour of real full size (but flawed) structures. Intensive research has been conducted in the last decade in order to understand and attempt to overcome these problems.

2.8.1 *Specimen Thickness and Geometric Effect of Specimens*

The classical Irwin approach to thickness considering that thickness has an effect on fracture toughness as conditions change from 'thin' (plane stress) through to 'thick' (plane strain) conditions as shown in Figure 2.40.

In thin, plane stress specimens there is negligible stress acting perpendicularly to the plate or sheet and all the planes of the plate through the thickness in the vicinity of the crack tip experience the same stress **[2, 74]**.

In a thick plate, the material at the crack tip in the centre of the plate is elastically constrained, there is a development of out of the plane stresses to accommodate what would otherwise be the Poisson deformation and thus through-thickness deformation is prevented (except near the plate surfaces) **[73]**.

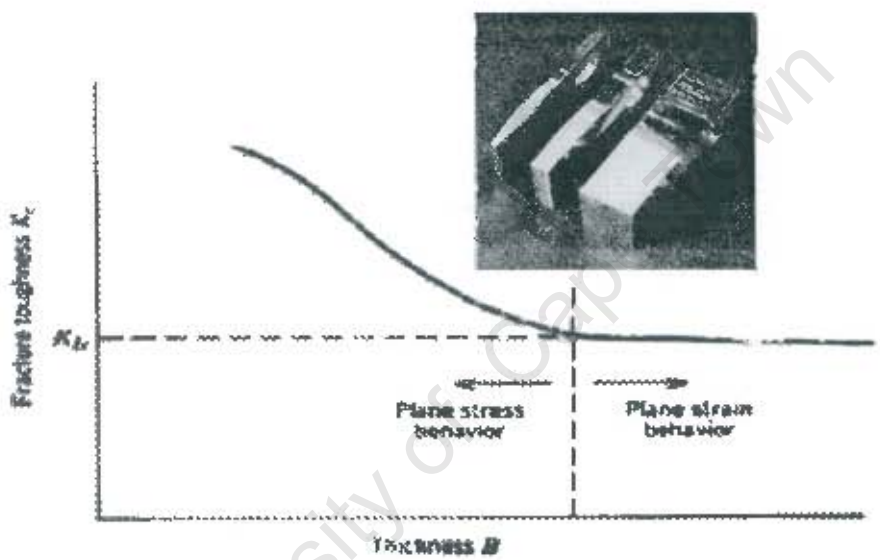

Figure 2.40: Effect of Specimen Thickness on Fracture Toughness [90].

As the specimen gets thicker and plane strain conditions are approached, a lower limit of toughness is reached, which is known as the plane strain fracture toughness, K_{IC}. The reason for this phenomenon is that the increase in toughness for thin specimens is due to the difference of stress state in plane stress and plane strain conditions. Under plane strain conditions higher stresses are generated leading to a lower toughness **[75]**.

Specimens used in plane strain fracture toughness testing are required to exceed certain minimum size criteria for the result to be valid **[1]**. These size requirements are designed to reduce the plastic zone size at fracture to a very small fraction on

typical dimensions in order to produce small- scale yielding conditions and reduce through thickness deformation and loss of plane strain constraint.

For metals, the limiting so-called "valid thickness" criterion is given by equation 2.23.

$$B, W\text{-}a, a > 2.5(K_{IC}/\sigma_y)^2 \qquad \textbf{2.23}$$

where B is the specimen thickness and W the width.

In toughness testing up to 2% stable crack growth is permitted in a valid test, so that K_{Ic} need not precisely be the initiation toughness **[1, 73, 75, 76]**.

The interpretation of the thickness effect upon fracture toughness is due to the original work done by George Irwin **[77]**. He based his conclusions on maximum load toughness of centre-cracked tension (CCT) and 3-point bend (SENB) specimens on two aluminium alloys which were combined with the specimens macroscopic fracture surface appearance. The aluminium used failed in a ductile manner.

Figure 2.41 (a) provides the trend line of thickness variation with toughness and Figure 2.41(b) shows the original data from George Irwin. Indeed these data show the difference in maximum load toughness between low constraint specimens with large but narrow i.e. so-called "slim" ligament ($\frac{B}{(W-a)}$), and high constraint specimens with short ligament. Nowadays, ductile fracture is commonly known to be connected with a rise in tearing resistance curve.

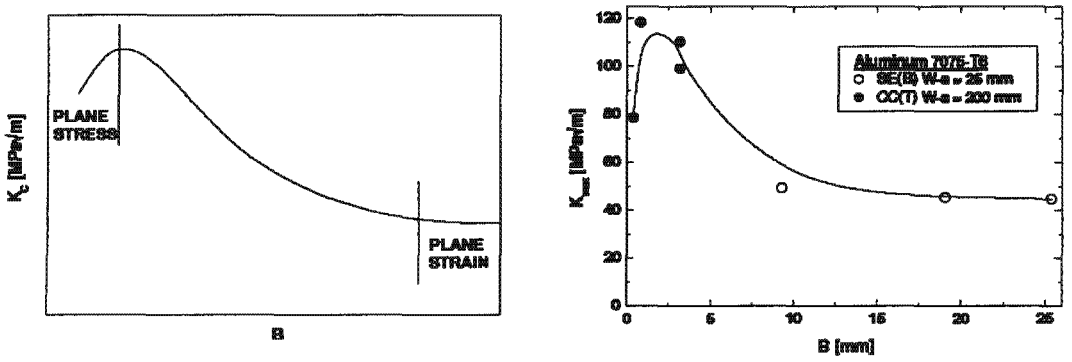

(a) (b)

Figure 2.41: (a) Schematic presentation of the assumption if thickness effect on fracture toughness [78].
(b) The original Irwin data used to postulate the classical thickness effect [77].

Besides material used, the steepness of the R curve is related to the loading geometry and how narrow the ligament is i.e. its slimness. CCT specimens with a slim ligament or a large (W-a) in relation to B show a steeper tearing resistance curve than bend specimens as shown in Figure 2.42.

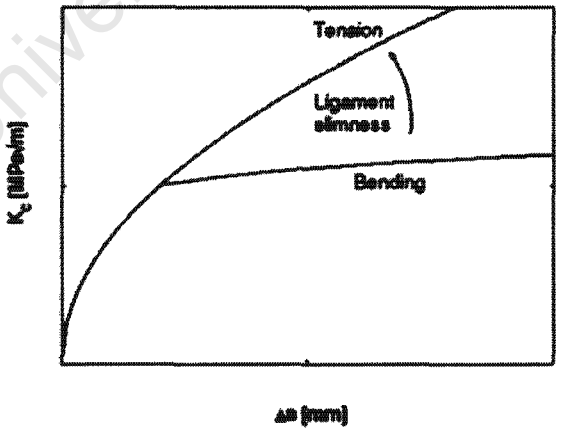

Figure 2.42: Schematic of the geometry effect on tearing resistance [78].

This is also shown in Gibson and Druce **[79]** and Priest's study **[80]**, and it explains part of the fracture toughness difference by Irwin **[77]**. It is important to note that the amount of ductile crack growth that corresponds to maximum load was found roughly to be proportional to the original ligament size. The dimension of the CCT specimen used by Irwin, had a 200mm long ligament compared to a 25mm ligament of the bend specimens which means that the crack growth was nearly 10 times larger than for the bend specimens. In his original test report, it was mentioned that the CCT specimens experienced large crack growth before maximum load.

Although the experiments undertaken did not really correspond to any conventional fracture toughness description, the postulated thickness effect was adopted as representing the "truth" of fracture behaviour. It was also used for the development of the ASTM E 399 testing standard. The assumption was that a valid K_{IC} value should represent a minimum toughness value of the material **[77]**. Wallin **[78]**, has recently given a critical assessment and review of the standard ASTM E 399.

2.8.2 Proposed Changes for the Standard ASTM E 399

The materials used for the development of the ASTM E 399, were Aluminium and Titanium alloys or extra high strength Steels. All the materials had common fracture behaviour, that is, they all failed in a ductile manner, hence they all showed a rising tearing resistance curve. The standard developers found a new problem when they observed that the expected decreasing trend with increase in specimen size actually showed the reverse as shown by the old data in Figure 2.43 **[81]**.

This increase in toughness led to the introduction of the additional demand of $P_{max}/ P_Q < 1.10$.

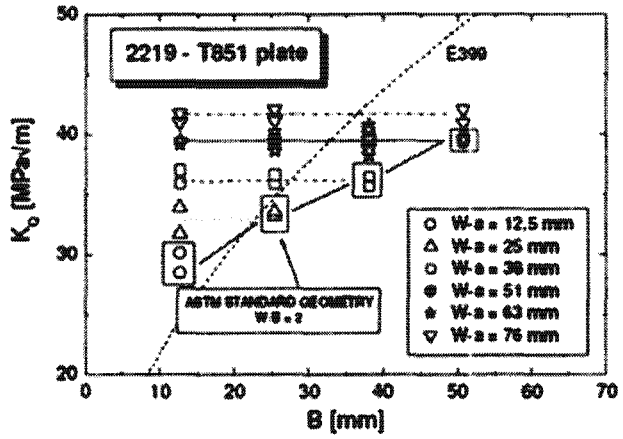

Figure 2.43: K_Q data used to develop ASTM E 399 showing increasing toughness with increasing specimen size [78, 81].

Even though the experimental data showed that it is the specimen ligament size (Figure 2.44), not thickness that controls the fracture toughness value, the beliefs of the plain-strain and plain stress were so strong that this evidence was disregarded [81].

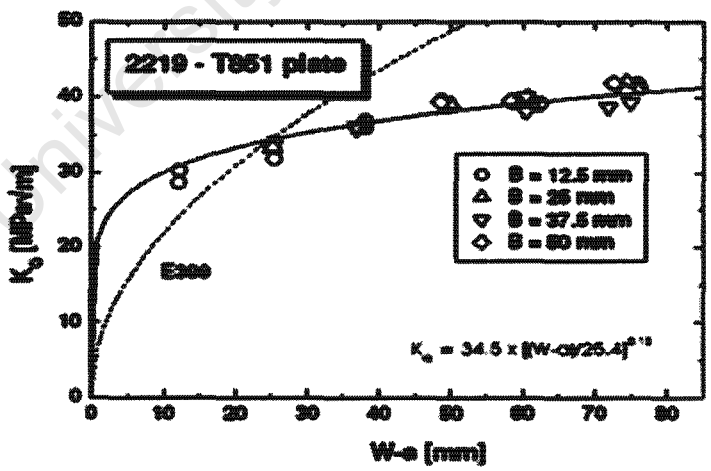

Figure 2.44: Similar data as in Fig 2.43 showing that ligament size controls the increasing toughness for Aluminium alloy [78, 81].

The ASTM E399 covers fracture toughness only for bend specimens. Newer data for those material types were recently examined in the view of the present understanding of the ductile fracture and compared to old available data.

2.8.3 Aluminium Fracture Toughness Data

Figure 2.45 shows the conventional results for the high strength aluminium alloy from May **[82]**. The thinnest and thickest specimens with the same ligament size show essentially the same fracture toughness. As for the intermediate specimens those with the smallest ligament produce lowest fracture toughness values. Figure 2.45(c) which had additional data and lacked ligament size information, also fails to show any clear dependence on thickness.

More recent data **[83]**, for a lower strength of aluminium alloy, behaves similarly, as shown in Figure 2.46. The K_Q scatter is less when plotted in terms of ligament size. The graphs also illustrate that specimens with various thicknesses but similar ligament size give the same fracture toughness. Other work due to Bray **[84]** shown in Figure 2.47 also show similar results. There is thus the same discrepancy about thickness effect on toughness in aluminium, but the consensus appears to be no significant effect of thickness on toughness.

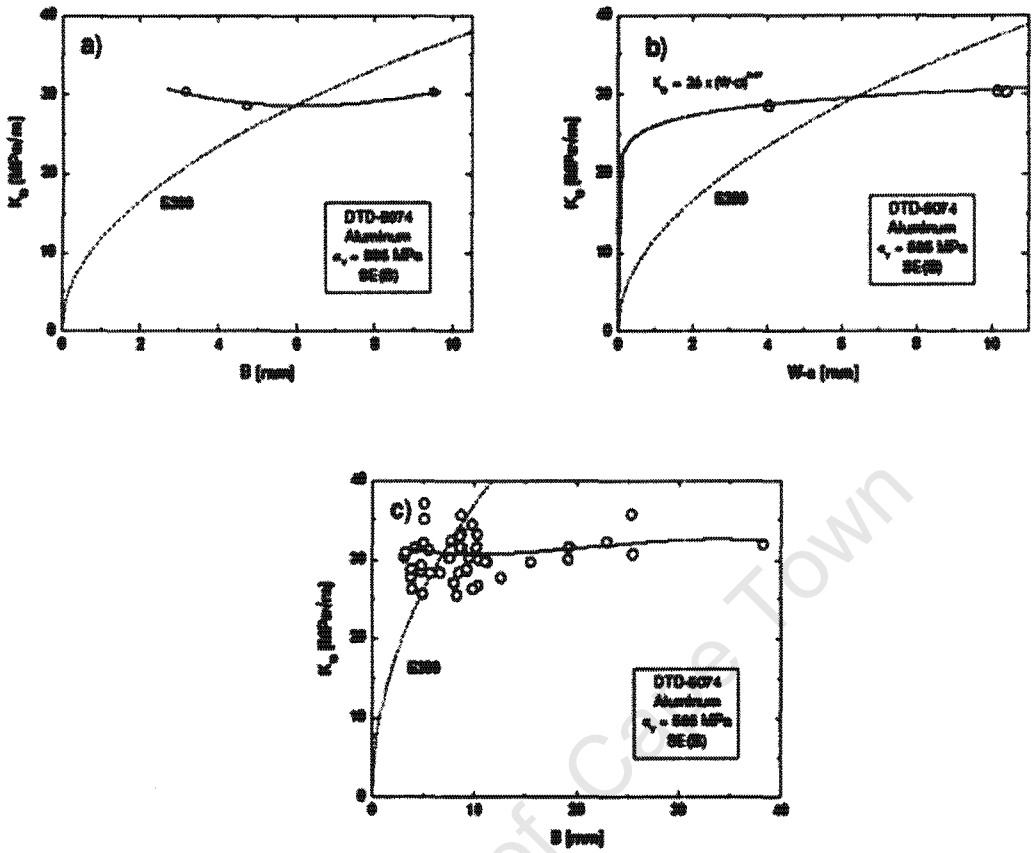

Figure 2.45: May's K_{IC} data [82] used to develop British K_{IC} standard showing no correlation with thickness but increasing toughness with increasing specimen ligament size.

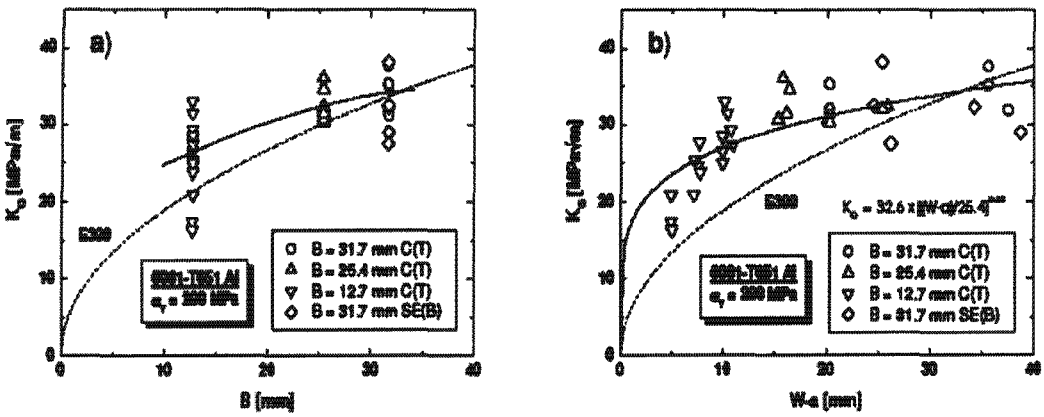

Figure 2.46: Joyce's data [83] showing increasing toughness with increasing specimen thickness and ligaments.

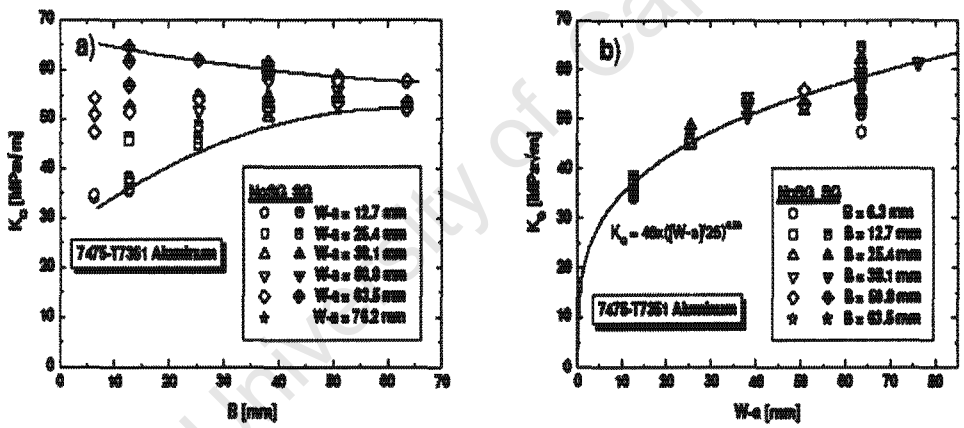

Figure 2.47: Recent K_{IC} data due to Bray [84] showing no significant correlation with thickness but increasing toughness with increasing specimen ligament size.

2.8.4 Titanium Fracture Toughness Data

Titanium alloys have significantly higher strength than aluminium alloys but comparable toughness. Early work, due to Jones and Brown **[85]** and shown in Figure 2.48a, show agreement with the ASTM E 399 standards due to the decrease in fracture toughness which then becomes constant when the specimens' thickness is increased. The data is affected by the ligament size, which indicate that the tearing resistance curve for this material is unaffected by the ligament geometry as long as the ligament is less than 5 times the specimen thickness, as illustrated in Figure 2.48b **[78, 85]**. Slimness in the ligament's geometry causes the tearing resistance curve to become increasingly steep. Hence by having a constant ligament size all the specimens experience approximately the same amount of crack growth at K_Q. Therefore a very slim ligament having steeper resistance curves will provide higher K_Q values. The behaviour is linked not to the absolute thickness of the specimen, but to the ligament geometry (B/ (W-a) < 0.2) **[85]**. Similar early data from May **[82]** also indicated similar results but not all the data were recovered about the ligament size (see Figure 2.49).

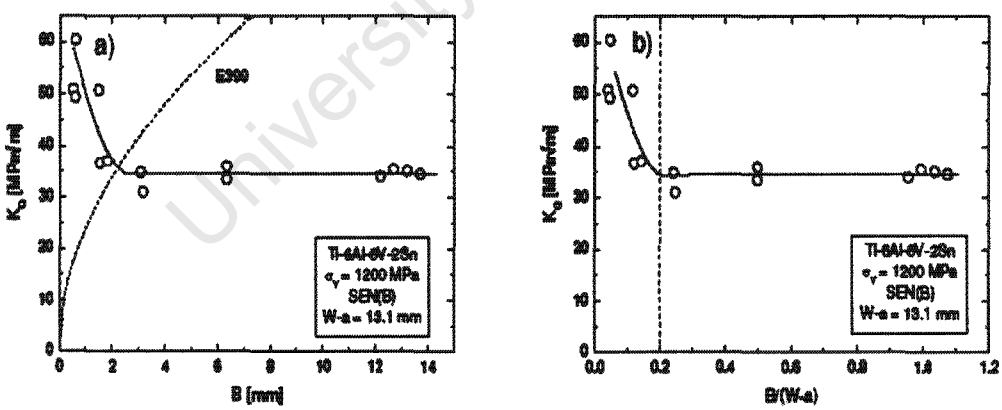

Figure 2.48: (a) Early Jones and Brown data [85] used to develop ASTM E 399 standard, showing reduction in fracture toughness followed by constant toughness with increasing specimen thickness and (b) The increase in toughness related to the slimness (B/(W-a)< 0.2).

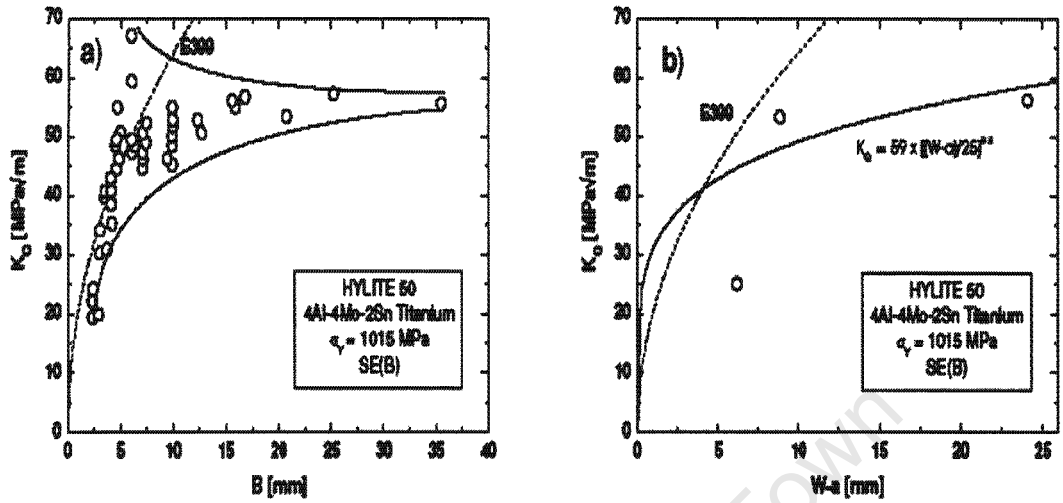

Figure 2.49: Early data from May [82] which were used to develop the British standard for fracture toughness showing increasing toughness with increasing specimen ligament size, but independence of thickness.

Similar behaviour, due to Munz *et al* **[86]** and Joyce and Tregoning **[83]**, is shown in Figure 2.50.

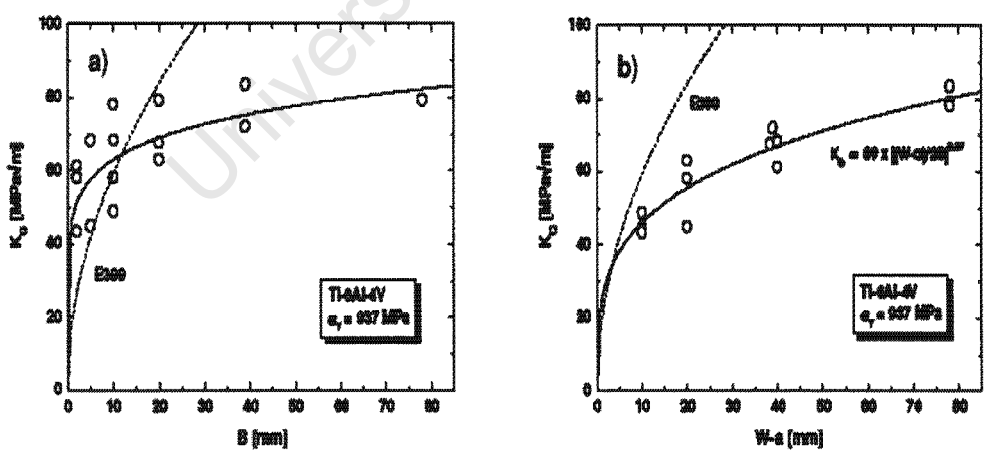

Figure 2.50: Joyce and Tregoning's data [83] showing fracture toughness with increasing specimen ligament size but not thickness.

2.8.5 High Strength Steel Fracture Toughness Data

As for the high strength steel alloys which were quenched and tempered like AISI 4340, similar observations are made with either the old data or the new data as seen in Figure 2.51 **[87]** and 2.52 **[88]**. In both cases, the fracture toughness increases again with ligament size and is not affected by the thickness of the specimen. The tearing curve shows the effect of ligament slimness on the steepness of the curve in Figure 2.51c.

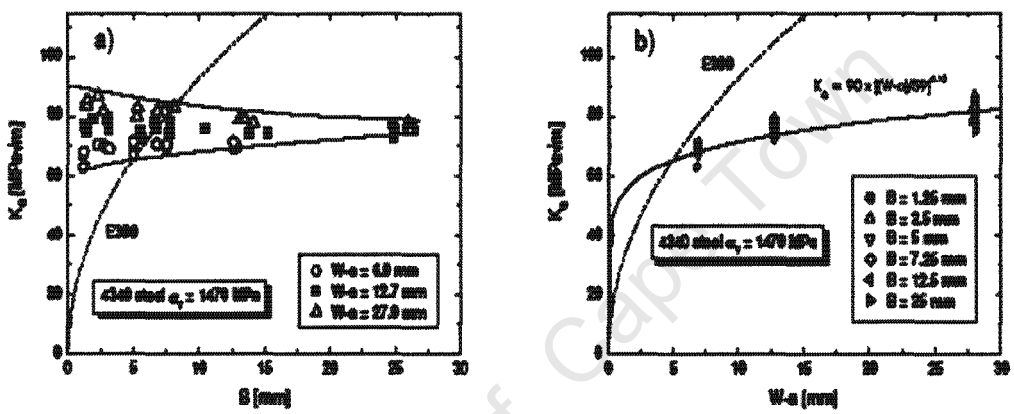

Figure 2.51: (a) & (b) Brown and Srawley data [87] showing increasing toughness with ligament size but not with thickness.

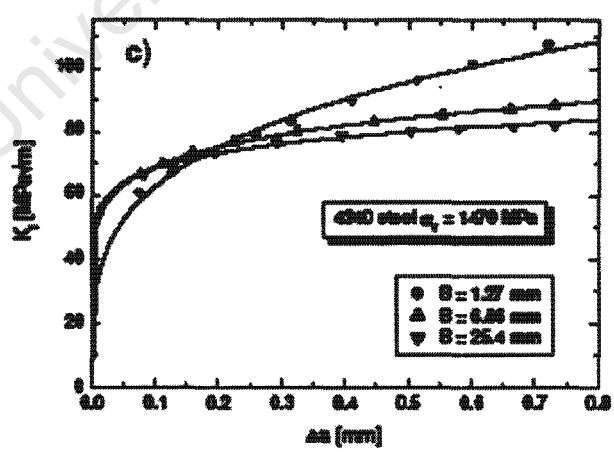

Figure 2.51(c): The effect of the ligament slimness [78].

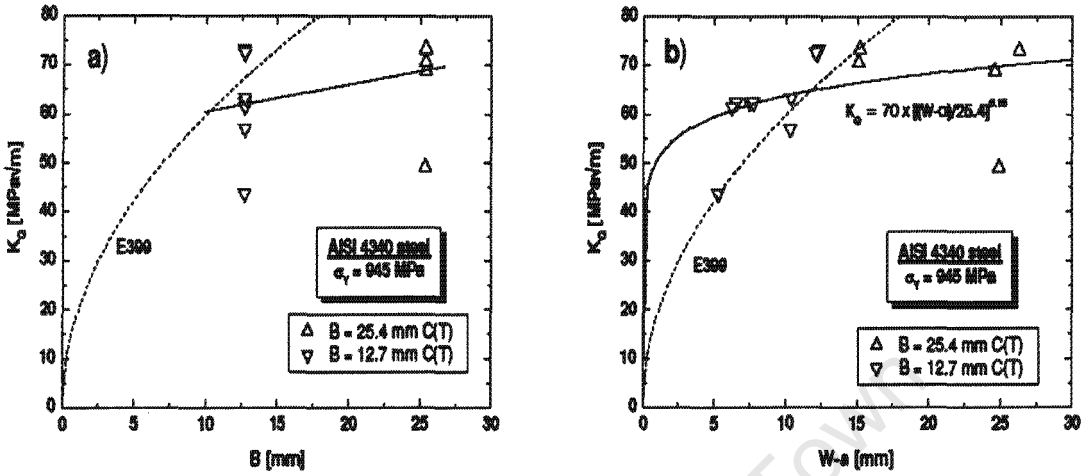

Figure 2.52 (a) & (b): Rolfe and Novak [88] K_{IC} data illustrating slight toughness increase with increasing specimen thickness and ligament size.

In the development of the ASTM E 399 standard, *maraging steels* (precipitation hardened steel with exceptionally high yield strengths) were also used, as this type of steel is ideal for linear elastic fracture tests. For the maraging steel tests there appears to be a more significant conventional thickness effect. The behaviour appears to be consistent with the assumption of the thickness effect where increase of thickness causes a decrease in fracture toughness until a constant limit is reached. This is shown in Figure 2.53. The reason given by Wallin **[78]** for this behaviour was that there was a lack of visible ligament size meaning that the tearing resistance curves for these maraging steels are flat. However, he clarifies that the fracture toughness increase is connected to slim ligaments, Figure2.53c.

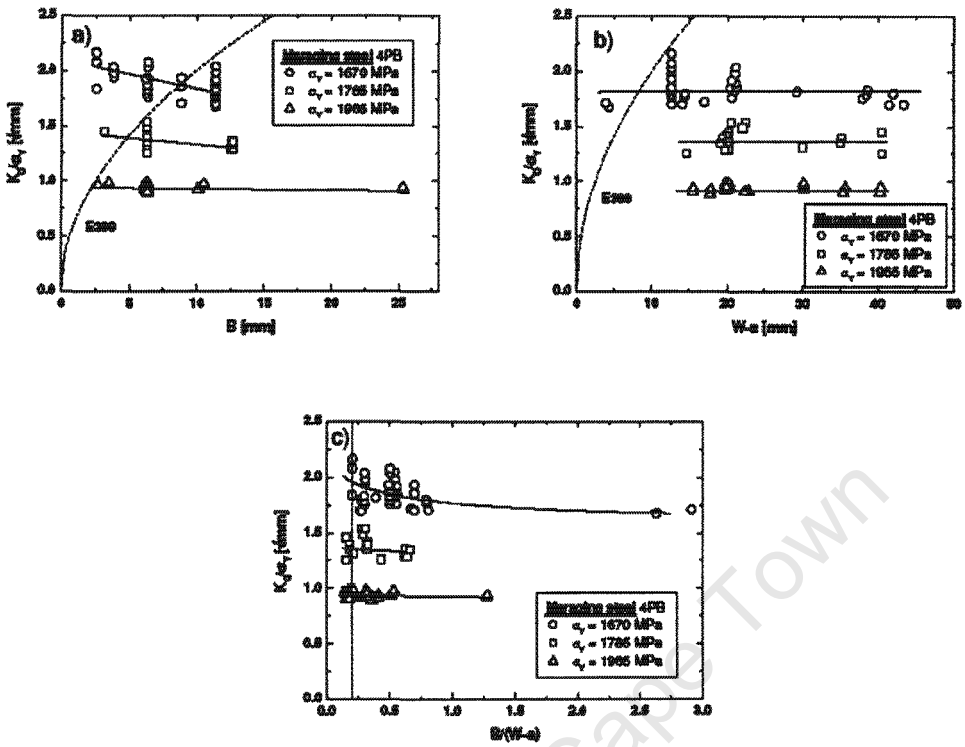

Figure 2.53: Maraging steel used for the development of the ASTM E 399 standard showing slight reduction in toughness with increasing specimen thickness without any significant effect of ligament size [78].

Toughness test behaviour by Wallin **[78]** is shown in Figure 2.54 where the fracture toughness increase is related to ligament slimness and not absolute specimen thickness. When the data from specimens with less slim ligaments were examined, the apparent thickness effect changed. From Figure 2.55, the large specimen behaviour is possibly caused by material in-homogeneity, rather than by the specimen size itself. From Figure 2.55a, the smallest specimens actually show a decreasing toughness with decreasing size, however, unfortunately, data of the ligament size information were not provided for these specimens **[78]**.

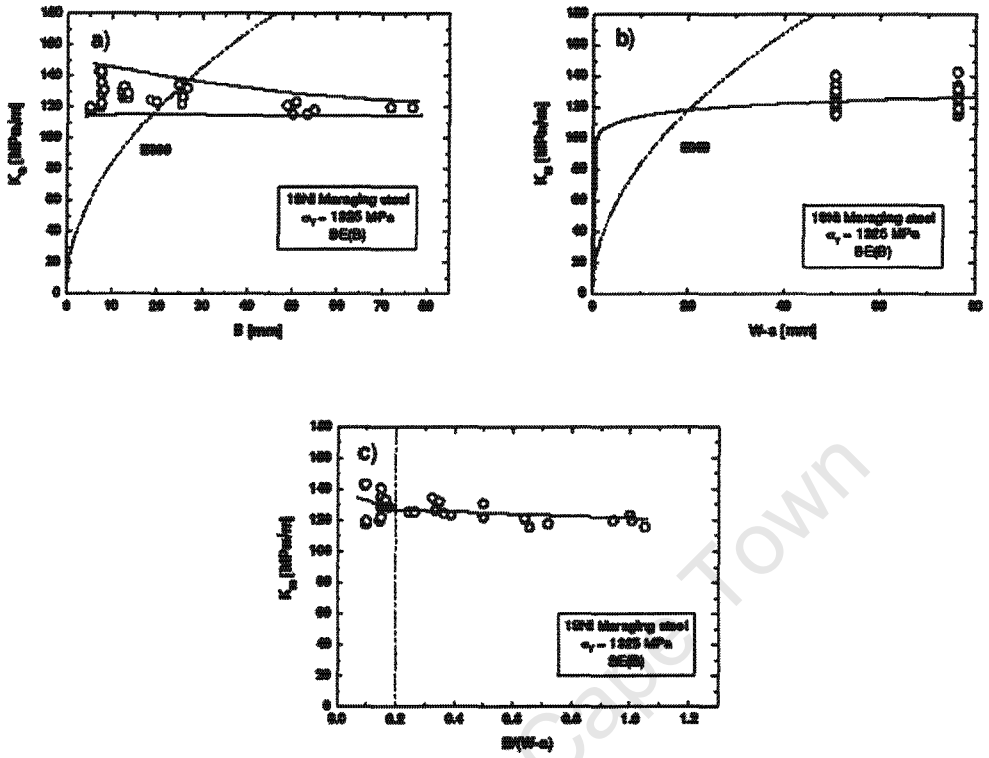

Figure 2.54: (a) & (b) Jones and Brown data for maraging steel used to develop ASTM E399 showing slightly reducing toughness with increasing specimen thickness, but no effect in ligament size. (c) Increase in toughness is related to ligament slimness [85].

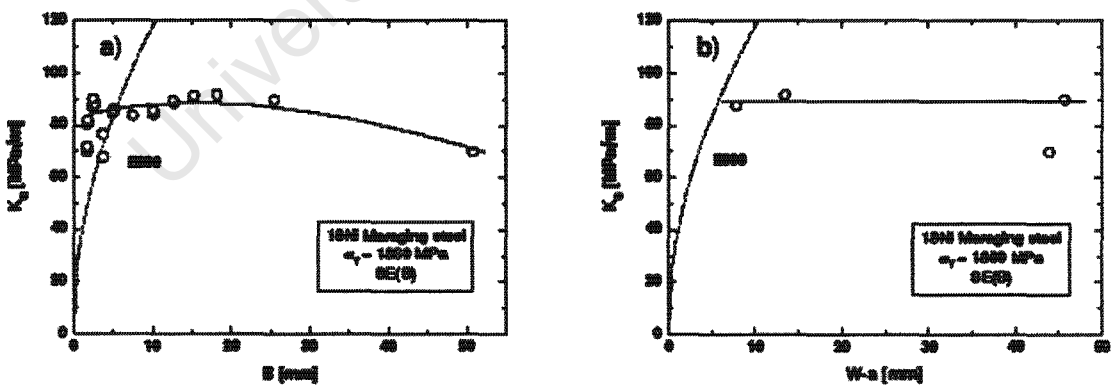

Figure 2.55: May's K_{IC} data used to develop the British K_{IC} standard showing no effect of specimen ligament size, but slight decrease with decreasing thickness [82].

Figure 2.56(a) shows old data of two maraging steels with typical moderate fracture toughness **[88]** and since these steels showed a flat resistance curve, the fracture toughness appears to be insensitive to both specimen thickness and ligament size. For higher toughness of the same steel type, it was found difficult to obtain valid K_{IC} results (see Figure 2.56(b)) **[88]**. The increase in toughness led to a typical increase in fracture toughness with increasing ligament size.

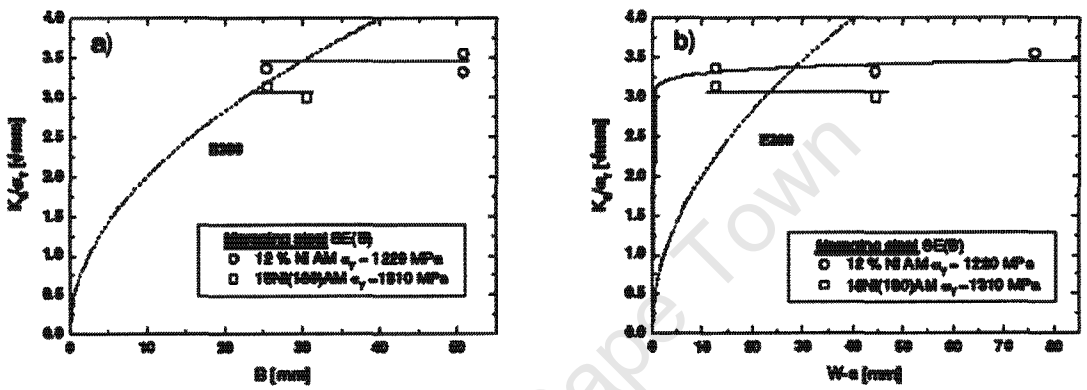

Figure 2.56(a): Rolfe and Novak's K_{IC} data [88] showing constant toughness both with increasing specimen ligament size and thickness.

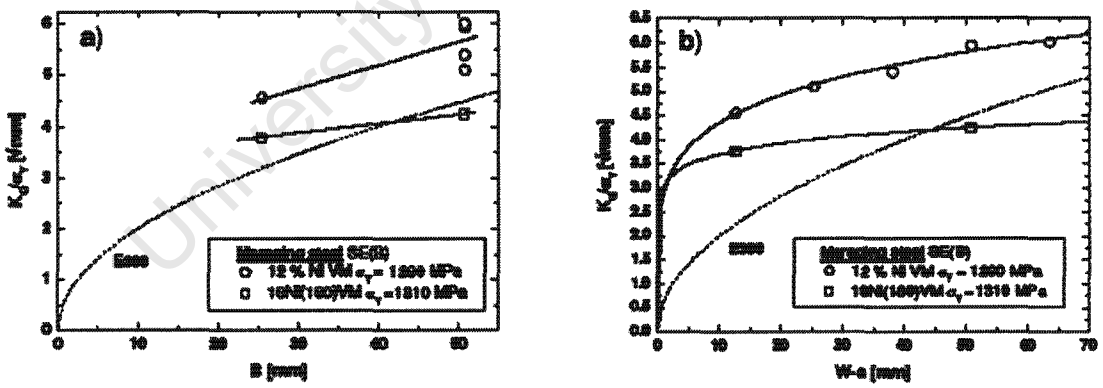

Figure 2.56(b): Rolfe and Novak's K_{IC} data [88] showing increasing toughness both with increasing specimen thickness and ligament size.

2.8.6 *The Significance of the $P_{max}/P_Q \leq 1.1$ Criteria*

For linear elastic situations, the crack driving force K_I is a function of load and crack length.

$$K_I = P.\ g(\text{geometry}).f(a/W) \qquad \textbf{2.24}$$

The ductile tearing resistance of material can be approximated using the power law expression.

$$K_I = A.\ \Delta a^m \qquad \textbf{2.25}$$

The combination of these equations leads to the amount of crack growth at maximum load is for linear- elastic loading is obtained in equation 2.26.

$$\Delta a_{max} = \frac{m.f}{f'} \qquad \textbf{2.26}$$

The amount of crack is governed by power of the tearing resistance curve and using this equation the amount of ductile crack growth at a load P_Q is easily estimated.

The crack growth for CT and SENB specimens are presented in Figure 2.57. P_Q corresponds quite closely to a 2% crack growth of the ligament in accordance with the result of Munz *et al.* **[86]**.

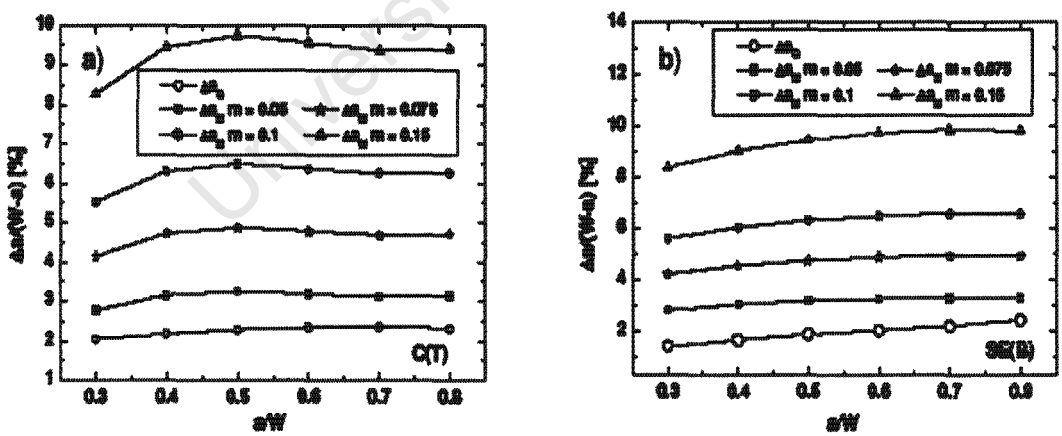

Figure 2.57: Theoretical estimation of crack growth at maximum load in a linear –elastic test. (a) C(T) specimen, (b) SE(B) specimen [78].

By knowing the crack growth both at P_{max} and P_Q, an estimation of P_{max}/P_Q ratio as a function of the crack length and tearing resistance curve steepness can be obtained **[78]**.

Figure 2.58 shows that the tearing resistance curve must be flat to satisfy the criterion P_{max}/P_Q i.e. m<0.1 and it is easier to fulfil the criteria with CT specimens than SENB specimens.

The P_{max}/P_Q ratio is a function of the ligament slimness (B/W-a) **[78]**. Based on simple analysis it has no significance concerning the matter of plane–strain. The ligament dependence of K_Q predicts an average P_{max}/P_Q ratio of approximately 1.24 and not 1.12. The ratio P_{max}/P_Q, is not related to the significance of K_{IC} and it unduly punishes the material with a good tearing resistance. Therefore Wallin contends that the criterion can be removed in the standards **[78]**.

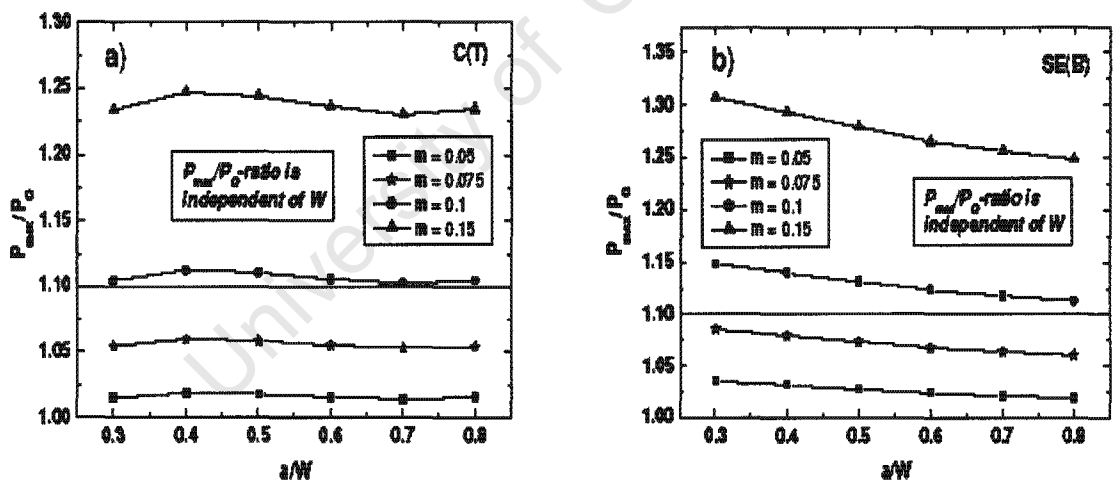

Figure 2.58: P_{max}/P_Q ratio as a function of crack length and tearing resistance curve steepness. (a) CT specimens & (b) SEB specimens,[78].

2.8.7 The Suggested Changes to be made to the ASTM E 399 Standard

Wallin and a group of fracture mechanics experts **[78]** have put forward some suggested changes based on their assessment of the ASTM E399 Standard.

These are

- The specimen thickness is not a controlling dimension in a K_{IC} test.
- The controlling dimension is the ligament size, which due to 95% secant definition of P_Q, leads to the specimen size dependent fracture toughness values.
- The ligament size dependence can be removed by introducing a ligament size dependent P_Q secant definition.
- The P_{max}/P_Q constraint criterion should be removed.
- The specimen size criteria can be somewhat relaxed and should be based on the ligament size not thickness, and moderate side-grooving should be allowed.
- The validity that should be based on ligament size can be changed from $2.5(K_I/\sigma_y)^2$ to $1.1(K_I/\sigma_y)^2$.

2.8.8 Fracture Toughness in the Ductile-to-Brittle Transition Regime

In the transition regime the failure behaviour of specimens made of ferritic steels depends on temperature, specimen size and multi-axiality of the stress state. Due to this, they show more or less plastic deformation and limited stable crack propagation before fracture. The following conclusions were made from the Euro dataset **[89]:**

- In the lower shelf regime at -154°C, no significant specimen size effect on fracture toughness was observed.
- From the temperature less than 0°C the lower tails of the toughness scatter bands were not significantly affected by the specimen size. The small specimen size can be used to determine the lower bound of the toughness

scatter band. Hence with decreasing specimen size, the toughness scatter increases due to the fact that the upper part of the scatter band is extended.

- ❖ Specimen size effects were observed at test temperatures where the fracture surfaces of the specimens showed single cleavage initiation sites. There was no significant size effect observations made at test temperature where no initiation sites were found. This was the case at the temperature T=-154oC.
- ❖ There has also been unique correlation which was found between the amount of ductile tearing and the fracture surface and the cleavage fracture toughness and it was found to be independent of the size of the specimen and test temperature.

The Euro fracture dataset has been extensively used to validate statistical procedures for the toughness data treatment in the ductile to brittle transition regime where the master curve concept and other methods proved the validity of the available data. The data of these conclusions are not given in this thesis and are provided in the Euro dataset **[89]**.

2.9 Summary

In this chapter the literature concerning Stress Intensity Factors (SIFs) has been reviewed, with special reference to computational determinations. The focus has been on thumbnail shaped cracks as there appears to be a dearth of SIFs information on crescent moon shaped cracks. In addition size effects on fracture toughness have also been examined and indicate that it may be in order to relax the thickness constraint conditions in conventional LEFM testing.

From this brief literature survey, it is apparent that there is a case to be made for determining SIF's **experimentally** for thumbnail type fatigue cracks and especially crescent moon shaped cracks- for which there is very little data. The experimental details of how this short coming was addressed are described in the following chapter.

3. Experimental Details

3.1 Introduction

It is apparent from the Introductory Chapter 1 and the previous Chapter 2, reviewing the literature in this field, that there are limited *experimental* studies of stress intensity factors for thumbnail and crescent moon shaped fatigue cracks in round bars. There is, however, a reasonable body of work on SIFs for thumbnail type cracks determined computationally. By contrast there are very few studies on SIFs for crescent moon shaped cracks, computationally or experimentally. This thesis provides an attempt to address this shortcoming from an experimental point of view, particularly with regard to thumbnail and crescent moon shaped cracks. The focus has been on crescent moon shaped cracks previously in tension but attention has also been given to thumbnail cracking, with loading in both bending and tension.

This Chapter discusses all the experimental techniques and details applied in this project to meet the intentions mentioned above. It comprises the material selection for the experiment, specimen development and specimen preparation in the form of machining, machines used, techniques and procedures for the fracture toughness testing, thumbnail testing and crescent moon testing in both bending and tension.

3.2 Specimen Description

3.2.1 Material Selection and Composition

The material selected for the experimental programme was a relatively high strength (475-570 MPa) aluminium alloy which has a low fracture toughness value (of typically 18-22 MPa$\sqrt{m}$) and exhibits a brittle characteristic behaviour. Two materials were chosen, nominally Al7075 T6 and Al2030 T3 because they met the requirements. Ideally it would have been preferable to used Al7075 T6 only, but this was in short supply and expensive, so the project was extended using a slightly less strong aluminium alloy, Al2030 T3. Such alloys have fine grain structures which contribute to its toughness and make it easier to

distinguish the between fatigue cracking region and fast fracture region. Hence they facilitate the measurements of crack features of crack length *2c* and crack depth *a*. In the subsequent determination of the fracture loads, the material exhibited more or less a linear characteristic in the load-deflection curves i.e. a straight-line stress- strain graph passing through the origin with a limited plasticity deformation. The chemical composition of both materials Al 7075 T6 and Al2030 T3 are shown in Tables 3.1 (a) and (b).

Zinc	**5.6 %**
Magnesium	**2.5%**
Copper	**1.6%**
Chromium	**0.2%**
Aluminium	**90.1%**

Table 3.1 (a): Chemical composition of the of Al 7075 T6

Si	Fe	Cu	Mn	Mg	Cr	Zn	Ti	Pb	Bi	Ni	Al
0.197%	0.220%	3.96%	0.632%	0.727%	0.019%	0.021%	0.019%	1.21%	0.002%	0.0019%	93.3%

Table 3.1 (b): Chemical composition and physical properties of Al2030 T3

- ***Yield Stress Testing of Material.***

The mechanical properties such as the yield stress σ_y and the ultimate tensile stress σ_{uts} and of Al7075 T3 and Al2030 T3 are shown in Table 3.2. Tensile tests were performed on ten tensile dogbone shaped specimens of the material using a Zwick tensile testing machine, which is described later in section 3.3.3. The tensile testing was undertaken in accordance with the ASTM E8-93 Standards **[92]** with a ramp rate of 0.005mm/s as shown in ***Appendix A.*** The method of the 2% offset was used to determine the yield stress. Figure 3.1 illustrates the dimensions used for the tensile testing specimens. A preload was applied to each specimen before the slow ramp tensile load.

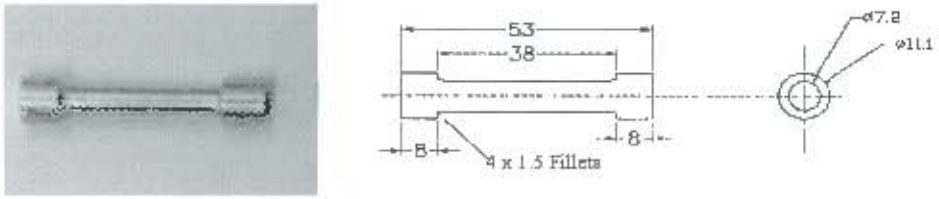

Figure 3.1: Tensile Testing Specimen

Material	Yield Stress	Ultimate Tensile Stress
Al 7075 T6	505 MPa	570 MPa
Al 2030 T3	354 MPa	476 MPa

Table 3.2: Mechanical properties of materials used.

3.2.2 Specimen Dimensions

The materials were very limited and costly. Due to this, Al7075 T6 could only be used to make a few thumbnail type specimens and about 23 specimens for the 14mm diameter crescent moon specimens. The Al2030 T6 was mostly used to design bigger specimens of the crescent moons type where the specimen's dimensions were limited by the chuck size in the rotation bending machine, which is discussed in section 3.3.1.

3.2.2.1 Fracture Toughness Specimens

According to the conventional dimensional requirements for Linear Elastic Fracture Mechanics (LEFM) **[94]** the valid thickness requirement is

$$B,\ W,\ a,\ b \geq 2.5\left[\frac{K_{IC}}{S_y}\right]^2 \qquad \textbf{3.1}$$

Where K_{IC} is the fracture toughness,

B is the thickness of the specimen,

W is the width of the specimen,

a and b are the crack length and remaining ligament (W-a), respectively and

S_y is the yield strength.

Assuming the fracture toughness to be 19kN$\sqrt{m}$, the validity thickness size according to equation 3.1 was 7.2mm thus indicating the choice of high strength aluminium as appropriate material as it exhibits a linear elastic fracture mechanics behaviour (LEFM). This constraint is perhaps less onerous, as it was highlighted in section 2.8.7 of chapter 2 that the valid thickness multiplier is probably down to 1.1 than 2.5 **[78]**.

The Single Edge Notch Bend Specimen (SENB) was used for the fracture toughness testing. This is a commonly used test specimen type due to its simplicity and ease of operation. A bar or rod, notched on one side, and **fatigue** pre-cracked is loaded in 3 point bending as shown in Figure 3.2. While various spans to width ratios possible, the 4:1 ratio is most commonly used and was employed here (but 8:1 is also encountered **[93]**). In the design of the particular SENB specimen, the specimen dimensions are shown in Figure 3.3 (a) and (b).

B = 0.5 W
S = 4 W
a = 0.45-0.55W

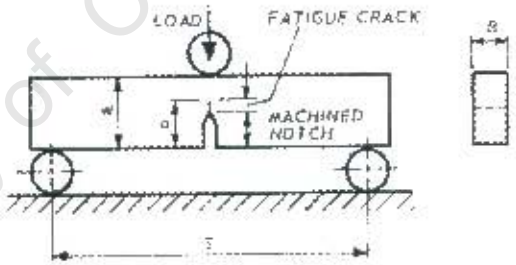

Figure 3.2: ASTM Standard Single Edge Notch Bend specimen [93].

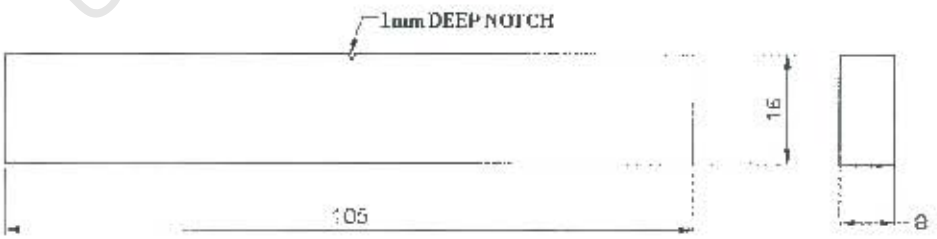

Figure 3.3 (a): Dimension for the fracture toughness SENB specimen for the Al7075 T6.

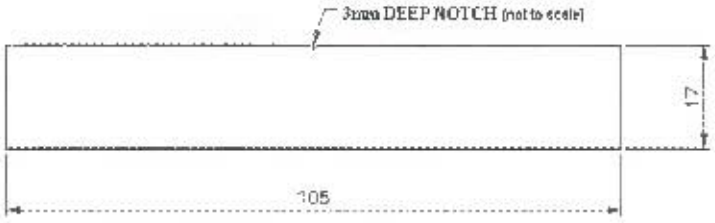

Figure 3.3 (b): Dimension for the fracture toughness SENB specimen for the 2030 T3.

3.2.2.2 Thumbnail Specimens

The diameter of these specimens was selected as 17mm, with a length of 105mm. To achieve the aim of developing fatigue cracks at different length and depths, the thumbnail specimens were notched in various ways or had holes drilled of various sizes and depth as shown in Figure 3.4 to create various shaped fatigue cracks. The specimens were loaded in bending in fatigue on the ESH machine (see section 3.3.2).

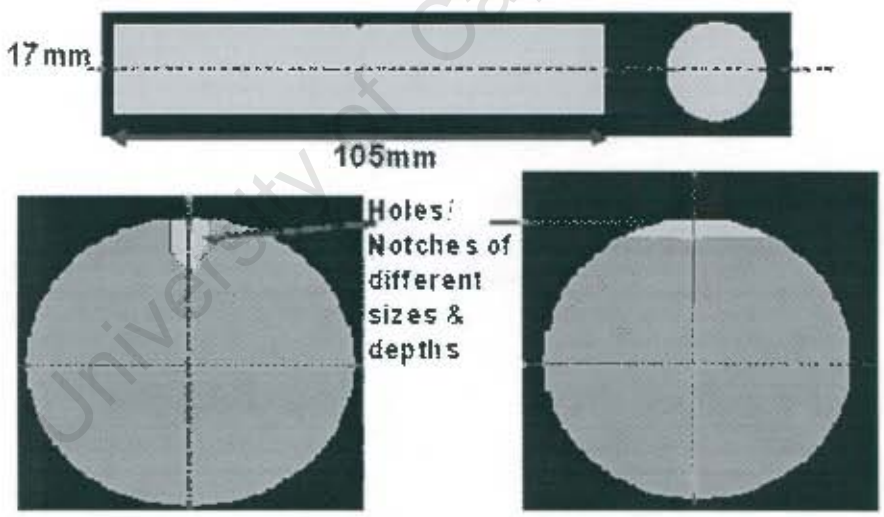

Figure 3.4: Dimensions of Thumbnail specimens.

3.2.2.3 *Development of Crescent Moon Cracks*

The development of the crescent moon cracking was quite a challenge of its own. The initial question was how to make sharp fatigue cracks with a crescent moon shape? The initial concept was to create a stress concentration by drilling three 1mm drilled holes along the periphery of the specimen which was subjected to bending fatigue using the ESH machine (see section 3.3.2). It was expected that as the cracks initiated at the edges of each hole, they would join up and ultimately form a crescent moon. Unfortunately, this approach was not successful. Although fatigue cracks initiated at each notch they finally grew into thumbnail fatigue crack shape as shown in Figure 3.5.

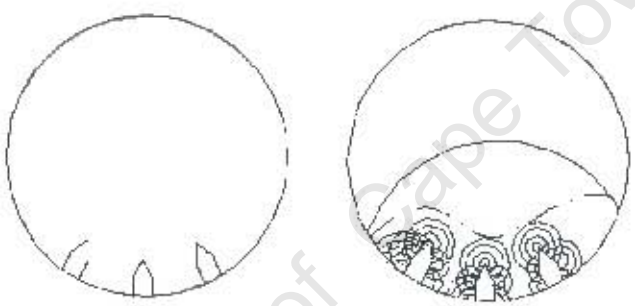

Figure 3.5: Three 1mm notches on the periphery resulted, unfortunately in thumbnail shape cracks.

It was therefore decided that the specimens should rather be loaded in rotational bending with the crack initiating from a distinct local stress concentration. The main difference between stationary shafts and rotating shafts subjected to the same bending moment was that in stationary shafts the tensile stress is confined to a portion of the shaft periphery. In rotating shafts, every point on the periphery experiences a tensile stress as it rotates once every revolution. This means that a crack initiates at any point along the periphery where there is a significant stress concentration.

To ensure that the crack initiated at a specific point on the specimen, stress concentrations were introduced on the specimen. The initial concept was to machine a circular V-notch at point B as shown in Figure 3.6.

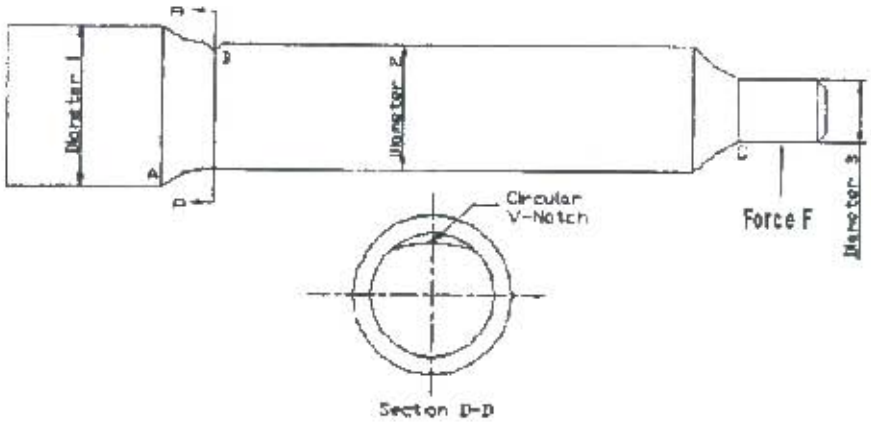

Figure 3.6: Crescent moon specimen with V-notch.

This idea was rather unrealistic since in practice one would not expect to find such notches on shafts, unless it was an act of sabotage! The crack that was developed using this idea was not perfectly of crescent moon shape and hence this concept was disregarded.

The concept was further extended with the formation of a step on the shaft as shown in Figure 3.7.

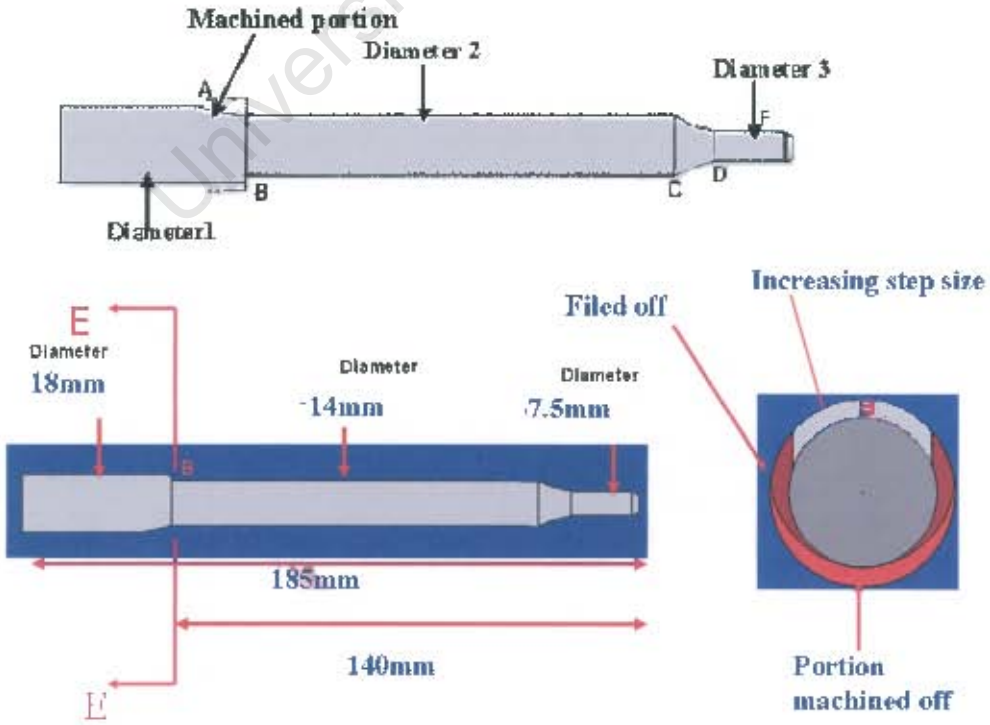

Figure 3.7: Crescent moon specimen with step.

The step size was different along the periphery and was at its maximum depth and sharpness at point B. The stress concentration is highest at this point where the crack initiated. The idea was successful since cracks were formed in a crescent moon shape as expected. The sizes of the specimen were calculated using stress concentration calculations. The diameters 1, 2 and 3 as shown in the Figure 3.7 were calculated. Diameter 1 was chosen to be 18mm due to the size of the Collet chuck of the rotational bending machine. Diameter 2 was calculated to be 14mm such that crack is sure to initiate at point B at a force F and the diameter 3 was given so that the specimen did not break. A simple stress analysis calculation was done for the crescent moon specimens to ensure that the crack indeed initiated at point B.

3.2.2.4 Stress Analysis and Crescent-moon Specimens Size Criteria

The objective was to design specimens of different sizes and lengths accordingly with the force constraints of the rotational bending machine modified for the purpose (***see section 3.3.1***), as well as considering the material limitations. The specimens consisted of three different types based on diameters as illustrated in Figure 3.8. These round specimens were loaded in rotational cantilever bending and developed fatigue cracks at the stress concentration feature, B as expected.

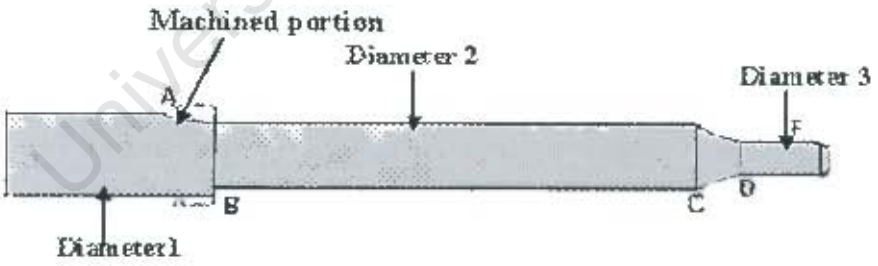

Figure 3.8: Crescent-moon specimens with 3 different diameters.

The specimen was designed in such a way as to raise the stress concentration at point B, where the crack grew along the periphery of the round bar at this highest stress concentration point. By using the simple bending moment equation 3.2,

$$\sigma = \frac{My}{I} \qquad 3.2$$

where σ is the stress, M is the moment from the point on the rod to the point force F, y is the distance from the neutral axis (NA) and I the second moment of area of the round bar, the stress concentration was found to be highest at point B*(see Appendix B)*. The stress difference between point A and point B was found to be approximately 60.4MPa. With diameter 1 as 18mm (due to the Collet chuck constraint) the diameter 2 was selected 14mm using a force of 250N applied at point F to initiate the crack. The length AF was set at138mm and BF was 130mm to be compatible with the rotational fatigue system.

To accommodate bigger specimen sizes, modifications were made on the rotational bending machine *(see section 3.3.1)* particularly to increase the Collet chuck size. With new available Collet chuck the modified shaft diameter was 26mm, 22mm and 18mm. Diameters 2 and 3 of the specimens were calculated using equation 3.2 *(see Appendix B)* and shown in Table 3.3.

Specimen No.		D1	D2	D3
		(m)	*(m)*	*(m)*
Spec[illegible] 1:	ROW 1	0.018	0.014	0.007
Specim[illegible]	ROW 2	0.022	0.017	0.0085
Specimen[illegible]	ROW 3	0.026	0.02	0.01

Table 3.3: Sizes of the diameters for specimens.

The lengths of the specimens were quite critical in terms of the material limitation and the rotational bending machine force capacity since the maximum hydraulic force produce by the machine was 800N. The number of specimens for each size was chosen as 12 and the lengths of the specimens were decided in such a way that the crack would initiate at a reasonable number of cycles and at a minimum force where the crack growth can be controlled **(*see Appendix B*).** The lengths of the specimens for each size are illustrated in Table 3.4. In appendix B, the range of forces for each size of specimen has been colour coded.

LENGTHS									
AF	BF	CF	DF	AE	CF-DF	TOTAL LENGTH OF EACH SPECIMEN			
(m)	(m)	(m)	(m)	(m)	(m)		(m)		
0.138	0.13	0.022	0.012	0.008	0.01		0.185	Specimen 1	
0.15	0.142	0.022	0.012	0.008	0.01		0.204	Specimen 2	
0.18	0.172	0.022	0.012	0.008	0.01		0.234	Specimen 3	

Table 3.4: Specifying the length of the specimens of each size.

The drawing of the specimen to actual size is shown in ***Appendix C*** and a picture of the specimens of the three different sizes is shown in Figure 3.9.

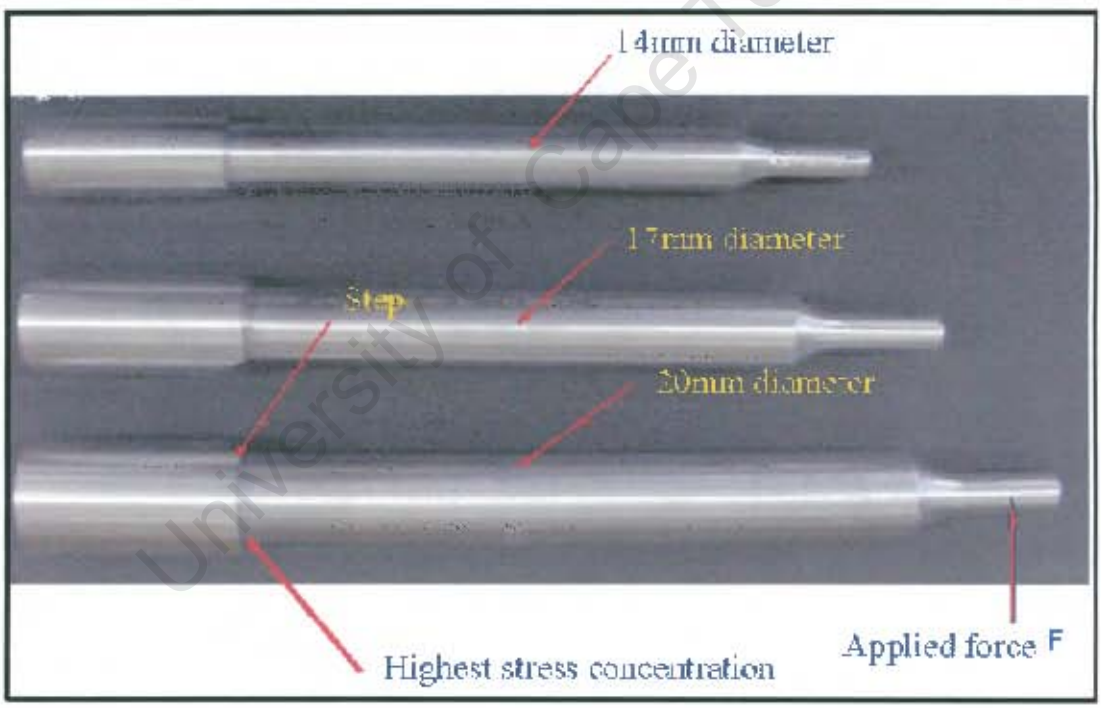

Figure 3.9: Different sizes of specimens.

3.3 Testing Equipment

3.3.1 Single Phase Rotating Bending Machine

The rotational bending fatigue tests were conducted on a custom made facility as shown in Figure 3.10 (a).

The single phase rotational machine, as shown below, consists of a

- 370W single-phase motor (with a rotational speed of 2850rpm)
- Force gauge, which can read up to 800N,
- Collet chuck used to grip the specimen,
- A self-alignment bearing,
- Revolution counter
- Rotation direction switch,
- Main operating switch

The specimen was inserted in the Collet chuck and was aligned by a self-aligning bearing as shown in Figure 3.10 (b). The point of interest was where the crack would initiate and grow at the stress concentration and is carefully viewed under the microscope. A C-spanner was used to ensure that the specimen was tightly gripped. The motor would not switch on unless a minimum force of 50N was provided. This minimum force is designed for a safety reason, that is, if the specimen happened to break during testing, the motor will switch off automatically.

Another fundamental difference in such a rotational bending machine is that rotational bending introduces asymmetrical crack front development from a single origin. During the rotation, the crack front has a tendency to extend in the opposite direction of the rotation. It was observed to swing about 15° around on the form a 'comma' shape crack as shown in Figure 3.11 (a) and (b). In the present project, in an attempt to avoid this asymmetrical crack development, the rotational fatigue was alternated. This was achieved by switching the direction of the rotation from clockwise and to anticlockwise after equal amount of cycles. The diagram in Figure 3.11(c) shows a schematic drawing of the types of

cracks that can occur from fatigue during service. The non-shaded region shows the crack shapes obtained.

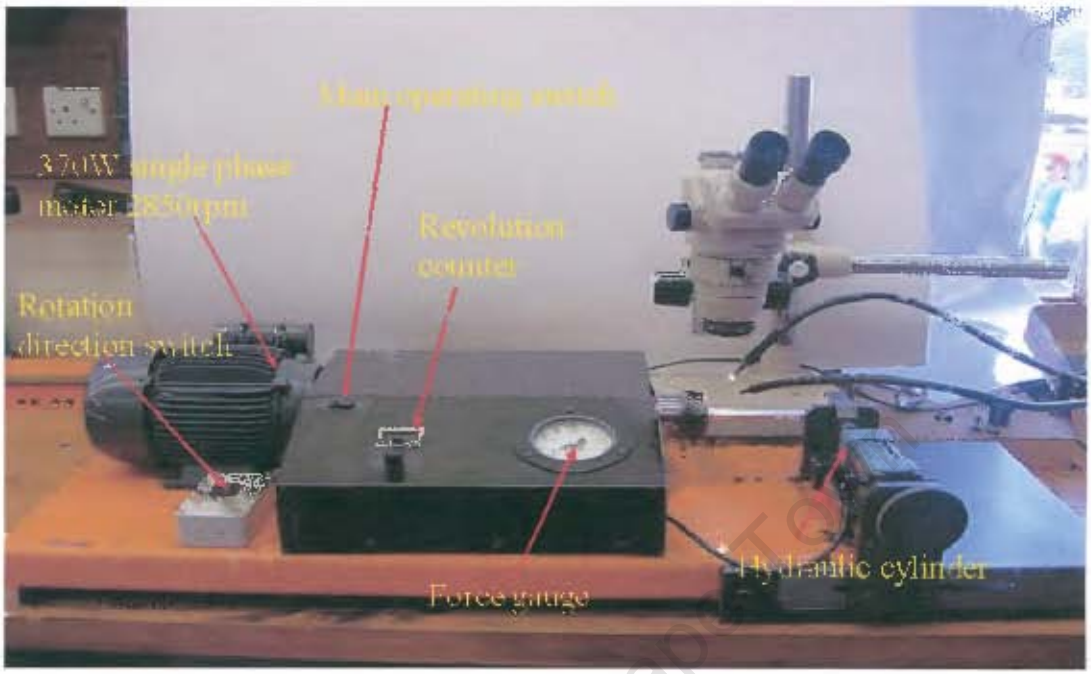

Figure 3.10 (a): The rotational bending machine.

Figure 3.10 (b): The alignment of the specimen with the bearing.

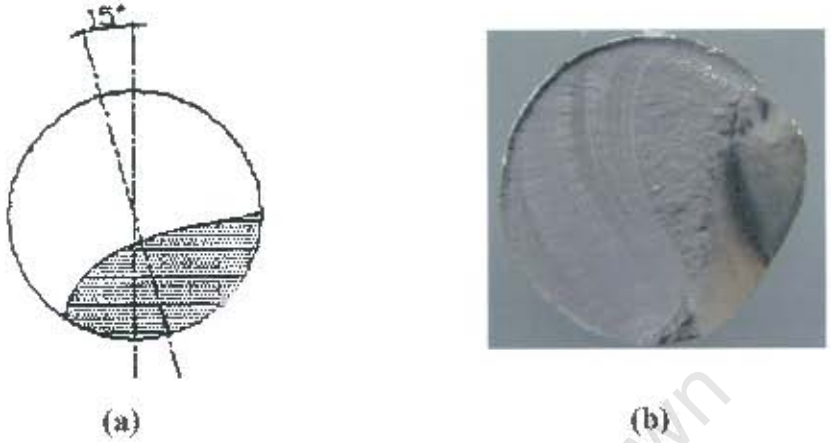

Figure 3.11 (a) and (b): Asymmetrical development cracks.

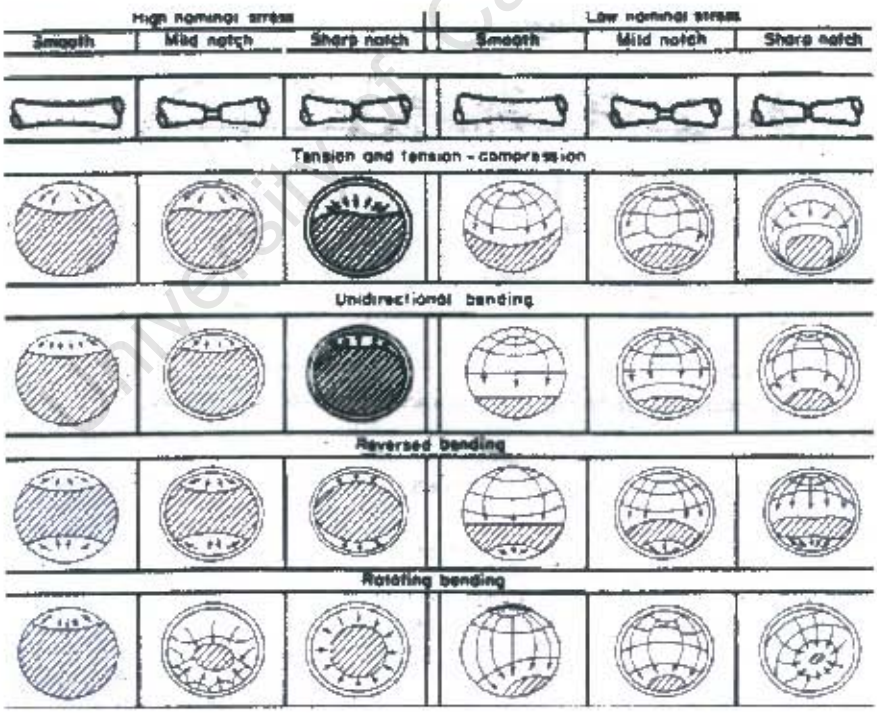

Figure 3.11 (c): Asymmetrical development cracks [73].

- ***Modifications to the Rotating Bending Machine***

The rotational bending machine was modified in various ways to optimise it for this test requirement. To be able to accommodate bigger specimens of diameter 26mm and a length of 234mm, the collet chuck was changed and an extension stand was designed and welded to the machine where the hydraulic cylinder could slide and be bolted further away as shown in Figure 3.12. This facilitated fatigue testing of longer cantilever specimens as required in the project. The shaft of the machine was redesigned for the tapered collets of different size to fit in as shown in Figure 3.13 and 3.14 and bushes of diameters 7mm, 8.5mm and 10mm were designed to hold the specimen at the self alignment bearing (see Figure 3.15 and *Appendix C for the drawings*).

Figure 3.12: Extension welded to the machine

Figure 3.13: Re-designed shaft for the rotational bending machine.

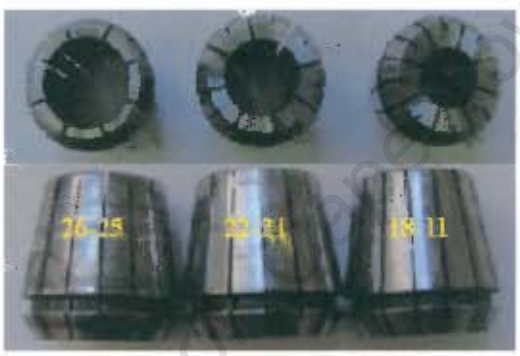

Figure 3.14: Tapered collets with different diameter range.

Figure 3.15: On the left is the bearing in the housing and on the right is the bush designed to fit in the bearing.

3.3.2 The Electro- Servo Hydraulic Fatigue Machine (ESH)

The Electro-Servo Hydraulic fatigue machine (ESH) is one which has a continuous electronic feedback system and is ideally used for fatigue work. With this kind of feedback system the servo-controller and servo-valve can be regarded as the 'heart' of the system. The servo-controller compares the desired performance (i.e. command signal) with the actual performance (as measured) to give an error signal, which is displayed. This error signal is amplified (servo valve amplifier) and conveyed in a negative feedback mode to the servo-valve, which corrects the actuator movement in the relevant direction.

The actuator, servo valve and associated hardware are all attached to an ideally stiff loading frame. Since the ESH is not perfectly rigid, there is some energy stored at fracture. The stiffness depends on the loading train and gain controls.

The ESH machine is electronically driven from an electronic control station where the mean and cyclic load, frequency, cross-head speed and cycle counts can be manipulated and controlled.

The working range of the ESH used for fracture toughness test are stated below

- Max Load ±100kN
- Cyclic Load ±50kN
- Frequency 0→15.00Hz
- Cross Head Speed > 0.025mm/s

The Servo Hydraulic Testing Machine (ESH) with control station is illustrated in Figure 3.16 (a)-(c).

In the experiment, two different ESH machines were used. The one described above was used for testing the fracture toughness specimens and thumbnail specimens which had a load capacity of 100kN. The other ESH machine had a capacity of 250kN, which was used to break the 20mm diameter crescent-moon

specimens in tension, and which required a load of approximately 150kN (if the cracks within the specimen were very small). The 250kN ESH machine consists of a control panel which has a digital meter and a cycle counter. The digital meter can be set to measure load, strain or stroke. Each measurement is displayed as a voltage range of -10V to +10V depending whether a tensile test or a compressive test is being performed.

(a)

(b)

(c)

Figure 3.16 (a): The ESH machine performing a fatigue toughness test

(b) :The control station.

(c) :The control panel from the 250kN ESH fatigue machine.

3.3.3 Zwick Testing Machine

The 200kN Zwick machine was used in the tensile testing experiments for the 14mm and 17 mm diameter crescent moon specimens. The Zwick machine was linked to a computerised system which contains a Microsoft Zwick Program. The programme is straightforward and by feeding the known data on the computer, such as the size and type of specimen, the load cell being used and the speed of the test, the Zwick can perform the test and even calculate the breaking stresses, time to failure, plastic deformation load, strain, stress, etc. The only problem encountered was that the machine in the laboratory did not have a 200kN grip to break the 20mm diameter crescent moon specimens (thus the experiment was extended to the 250kN ESH testing machine as mentioned in section 3.3.2). Figure 3.17 shows the Zwick machine, with wedge grips that can hold a maximum force of 100kN, ready to perform a tensile test on a 17mm diameter specimen.

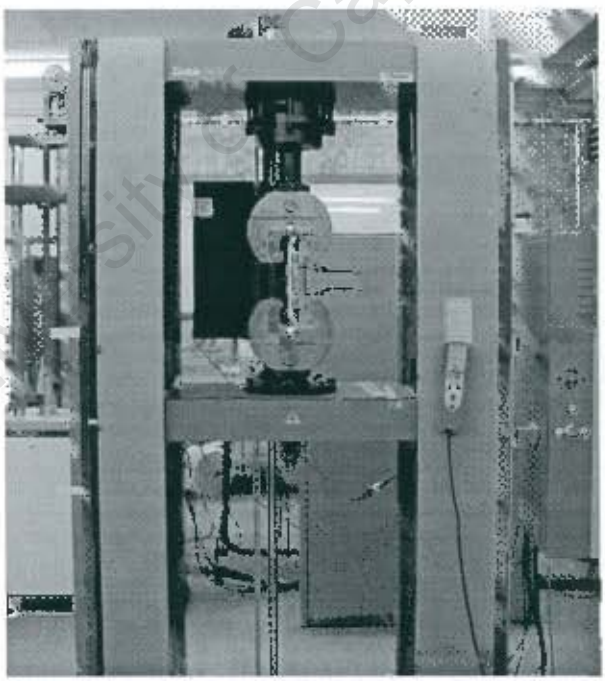

Figure 3.17: The Zwick machine used to break the 14mm and 17mm diameters crescent-moon specimens in tension.

3.4 Fracture Toughness Test

3.4.1 Procedure of Fracture Toughness Experiment

Fracture toughness tests were conducted in accordance with the code BS 7448 1991 using single edge notch bend (SENB) specimens. The specimens were oriented so that the specimens were longitudinal and the notch transverse – thus faithfully simulating the actual fatigue crack condition.

3.4.1.1 Specimen Preparation

Fracture toughness specimens of dimensions shown in Figure 3.3 were fatigued in bending using the 100kN ESH machine. The specimens were first polished on one side in the vicinity of the notch by the use of fine polishing paper of different grades, and finally polished off with a cloth buffer. This was undertaken to provide a polished mirror surface to facilitate observation of the growing fatigue crack. Using a sharp edge, the polished surfaces were carefully scaled (up to about 8mm) to provide reference points to monitor fatigue crack growth when viewed under the microscope, as shown in Figure 3.18.

Figure 3.18: Polished surface of SENB specimen.

3.4.1.2 Fatigue Load Estimation

For a Single Edged Notch Bend (SENB) specimen, the load required for a crack to initiate was calculated and estimated by using the equation 3.3 which gives an estimate of the limit load F_L.

$$F_L = \frac{Bb^2 S_y}{6W} \qquad 3.3$$

Where B, b and W are the dimension of the specimen and S_y is the yield stress of the Al7075 T6 and Al2030 T3 respectively. The orientation used was L-R where the crack grows in the radial direction. Fatigue initiated at typically 40%to 60% of the limit load, F_L. The toughness specimens were pre-cracked at 10Hz with an R ratio of 0.1.

3.4.1.3 Fatigue Pre-cracking

The specimen was carefully placed on the bending stand of the ESH machine with its respective span length and loaded in three point bending as shown in Figure 3.19. As a precaution the amplitude on the ESH was set to zero reading and the counter was reset.

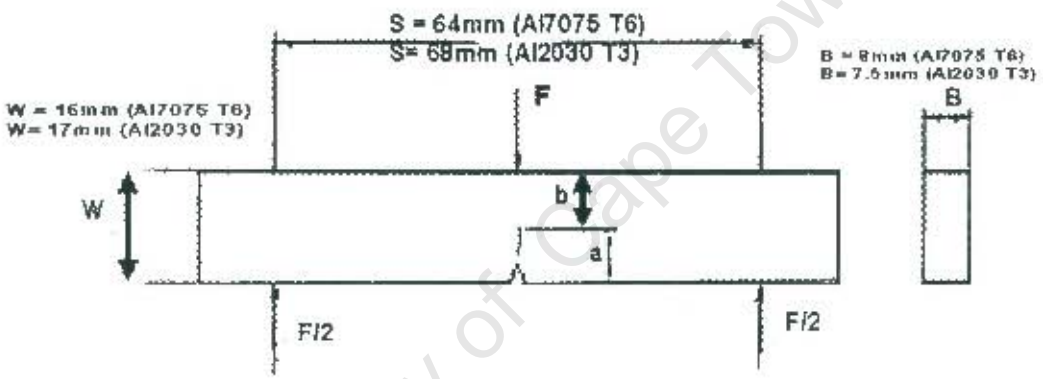

Figure 3.19: Specimen used to determined fracture of toughness.

A travelling microscope with the aid of two fibre-optic beam lights was used to monitor and measure the crack length of the specimen. The microscope was positioned and focused perpendicular to the specimen. The graticule reading of the microscope was aligned parallel to the notch of the specimen.

As the cycling amplitude was switch on, the counter started automatically. At typically between 2000 to 4000 cycles, the material started to exhibit fatigue crack initiation. Figure 3.20 shows a typical specimen on the bending stand (at 68mm span under fatigue process at 10Hz).

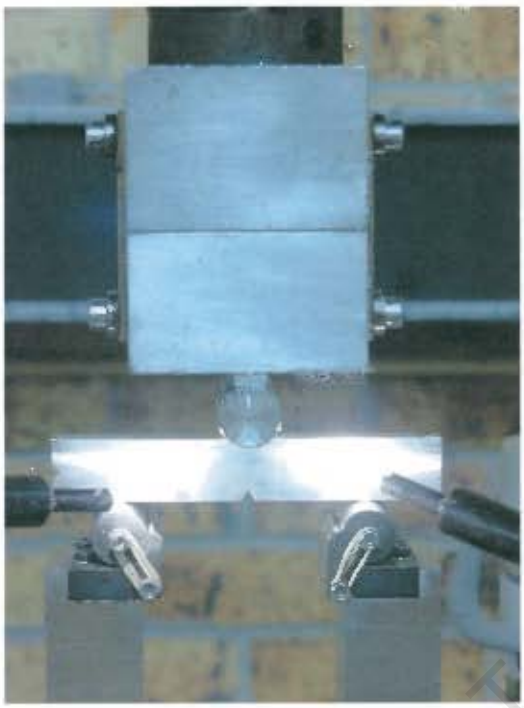

Figure 3.20: SENB specimen under bending fatigue.

The crack was allowed to grow almost half way through the specimen to an a/W value between 0.45 and 0.55. This was achieved by controlling the rate of crack growth. The amplitude load was reduced accordingly such that the crack growth rate did not exceed 2.5 $\times 10^{-4}$mm/cycles. During fatigue pre-cracking each specimen was periodically stopped and the load was adjusted if necessary. ***Appendix D*** shows an example of how the crack growth rate was controlled.

3.4.1.4 Ramping Load Stage

The specimens were fitted with knife-edges about 9mm apart, (which were attached with screws into the specimen) to which to a clip gauge was attached. The clip gauge was used to measure the deflection during the ramp loading and opening of the crack. The clip gauge and the load signal were both connected to a graph plotter from which the load versus deflection curve was obtained as shown in Figure 3.21 and ***Appendix D.*** The ESH also recorded the ramping data which were plotted as seen in ***Appendix D***.

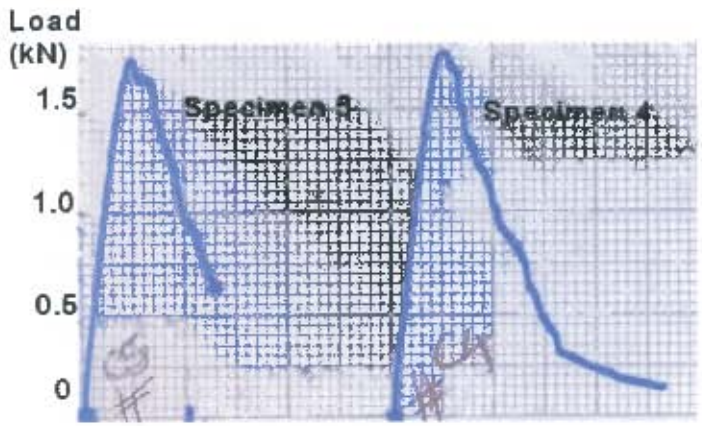

Figure 3.21: Load versus deflection curve.

3.4.1.5 Measurement of the Fracture Surface

The crack for each specimen was measured at 4 quarter points in accordance with the UK standards, as shown in Figure 3.22.

Figure 3.22: Crack measurement for fracture of toughness.

Thus the average crack length a, was determined by using the following equation *(see Appendix D)*,

$$a_{average} = \left[\frac{a_{1/4} + a_{1/2} + a_{3/4} + \left(\frac{a_0 + a_5}{2} \right)}{4} \right] \quad 3.4$$

3.5 Thumbnail Test

- ***Procedure for Thumbnail Fatigue Cracking***

The behaviour of an edge crack in a round shaft in practice is very complex. It really depends on the geometry and the actual type of load. There are two main categories for the shape of cracks in unnotched or mildly notched components under tension or pure bending:

- Straight-front crack;
- Thumbnail shaped crack.

The specimens were all fatigued in 3 point bending on the ESH fatigue machine with a span of 64mm. About 37% of the load limit was used to fatigue the specimens. Fatigue cracks of different lengths and depths were grown on respective specimens. The cracks were monitored by using a microscope and at the same time controlled by reducing the load. The load was reduced to ensure that the crack grows at a constant rate not more than 2.5 X 10^{-4}mm/cycle

The fatigue specimens were broken in 3 point bending and a plotter was used to record the load and displacement trace of the fast fracture ***(see Appendix E).*** Figure 3.23 illustrates a picture of a broken specimen. The shiny part represents the fatigue region and the dull part represents the fast fracture region. The length *2c* and depth *a* of the fatigue crack were carefully measured and recorded. The deeper the drill holes the deeper and rounder (i.e. larger a/2c ratio) the fatigue crack shape.

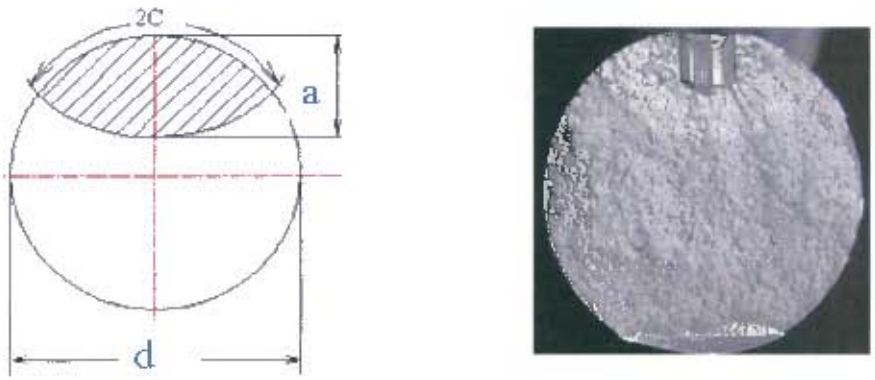

Figure 3.23: Measurement of fatigue crack recorded for thumbnail specimens.

3.6 Crescent Moon Test

3.6.1 Procedure for Crescent-moon Test

For the cracks to grow at different depths and lengths into the round bar at point B, a portion of the specimen was machined off in a smooth "shaved" manner, as shown earlier in Figure 3.7. The specimens were first polished on one side in the vicinity of the notch by the use of fine polishing paper of different ranges, and finally polished off with a cloth buffer. The experiment was undertaken cautiously over a range of crack lengths and depths, such that the Y compliance data is well distributed when plotted against their aspect ratio a/d and a/2c parameters.

The longer the circumferential step size, the longer the surface crack length 2c that could be grown into the specimen, and by adjusting the step length the length 2c of the crack could be controlled. The specimens were all fatigued on the rotational bending machine. The objective of the experiment was to avoid asymmetrical crack development as described in section 3.3.1.

All the 14mm diameter specimens were loaded up to 250N; the 17mm diameter specimens were loaded with a maximum force of 380N and for the 20mm diameter specimens a force of 450N was used. The direction of the rotation was changed for every 5,000 cycles so as to avoid asymmetrical cracking in the shape of a "comma", see Figure 3.11b. Cracks for the 14mm diameter round bar initiated after about 11,000 cycles; for the 17mm diameter samples cracks initiated after approximately 24000 cycles and for 20mm diameter samples after approximately 29000 cycles.

Crack initiation was observed in the microscope, but was also indicated by the formation of fine black powder, which is a consistent sign of fretting fatigue. With the aid of the surfaces being polished and a microscope the progress of the cracks were readily followed. A red ink was also used as a flaw indicator in order to track the crack. This was done by applying a tiny drop of the ink, which seeps into the crack of the specimen where its length could be estimated by using a minimised paper copy of a scaled ruler. The applied load was reduced conventionally and proportionally as the crack was grown to different lengths along the surface of the specimen. ***Appendix F*** shows an example of how readings were recorded during the growth of the crack for a specimen. The number of clockwise rotations was set equal to the number of anticlockwise rotation for each specimen, so that a crescent moon crack shape was obtained at the same time avoiding asymmetrical "comma" crack shapes.

3.6.2 Specimen Modification after Fatigue

Once the fatigue cracks were grown to different relative lengths and depths as required by the experimental programme, the respective specimens were taken to the workshop for the stress concentration step to be completely machined away until the diameter was constant throughout, as a simple round bar containing a crescent moon fatigue crack with diameters 14mm, 17mm and 20mm as illustrated by the drawings in Figure 3.24.

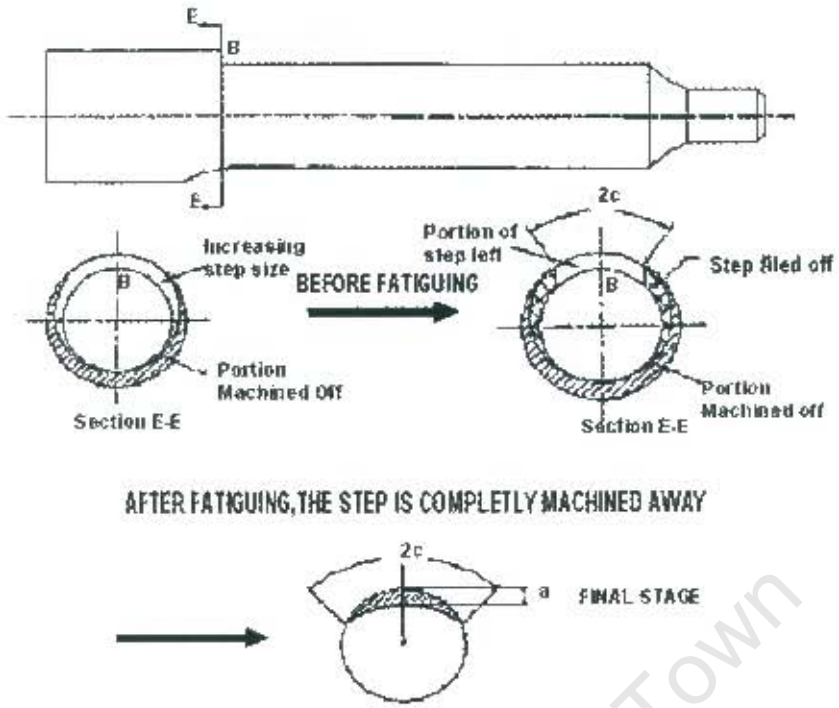

Figure 3.24: Final stage reach by specimen before breaking in tension.

3.6.3 Tensile Testing

The specimens were then ramped under tension on the Zwick 100kN tensile testing machine or the ESH fatigue testing machine (see Figures 3.235(a) and (b)) and the load versus displacement graph for each specimen was obtained from the plotter (***see Appendix F***). Gripping the specimens was sometimes a problem since the crack was located only 50mm away from the end of the specimens, which led to a relatively short gripping length. Clearance was needed by the crack so that the specimens broke at the crack. However, slipping of the specimen in the grips occasionally happened (5% of the cases). Some specimens did not break at the fatigue crack since the grip tends to squash the top part of some specimens and cause a local stress concentration and reduction in area sufficient for the specimen to break at that point.

(a) (b)

Figure 3.25: (a) Zwick tensile testing machine about to grip a 17mm diameter round bar.

(b) ESH test machine ready to break a 20mm diameter round bar.

3.6.4 Measurement of the Crescent moon Fatigue Crack

Every crack of each specimen was measured carefully with a vernier, and the deepest depth of crack ***a*** was recorded. The length ***2c*** was measured by using a masking tape which was carefully stuck around the bar where the length was marked, measured and recorded as shown in Figure 3.26.

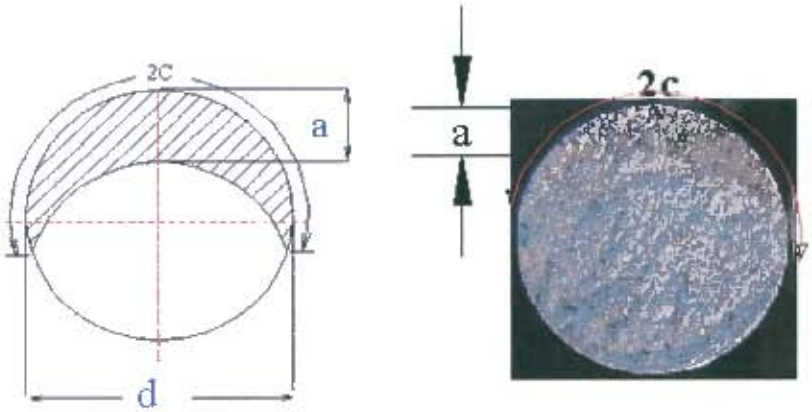

Figure 3.26: Measurement recorded for crescent moon specimens.

3.7 Summary

This chapter has considered the experimental specimens and processes necessary to measure fracture toughness and also generate fatigue cracks of two different types, thumbnail and crescent moon shapes. Together with the flaw dimensions, fracture toughness, stress at fracture and the Y compliance factor can be determined. This is discussed in the following chapter, along with the effect (on Y compliance factor) of aspect ratio, a/2c, relative depth a/d and specimen size, for both crack types predominately in tension (but also in bending).

4. Results and Analysis

4.1 Introduction.

This chapter presents the results of the Y compliance determinations as a function of aspect ratio, relative depth and thickness effect, as derived from experimental work undertaken in the project. It also presents the results for the fracture toughness of the aluminium alloys used followed by the determination of the normalised Y compliances.

- ***Formulae used for Fracture Toughness.***

The fracture toughness was calculated using the formula below,

$$K_Q = \frac{P_Q S}{BW^{1.5}} f\left(\frac{a}{W}\right) \qquad 4.1$$

Where P_Q is the assessed maximum load at the end of the linear portion of the load deflection curve during ramping and which turned out predominantly to be the load at failure. The other parameters have their usual meanings: a, crack length, B the thickness of the specimen, W, the width of the specimen, and S is the span as shown in Figure 4.1a. The load obtained from the graph for each specimen can be found in the ***Appendix D*** generated by the ESH fatigue machine and a plotter.

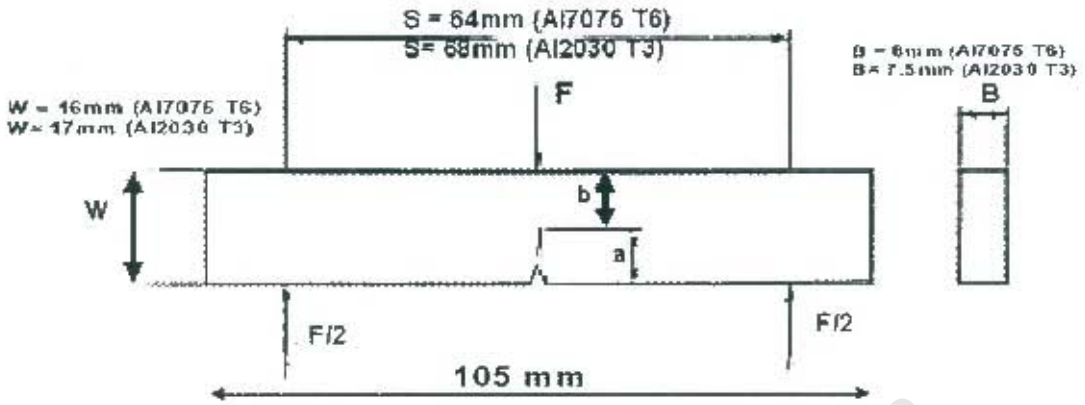

Figure 4.1a: Dimension of the fracture toughness specimen for both alloys used.

The value $f\left(\frac{a}{W}\right)$ **is expressed as shown in equation 4.2,**

$$f\left(\frac{a}{W}\right)=\frac{3\left(\frac{a}{W}\right)^{0.5}\left[1.99-\left(\frac{a}{W}\right)\left(1-\frac{a}{W}\right)\left(2.15-\frac{3.93a}{W}+2.7\frac{a^2}{W^2}\right)\right]}{2\left(1+\frac{2a}{W}\right)\left(1-\frac{a}{W}\right)^{1.5}} \qquad 4.2$$

4.2 *Fracture Toughness Results.*

4.2.1 Determination of Fracture Toughness for the Al7075 T6.

This material was found to be of a brittle characteristic and from BS7448 1991, the 5% slope offset was not applied to determine the force P as the peak load was sufficient (***see Appendix D***).

To be regarded as a valid measure of K_{IC}, the value of fracture of toughness obtained must satisfy the validity criterion. It can be accepted only if,

$$\mathbf{a, B, W\text{-}a} \geq 2.5\left(\frac{K_{IC}}{S_y}\right)^2 \qquad 4.3$$

Table 4.1 illustrates the fracture toughness results obtained for the material used.

Specimen No	$a_{average}$ (mm)	B (mm)	W (mm)	f(a/w)	Force P (kN)	K (Pa√m)	K (MPa√m)	
C1	0.00767	0.00789	0.0161	2.473804	1786	17543281.858	17.54	
C2	0.0082	0.00793	0.0161	2.743016	1713	18563237.332	18.56	
C3	0.00575	0.00799	0.0161	1.764802	2860	19790488.904	19.79	
C4	0.00798	0.00799	0.0161	2.626146	1775	18277282.785	18.28	
C5	0.00787	0.008	0.0161	2.570514	1750	17616079.885	17.62	
					Mean =	18358074.15	18.36	(MPa√m)
					Std deviat	. =	0.910356	

Table 4.1: Results of fracture toughness of the Al7075 T6.

From equation 4.3, $\mathbf{2.5}\left(\frac{18.358}{505}\right)^2 = \mathbf{3.3\ mm.}$

Hence since the dimension of the specimens satisfies the validity criterion, the fracture toughness of 18.358MPa√m was taken as the K_{IC} actual fracture toughness of the material and the behaviour can be regarded as satisfying LEFM conditions.

- ***Fracture surfaces of the Al7075 T6 fracture toughness specimens***

Figure 4.1b: Fracture toughness specimen for Al7075 T6. ***(See Appendix E for Al2030 T3)***

4.2.2 Determination of Fracture Toughness for the Al2030 T3.

Using the similar procedure in section 4.2.1, the determination of the high strength low toughness alloy Al2030 T3 was found. The 5% slope offset was used for the Al2030 T3 alloy to determine the force P as shown in ***Appendix D***.

From equation 4.3 the so called "valid thickness" was determined,

$$\mathbf{2.5}\left(\frac{19.693}{353.7}\right)^{2} = \mathbf{7.74\ mm.}$$

The dimensions B of the specimens were slightly less than the validity criterion of equation 4.3. However as was mentioned in Literature review (Chapter 2 section 2.8.7) it is arguable that the validity equation coefficient 2.5 can be replaced by a value closer to 1.1 in which case the specimen dimensions are clearly compatible with the LEFM behaviour. Table 4.2 shows the fracture toughness of the Al2030 T6.

Specimen No	a average (mm)	B (mm)	W (mm)	f(a/w) dimensionless	Force Max (N)	Force P (N)	Kp (Pa√m)
A1	0.00824	0.00748	0.01700	2.536712	1961	1940	18.33
A2	0.00931	0.00750	0.01700	3.118477	1955	1920	19.72
A3	0.00809	0.00750	0.01700	2.471577	2301	2225	20.84
A4	0.00831	0.00750	0.01700	2.571722	2141	2135	20.26
A5	0.00850	0.00750	0.01700	2.662500	1977	1875	18.02
A6	0.00849	0.00750	0.01700	2.656299	1757	Ignored	Ignore
A7	0.00911	0.00750	0.01697	3.005262	2092	2020	20.49
A8	0.00850	0.00749	0.01700	2.662500	2283	2100	20.18
				Mean		19.69	MPa√m
				New Std Deviation		1.1	MPa√m

Table 4.2: Fracture toughness results of Al2030 T6.

4.3 *Determination of the Y- Compliance from Thumbnail Cracks in Bending.*

- ***Y Compliance for Specimens in Bending.***

The Y compliance was determined from the equation

$$Y = \frac{K_{IC}}{\sigma_{fail_{Bending}} \sqrt{\pi a_{crit}}} \qquad \textbf{4.4}$$

The specimens were ramped under bending and the stress of failure was derived as shown.

$$\text{Failure Load P} = \frac{4M}{L} \qquad \textbf{4.5}$$

As we know $\sigma_{bending} = \frac{My}{I}$ where y is taken d/2.

$$\text{And} \quad I = \frac{\pi d^4}{64} \qquad \textbf{4.6}$$

$$\text{Thus } \sigma_{bending} = \frac{8PL}{\pi d^3} \qquad \textbf{4.7}$$

Where P = failure load (***see Appendix E***), L = span length and d = specimen diameter

The span used was 64mm and d was 17mm.

The result obtained are tabulated in Table 4.3

Specimen	a	2c	Force P		Stress		
No	(mm)	(mm)	(N)	a/d	(Mpa)	a/2c	Y
B1a	5.58	15.3	6612	0.328235	219334106	0.364706	0.632163
B1b	7	21.1	4806	0.411765	159425244	0.331754	0.776508
B2a	6.78	17	5620	0.398824	186427356	0.398824	0.674726
B3a	4	10.75	8222	0.235294	272741231	0.372093	0.600442
B3b	6.78	19.2	5178	0.398824	171765275	0.353125	0.732322
B3c	7.8	21.5	3902	0.458824	129437641	0.362791	0.906034
B4a	4.4	9.5	9284	0.258824	307970060	0.463158	0.507011
B4c	3.65	9.5	9596	0.214706	318319734	0.384211	0.53867
B5a	6.32	13.75	7352	0.371765	243861480	0.459636	0.534213
B5b	5.4	12.55	8234	0.317647	273139297	0.430279	0.516025

Table 4.3: Y compliance of Thumbnail crack shapes results

Figure 4.2(a), the trend of the graph of Y against a/d, shows a typical concave up relationship with a minimum point of (0.28, 0.51). The absolute maximum point is shown by the highest value of Y and a/d, on the right hand side. This point was from specimen B3c (as shown from the Table 4.3) and had the deepest crack length compared to the other specimens. Having a deep crack in the round bar decreases the breaking stress. Hence it is more liable to break with a smaller force as shown in Table 4.3.

Figure 4.2(b) shows the relationship between Y compliance factor and the aspect ratio of a/2c for a/d $\leq$ 0.458. The range obtained from actual experiment is $0.33 \leq a/2c \leq 0.46$. The trend of the curve shows a decrease in Y value with an increase in a/2c. The set of data is rather clustered and the trend difficult to determine and a wider range of a/2c could (in hindsight) have been developed.

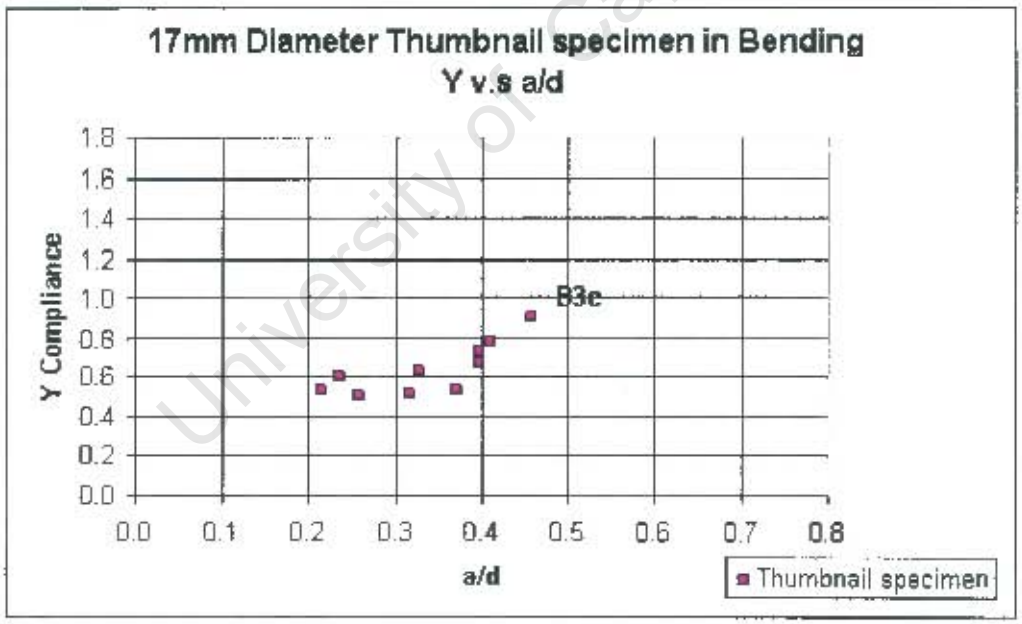

Figure 4.2(a): Graph of Thumbnail specimens in bending Y compliance vs. a/d.

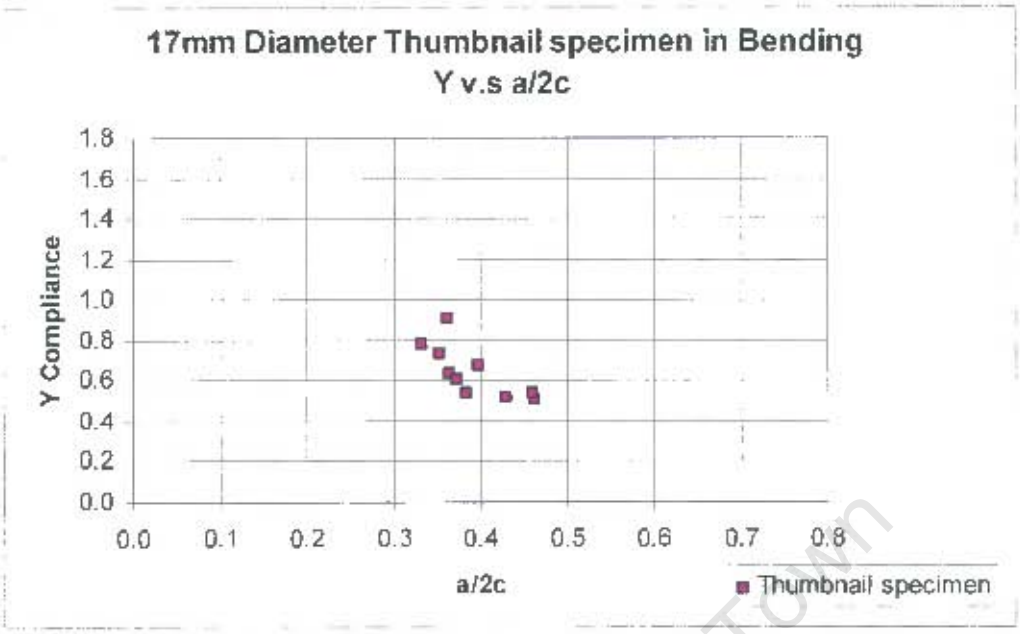

Figure 4.2(b): Graph of Thumbnail specimens in bending Y compliance vs. a/2c.

- *Pictures of the fractured thumbnail specimens.*

Figure 4.2(c): Fracture surfaces of broken thumbnail specimens in bending.

From the photograph it can be seen how the fatigue crack were grown with the applied stress concentration (drilled holes or notches of different sizes). The

specimens having notched stress concentrations formed a shallower thumbnail fatigue crack shape than when using drilled holes as a stress concentration, which tended to result in a rounder shape, as shown in Figure 4.2c for specimen B1a and B1b.

4.4 *Determination of the Y- Compliance from Crescent moon Cracks in Tension.*

4.4.1 Y Compliance for Specimens in Tension.

The normalized Y compliance was determined from equation 4.8,

$$Y = \frac{K_{IC}}{\sigma_{fail_{tension}} \sqrt{\pi a_{crit}}} \qquad \textbf{4.8}$$

Equation 4.8 was used to find Y, the dimensionless stress intensity factor. Since this test was done in tension.

Therefore $\sigma_{tension} = \frac{P}{A}$ **4.9**

Where P is the failure load as shown in ***Appendix F*** and A is the cross-section area of the specimen.

$A = \pi r^2$ where r is the radius of the specimen.

The Y compliance of the round bars of respective diameters 14mm, 17mm and 20mm was determined. Tables 4.4, 4.5, 4.6 and 4.7 illustrate the results of specimens of diameter 14mm using Al7075 T6, 14mm, 17mm and the 20mm using Al2030 T3 respectively. For each specimen the crack depth **a** and length **2c** was measured and the respective aspect ratios a/d and a/2c were calculated. The stress using a circular cross-section for each specimen was also reckoned. Twenty three crescent moon specimens from the material Al7075 T6 was obtained. No meaningful results were obtained for specimens D12, C7, B11 and B12 since they did not break at the crack due to gripping problems during the tensile test.

4.4.2 The 14mm Diameter Crescent moon Specimens.

Specimen No	a (mm)	2c (mm)	Force (N)	Stress (Mpa)	Aspect ratio a/d	Aspect ratio a/2c	Y Compliance
A1	0.72	13	66631.04	432.84	0.051	0.038	0.8918
A2	2.1	26	50440.32	327.67	0.150	0.096	0.6898
A3	2.2	21.5	46081.28	299.35	0.157	0.116	0.7377
A4	4	19	34374.14	223.30	0.286	0.211	0.7334
A5	2.9	25	44773.57	290.85	0.207	0.116	0.6613
A6	1.8	27.5	46704	303.39	0.129	0.065	0.8047
A7	0.5	11.5	68499.2	444.98	0.036	0.043	1.0409
A8	1	22.5	60403.84	392.39	0.071	0.044	0.8347
A9	1.5	18	56978.88	370.14	0.107	0.083	0.7225
A10	0.4	18	69682.37	452.67	0.029	0.022	1.1441
A11	1.2	19	62707.9	407.36	0.086	0.063	0.7340
A12	0.6	17	72546.88	471.27	0.043	0.035	0.8972
A13	0.4	23	73107.33	474.91	0.029	0.017	1.0905
A14	0.5	17.5	66070.59	429.20	0.036	0.029	1.0792
A15	0.5	27	70367.36	457.11	0.036	0.019	1.0133
A16	2.2	12.5	50936.5	330.90	0.157	0.176	0.6673
A17	0.8	11.8	69744.64	453.07	0.057	0.068	0.8082
A18	2.1	15	57165.7	371.36	0.150	0.140	0.6086
A19	4.35	18.3	33004.16	214.40	0.311	0.238	0.7325
A20	6.04	21.7	20549.76	133.49	0.431	0.278	0.9983
A21	6.28	20.5	21795.2	141.58	0.449	0.306	0.9231
A22	8.94	25.4	14945.28	97.09	0.639	0.352	1.1283
A23	6.53	24.7	16190.72	105.18	0.466	0.264	1.2186

Table 4.4: Results of 14mm diameter crescent moon specimens using Al7075 T6 material.

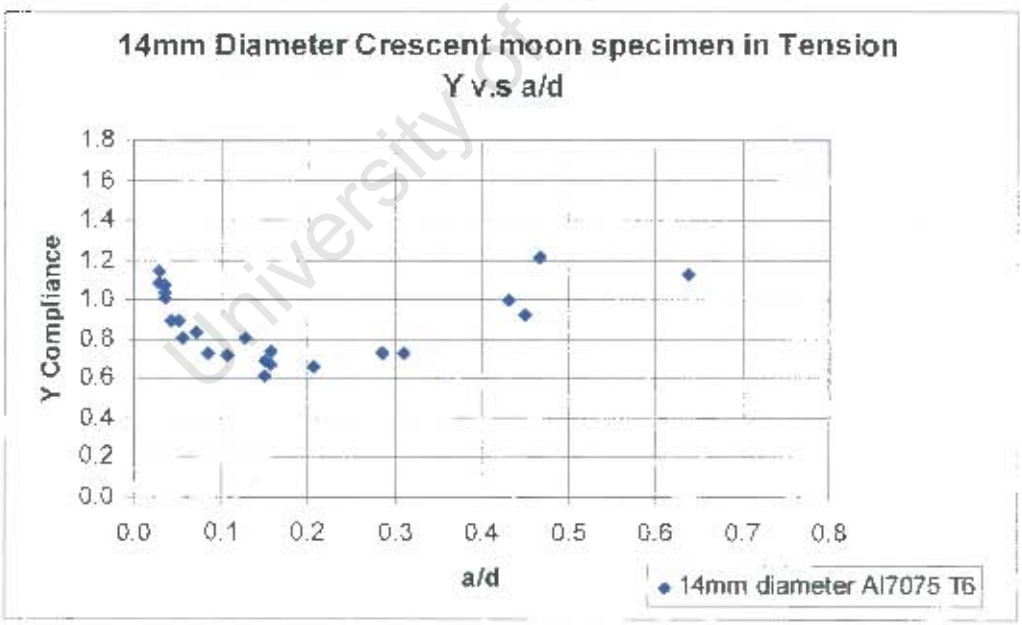

Figure 4.3(a): Graph of 14mm diameter Crescent moon specimens in tension Y vs. a/d.

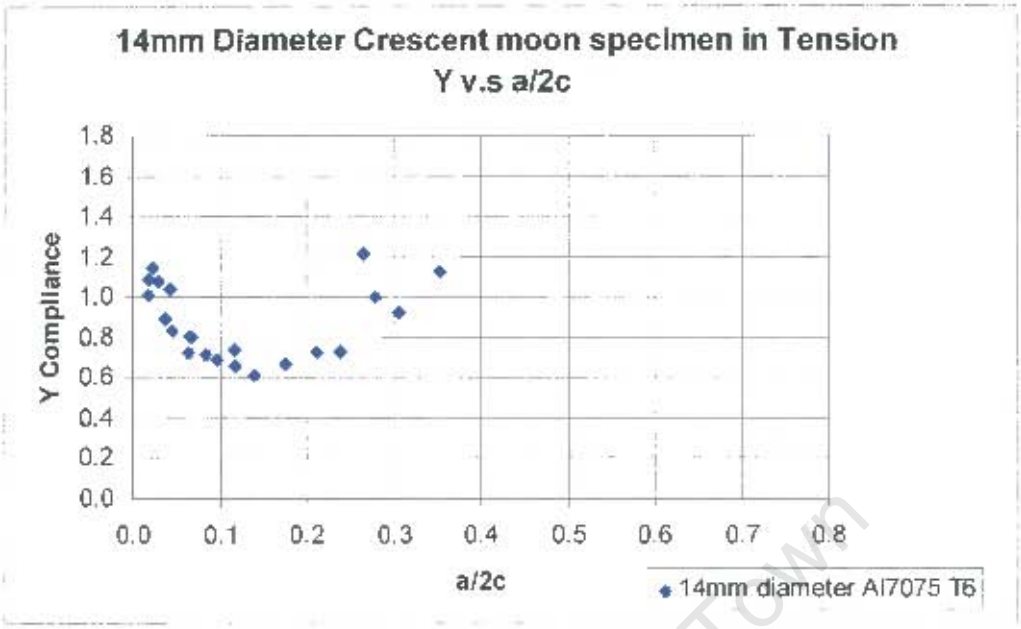

Figure 4.3(b): Graph of 14mm diameter Crescent moon specimens in tension Y vs. a/2c.

Figure 4.3(a) suggests that Y has a concave up relationship with a/d. The range of values covered by Al7075 T6 for the 14mm diameter $0.029 \leq a/d \leq 0.639$. Y has a minimum value 0.6 when a/d equals 0.15. The concave up trend in Figure 4.3(a) is much wider than that in Figure 4.3(b). This is because a/2c is very seldom greater than 0.5. The data of Y compliance of the 14mm diameter of the Al7075 T3 was added to that obtained for similar diameter for Al2030 T6. Table 4.5(a) illustrates the results obtained for the 14mm diameter crescent moon specimen using the Al2030 T3 material.

Specimen No.	Force N	a mm	2c mm	d mm	a/2c	a/d	Stress MPa	Y Compliance
D1	20340	7	36	14	0.19444	0.50000	102.10	1.09504
D2	27000	5	28	14	0.17857	0.35714	175.40	0.89586
D3	36260	4.5	21.5	14	0.20930	0.32143	235.55	0.70315
D4	35450	4.5	28	14	0.16071	0.32143	230.29	0.71922
D5	36330	5.5	17	14	0.32353	0.39286	236.00	0.63480
D6	36030	5	19	14	0.26316	0.35714	236.00	0.66578
D7	55450	0.5	34	14	0.01765	0.04286	360.21	1.25824
D8	60910	1	28.5	14	0.03509	0.07143	395.60	0.88795
D9	53290	2	16	14	0.12500	0.14286	346.10	0.71767
D10	40150	3.5	23.5	14	0.14894	0.25000	260.92	0.72005
D11	40380	4.2	26.5	14	0.15849	0.30000	262.31	0.65357

Table 4.5a: Results of the Y-compliance for 14mm diameter crescent moon specimens using Al2030 T3.

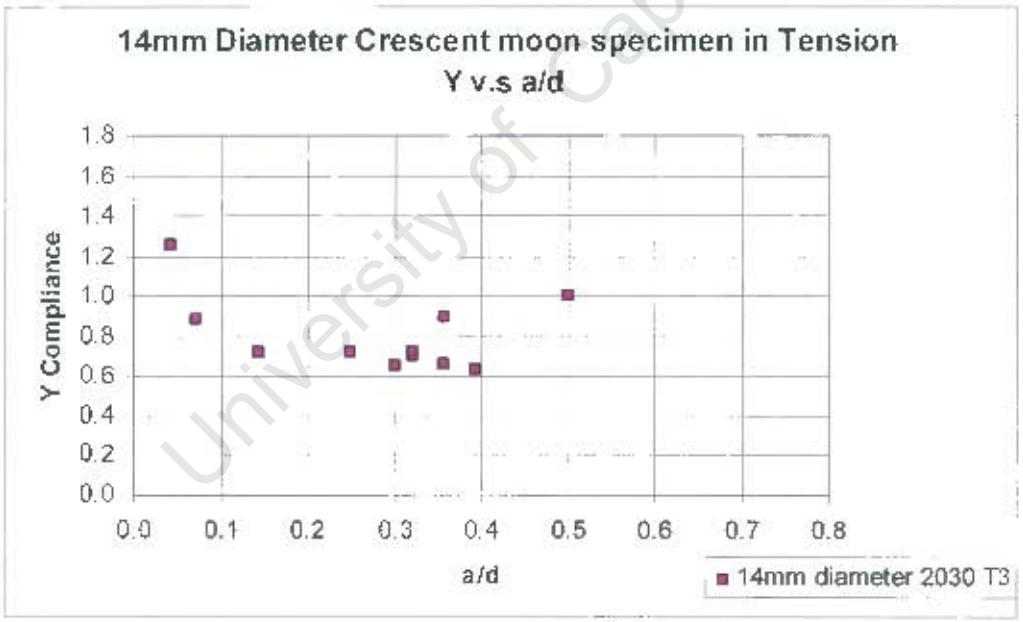

Figure 4.4(a): Graph for the 14mm diameter round bar, Y compliance vs. a/d.

Figure 4.4(a) shows how the stress intensity factor Y varies with relative depth. The trend shows a concave up curve. Scatter in the results indicate slightly different values of Y for nominally similar a/d. As the fatigue crack depth a decreases i.e. as

a/d→0, the stress intensity factor follows a negative slope trend with an increase in value. The shortest crack depth recorded from the experiment was from specimen D7 with a = 0.6mm and it provides a high value of Y which is 1.26 as shown in Table 4.5.

Fracture stresses for small cracks have lower stress values resulting to higher values of Y. It was also noticed from the graph that the bigger the crack depth, the higher the Y compliance value as shown by specimen D1 in Table 4.5. The range of a/d obtained for the 14mm diameter experiment was $0.04 \leq a/d \leq 0.5$.

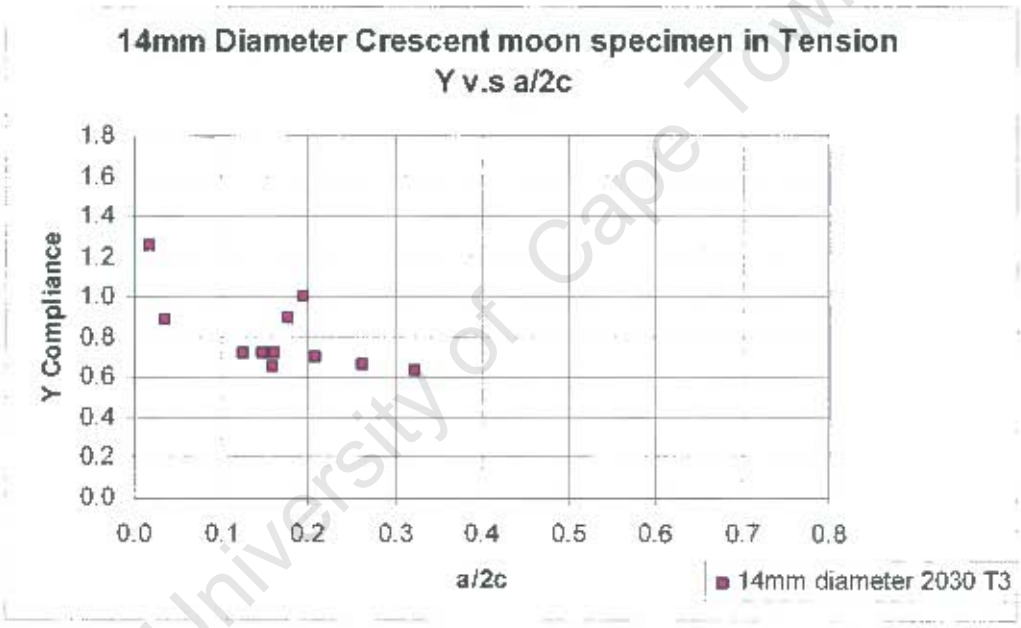

Figure 4.4(b): Y compliance against a/2c aspect ratio.

The range of values obtained was $0.17 \leq a/2c \leq 0.32$. Once again, a/2c cannot be greater than 0.5. As a/2c decreases the Y compliance increases which shows that fracture stress for small cracks have lower stress values resulting to higher values of Y.

Figure 4.4(c) and 4.4(d) shows the trend of Y compliance for both materials Al7075 T6 and Al2030 T3 on the same scale for respective aspect ratios a/d and a/2c. Y values for both materials merge together and follow the concave up trend. However data points were not obtained in the range of $0.5 \leq a/d \leq 0.639$. As a/d decreases the Y values increases with a negative gradient. Smaller cracks still exhibit large values of Y.

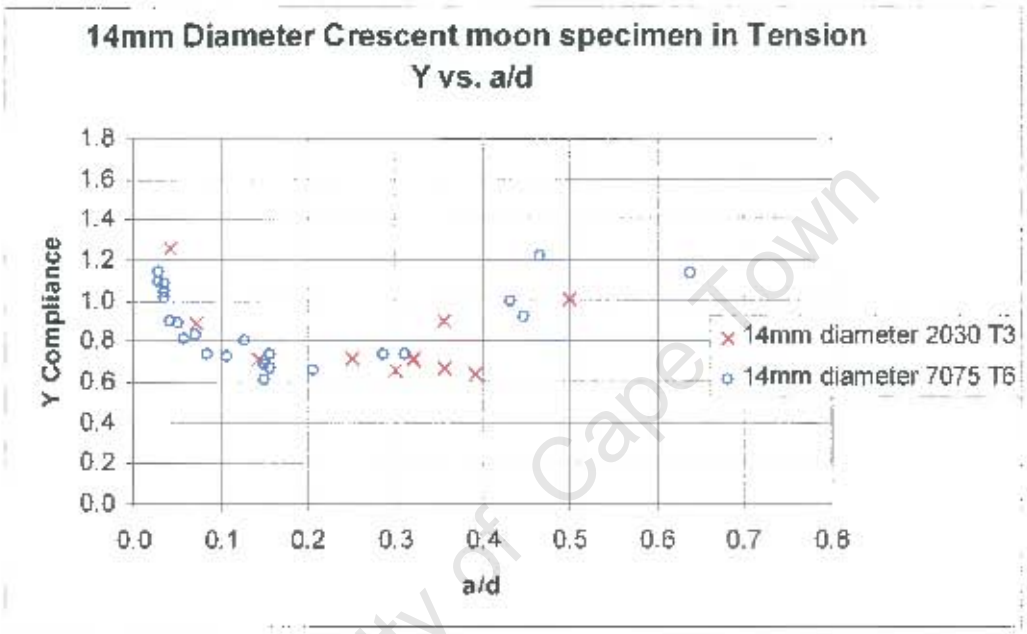

Figure 4.4(c): Y compliance of both materials of diameter 14mm vs. a/d.

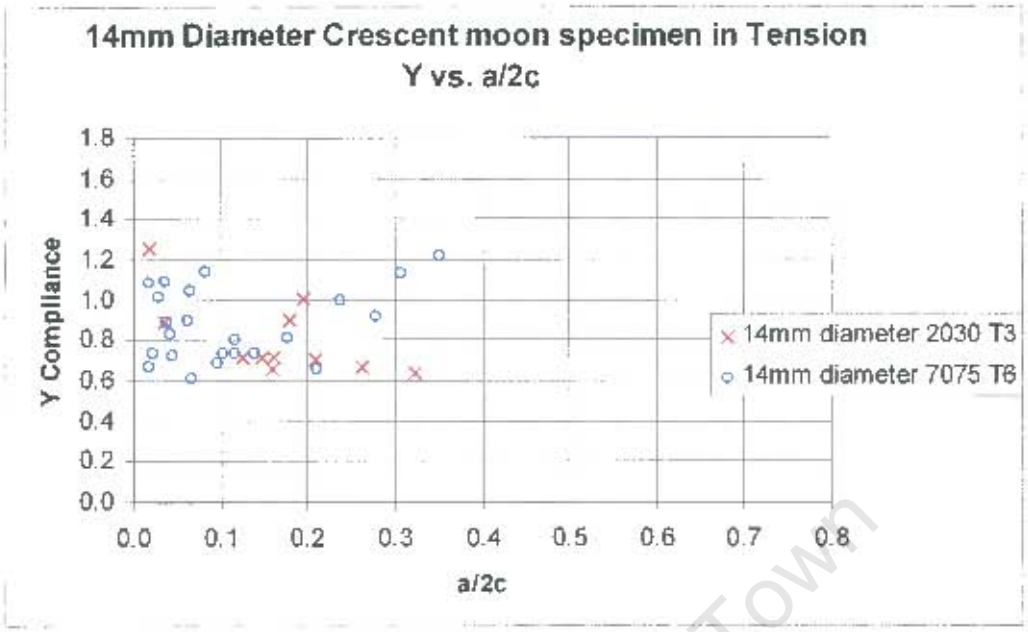

Figure 4.4(d): Y compliance of both materials of diameter 14mm vs. a/2c.

In the range a/d ≥ 0.15 in Figure 4.4(c), it was observed that specimens having nominally similar a/d values have Y compliance increases with decrease in a/2c. The Table 4.5(b) shows the values of Y and a/2c for nominally similar a/d values. Figure 4.4(e) shows how as a/2c increases Y decreases for the same relative depth ratio a/d.

a/d	a/2c	Y Compliance
0.15	0.14	0.6086
	0.096	0.6895
0.157	0.176	0.6673
	0.116	0.7377
0.32	0.161	0.7192
	0.2093	0.7032
0.357	0.17857	0.8958
	0.2631	0.6657

Table 4.5(b): Values of Y and a/2c for the same a/d value.

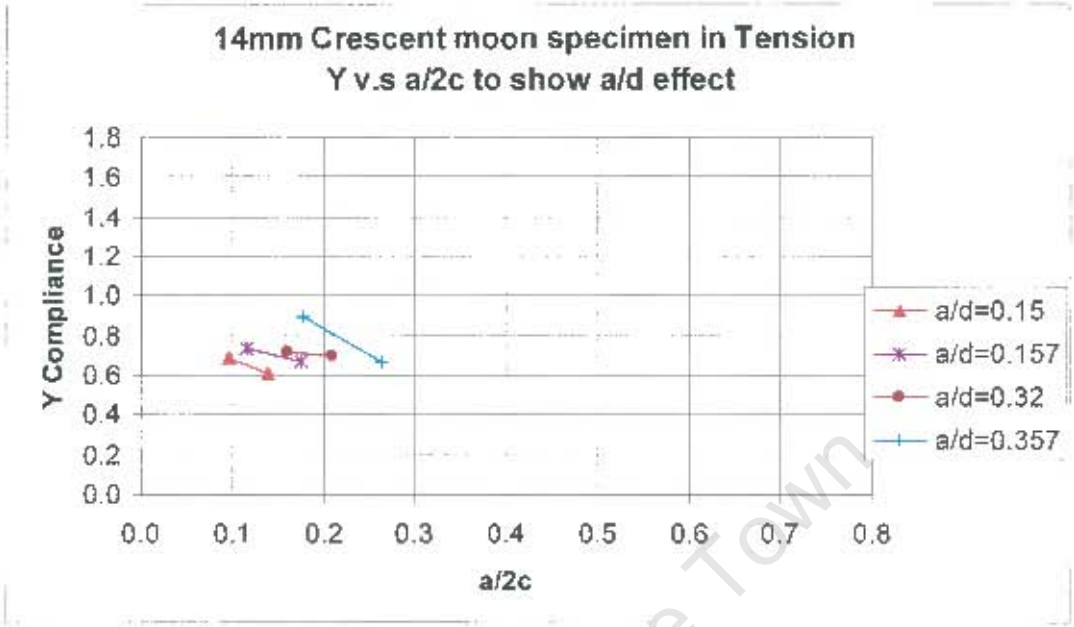

Figure 4.4(e): Values of Y vs. a/2c having similar values of a/d.

- ***Fractured surfaces for the 14mm diameter crescent moon samples.***

Figure 4.5 (a) and (b) show the fracture surfaces of the 14mm diameter crescent moon specimens broken in tension for the Al7075 T6 and 2030 T3 respectively.

Figure 4.5 (a): Crescent moon fatigue cracks of 14mm diameter Al7075 T6.

Figure 4.5 (b): Crescent moon fatigue cracks of 14mm diameter Al2030 T3.

4.4.3 The 17mm Diameter Crescent moon Specimens.

Specimen No.	Force N	a mm	2c mm	d mm	a/2c	a/d	Stress MPa	Y Compliance
C1	16780	8.5	44.5	17	0.19101	0.50000	73.93	1.63014
C2	38480	8	27.5	17	0.29091	0.47059	169.53	0.73273
C3	36860	8.5	31	17	0.27419	0.50000	162.39	0.74210
C4	51000	7	19.5	17	0.35897	0.41176	224.95	0.59033
C5	28810	8.5	32	17	0.26563	0.50000	126.93	0.94945
C6	58550	5	22	17	0.22727	0.29412	257.95	0.60914
C9	83010	1.2	22	17	0.05455	0.07059	365.71	0.87701
C10	85910	2	31	17	0.06452	0.11765	378.49	0.65640
C11	74920	3	31	17	0.09677	0.17647	330.07	0.61456
C12	77510	0.8	37	17	0.02162	0.04706	341.48	1.15033

Table 4.6: Results of the Y-compliance for 17mm diameter crescent moon specimens using Al2030 T3.

From Table 4.6, the graphs of Y vs. a/d aspect ratios and a/2c were plotted which are illustrated in Figure 4.6 (a) and (b)

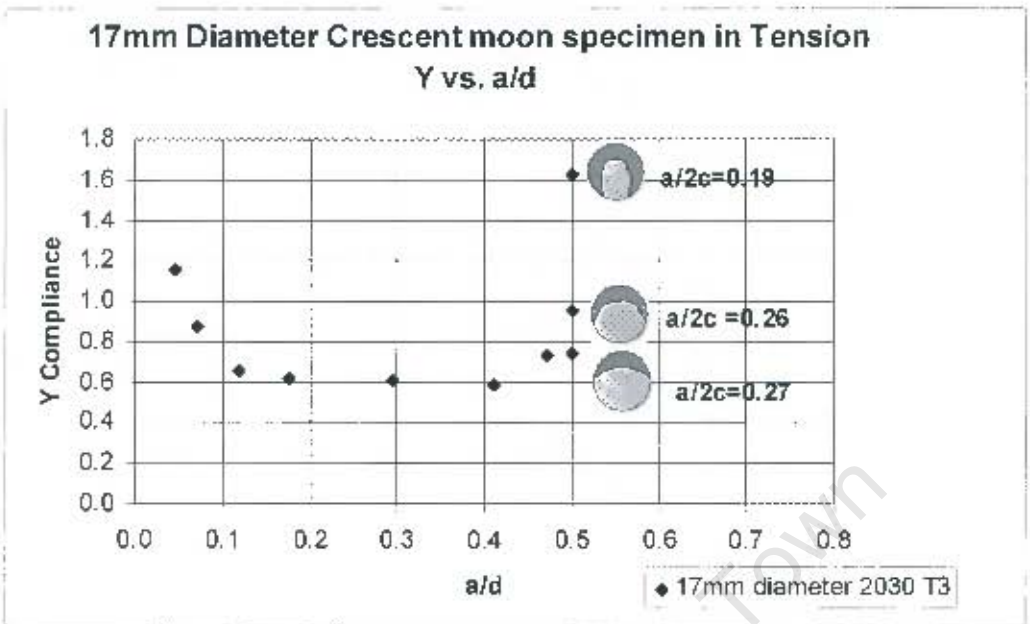

Figure 4.6 (a): Stress intensity factor Y vs. a/d for 17mm diameter crescent moon specimens.

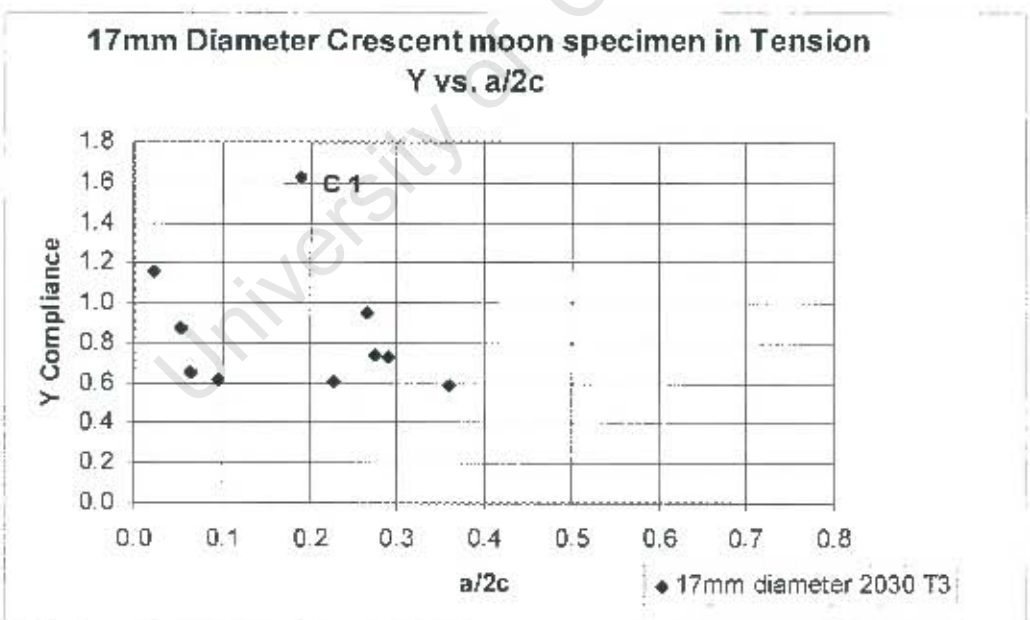

Figure 4.6 (b): Stress intensity factor Y vs. a/2c for 17mm diameter crescent moon specimens.

From Figure 4.6(a), the graph shows a concave up curve. Only eleven data points were available for the 17 mm diameter crescent moon test. The Y compliance data lies in the range $0.047 \leq a/d \leq 0.5$. At a/d =0.5 on the graph shows how as a/2c decreases Y increases for three specimens having the same a/d values i.e. C1, C3 and C5.

Figure 4.6 (b) also shows the trend of a concave up curve if data points were obtained in the range $0.1 \leq a/2c \leq 0.2$. The graph shows that a/2c cannot be greater than 0.5. The maximum Y value obtained was to 1.63 for an a/2c of 0.19 and was exhibited by a large crack as shown in Figure 4.6 (c).

- ***Pictures of the fractured surfaces for the 17mm diameter.***

Figure 4.6 (c): Fracture surface of C1 (a large crescent moon crack)

Figure 4.6(d): Crescent moon fatigue cracks for the 17mm diameter specimens broken in tension.

From Figure 4.6(d) specimen C6, C4, C3 and C12 were found to be not perfectly crescent moon shaped fatigue cracks. This happened due to overloading during the fatigue test and this force the crack to be asymmetrical that is more in the form of a "comma" shape.

4.4.4 The 20mm Diameter Crescent Moon Specimens

In a similar way, Y compliance values for the 20mm diameter specimens were determined as a function to their respective depth and aspect ratios a/d and a/2c. The results are illustrated in Table 4.7 and by the graphs in Figure 4.7 (a) and (b).

Specimen	Force	a	2c	d	a/2c	a/d	Stress	Y
No.	N	mm	mm	mm			MPa	Compliance
B1	79900	7	20	20	0.3500	0.35	254.33	0.52215
B2	19100	14.5	53.5	20	0.2710	0.725	60.80	1.51765
B3	57200	10	33.5	20	0.2985	0.5	182.07	0.81023
B4	44300	11.5	38.5	20	0.2987	0.575	141.01	0.73474
B5	45500	11	37.5	20	0.2933	0.55	144.83	0.73144
B6	56200	9.5	31	20	0.3065	0.475	178.89	0.63722
B7	112000	1.5	26	20	0.0577	0.075	356.51	0.80468
B8	68100	5	45.5	20	0.1099	0.25	216.77	0.72486
B9	105000	2.5	45.5	20	0.0549	0.125	334.23	0.66486
B10	105000	2.5	26	20	0.0962	0.125	334.23	0.66486

Table 4.7: Data obtained for Y compliance for the 20 mm diameter crescent moon specimens.

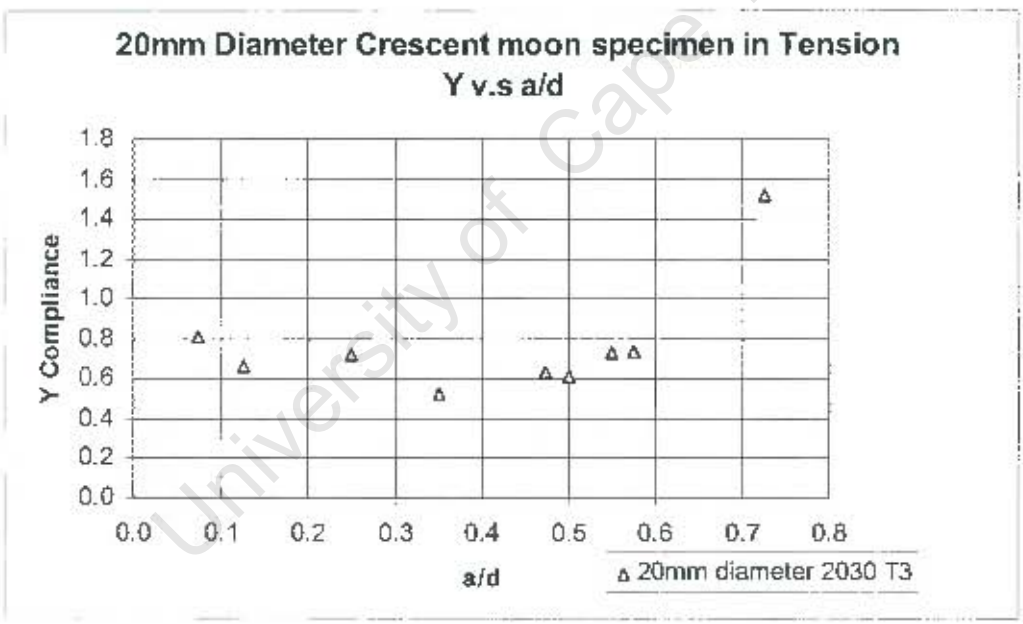

Figure 4.7 (a): Y compliance vs. a/d for the 20mm diameter specimens.

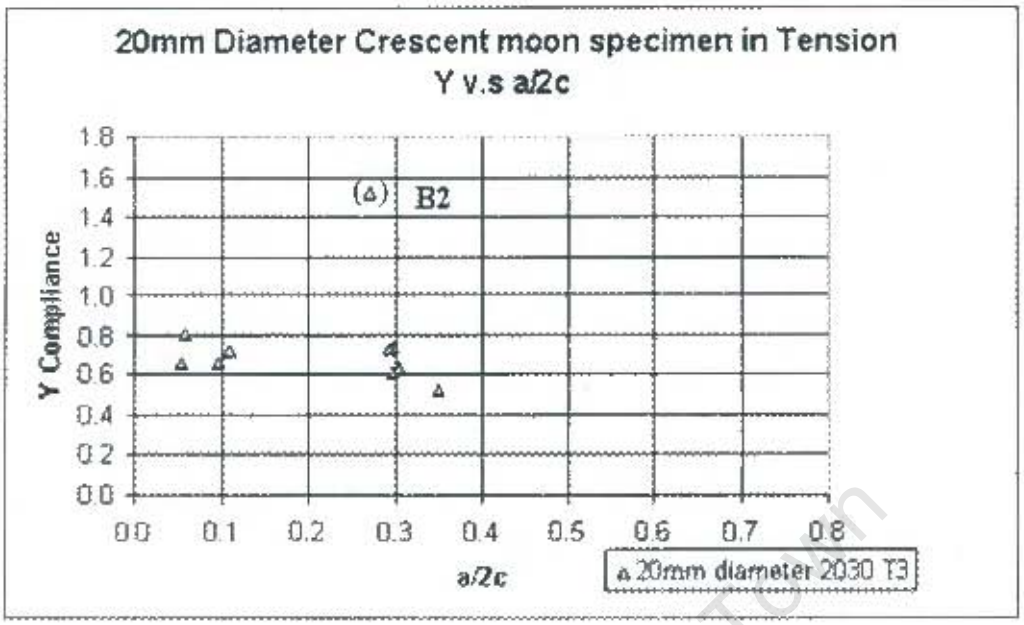

Figure 4.7 (b): Y compliance vs. a/2c for the 20mm diameter specimens.

The SIF values are found within the range $0.075 \leq a/d \leq 0.725$ as shown in Figure 4.7(a). The data points are widely spread showing a concave up curve trend. Figure 4.7 (b) illustrate the Y compliance data plotted against a/2c ratio within a smaller range $0.054 \leq a/2c < 0.350$. The data did not show a marked trend since there was significant data within the range $0.1 \leq a/2c \leq 0.3$ (specimens there broke in the grips unfortunately). Point B2 in Figure 4.7 (b) was located completely out of the cluster of the data points. It was found to have a deeper fatigue crack among the other broken specimens as shown in Table 4.7. A picture of the fatigue crack fracture surface is illustrated in Figure 4.7 (c). Figure 4.7(d) shows the crescent moon fatigue cracks obtained for the 20mm diameter specimens. It was observed during the experiment that curved fronted cracks gradually changed to straight fronted cracks by mid thickness. This transition occurs as the crack length a tends to approach the radius r of the cross section of the bar and 2c tends to half the circumference. In other words to achieve such crack shapes a/2c must tend to $1/\pi$.

- *Picture of the 20mm crescent moon fatigue cracks*

Figure 4.7 (c): Specimen B2 with a fatigue crack length a = 14.5mm and high SIF value of 1.51.

Figure 4.7 (d): The Crescent moon fatigue cracks for the 20mm diameter specimen broken in tension.

4.5 *Comparing Bending Thumbnail Specimens with Crescent Moon Specimens in Tension*

From Figure 4.13 (a) it is observed that the Y compliance factor for tension tends to be higher than for bending though there was a lack of data in the range a/d>0.5 . The thumbnail data points could not be properly compared since they lied only in the range 0.2< a/d <0.5. Similar observations were made for Figure 4.13(b) that is Y compliance in tension shows higher values that that in bending.

Figure 4.13 (a): Comparing the Y compliance for tension and bending against a/d relative depth.

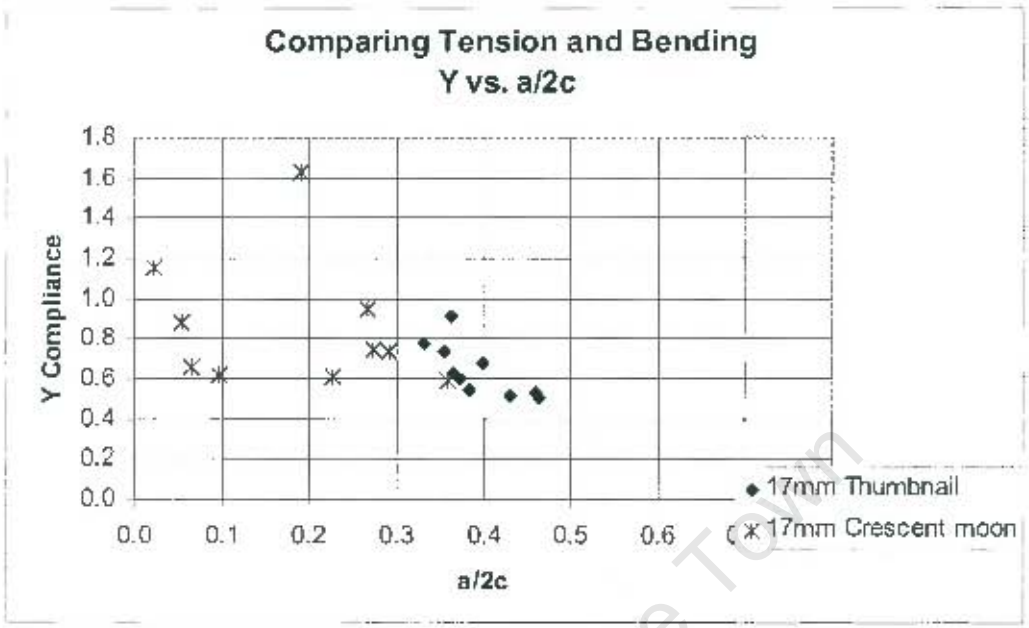

Figure 4.13(b): Comparing the Y compliance for tension and bending against their respective a/2c aspect ratio.

4.6 *Size Effect on Y- Compliance*

Figure 4.14: Picture of some broken specimen in tension of different sizes in the experiment.

Figure 4.14 shows some of the broken specimens of different sizes. The stress intensity factors for specimens of different sizes were also compared with their respective relative depths a/d and aspect ratios a/2c as shown in Figure 4.15 (a) and (b) respectively.

Figure 4.15 (a): Effect of size on Y compliance data with respect to a/d relative depth.

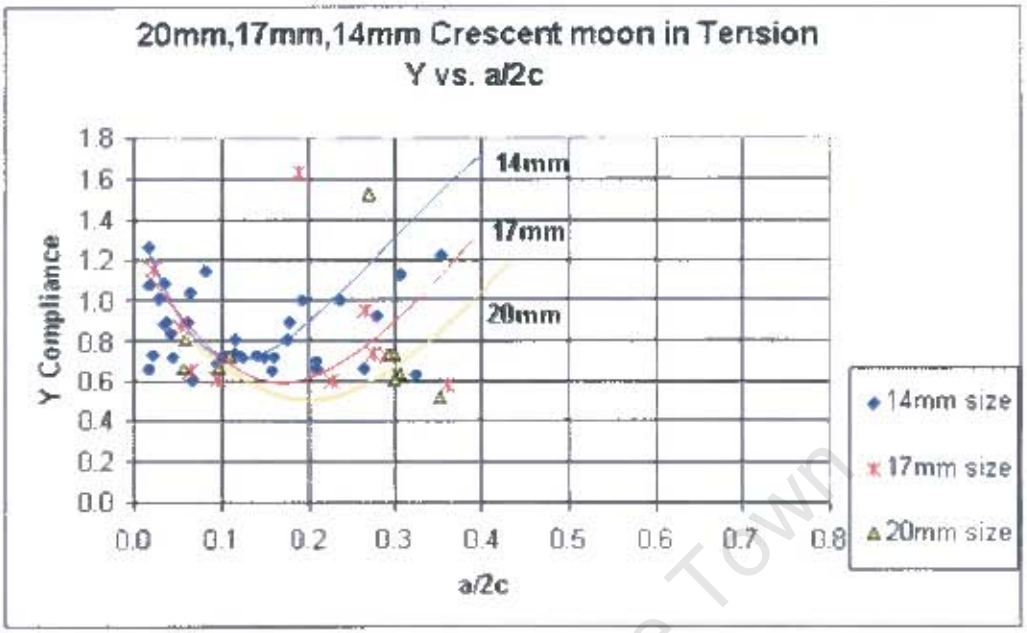

Figure 4.15 (b): Effect of size on Y compliance data with respect to their aspect ratios.

From Figure 4.15 (a) and (b) it was observed that as the sizes of the specimen increases from 14mm to 20mm, the concave up curves generated by the Y compliance tends to shift lower and wider to the right hand side. a/2c values seems to be distorted as size increases but still shows a tendency that Y values decreases as size increases. It was also observed from Figure 4.15 (a) that the points having the same a/d value irrespective of their sizes e.g. in this case at a/d =0.5, their a/2c decreases as their respective stress intensity factor increases.

4.7 Summary

The fracture toughness of both materials Al7075 T6 and Al2030 T3 were measured and found to be 18.6MPa$\sqrt{m}$ and 19.7MPa$\sqrt{m}$ respectively. The equations 4.4 and 4.8 were used to calculate the Y compliance for specimens in bending and tension for the thumbnail and crescent moon shapes fatigue cracks respectively. Graph of stress intensity factors relative to the depth a/d and aspect ratio a/2c were plotted and compared. The results show an upper concave upwards trend. Y compliance for tensile specimens tends to be higher than the Y values for bending. Size seems to affect Y compliance values in that the bigger the specimens, the lower are the values of the Y compliance factors.

5. Discussion

5.1 Introduction

In the previous chapter, the results of Y compliance obtained from the thumbnail fatigue crack shapes broken in bending, and crescent moon fatigue crack shapes broken in tension, were analysed as a function of their respective relative depths a/d and aspect ratios a/2c as well as the size effect.

This Discussion chapter presents both an internal consideration of the authors own results and comparison of these results with those of other authors in the Literature review, as described in chapter 2. The Y compliance stress intensity values for the crescent moon type cracking do not appear to have been reported previously, either computational or experimental sources. Most published Y compliance data were computationally derived for thumbnail fatigue cracks, in either bending or tension.

However some previous students (Radebe **[68]** and Fleuriau **[69]**), working at UCT under Tait's supervision, have produced some valuable data of crescent moon fatigue cracks in bending, together with some thumbnail fatigue cracks in both bending and tension. These Y compliance data were combined together with the results for the present project and was compared to the other available data from published literature, particularly (Carpinteri **[7]**, Ng and Fenner **[8]**, Si **[10]**, Da Fonte and De Freitas **[3]**, Shiratori *et al.* **[45]** and Newman and Raju**[6]**).

The Discussion chapter further compares the Y compliance data obtained by assuming the fast fracture region was

(i) firstly the full original circular area and comparing this to

(ii) the "corrected" Y compliance data by calculating the *actual* fast fractured area.

This interpretation of Y was also compared to published stress intensity factors obtained by authors from the literature.

5.2 *Y Compliance Data and General Trends obtained in the same Laboratory*

Figure 5.1(a) shows the available stress intensity results in tension versus the relative crack depth a/d obtained from the same laboratory. Fleuriau's Y compliance data follows the trend of the Y compliance for the 14mm of the present result in the range of $0.27<a/d<0.45$. Fleuriau's data shows slightly higher values in the range $0.33<a/d<0.39$.

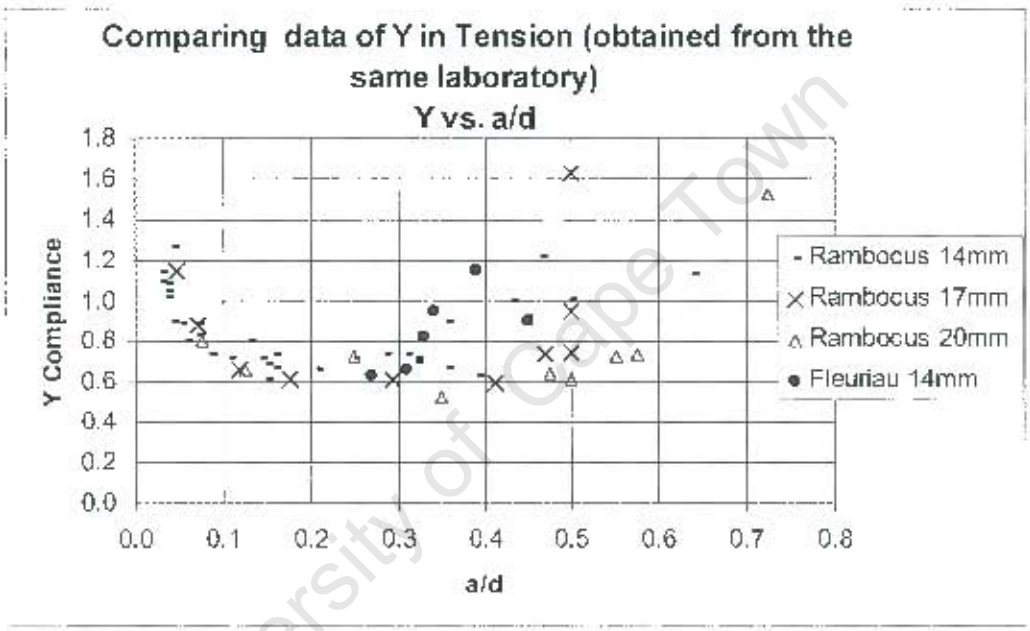

Figure 5.1 (a): Results of Y compliance factors in tension for both Fleuriau [ref] and present study results of Rambocus versus a/d (in the same lab).

The data was plotted against a/2c and from Figure 5.1(b), it can be seen that a/2c are not greater than 0.5. From Fleuriau's data not much can be commented since it consisted very few data points. The six data points lies in the range of $0.08 \leq a/2c \leq 0.33$ which are consistent with the 14mm specimens.

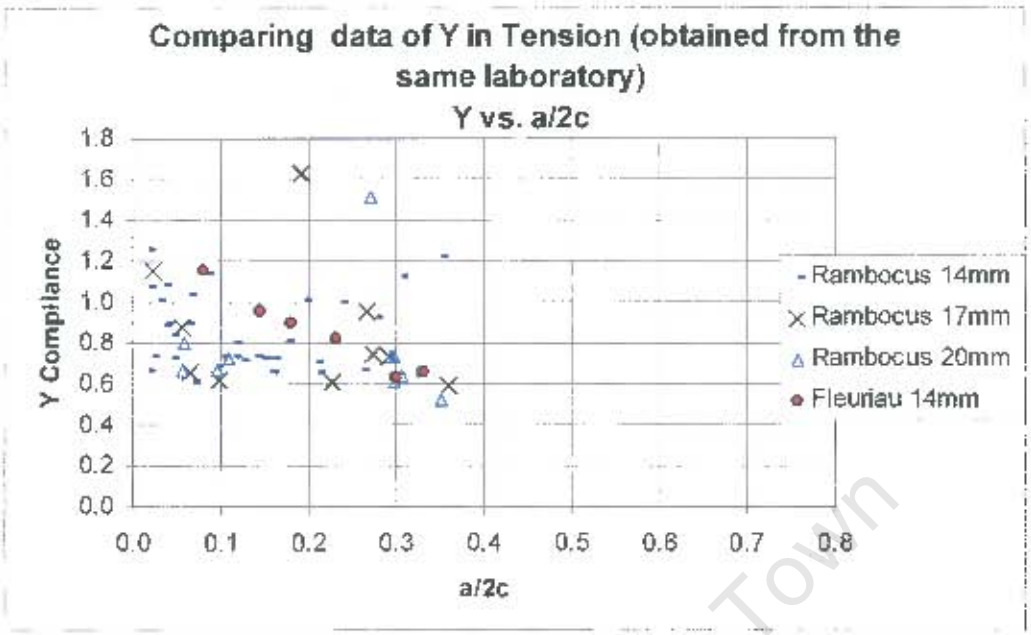

Figure 5.1 (b): Results of Y compliance factors in tension for both Fleuriau [ref] and present study results of Rambocus versus a/2c aspect ratio (in the same lab).

Figure 5.2 (a) shows the Y compliance results of Radebe **[68]** against the relative depth a/d (which consisted of some fatigue cracks as crescent moon and thumbnail) compared to the present Y results obtained in bending. The results obtained from the present study were Y compliance data for the 17mm diameter round thumbnail specimens. From the graph, both 17mm thumbnail specimens appeared to follow the same general trend i.e. concave up.

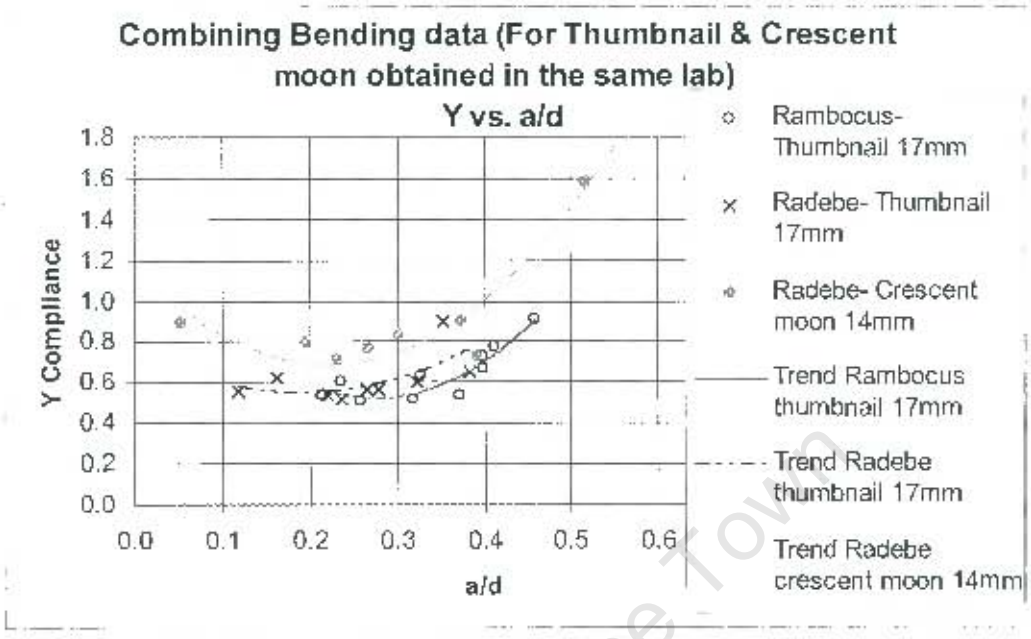

Figure 5.2 (a): Results of Y compliance factors in bending for both Radebe [68] and present study results of Rambocus versus a/d (in the same lab).

Figure 5.2 (b) shows the results of the stress intensity factors when plotted against a/2c. Once again, Y values are not found in the range a/2c>0.5. The range of values of Y lies in the region $0.036 \leq a/2c \leq 0.46$. For the 14mm crescent moon data, the trend is a concave up curve in the range of $0.036 \leq a/2c \leq 0.28$. The trend of the Y compliance values for the 17mm diameter is lower than that of the14mm diameter.

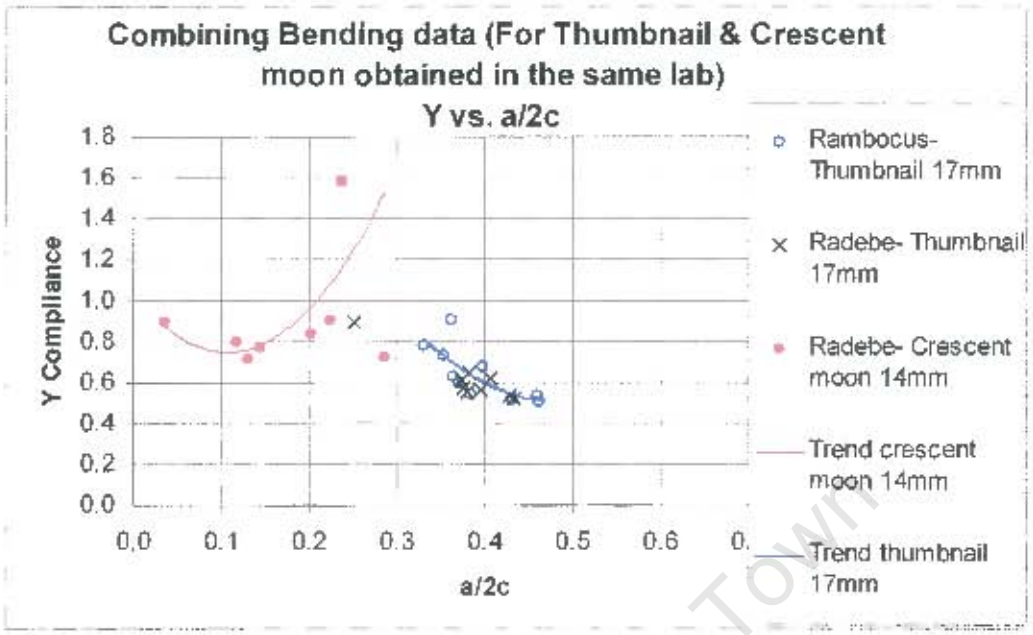

Figure 5.2 (b): Results of Y compliance factors in bending for both Radebe [ref] and present study results of Rambocus versus a/2c aspect ratio (in the same lab).

5.3 *Comparing Tension and Bending*

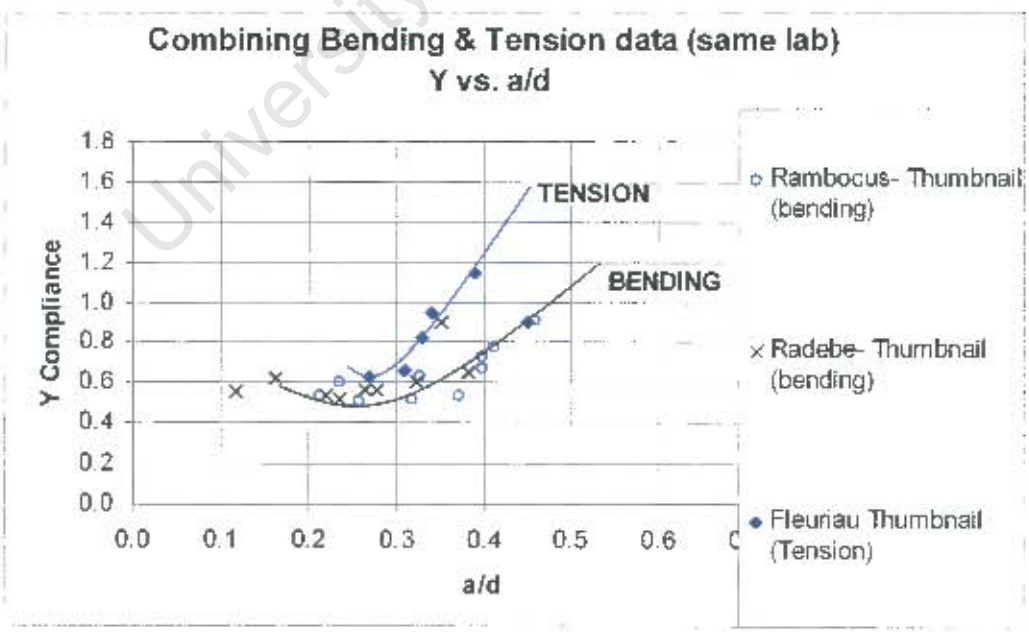

Figure 5.3: Comparing bending and tension

Figure 5.3 compares the experimental Y compliance values determined in this project for both bending specimens and tensile specimens. Fleuriau's data ranging from $0.33 \leq a/d \leq 0.39$ shows high value of Y compliance for thumbnail specimens in tension. The Y data for the bending are lower than those of tension. This trend of the tensile Y data (and curvature) being above the bending curve is consistent with the theoretical studies by Ng and Fenner **[8]**, (as shown in Figures 2.3 and 2.4), Si **[10]** (Figures 2.9, 2.10 and 2.12) and others, as shown in Figure 2.17.

5.4 *The a/2c Ranges*

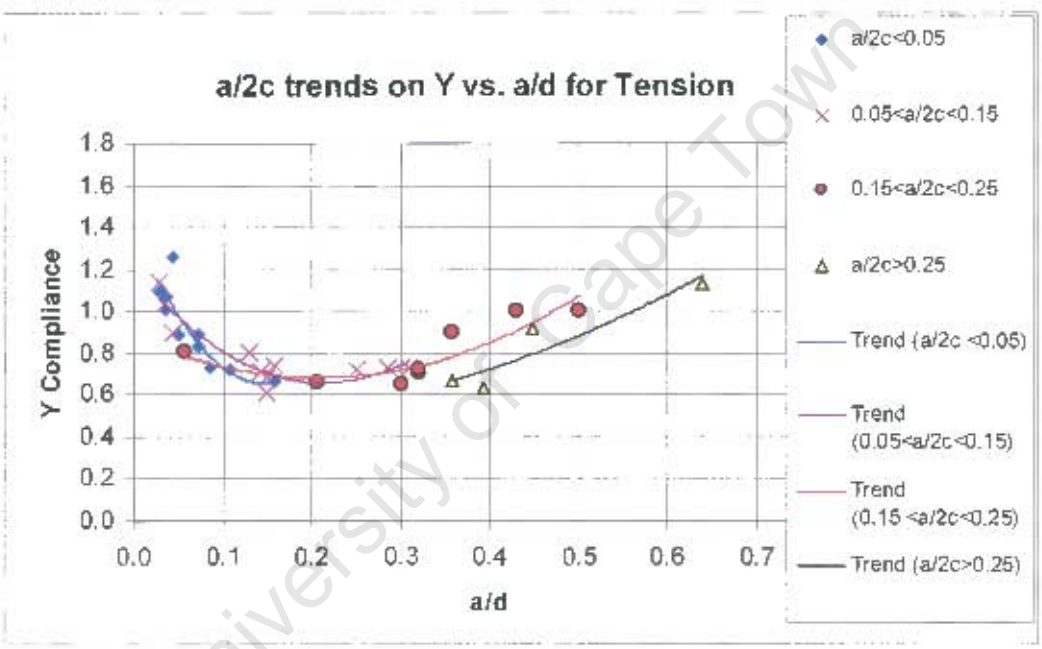

Figure 5.4: The a/2c range

From the set of data obtained the Y values for the 14mm crescent moon were the most numerous. The data were arranged to provide hindsight where the a/2c values distributed along the a/d axis with the respective Y compliance values as shown in Figure 5.4. It was observed that Y compliance values having aspect ratios $a/2c < 0.05$ were in the range of $0.028 \leq a/d \leq 0.15$; $0.05 < a/2c < 0.15$ were in the range of $0.028 \leq a/d \leq 0.28$; $0.15 < a/2c < 0.25$ were in the range of $0.05 \leq a/d \leq 0.5$ and for the values of $a/2c > 025$ were in the range of $0.35 \leq a/d \leq 0.63$.

5.5 Comparing Experimental Y Compliance Results to Published Computational Stress Intensity Data

The solutions for the stress intensity factors cannot be easily compared, because assumptions of crack shape are not often identified or different parameters have been used by different authors. For example, Carpinteri compared the Y values using a semi-elliptical parameter a/b and a/d as relative depth ratios as defined in the Literature chapter (section 2.4). Different computational codes are used in the finite element process with different number of nodes, elements, meshes and boundary condition assumptions, which cause lots of dispersion in the computational result of the Y compliance.

5.5.1 Comparing Y Experimental Compliance Values with Computational Values in Tension

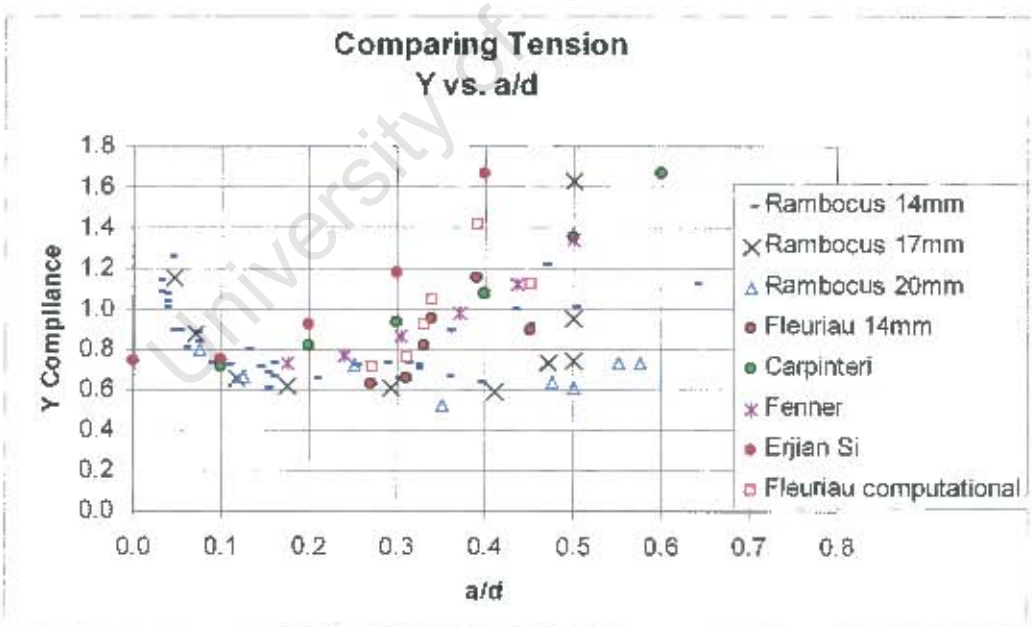

Figure 5.5 (a): Comparing experimental Y compliance values with available computational data of Y compliance from literature in tension.

Figure 5.5(a) provides the results in tension comparing available published computational data to nominally similar experimental results. The data of each author shows a concave up trend. The Y compliance stress intensity values for the experimental 14mm crescent moon cracks from the present study, together with Fleuriau's compliance values, were consistent with the work of Carpinteri **[7]** for a/b=1 at the deepest crack point A. they also compared to Fenners' **[8]** results where the Y compliance values have an angular position $\phi = 0.00$ degree in the range of $0.1 \leq a/d \leq 0.46$. Si **[10]** who proposed a synthesised and normalised stress intensity factor as a function of relative crack depth by combining results of Murakami **[34]**, Athanassiadis **[27]**, Newman **[6]** and Daoud **[9]** shows high values of stress intensity factors and was not close to the experimental trend.

Experimental values in the range of $a/d < 0.1$ shows an increase in Y compliance compared to the computational data from the other authors. In other words, experimental data shows that small cracks experience small fracture stresses that result in high compliance values compared to the computational data.

The trend obtained from the experimental results showed that the stress intensity values seem to get lower in value as the size of the specimen increases. The stress intensity trends showed by comparing 17mm and 20 mm diameter specimens for the crescent moon fatigue cracks were lower than those of Carpinteri **[7]** who used a 50mm diameter in his computational analysis. In this case the computation work seems to be at variance, when comparing Y compliances relative to the size of the specimens used in the experimental work. The Y compliance values for the 50mm diameter trend were expected to be lower than the (experimental) values of the 20mm diameter.

5.5.2 Comparing Experimental Y Compliance Values with Y Computational Values in Bending

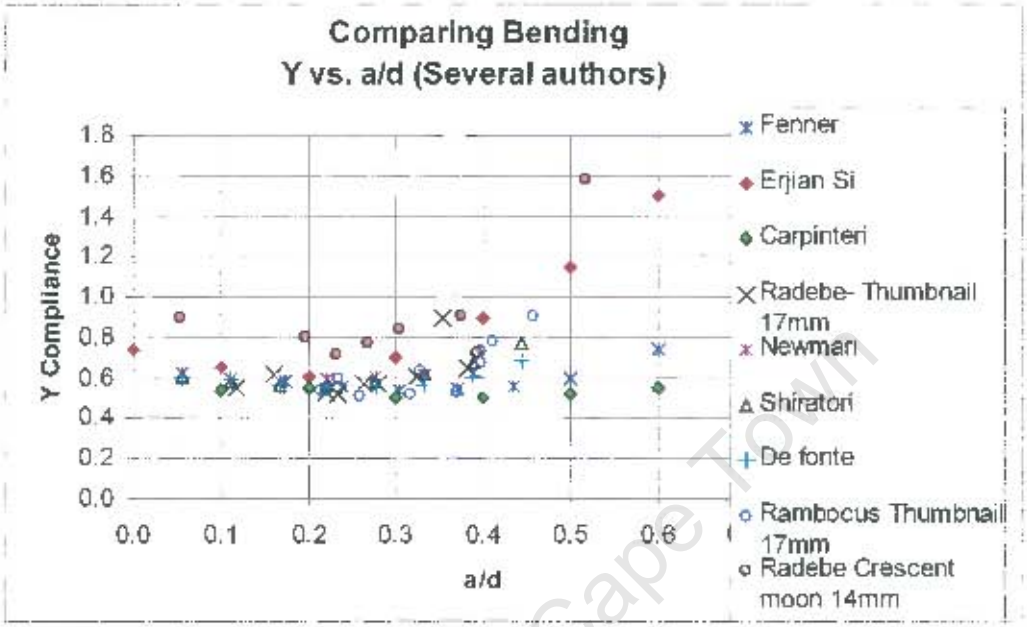

Figure 5.5 (b): Comparing experimental Y compliance thumbnail values with available computational data of Y compliance from literature in bending.

Figure 5.5(b) illustrates the experimental Y compliance values obtained compared with the computational values of Y in bending. Both experimental and computational trends show concave up curves. The experimental thumbnail Y compliance values from both Radebe **[68]** and the present study (Rambocus) were consistent with the results of some authors i.e. Carpinteri **[7]**, Newman **[6]**, Shiratori **[45]** and Da Fonte **[3]** in the range of $0.1 < a/d \leq 0.4$. The Y compliance values of the crescent moon of the 14 mm specimens performed by Radebe were found higher than all the other authors.

5.5.3 Thumbnail to Crescent Moon Fatigue Shapes (from Carpinteri Results Using the a/b Aspect Ratios).

Carpinteri's results **[7]** for bending had a range of Y compliance values obtained from thumbnail to straight chord cracks ranging from a/b =1 to a/b =0.0 with a relative depth range a/d of 0.1 to 0.6. His values were plotted together with Radebe's Y values from crescent moon. From the graph in Figure 5.6(a) it was observed that the shape of the crack changes from thumbnail to straight fronted crack as a/b changes from a/b = 1.0 to a/b=0.0. The Y compliance values generated from crescent moon crack were found to lie above the a/b=0.0 (straight fronted crack). In other words it could happened that for a/b <0.0 (even this is meaningless in terms of an ellipse) that a/b is negative, the trend in crescent moon fatigue behaviour crack are expected as shown in Figure 5.6(b). The Radebe and Rambocus' results for thumbnail shapes, is consistent with this trend by Carpinteri **[7]**.

Similarly increasing Y trend direction behaviour from round thumbnails to chords (to crescent moon, nominally) as shown in Figures 5.6(a) and 5.6(b) is also consistent with the suggested computational trends summarised by Si **[10]**, as shown in Figures 2.7(a) and 2.7(b).

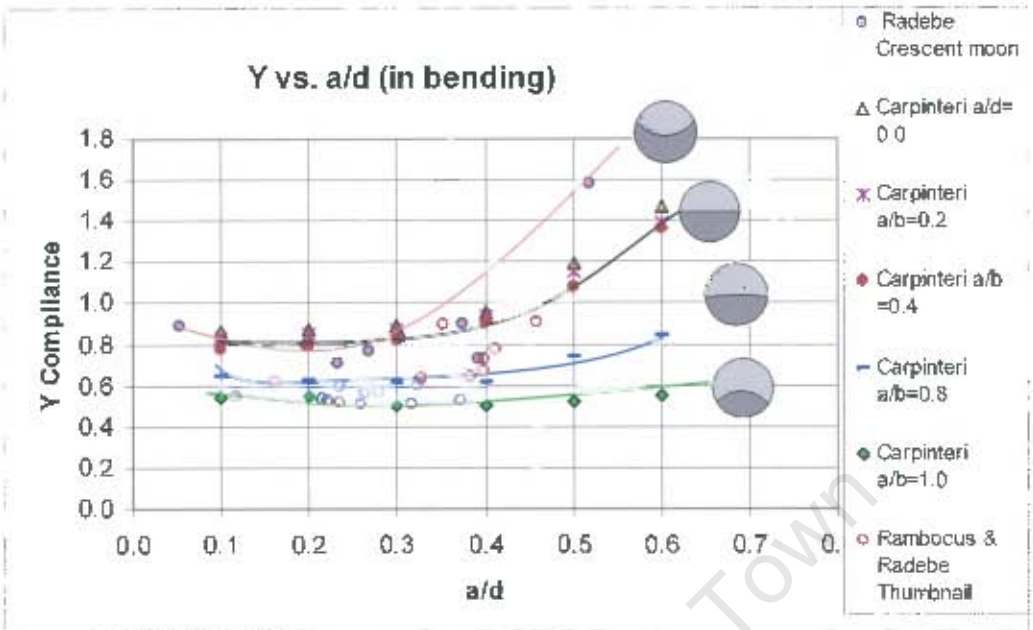

Figure 5.6 (a): Carpinteri's Y values from thumbnail to straight-fronted fatigue cracks for the aspect ratios of a/b compared to Radebe's Y compliance values from crescent moon fatigue cracks.

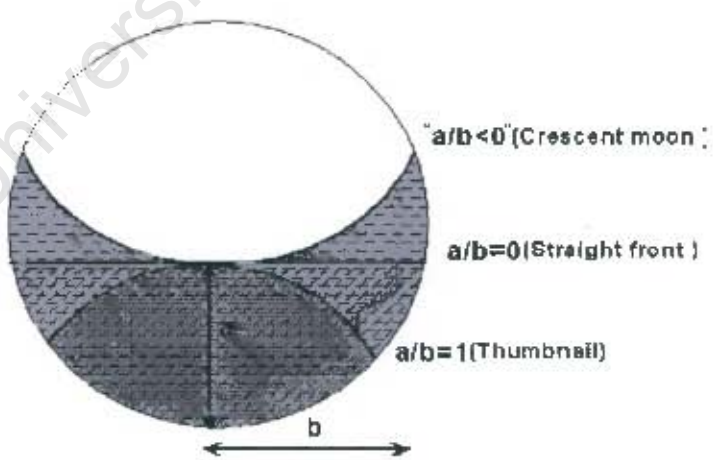

Figure 5.6(b): Crescent moon formation when a/b <0

5.6 *Calculating Y-Compliance using Fast Fracture Area in Bending*

It is apparent from the results, that at large crack length values the Y compliance value increases substantially (e.g. see Figures 4.3a, 4.4a, 4.6a, b etc). In addition the Y value at such large cracks depth departs from the calculated values at large a/d. From the Literature review chapter 2, (in Figures 2.3, 2.4, 2.7, 2.9, 2.17 etc) also it can be seen that some high values of Y for large a/d. It is then considered that the argument of Y validity for large deep cracks becomes tenuous. What are the relative crack depth limits for using the Y compliance stress intensity function?

In an attempt to consider the effect of this feature, and to evaluate sensitivities on the Y function, the size of the final fast fracture region was considered.

From equation 4.4 or 4.8, $Y = \dfrac{K_{IC}}{\sigma_{fail}\sqrt{\pi a_{crit}}}$.

The perceived Y values are too high at large a/d values, but the fracture toughness is rationally constant (for one material) and the crack depth a is measured. The only other parameter is the fracture stress σ_f, which may be considered too low and could arguably be larger.

Since in bending,

$$\sigma_{bending} = \frac{My}{I} = \frac{P_F L y}{4I} \quad \text{(from equation 4.5)} \qquad \textbf{5.1}$$

and the fracture load P_F and distance to the neutral axis, y, is fixed (for a specimen), the use of I for the section needs reconsideration, since the actual final fast fracture area is very much smaller than that for a full diameter round bar that is assumed. If one was to use a smaller second moment of area I_{new} based on the actual fast fracture area, I_{new} would be smaller than the usual $I = \dfrac{\pi d^4}{64}$. As a consequence, the σ_f calculated from the failure load would be bigger and the consequent Y value

Earlier calculations for the failure stress were undertaken using the second moment of area of a circular cross section. However this may not be the exact stress at the crack tip due to the reduced unbroken ligament size. The region of the fast fracture was not circular for all the specimens. To reduce the error, the fast fracture regions for thumbnail specimens were carefully plotted and drawn on AutoCAD where the second moment of area and cross sectional area were calculated respectively. The fast fracture regions measured in AutoCAD are illustrated in ***Appendix G***. Figure 5.7 illustrates the fast fractured region plotted in AutoCAD.

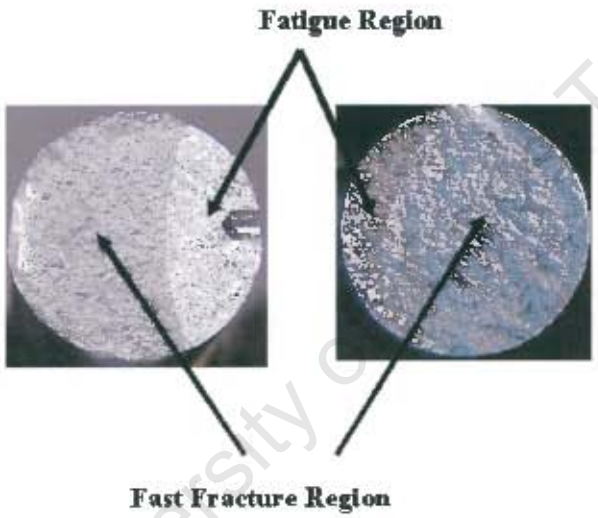

Figure 5.7: Fatigue crack region and fast fracture region of thumbnail and crescent moon specimens.

The procedures for the AutoCAD program to obtain the area or second moment of area were the following:

- Type REGION- selects the object.
- Press Enter
- Type MASSPROP- reselects the object.
- Press Enter.
- The AutoCAD text window will appear with all the properties of the region.

- The AutoCAD text window will appear with all the properties of the region.
- The distance from the centroid of the fast fracture region to the crack tip is determined using the dimension command.

Table 5.1 illustrates the corrected Y compliance value with the second moment of area for each plotted fast fractured region.

Specimen No	a (mm)	2c (mm)	Force P (N)	a/d	Stress (MPa)	a/2c	Y Compliance	Y centroid (m)	I (m^4)
B1a	5.58	15.3	6012	0.328	235.28	0.365	0.569	0.00481	2.16E-09
B1b	7	21.1	4806	0.412	262.59	0.332	0.471	0.00437	1.28L-09
B2a	6.78	17	5020	0.399	231.06	0.399	0.544	0.00412	1.69E-09
B3a	4	10.75	8222	0.235	271.61	0.372	0.603	0.00537	2.60E-09
B3b	6.78	19.2	5178	0.399	224.47	0.353	0.56	0.00465	1.72E-09
B3c	7.8	21.5	3902	0.460	259.2	0.363	0.452	0.00402	9.09E-10
B4a	4.4	9.5	9234	0.259	200.32	0.463	0.557	0.00575	3.05E-09
B4c	3.65	9.5	9096	0.215	305.97	0.384	0.56	0.0062	3.11E-09
B5a	6.32	13.75	7352	0.372	253.5	0.46	0.514	0.00439	2.04E-09
B5b	5.4	12.55	8234	0.318	270.56	0.43	0.521	0.00562	2.74E-09

Table 5.1: Corrected Y compliance value for thumbnail fatigue cracks in bending.

Specimen No	Stress (MPa) Using Circular cross section	Stress (MPa) Using actual fast fracture region (with AutoCAD)
B1a	219.33	235.28
B1b	159.42	262.59
B2a	186.43	231.06
B3a	272.74	271.61
B3b	171.77	224.47
B3c	129.44	259.2
B4a	307.97	200.32
B4c	318.32	305.97
B5a	243.00	253.5
B5b	273.14	270.56

Table 5.2: Comparing the stresses using a circular region as a fast fracture to the actual fast fracture region in bending.

From the Table 5.2, we can deduce that in most cases there was an underestimate of the stresses used when assuming the fractured region to be circular. For small cracks the error is fairly small but for deep crack length, for example specimen B3c, the error is almost 50%. Figure 5.8 illustrates how Y compliance values for deep cracks would be corrected if this approach was considered meaningful. It can be

seen that reprocessing of the bending results, using the more realistic I value, indicates that the Y values for large a/d are reduced.

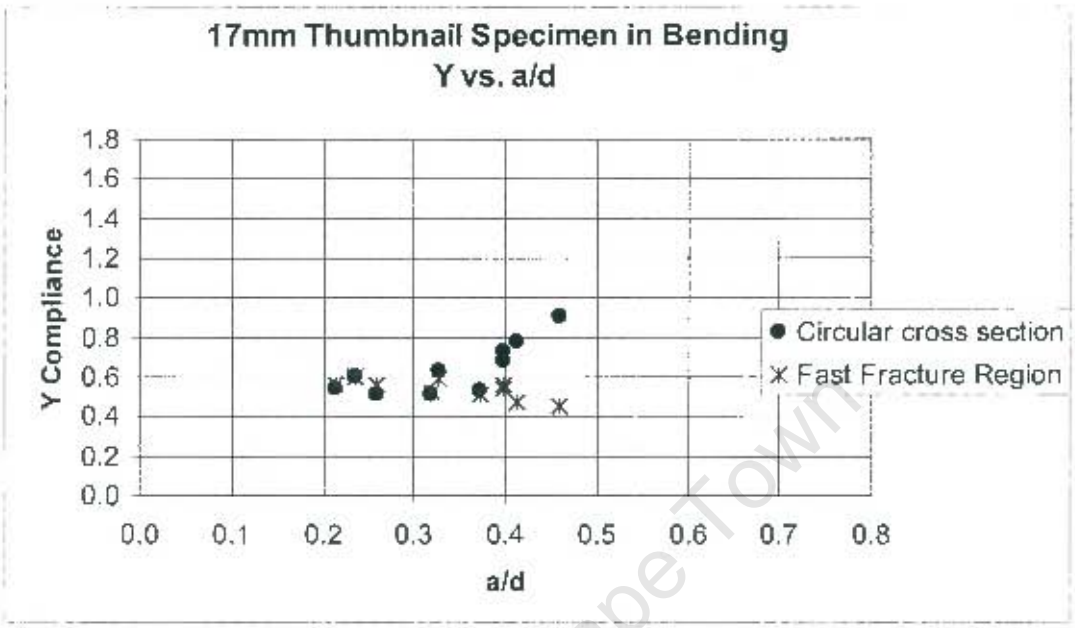

Figure 5.8(a): Corrected Y compliance for thumbnail specimen vs. a/d

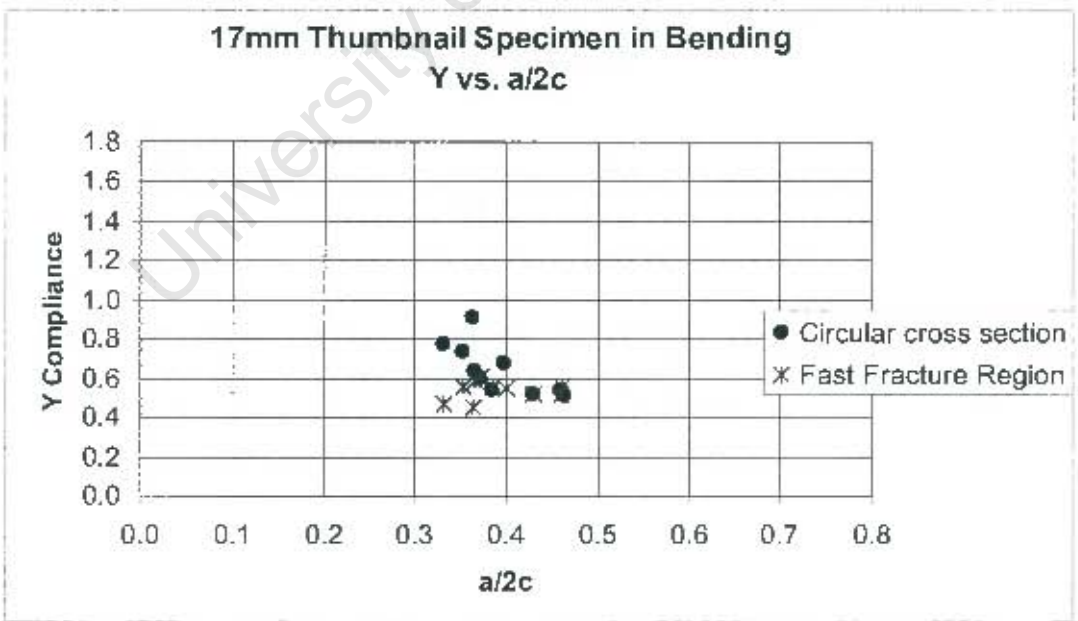

Figure 5.8(b): Corrected Y compliance for thumbnail specimen vs. a/2c.

5.7 Calculating Y-Compliance using Fast Fracture Area in Tension

For tension, the only variable that changes in calculating the stress is the area of the fast fractured region. In fracture mechanics it is well recognised that one should consider the remote stress (using the full, non fractured area), and not make allowance for reduced crack plane area. In the present case, however, in the case of large crack depths, this reduced area method was considered- if for no other reason than to evaluate **sensitivity** of Y to large crack depths. Once again the bigger the crack, the more Y values are affected by assuming the fast fracture region as a circular region. The stress in tension is usually calculated by equation 5.2,

$$\sigma_t = \frac{P}{A_{Circular}} \qquad \textbf{5.2}$$

Where $A_{Circular}$ is the area of the cross section of the round specimen and P is the breaking load. The region of the fast fracture is plotted on the Auto Cad to provide the new area A_{new} to calculate the corrected stress and hence the corrected Y values. Tables 5.3-5.7 illustrate the results obtained for the stress intensity factor when the fast fractured region is considered instead of using the circular cross section. It shows the amount of error in the stress concentration at the crack tip which can be over 50% for large cracks and which affects the value of the Y compliance. Figure 4.11(a)-(f) compares the Y compliance datum obtained for the two different regions with their respective aspect ratios a/d and a/2c for each specimen size.

For 14 mm diameter Specimen No	Fast fracture Area mm^2	Stress (using circular region) (MPa)	Y compliance (using circular region Area)	Corrected Stress (MPa)	Corrected Value Y compliance	% Error in Stress
A1	145.00	309.17	0.8918	234.45	0.8400	-32
A2	128.50	234.05	0.6898	200.27	0.5758	-17
A3	124.10	213.82	0.7377	189.45	0.5947	-13
A4	109.39	159.50	0.7334	160.32	0.5212	1
A5	117.60	207.75	0.6613	194.25	0.5052	-7
A6	118.04	216.71	0.8047	201.87	0.6170	-7
A7	147.00	317.84	1.0409	237.75	0.9940	-34
A8	140.77	280.28	0.8347	218.93	0.7633	-28
A9	134.60	264.39	0.7225	215.98	0.6317	-22
A10	140.00	323.33	1.1441	253.94	1.0405	-27
A11	144.00	290.97	0.7340	222.18	0.6866	-31
A12	149.00	336.62	0.8972	248.41	0.8684	-36
A13	150.00	339.22	1.0905	248.66	1.0626	-36
A14	143.00	306.57	1.0792	235.73	1.0025	-30
A15	148.00	326.51	1.0133	242.58	0.9742	-35
A16	136.60	236.36	0.6673	187.51	0.6008	-26
A17	147.89	323.62	0.8082	240.61	0.7785	-34
A18	134.83	265.25	0.6086	218.32	0.5331	-23
A19	100.15	153.14	0.7325	168.14	0.4765	9
A20	80.80	95.35	0.9983	129.76	0.5240	27
A21	81.58	101.13	0.9231	136.34	0.4891	26
A22	59.25	89.35	1.1283	128.69	0.4343	46
A23	83.00	75.13	1.2186	131.12	0.4987	43

Table 5.3: Corrected Y compliance values with corrected stresses (for 14mm diameter crescent moon using the Al7075 T6 material)

Specimen No.	Fast fracture Area mm^2	Stress (using circular region) (MPa)	Y compliance (using circular region Area)	Corrected Stress (MPa)	Corrected Y Compliance	%Stress Error
D1	39.28	132.13	1.005	517.84	0.2564	74.5
D2	56.57	175.40	0.896	477.27	0.3292	63.3
D3	109.74	235.55	0.703	330.43	0.5013	28.7
D4	103.06	230.29	0.719	343.97	0.4815	33.1
D5	114.04	236.00	0.635	318.56	0.4703	25.9
D6	108.00	236.00	0.666	336.37	0.4671	29.8
D7	138.53	360.21	1.259	400.28	1.1332	10.0
D8	141.73	395.68	0.888	429.77	0.8175	7.9
D9	142.39	346.18	0.718	374.26	0.8638	7.5
D10	114.86	260.82	0.720	349.54	0.5373	25.4
D11	117.68	262.31	0.654	343.13	0.4998	23.8

Table 5.4: Corrected Y compliance values with corrected stresses (for 14mm diameter crescent moon using the Al2030 T3 material)

For 17mm Specimen No.	diameter Uncracked Area mm^2	Stress (using circular region) (MPa)	Y compliance (using circular region Area)	Corrected Stress (MPa)	Corrected Y Compliance	%Stress Error
C1	43.76	73.93	1.6301	383.45	0.3143	80.7
C2	111.04	169.53	0.7327	346.53	0.3585	51.1
C3	116.51	162.39	0.7421	316.38	0.3809	48.7
C4	159.79	224.95	0.5903	319.54	0.4156	29.6
C5	99.67	126.93	0.9495	289.05	0.4169	56.1
C6	165.14	257.95	0.6091	354.55	0.4432	27.2
C9	215.89	385.71	0.8770	384.50	0.8342	4.9
C10	211.33	378.49	0.6564	406.52	0.6111	6.9
C11	193.69	330.07	0.6148	386.81	0.5244	14.7
C12	188.03	341.48	1.1503	412.23	0.9529	17.2

Table 5.5: Corrected Y compliance values with corrected stresses (for 17mm diameter crescent moon using the Al2030 T3 material)

For 20mm Specimen No.	diameter Uncracked Area mm^2	Stress (using circular region) (MPa)	Y compliance (using circular region Area)	Corrected Stress (MPa)	Corrected Y Compliance	%Stress Error
B1	230.35	254.33	0.5221	346.86	0.3829	26.7
B2	34.55	60.60	1.5176	552.75	0.1669	89.0
B3	152.05	182.07	0.6102	376.19	0.2953	51.6
B4	133.40	141.01	0.7347	332.09	0.3120	57.5
B5	138.31	144.83	0.7314	333.81	0.3174	56.6
B6	150.81	178.89	0.6372	372.65	0.3059	52.0
B7	296.84	356.51	0.8047	377.31	0.7603	5.5
B8	211.56	216.77	0.7249	321.90	0.4881	32.7
B9	283.07	334.23	0.6649	370.93	0.5991	9.9
B10	294.30	334.23	0.6649	356.78	0.6228	6.3

Table 5.6: Corrected Y compliance values with corrected stresses (for 20mm diameter crescent moon using the Al2030 T3 material).

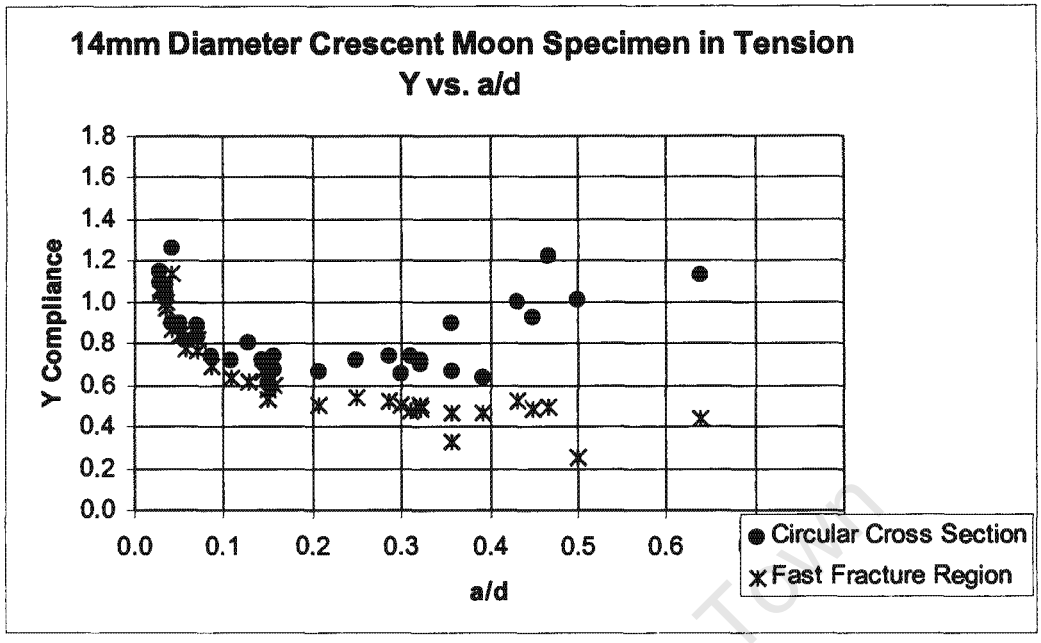

Figure 5.9 (a): Graph comparing Y compliance values with corrected new Y values with their respective aspect ratios a/d for 14mm diameter specimens.

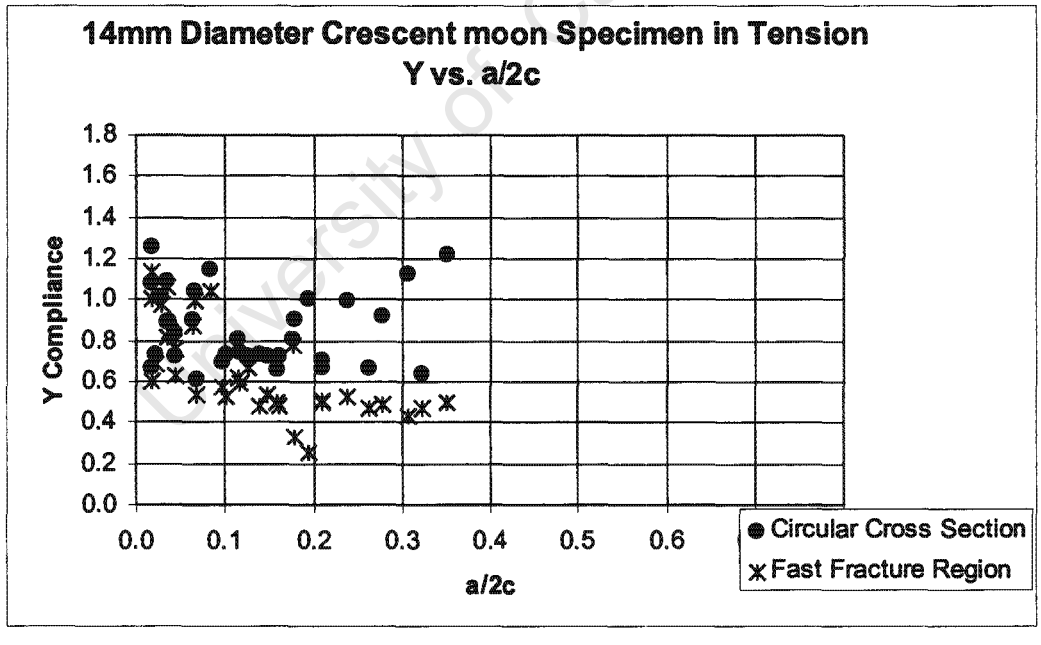

Figure 5.9 (b): Graph comparing Y compliance values with corrected new Y values with their respective aspect ratios a/2c for 14mm diameter specimens.

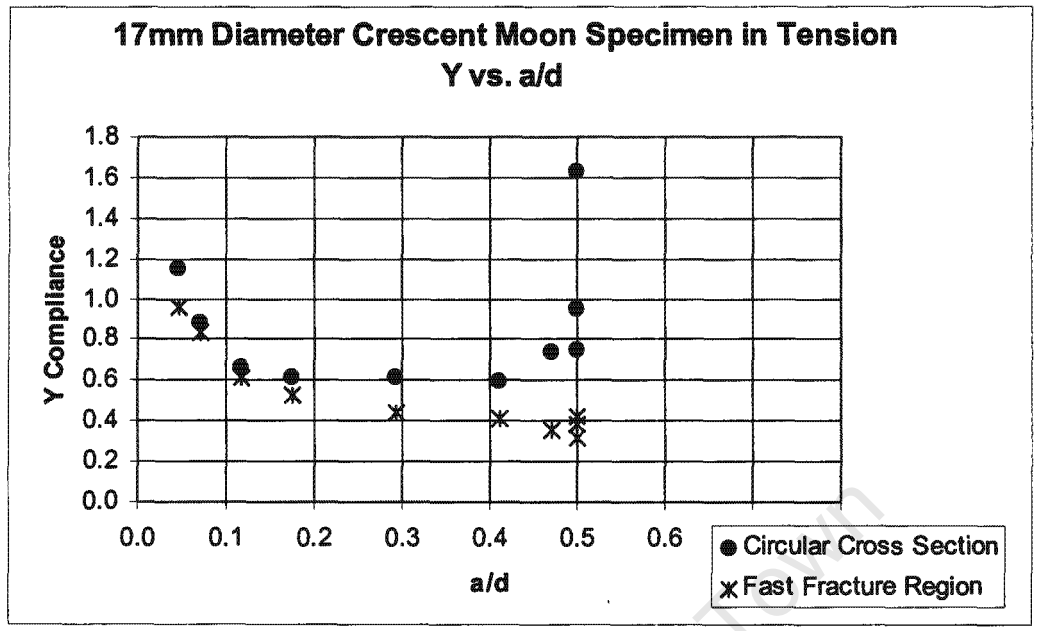

Figure 5.10 (a): Graph comparing Y compliance values with corrected new Y values with their respective aspect ratios a/d for 17mm diameter specimens.

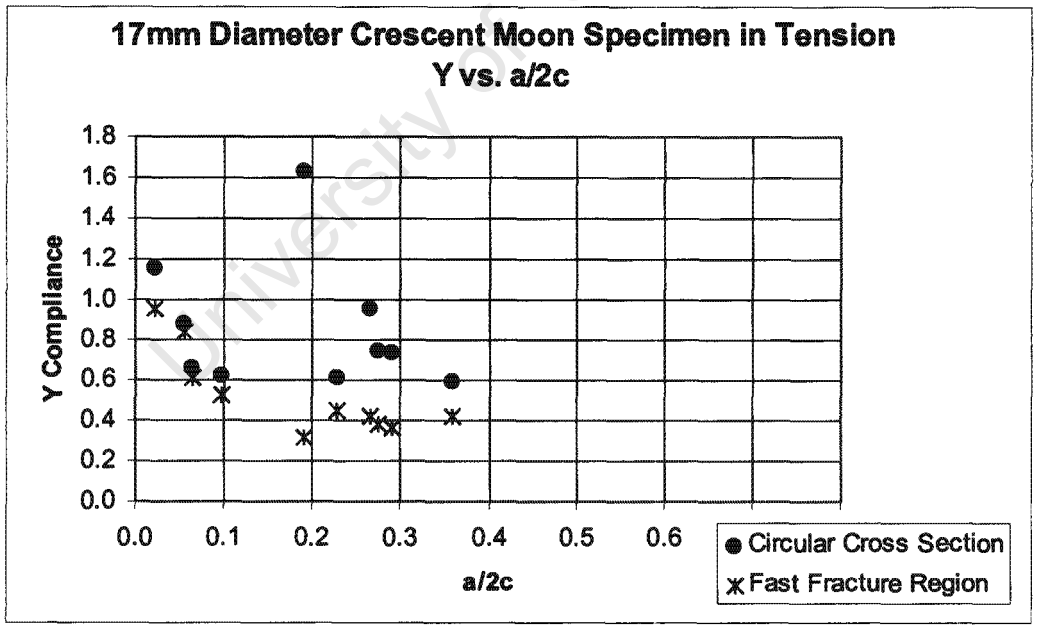

Figure 5.10 (b): Graph comparing Y compliance values with corrected new Y values with their respective aspect ratios a/2c for 17mm diameter specimens.

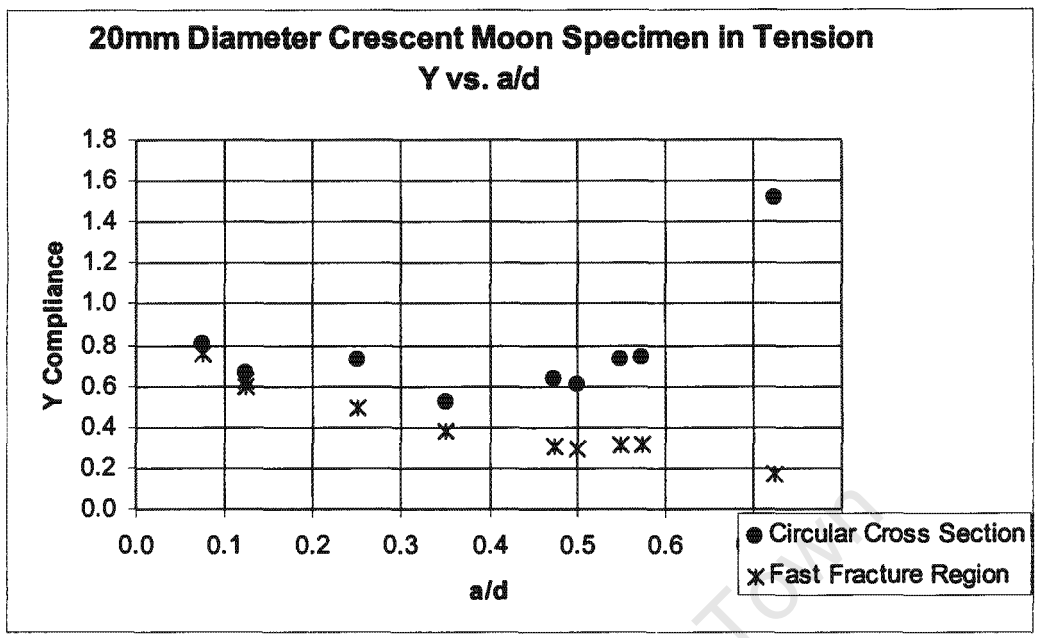

Figure 5.11 (a): Graph comparing Y compliance values with corrected new Y values with their respective aspect ratios a/d for 20mm diameter specimens.

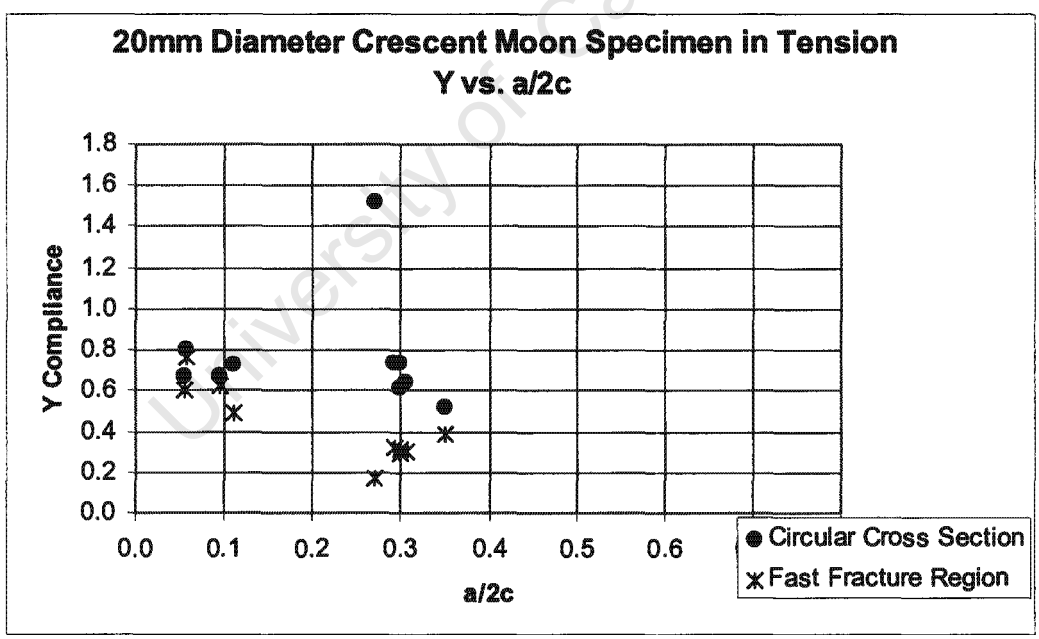

Figure 5.11 (b): Graph comparing Y compliance values with corrected new Y values with their respective aspect ratios a/2c for 20mm diameter specimens.

The stress intensity factors when using a circular section generally has higher values than the stress intensity factor when calculated using the fast fractured region

as shown in Figures 5.9 to 5.11. It was also observed that the extreme high stress intensity values for large cracks were corrected when using the fast fracture region in the calculation of the stress concentration at the crack tip. The specimens for each size having stress error greater than 70% were D1, C1 and B2 which had deep cracks as shown in Figure 5.12.

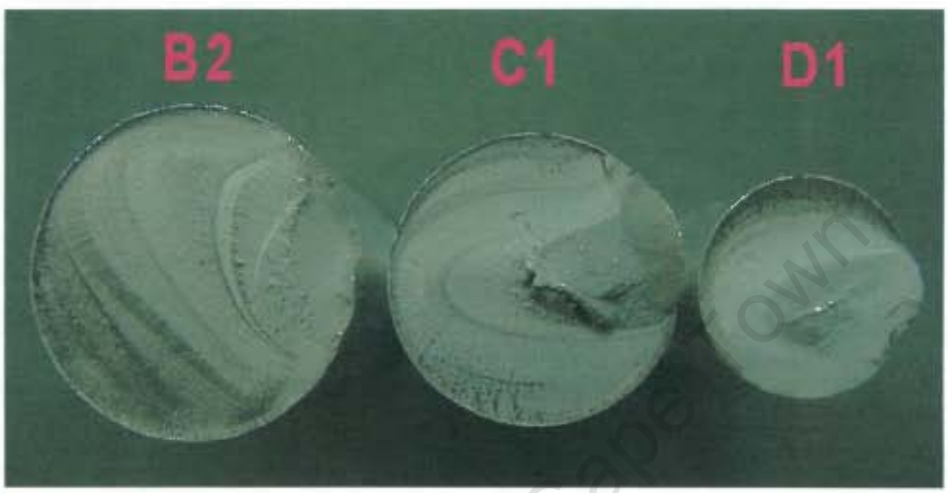

Figure 5.12: Deep crescent moon cracks that experience more that 70% stress error when using a circular region.

The corrected Y compliance values for each specimen were plotted on the same scale with the respective relative depths and aspect ratios and it was observed as the size increases the Y compliance datum tend to decrease as their respective aspect ratios increases as shown in Figures 5.13 and 5.14.

Figure 5.13: Corrected Y values of different specimen sizes vs. a/d.

Figure 5.14: Corrected Y values of different specimen sizes vs. a/2c aspect ratio.

5.8 Error Analysis

Error analysis is the evaluation of uncertainty in measurement. Experience has shown that no measurement, however carefully made, can be completely free of uncertainty. An error analysis was evaluated for the Y compliance factor in both bending and tension. The normalised stress intensity factor is given by

$$Y = \frac{K_{IC}}{\sigma_{net}\sqrt{\pi a_{crit}}}.$$

Here K_{IC} is the fracture toughness of the two materials used, for either 18.36MPa√m (Al7075 T6) or 19.69 MPa√m (Al2030 T3). They have both an approximate standard deviation of 1.1 MPa√m which contribute to a total normalised uncertainty of ±0.06.

The material Al2030 T3, indeed was not the perfect material to be used for this test series, since some specimens experienced some shearing and tearing in the latter parts of the cracks which created difficulty in the crack measurement and could contribute to uncertainty of both the fracture load at the measured crack as shown in Figure 5.15.

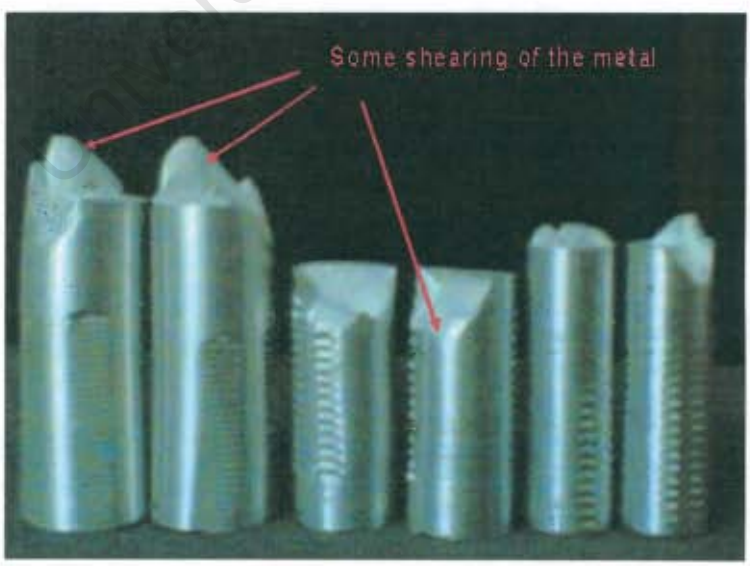

Figure 5.15: Shearing of the specimens when broken in tension.

The measurements of the crack could be read to 0.25mm, that is the crack a has a measurement error of uncertainty, when normalised for a typical worst case crack of length 2.5mm of ±0.10. This considered a worst case because crack depths were generally deeper than 2.5mm.

The only difference from the tension and bending is the stress calculation. The stress in bending was calculated as $\sigma_{bending} = \frac{8PL}{\pi d^3}$ (from equation 4.7) and that of tension $\sigma_{tension} = \frac{P}{A}$ (from equation 4.9).

By considering the bending case, the measurements from the span L by using a vernier calliper has a normalised uncertainty of ±0.01 and the diameter for $\sigma_{bending}$ has a total normalised uncertainty, when considering second moment of area, I, of 0.03 (3×0.01). The uncertainty in the force P was neglected by assuming the force measured by the digital apparatus to be accurate. Hence $\sigma_{bending}$ has a total normalised error of ±0.04. Similarly, for the stress in tension, only the area was considered and contributes a normalised error of ±0.02.

Using the uncertainty rule from **[91]**, to calculate the uncertainties δx…δz and measured values are used to complete the function q(x,…,z). If the uncertainties in x,…,z are independent and random, then uncertainty in q is given by equation 5.3.

$$\delta q = \sqrt{\left(\frac{\delta q}{\delta x}\delta x\right)^2 + \ldots + \left(\frac{\delta q}{\delta z}\delta z\right)^2} \qquad \textbf{5.3}$$

The uncertainty for the Y compliance was calculated for bending and tension using equation 5.3 as follows (for K_{IC}, σ and a respectively)

$$Y_{bending} = \sqrt{(0.06)^2 + (0.04)^2 + 0.5(0.1)^2} = 0.10$$

$$Y_{tension} = \sqrt{(0.06)^2 + (0.02)^2 + 0.5(0.1)^2} = 0.095$$

For convenience, the uncertainties in the Y values were approximated to 10% for the worst case, and were considered to show the trends, to within about 10%.

5.9 *Summary*

From the results obtained in Chapter 4, it was seen that Y compliance values shows concave up trends for both tension and bending. The Y values in tension are found to be higher than those of bending. The range of a/2c cannot be greater than 0.5. Carpinteri's bending results [7] show a trend of increasing Y as a/b goes from1.0 to 0.0 and the present results of Y for crescent moon shape i.e. as a/b<0 tend to support this trend (Figure 5.6). The Y compliance values were also compared to those in the literature. The computational results of Carpinteri [7], Ng and Fenner [8] and Da Fonte and De Freitas [3] best fit the experimental results obtained. The error of both Y compliance in tension and bending was estimated about 10% for the worst case.

6. Conclusions and Recommendations

6.1 Conclusions

The Y compliance functions have largely been developed theoretically and computationally, but relatively little experimental data is available **[5, 11]**. This is particularly the case for so called "crescent moon" and "thumbnail" shaped cracks in round bars, even though these shapes are frequently encountered in practice. Several authors have studied this question for semi elliptical cracks in round and cylindrical sections, as well as in rectangular bars, but mostly analysed from a finite element point of view as seen in this thesis.

This thesis has set out to use an experimental technique to generate a range of fatigue crack shapes, from thumbnail, through chords to crescent moon, and for a range of crack depths. From the fracture stress of these samples, and the materials K_{IC} toughness, an estimate of Y compliance at fracture was obtained. Based on the findings and analysis of the experiments investigated in this thesis the following conclusions may be drawn.

- The general trends for Y compliance factors for either bending or tension have "concave-up" curves for both the relative depth a/d and aspect ratios a/2c respectively.

- The present study Y compliance thumbnail values were consistent with reported values for thumbnail cracking obtained by Carpinteri **[7]**, Fenner **[8]** and Da Fonte **[3]** in the range $0.1 \leq a/d \leq 0.4$ in tension and bending.

- In bending it was observed that the relative increase in surface crack length 2c, leading to flaw shapes changing from thumbnail (Carpinteri's a/b=1), through a straight-fronted shape (Carpinteri's a/b=0) to crescent moon

(a/b≤0, if this were meaningful), leads to a steady increase in Y function (see Figure 5.6).

- Experimental values of Y, when compared to their computational counterpoints, show that the fracture stress for small cracks have lower stress values resulting to higher values of Y.

- It was observed that Y compliance values for thumbnail cracking that Y in tension is always higher than bending.

- From observation, none of the Y values were found in a range a/2c>0.5. The implication is that at most cracks were semi-circular as might be expected but never deeper than this experimentally.

- By way of evaluating sensitivity to fast fracture area, the Y compliance was recalculated using a reduced (actual) fast fracture area from both bending and tension. At large crack lengths this tends to reduce the Y values and reduce the scatter. The applicability of conventional Y compliance and linear elastic fracture mechanics (LEFM) in this suggested be questionable at deep crack lengths.

- It was observed that Y increases as a/2c gets smaller for a specific relative ratio of a/d.

- For increasing specimen diameters, the Y compliance "concave up" trends tend to exhibit lower values.

6.2 *Recommendations*

As seen from the conclusions, some of the experimental Y results are at variance with some computational values of Y particularly at large crack lengths. These experimental results obtained, can be further analysed by using a three dimensional finite element method to have a better comparison between computational and experimental, and this study should be undertaken. This is particularly the case for crescent moon cracking and for deep cracking.

From the literature, no studies have been made on the Y compliance values of the crescent moon cracks either experimentally or computationally. This field should be more exploited together with experimental Y values for thumbnail crack shapes.

Size effect should be considered in every experiment performed since it seems to affect the Y compliance values. From literature size effect seems not to have been investigated extensively.

List of Reference

[1] Chell G.G., "Developments in Fracture Mechanics-2, The Mechanics and Mechanisms of Fracture in Metals", *Applied Science Publishers LTD* 1981, pp1.

[2] Tait R.B., "Material Selection in the Mining Industry- Mechanical properties and elementary fracture mechanics" SAIMM Physical Metallurgy School 16/Feb/1987 Mintek.

[3] Manual da Fonte and Manuel de Freitas "Stress Intensity factors for semi-elliptical surface cracks in round bars under bending and torsion." *International Journal of Fatigue* Vol. 21, 1999, pp 457-463.

[4] Internet Source: http://www.norrisrods.com/failureanalysis

[5] Tait R.B., Herbert B.C and Horn M., "An experimental study of semi-elliptical cracks in bending", *Fracture* 1994, University of Wits, Johannesburg, Dec 1994.

[6] Newman J.C. and Raju I.S., "An empirical stress intensity factor equation for the surface crack", *Engineering Fracture Mechanics*, Vol.15, No 1-2, 1981 pp 185-192,.

[7] Carpinteri, A., "Elliptical-arc surface cracks in round bars", *Fatigue and Fracture of Engineering Materials and Structures*, Vol.15 Nov 1992 pp1141-1153.

[8] Ng C.K and Fenner D.N., "Stress intensity Factors of an edge cracked circular bar", *International Journal of Fracture*, Vol. 36, 1988 pp 291-303,.

[9] Daoud O.E.D. and Cartwright D.J., *Engineering Fracture Mechanics*, Vol. 19, 1984 pp 701-707,.

[10] Si E., "Stress intensity factors for edge cracks in round bars", *Engineering Fracture Mechanics*, Vol. 37, 1990 pp807-812,.

[11] Mckellar D.K., R.B. Tait and A.S. Douglas, "Determination of the stress intensity for semi-elliptical flaws in bending", *CIMNE*, 1997 pp 227-246,.

[12] Nishioka T and Alturi SN, "Analytical solution for elliptical cracks and finite element alternating method for elliptical surface cracks subjected to arbitrary loadings", *Engineering Fracture Mechanics*, Vol.17, 1983 pp 247-268.

[13] Shivakumar KN and Newman Jr JC. "Stress intensity factors for large aspect ratio surface and corner cracks at semicircular notch in tension specimen", *Engineering Fracture Mechanics*, Vol.38, 1991 pp.467-673,.

[14] Chen H and Li Z. "Stress intensity factor of sucker rods by using the domain–decomposition and the finite element method", *Journal of Engineering Mathematics*, Vol. 11, 1994 pp 81-86,.

[15] James LA and Anderson WE. "A simple experimental procedure for stress intensity factor calibration", *Engineering Fracture Mechanics*, Vol. 1, 1969 pp 565-568,.

[16] Smith F.W, Emery A.F and Kobayashi, A.S. Stress Intensity Factors from Semi-Circular Cracks, Part 2: Semi- Infinite Solid. *J. Appl. Mechanics*, 1967, pp 953-959.

[17] Smith F.W. and Alavi M.J. Stress Intensity Factors for a Part Circular Surface Flaw. *Proc. Int. Conf. Press Vessel Technology*. 1969 ASME.

[18] Smith, F.W. and Emery A.F. And Kobayashi, A.S Stress Intensity Factors from Semi-Circular Cracks, Part2: Semi- infinite Solid. *J. Appl. Mechanics* 1967 pp953-959.

[19] Rice, J.R. and Levy, N. The Part Through Surface Cracks in Elastic Plate. *J. App. Mech.* 1972, pp185-194.

[20] Nisantani,H. and Murakami,Y *Int. J. Fracture,* Vol 10, 1974, pp 353-368.

[21] Pickard, A.C., Stress Intensity Factors for Cracks with Circular and Elliptical Crack Fronts, Determined by 3-D FEM. Proc. Of 2^{nd} *Intnl. Conf. Numerical Methods in Fracture Mechanics*, (Owen and Luxmore, eds.) Swansea, 1980, pp 599-614.

[22] Newman, J., A Review and Assessment of Stress Intensity Factor Equation for Surface Cracks. ASTM STP 687, 1979, pp 16-42.

[23] Hosseini, A. and Mahmoud, M.A., Evaluation of Stress Intensity Factors and Fatigue Growth of Surface Cracks in Tension Plates. *Eng. Fracture Mechanics* 1985, pp 957-973.

[24] McGowan, J. A Critical Evaluation of Numerical Solutions to the Surface Flaw Problem. *Experimental Mech*, Vol 20, 1980, pp 253-264.

[25] Carpinteri, A., Stress Intensity Factors for Semi Elliptical Surface cracks under Tension or Bending, *Eng. Fracture Mechanics* Vol. 38 1991, pp 327-334.

[26] Carpinteri, A. Surface Flaw Stress Intensity Factor Computation with Quarter Point Elements. *J. Strain Analysis*, Vol. 28, 1993, pp 117-123.

[27] Athanassiadis, A., Boissenot, J.M., Brevet, J., Francois, D. and Raharinaivo, A. Linear Elastic Fracture Mechanics Computations on Cracked Cylindrical Tension Bodies. *Int. J. Fracture* Vol.17, 1981, pp 553-556.

[28] Nezu, K., Machida, S. and Nakamura, H. *25th Japan Congress on Metal Research, Metallic Materials,* 1982, pp87-92.

[29] Forman, R.G. and Shivakumar, V. Growth Behaviour of Surface Cracks in the Circumferential Plane of Solid and Hollow Cylinders. *Fracture Mechanics* Vol.17, ASTM STP 905, 17th National Symposium on Fracture Mechanics, Albany New York, 1986, pp 59-74.

[30] Blackburn, W.S., *Engineering Fracture Mechanics* Vol. 8 ,1976, pp731-566

[31] Salah El Din, A.S., and Lovegrove, J.M., *International Journal of Fatigue,* Vol.3, 1981,pp 117-124.

[32] Caspers M., and Mattheck C., Weighted average stress intensity factors of circular-fronted cracks in cylindrical bars. *Fatigue Fracture Engng Mater. Structure* Vol. 9,1987, pp. 329-341.

[33] Raju I.S., and Newman J.C., Stress intensity factors for circumferential surface cracks in pipes and rods under tension and bending loads, ASTP STP Vol. 905, 1986, pp 789-805.

[34] Murakami, Y. (Editor-in-Chief), Stress Intensity Factors Handbook. Committee on Fracture Mech. The Society of Materials Science, Japan Vol. 2, Oxford: Pergamon Press, 1987, pp 657-658.

[35] Bush A. J., Stress intensity factors for single-edge-crack solid and hollow round bars loaded in tension. *J. Testing and Eval.* Vol. 9, 1981, pp. 216-223.

[36] Bush A.J., Experimentally determined stress- intensity factors for single-edge-crack round bars loaded in bending., *Exp. Mech.* Vol. 16, 1976, pp 249-257.

[37] Blackburn W.S., Calculation of stress intensity factors for straight cracks in grooved and ungrooved shafts. *Engng Fract. Mech.* Vol. 8, 1976, pp.731-736.

[38] Astiz M.A andElices M., On the application of the stiffness derivative method to two and three- dimensional fracture problems. In Proceedings of the *2nd Int. Conf.* on Numerical methods in Fracture Mechanics, 1980, pp. 93-106.

[39] Ouchterlony F., Extension of the compliance and stress intensity formulas for the single edge crack round bar in bending. In Fracture mechanics for Ceramics, Rocks and Concrete, ASTM STP 745, 1981, pp. 237-256. ASTM Philadephia, Pa.

[40] Trantina G.G., De Lorenzi H. G. and Wilkening W.W., Three-dimensional elastic-plastic finite element analysis of small surface cracks. *Engng Fract. Mech.* Vol.18, 1983, pp. 925-938.

[41] Mackay T.L. and Alperin B.J., Stress intensity factors for fatigue cracking in high-strength bolts *Engng Fract. Mech.* Vol.21, 1985, pp. 391-397.

[42] Lorentzen T., Kjaer N.E. and Henriksen T., The application of fracture mechanics to surface cracks in shafts. *Engng Fract. Mech.*, Vol.23, 1986, pp. 1005-1014.

[43] Hojfeldt E.and. Ostervig C.B, Fatigue crack propagation in shafts with shoulder fillets. *Engng Fract. Mech.* Vol. 25, 1986, pp.421-427.

[44] James L.A. and Mills W.J., Review and synthesis of stress intensity factor solutions applicable to cracks in bolts. *Engng Fract. Mech.* Vol. 30, 1988, pp. 641-654.

[45] Shiratori M., Miyoshi T., Sakay Y and. Zhang G.R, Analysis of stress intensity factors for surface cracks subjected to arbitrarily distributed surface stresses. 1986, *Trans. Jap. Soc. Mech. Engrs.*

[46] . Nord K. J and. Chung T. J, Fracture and surface flaws in smooth and threaded round bars. *Int. J. Fract.* Vol.30, 1986, pp. 47-55.

[47] Caspers M., Mattheck C. and Munz D., Fatigue crack propagation in round bars. *Z. Wkstofftech.* Vol. 17, 1986, pp.327-333.

[48] Da Fonte MA, Freitas MM. Fatigue crack growth under rotating bending and steady torsion. *Proc Fourth Int. Conf.* on Biaxial/ Multiaxial Fatigue 94, 1994, 1; 159-70.

[49] Da Fonte MA and Freitas MM. Semi- elliptical crack growth under rotating or reversed bending combined with steady torsion. *Fatigue Fract Engng Mater Struct* 1997; 20 (6):895-906.

[50] Barsoum R. On the use of isoparametric finite elements in linear fracture mechanics. *Int J Num Meth Engng* 1976; 10: 25-37.

[51] Henshell R and Shaw K. Crack tip finite elements are unnecessary. *Int J Num Meth Engng 1*975; 9:445-507.

[52] Carpinteri, A. Propagation of surface cracks under cyclic loading. In: Carpinteri A. editor. Handbook of Fatigue Crack Propagation in Metallic

Structures, Chapter 18. Amsterdam: Elsevier Science Publishers B.V., 1994: 653-705.

[53] Carpinteri A and Brighenti R. Fatigue propagation of surface flaws in round bars: a three- parameter theoretical model. *Fatigue Fract Engng Mater Struct* 1996; 19: 1471-1480.

[54] Carpinteri A and Brighenti R. Part through cracks in round bars under cyclic combined axial and bending loading. *Int J Fatigue* 1996; 18: 33-39.

[55] Freitas MM and Francois D. Analysis of fatigue crack growth in rotary bend specimens and railway axles. *Fatigue Fract Engng Mater. Struct* 1995; 18: 171-178.

[56] Pook LP. A finite element analysis of the angle crack specimen. In: Rossmanith HP, Miller KJ, editors. Mixed- mode fatigue and fracture, ESIS 14. London: *Mechanical Engineering Publications* 1993:285-302.

[57] Benthem JP. *Int Journal Solids Struct* 1977; 13:479.

[58] Bazant ZP and Estensoro LF. Proc 4th *Int Conf Fracture* 1977;3A: 371-85

[59] Benthem JP. *Int J Solids Structures* 1980; 16:119.

[60] Shen G and Glinka G. *Theor Appl Fract Mech* 1991; 15: 247

[61] Guo W. and Shen H., Li H., Stress intensity factors for elliptical surface cracks in round bars with different stress concentration coefficient, *Int J of Fatigue*, vol 25, (2003), pp 733-741.

[62] Heywood RB. In: Designing against fatigue. London: Chapman and Hall; 1962, pp 114-126.

[63] Lin XB. Fatigue growth simulation for cracks in notched and unnotched round bars. International Journal of Mechanical Science 1998; 40: 405-419.

[64] Stanley P. In: Fracture mechanics in engineering practice. London: Applied Science Publishers; 1977, pp 62.

[65] Li Z and Chen H. The 3D finite analysis of stress intensity factor of elliptical surface crack in sucker rods. China Petroleum Machinery 1994; 22:20-24.

[66] Wei J and Zhong B. Experimental research on stress intensity factor for surface crack at external thread root of threaded connection. Chinese journal of Mechanical Engineering 1994; 30: 37-43.

[67] As referred by W. Guo, H. Shen, H. Li. Stress intensity factors for elliptical surface cracks in round bars with different stress concentration coefficient. International Journal of Fatigue, Vol.25, 2003, pp 733-741. (Modified James Anderson Method with 3d effects of fatigue crack propagation considered, Journal of Engineering Material and Technology)

[68] Radebe D.B. Experimental study of semi-elliptical surface cracks in round bars. Undergraduate thesis at University of Cape Town in 2000 under R.B.Tait supervision.

[69] Fleuriau D. F.E.M and experimental determination of the stress intensity distribution for different flaw shapes for round bars in tension. Undergraduate thesis at University of Cape Town in 1997 under R.B. Tait supervision.

[70] Rambocus O.S., An experimental study of semi-elliptical surface cracks in round bars in bending and tension. Undergraduate thesis at University of Cape Town in 2002 under R.B. Tait supervision.

[71] Kim Y., Chao Y.J., Zhu X.K., "Effect of specimen size and crack depth on 3D crack-front constraint for SENB specimens." International Journal of Solids and Structures 40 (2003) pp 6267-6284.

[72] Wallin K. " Master curve analysis of ductile to brittle transition region fracture toughness round robin data- the "EURO" fracture toughness curve." VTT Manufacturing Technology Publication 1998.

[73] Fuchs H.O. and Stephens R.I., *Metal Fatigue in Engineering*. Wiley, New York (1980).

[74] Fracture Toughness of High-Strength Materials, The Department of Metallurgy, University of Sheffield, 27 March 1968.

[75] Dominique P. Miannay, "Fracture Mechanics" Mechanical Engineering series 1997.

[76] Ewalds H.L. and Wanhill R.J.H., "Fracture Mechanics" Edward Arnold Publishers Ltd, 1984.

[77] Irwin, G.R., "Fracture Mode Transition for a Crack Traversing a Plate," Journal of Basic Engineering, 1960, pp 417- 425.

[78] Wallin, K.R.W., "Critical Assessment of the Standard ASTM E 399," Fatigue and Fracture Mechanics: 34th Volume, ASTM STP 1461, S.R. Daniewciz, J.C. Newman and K.-H. Schwalbe, Eds., ASTM International, West Conshohocken, PA, 2004.

[79] Gibson G.P. and Druce S. G., "Effect of specimen size and geometry on ductile crack growth resistance. UKAEA Hardwell, report no R12138, 1986. Submitted for publication in Int J of Fracture.

[80] Priest A.H., "Size Effects in Fracture toughness testing procedures." British Steel Corporation, Paper presented at a seminar by the Material Group of the Engineering Sciences Division of the Institution of Mechanical Engineers 1986.

[81] Kaufman, J.G. and Nelson, F., "More on Specimen Size Effects in Fracture Toughness Testing, "Fracture Toughness and Slow- Stable Cracking, ASTM STP 559, American Society for Testing and Materials, Philadelphia, 1970, pp 41-62.

[82] May, M.J., "British Experience with Plain Strain Fracture (K_{IC}) Testing", ASTM STP 463, 1970 pp 42-62.

[83] Joyce J.A. and Tregoning R., " Development of Consistent Size Criteria for ASTM Combined Fracture Mechanics Standards, " Fatigue and Fracture Mechanics: 30th Volume, ASTM STP1360, K.L. Jerina and P.C. Paris, Eds., American Society for Testing Materials, West Conshohocken, PA, 2000, pp. 357-376.

[84] Bray, G.H., " Effects of Specimen Size and Side- Grooving in Plane Strain Fracture Toughness Testing of Aluminium Alloys," ASTM technical committee E08 meeting May 7,2001.

[85] Jones, M.H and Brown, W.F.Jr., "The influence of Crack length and Thickness in Plane Strain Fracture Toughness Testing, ASTM STP 463, American Society for Testing and Materials Philadelphia,1970, pp 63-101.

[86] Munz, D., Galda, K.H. and Link, F., "Effect of Specimen Size on Fracture Toughness of a Titanium Alloy," Mechanics of crack growth, ASTM STP 590, American Society for Testing and Materials, Philadelphia, 1976, pp. 219-234.

[87] Brown, W.F.Jr. and Srawley, J.E., " Plane Strain Fracture Toughness Testing and Materials", Philadelphia, 1969, pp145

[88] Rolfe, S.T. and Novak, S.R., "Slow- Bend K_{IC} Testing of Medium-Strength High-Toughness Testing", ASTM STP 463, American Society for Testing and Materials, Philadelphia, 1970, pp 124-159.

[89] Heerens J, Pfuff M, Hellmann D and Zerbst U. "The lower bound procedure applied to the Euro fracture toughness dataset." Engng Fract Mech 2002;69: pp 483-495.

[90] Dowling, N.E, Mechanical Behaviour of Materials, Engineering Methods for Deformation, Fracture, and Fatigue Publisher Prentice Hall 2nd Edition 1999.

[91] Taylor J.R., An Introduction to Error Analysis- The Study of Uncertainties in Physical Measurements. 2nd Edition. University of Science Books Sausalito, California, 1997.

[92] Standard Test Methods for Tension Testing of Metallic Materials E8-93.

[93] Ewalds, H.L. and Wanhill, R.J.H. Fracture Mechanics. publ. Edward Arnold and Delftse Uitgewers Maatshappij, 1984.

[94] Fracture Mechanics toughness tests BS7448 1991 part 1. BSI Standard.

APPENDIX A:

Tensile Testing Stress versus Strain

Tensile testing graphs of stress versus strain for the Al 2030 T3 material

Specimen 1

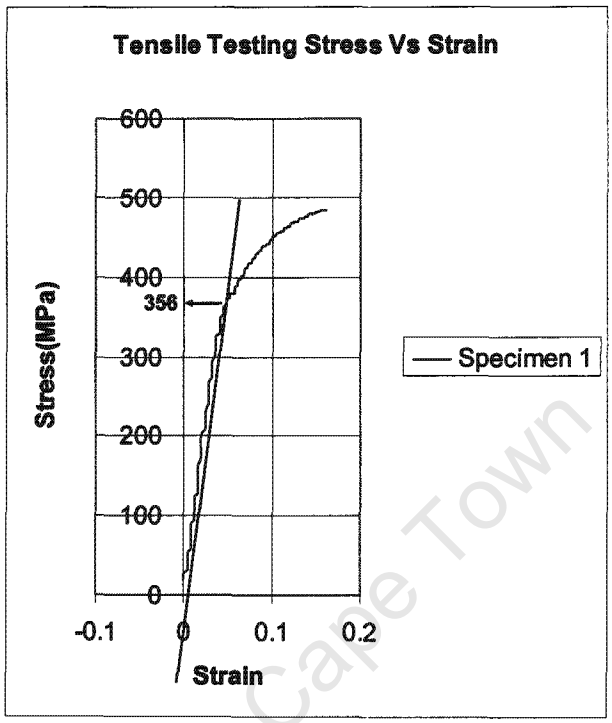

Specimen 2

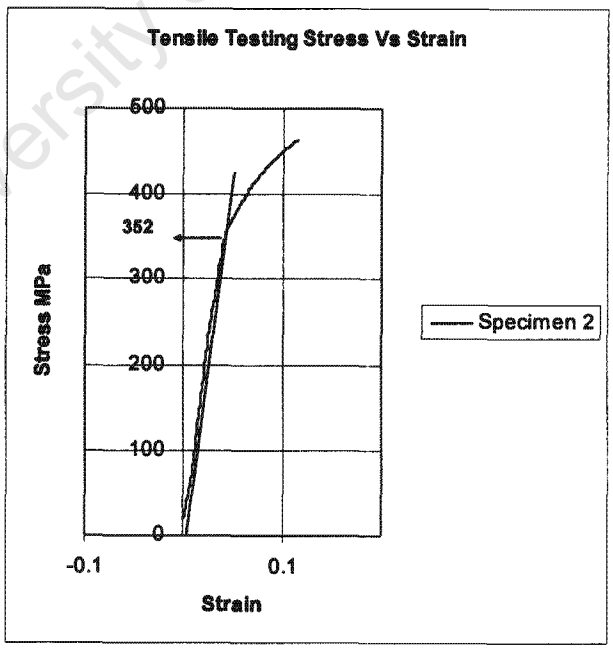

Specimen 3

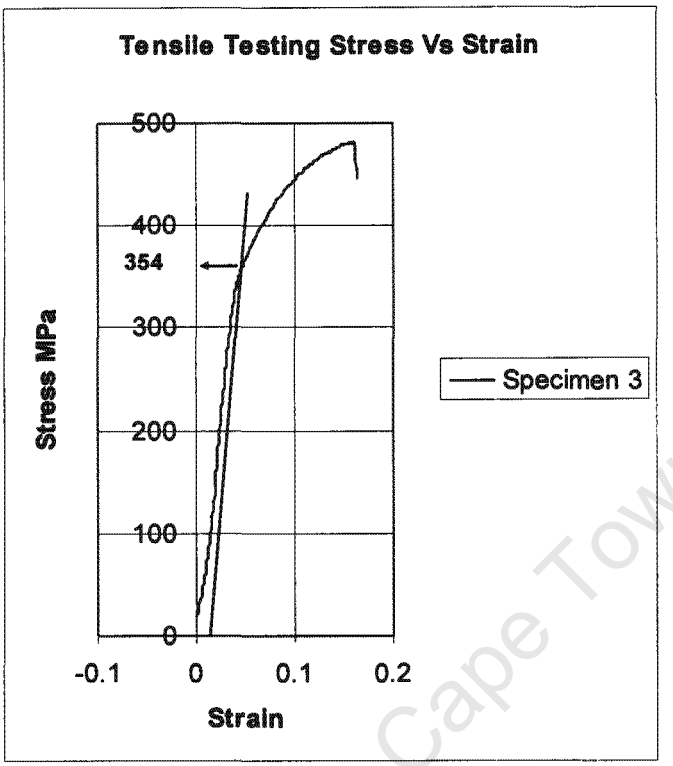

Specimen 4

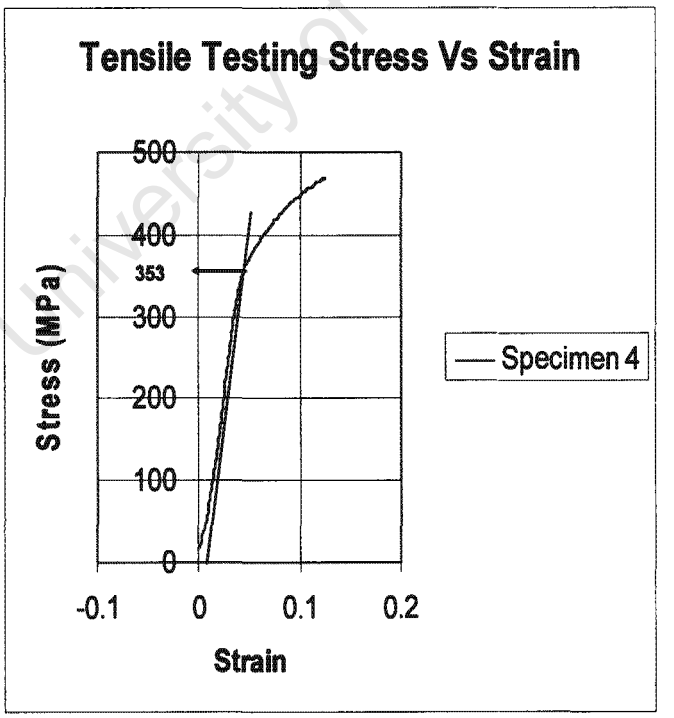

Specimen 5

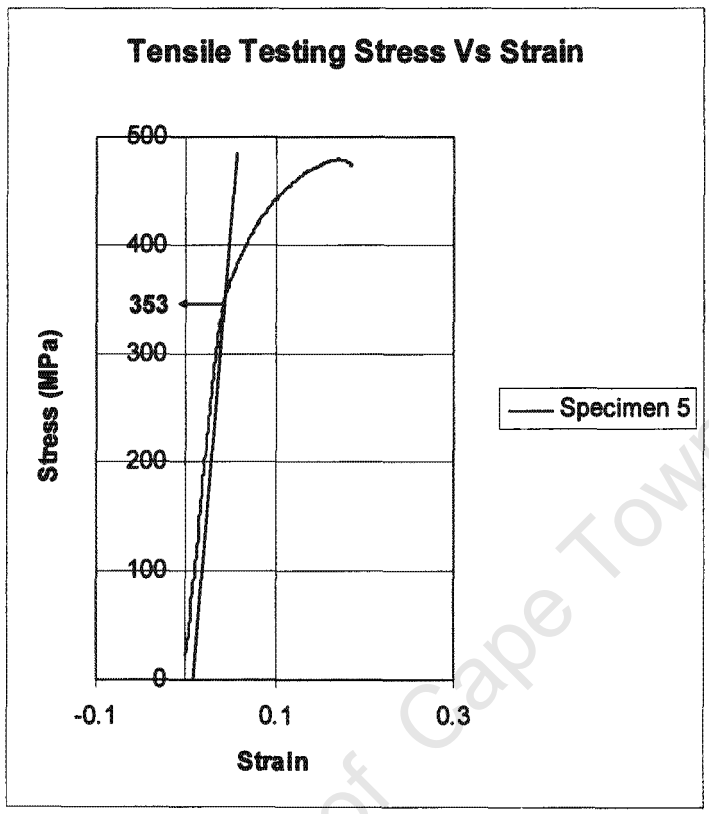

Specimen 6

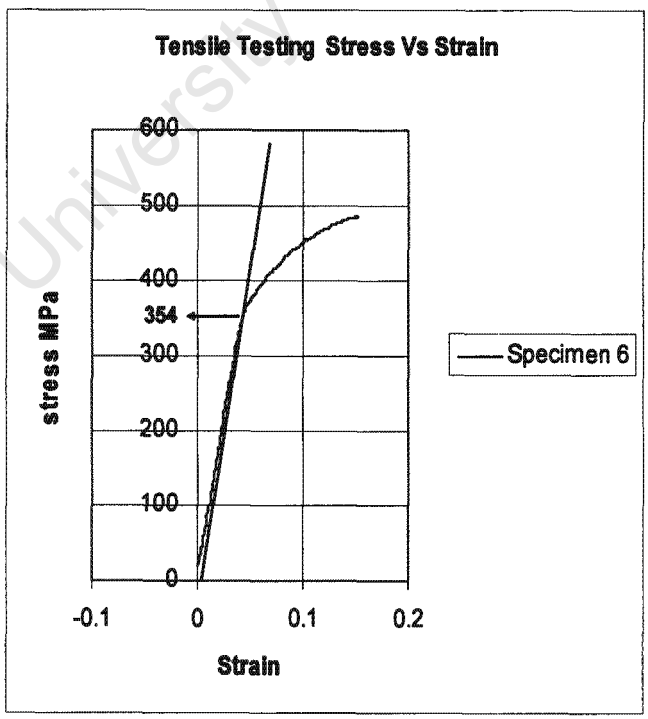

Specimen 7

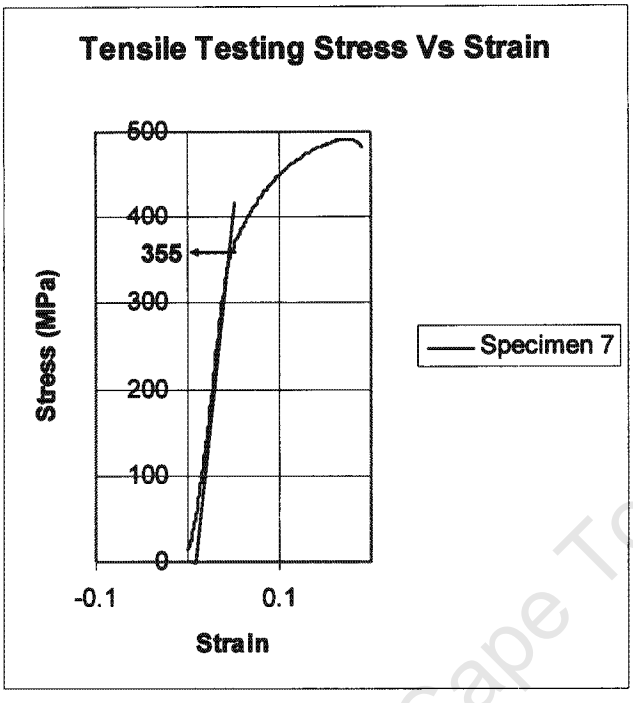

Specimen 8

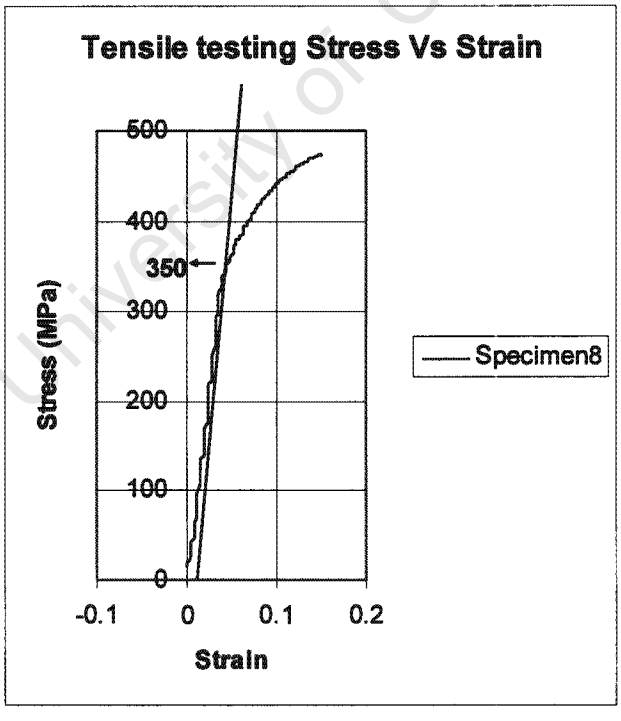

Specimen 9

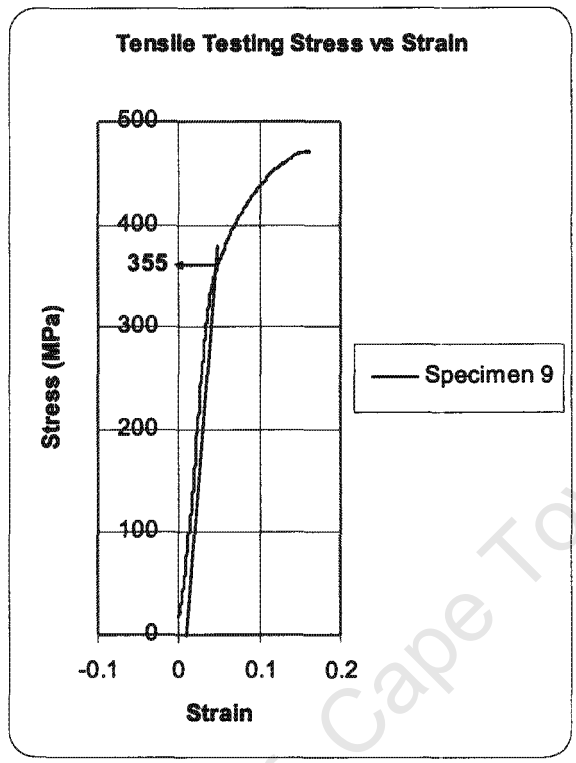

Specimen 10

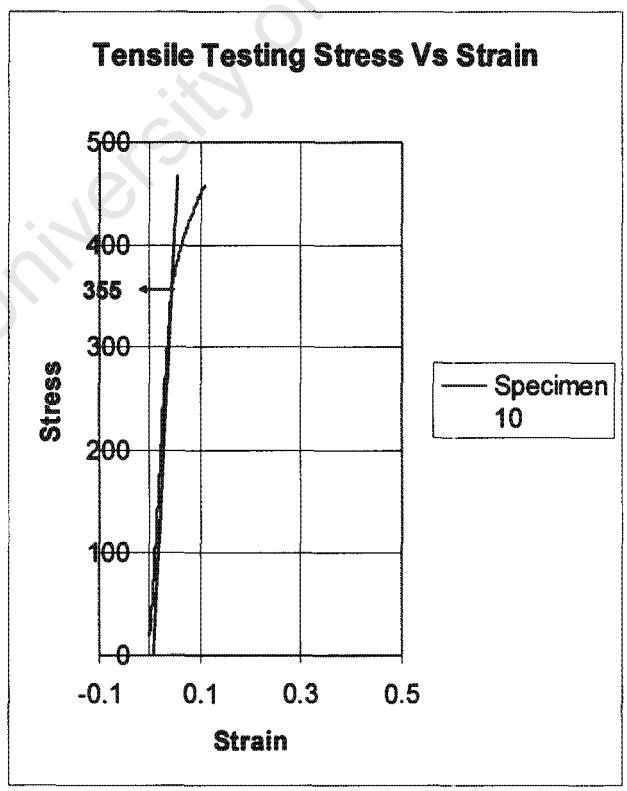

Specimen No.	Yield Stress	Ultimate Tensile Strength
	MPa	MPa
# 1	356	484
# 2	352	463.8
# 3	354	481.8
# 4	353	468.1
# 5	353	479.5
# 6	354	484.7
# 7	355	491.5
# 8	350	474.3
# 9	355	471.3
# 10	355	458.9
Total	3537	4757.9
Average Value	**353.7**	**475.8**

APPENDIX B

(Stress Concentration Calculations)

ANALYSING THE STRESS CONCENTRATION ON THE SPECIMEAL2030T3

Let point of force be point F

DIFFERENT DIAMETERS & LENGTHS

PLATE WIDTH

The Second moment of Area

	D1	D2	D3	I1	I2	I3
	(m)	(m)	(m)	(m^4)	(m^4)	(m^4)
ROW 1	0.018	0.014	0.007	5.15E-09	1.95E-09	1.18E-10
ROW 2	0.022	0.017	0.009	1.15E-08	4.1E-09	2.56E-10
ROW 3	0.026	0.02	0.01	2.24E-08	7.85E-09	4.91E-10
ROW 4	0.03	0.023	0.012	3.98E-08	1.37E-08	8.59E-10

LENGTHS

(m)	(m)	(m)	(m)	
0.138	0.13	0.022	0.012	
0.15	0.142	0.022	0.012	
0.18	0.172	0.022	0.012	
0.22	0.212	0.022	0.012	

Increase the lengths by difference From original length

(m)	(m)	
0.008	0.01	
0.008	0.01	
0.008	0.01	
0.008	0.01	

(m)	
0.185	
0.204	
0.234	
0.267	

Forces used for creating cracks in the specimens on different Diameters

FORCE	STRESS	STRESS		STRESS	STRESS		STRESS	STRESS		STRESS	STRESS								STRESS	STRESS		STRESS	STRESS	
F	A1	B1	B1-A1	C1	D1	D1-C1	A2	B2	B2-A2	C2	D2	D2-C2	A3	B3	B3-A3	C3	D3	D3-C3	F	A4	B4	B4-A4	C4	B4	B4-C4
(N)	(MPa)	(MPa)	(MPa)	(MPa)	(MPa)	(MPa)	(MPa)	(MPa)	(MPa)	(MPa)	(MPa)	(MPa)	(MPa)	(MPa)	(MPa)	(MPa)	(MPa)	(MPa)	(N)	(MPa)	(MPa)	(MPa)	(MPa)	(MPa)	(MPa)
0	0.0	0.0	0.0	0.0	0.0	0.0	0.0	0.0	0.0	0.0	0.0	0.0	0.0	0.0	0.0	0.0	0.0	0.0	0	0.0	0.0	0.0	0.0	0.0	0.0
50	12.1	24.1	12.1	4.1	17.8	13.7	7.2	14.7	7.5	2.3	10.0	7.7	5.2	10.9	5.7	1.4	6.1	4.7	50	4.1	8.5	4.3	0.9	4.0	3.1
100	24.1	48.3	24.2	8.2	35.6	27.5	14.3	29.4	15.1	4.6	19.3	14.8	10.4	21.6	11.5	2.9	12.2	9.4	100	8.3	17.7	9.4	1.8	8.0	6.2
150	36.2	72.4	36.2	12.2	53.5	41.2	21.5	44.2	22.6	6.9	29.0	22.0	15.6	32.8	17.2	4.2	18.3	14.1	150	12.4	26.6	14.2	2.8	12.1	9.3
200	48.2	96.5	48.3	16.3	71.3	54.9	28.7	58.9	30.2	9.1	38.8	29.7	20.9	43.8	22.9	5.5	24.4	18.9	200	16.6	35.5	18.9	3.7	16.1	12.4
250	60.3	120.6	60.4	20.4	89.1	68.7	35.9	73.6	37.7	11.4	48.8	37.4	26.1	54.7	28.7	7.0	30.6	23.6	250	20.7	44.4	23.6	4.6	20.1	15.5
300	72.3	144.8	72.5	24.5	106.9	82.4	43.0	88.3	45.3	13.7	58.7	45.0	31.3	65.7	34.4	8.4	36.7	28.3	300	24.9	53.2	28.3	5.5	24.1	18.6
350	84.4	168.9	84.5	28.5	124.7	96.1	50.2	103.0	52.8	15.9	68.5	52.5	36.5	76.6	40.1	9.8	42.8	33.0	350	29.0	62.1	33.0	6.4	28.1	21.7
400	96.4	193.0	96.6	32.7	142.6	109.9	57.4	117.8	60.4	18.2	78.3	60.0	41.7	87.6	45.9	11.2	48.9	37.7	400	33.2	71.0	37.8	7.4	32.1	24.8
450	108.5	217.2	108.7	36.7	160.4	123.6	64.6	132.6	67.9	20.5	88.2	67.5	46.9	98.5	51.6	12.6	55.0	42.4	450	37.3	79.9	42.5	8.3	36.2	27.9
500	120.5	241.3	120.8	40.8	178.2	137.3	71.7	147.3	75.5	22.8	98.0	75.2	52.2	109.5	57.3	14.0	61.1	47.1	500	41.5	88.7	47.2	9.2	40.2	31.0
550	132.6	265.4	132.8	44.9	196.0	151.0	78.9	161.9	83.0	25.1	107.8	82.7	57.4	120.4	63.1	15.4	67.2	51.8	550	45.6	97.6	52.0	10.1	44.2	34.1
600	144.6	289.5	144.9	49.0	213.8	164.8	86.1	176.6	90.5	27.4	117.4	90.1	62.5	131.4	68.8	16.8	73.3	56.5	600	49.9	106.5	56.7	11.1	48.2	37.2
650	156.7	313.7	157.0	53.1	231.6	178.5	93.3	191.4	98.1	29.6	127.1	97.7	67.6	142.3	74.5	18.2	79.5	61.2	650	53.9	115.4	61.4	12.0	52.2	40.3
700	168.7	337.9	169.1	57.2	249.5	192.3	100.4	206.1	105.6	31.9	136.9	105.4	73.0	153.3	80.3	19.6	85.6	66.0	700	58.1	124.2	66.1	12.9	56.3	43.4
750	180.8	361.9	181.2	61.2	267.3	206.0	107.6	220.8	113.2	34.2	146.6	112.9	78.2	164.2	86.0	21.0	91.7	70.7	750	62.2	133.1	71.0	13.8	60.3	46.5
800	192.8	385.1	193.2	65.3	285.1	219.8	114.8	235.4	120.7	36.5	156.2	120.2	83.5	175.2	91.7	22.4	97.8	75.4	800	66.4	142.0	75.6	14.7	64.3	49.6

APPENDIX C:

(Drawings of specimens and modification made for the rotational bending machine)

14mm diameter Crescent Moon Specimen

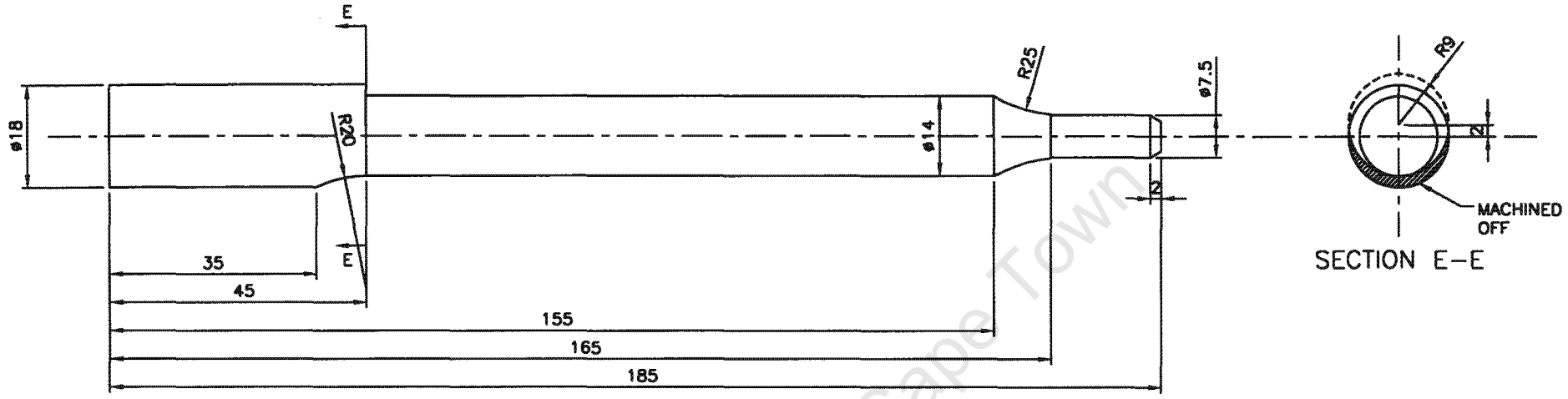

Thumbnail Specimen

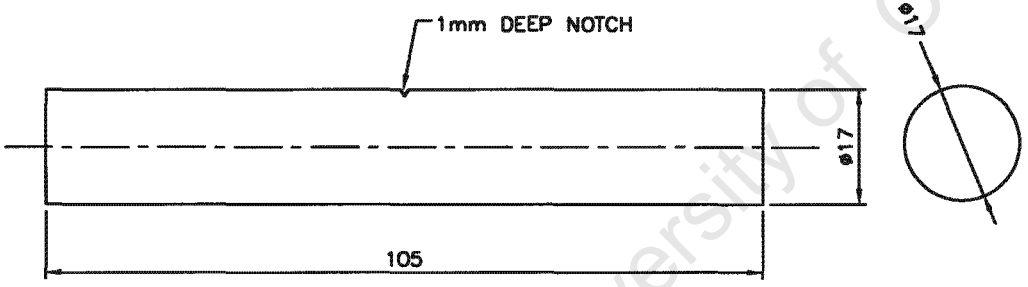

Tensile Specimen

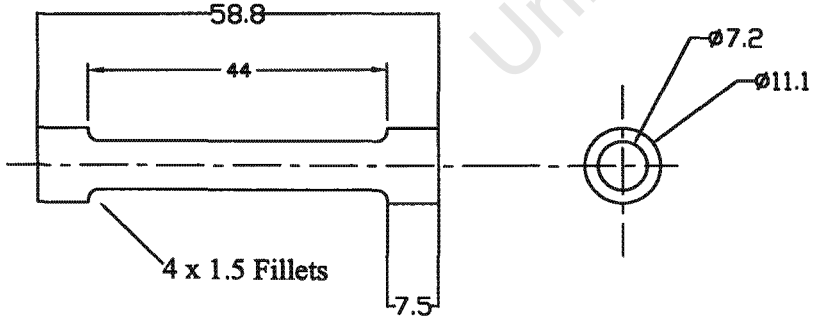

Crescent moon 14mm	AL2030 T3	12
Crescent moon 14mm	Al7075 T6	23
Tensile specimen	AL2030 T3	10
Thumbnail	Al7075 T6	12
Description	Material	No. OFF

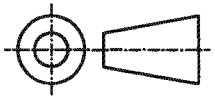

UNIVERSITY OF CAPE TOWN
DEPARTMENT OF MECHANICAL ENGINEERING
SEMI-ELLIPTICAL CRACKS 2002

TITLE
SPECIMENS

DIMENSIONS IN MILLIMETRES (mm)
TOLERANCES UNLESS OTHERWISE STATED
0.1 mm

SCALE	DATE	SHEET OF
1 : 1	22 MAY 2004	1 1

DRAWN BY: OS RAMBOCUS

DWG. NO.

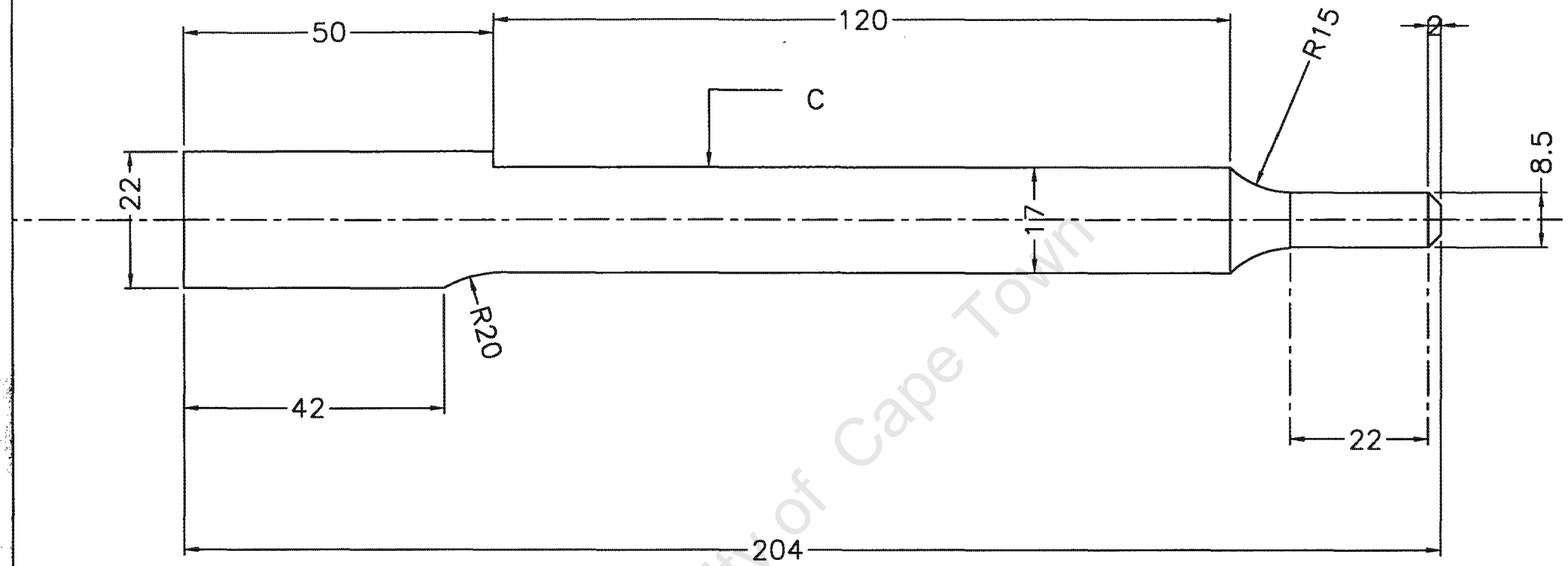

Part No	Description	Material	No Off

17mm diameter specimen (not to scale)

UNIVERSITY OF CAPE TOWN
DEPARTMENT OF MECHANICAL ENGINEERING
SEMI-ELLIPTICAL CRACKS 2002

TITLE
CRESCENT MOON SPECIMEN

DIMENSIONS IN MILLIMETRES (mm)
TOLERANCES UNLESS OTHERWISE STATED
0.1 mm

DATE
09/02/2004

SHEET OF
1 1

DRAWN BY
OS RAMBOCUS

DWG. NO.

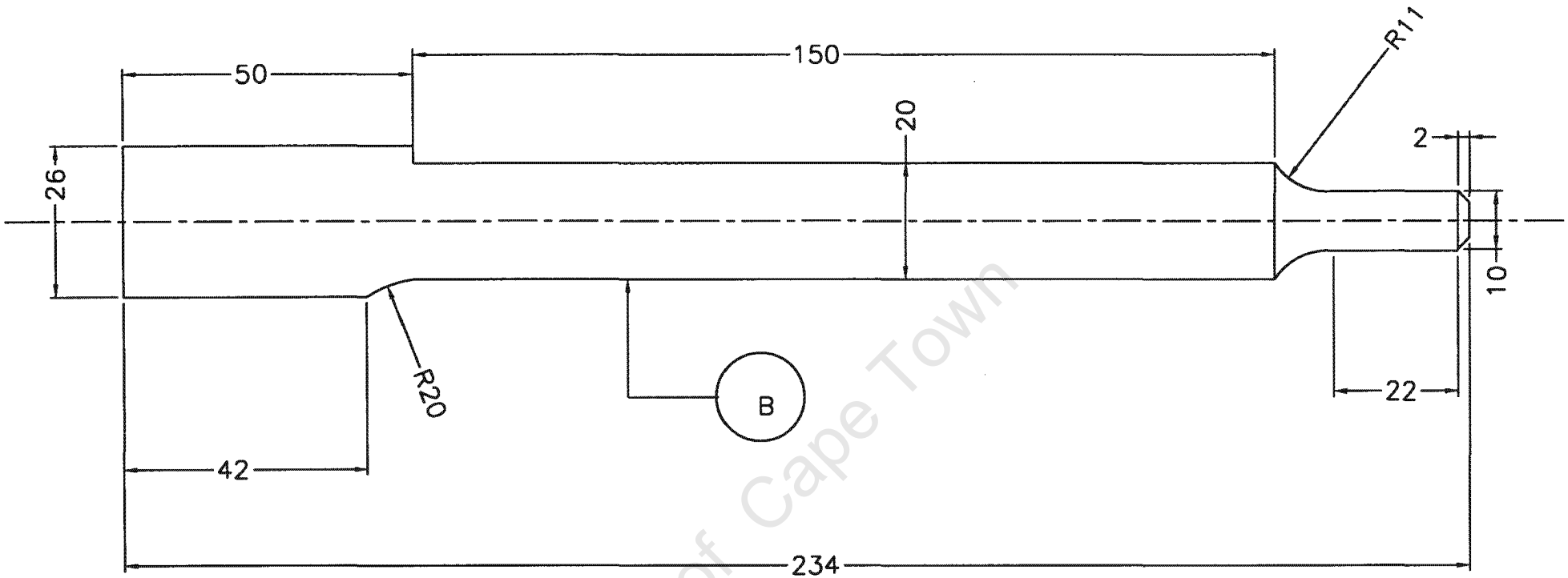

B	20mm diameter	AL2030T3	12
Part No	Description	Material	No Off

20mm Specimen (Not to scale)

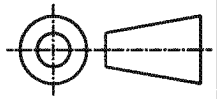

UNIVERSITY OF CAPE TOWN
DEPARTMENT OF MECHANICAL ENGINEERING
SEMI-ELLIPTICAL CRACKS 2002

TITLE
CRESCENT MOON SPECIMEN

DIMENSIONS IN MILLIMETRES (mm)
TOLERANCES UNLESS OTHERWISE STATED
0.1 mm

DATE
17/02/2004

SHEET OF
1 1

DRAWN BY
OS RAMBOCUS

DWG. NO.

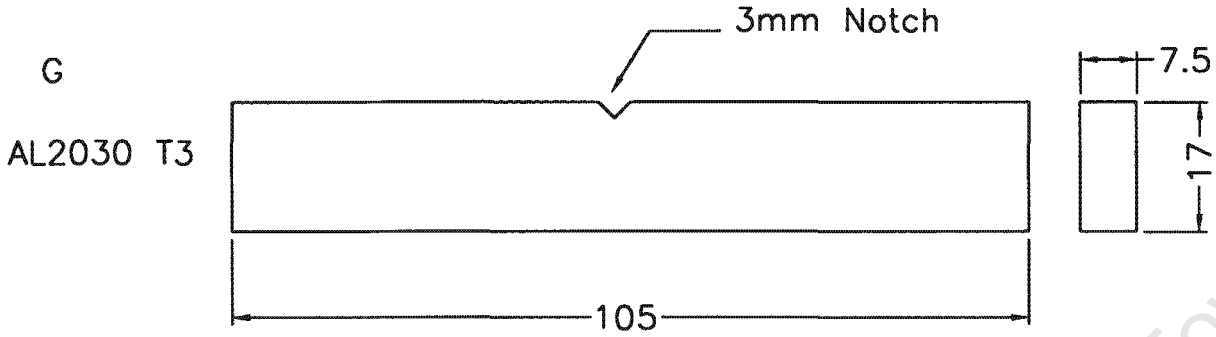

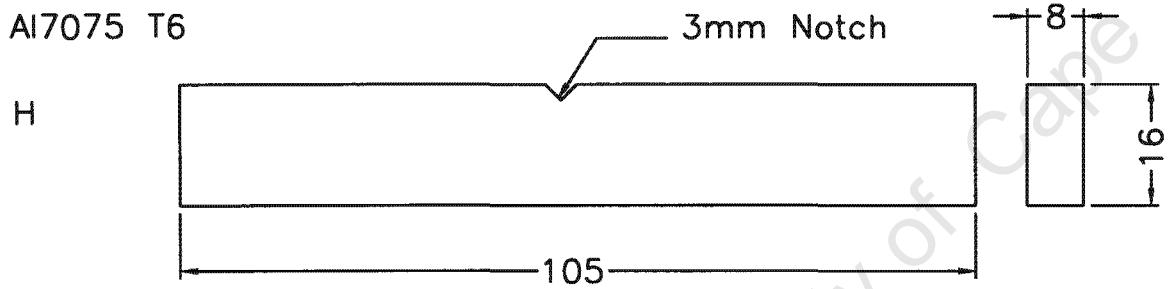

Fracture toughness Specimens SENB

Part No	Description	Material	No Off
H	fracture toughness	Al7075 T6	5
G	fracture toughness	AL2030T3	8

UNIVERSITY OF CAPE TOWN
DEPARTMENT OF MECHANICAL ENGINEERING
SEMI-ELLIPTICAL CRACKS 2002

TITLE
CRESCENT MOON SPECIMEN

DIMENSIONS IN MILLIMETRES (mm)
TOLERANCES UNLESS OTHERWISE STATED
0.1 mm

DATE 7/02/2004

SHEET 1 OF 1

DRAWN BY OS RAMBOCUS

DWG. NO.

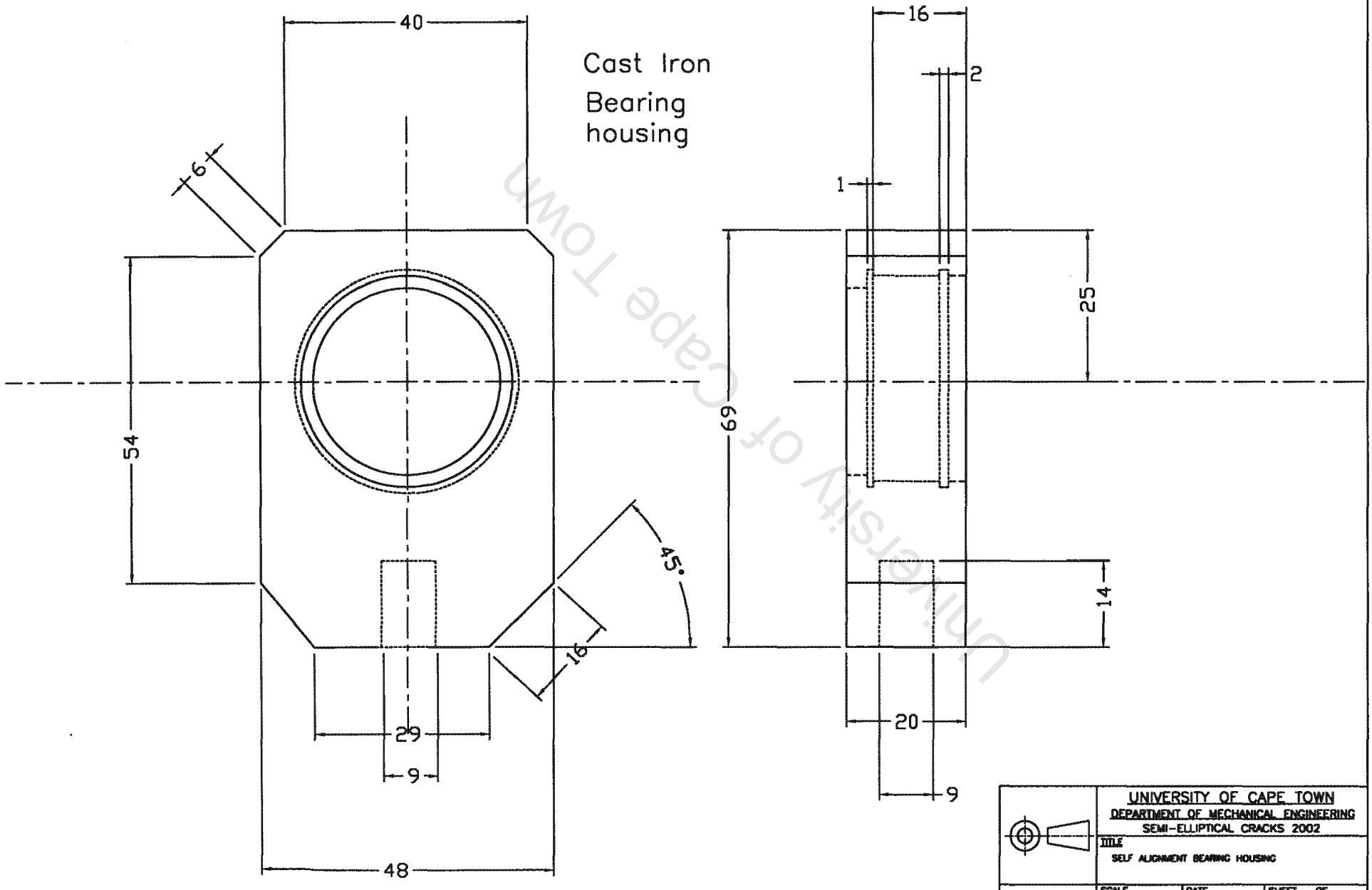

UNIVERSITY OF CAPE TOWN
DEPARTMENT OF MECHANICAL ENGINEERING
SEMI-ELLIPTICAL CRACKS 2002

TITLE: SELF ALIGNMENT BEARING HOUSING

DIMENSIONS IN MILLIMETRES (mm)
TOLERANCES UNLESS OTHERWISE STATED 0.1 mm

SCALE: 1 : 1

DATE: 28th July 2004

SHEET 1 OF 1

DRAWN BY: OS RAMBOCUS

DWG. NO.

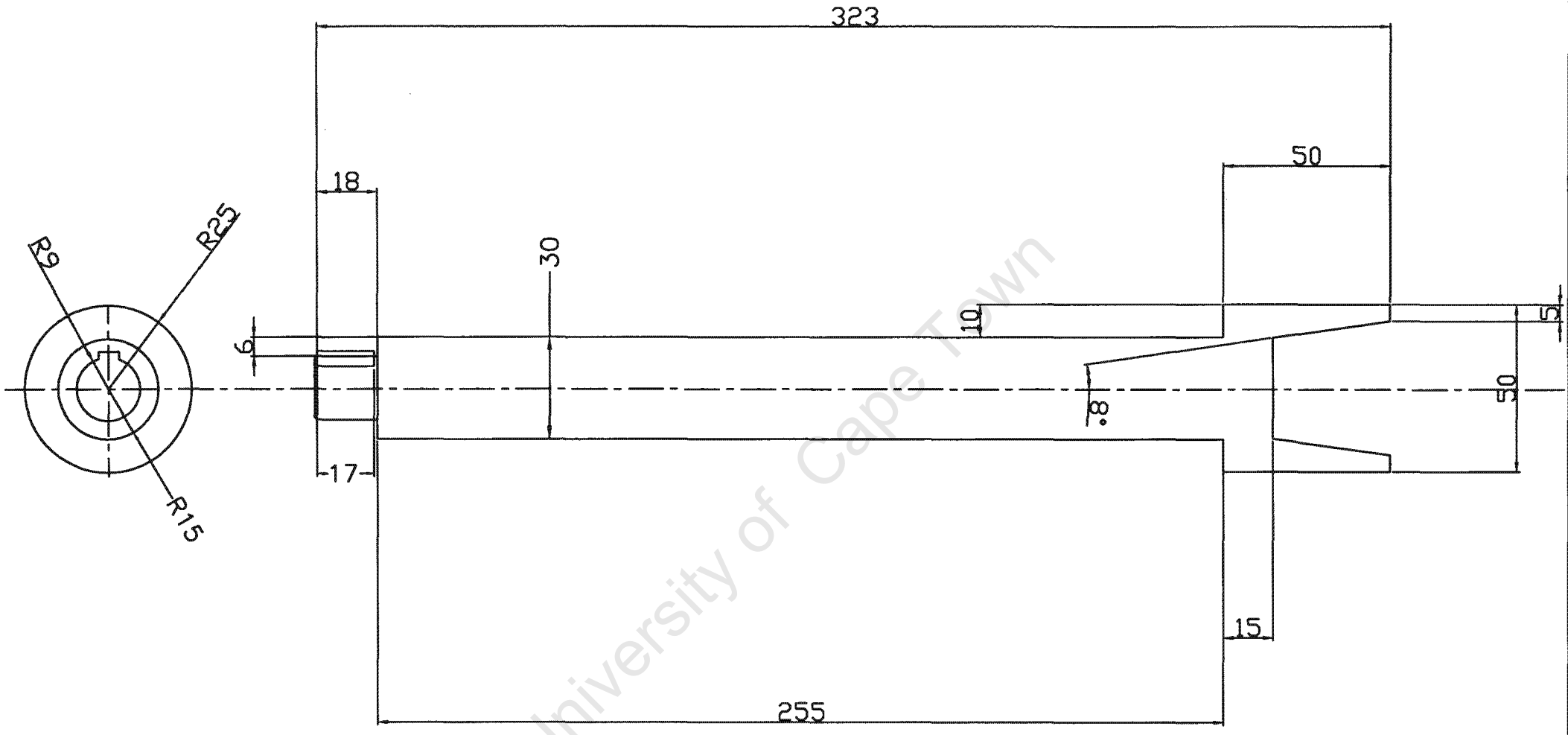

Shaft material– mild steel.

Key Size is
6.2 x 4.5
mm

UNIVERSITY OF CAPE TOWN
DEPARTMENT OF MECHANICAL ENGINEERING
SEMI–ELLIPTICAL CRACKS 2002

TITLE **SHAFT**

DIMENSIONS IN MILLIMETRES (mm)
TOLERANCES UNLESS OTHERWISE STATED
0.1 mm

DATE 6th/02/2004

SHEET 1 OF 1

DRAWN BY OS RAMBOCUS

DWG. NO.

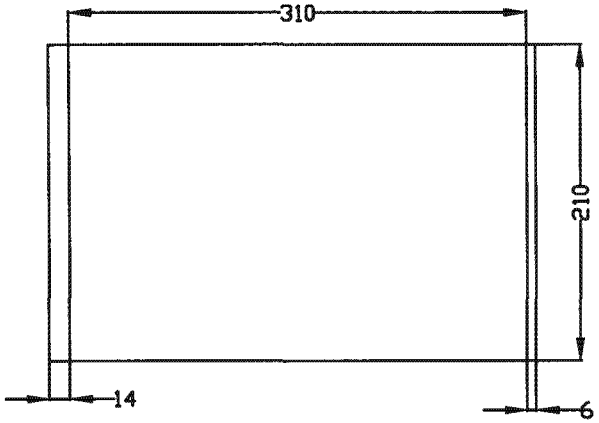

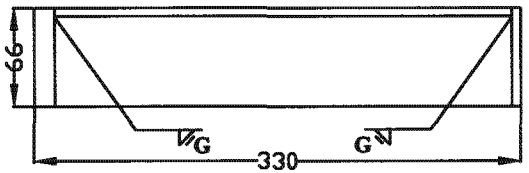

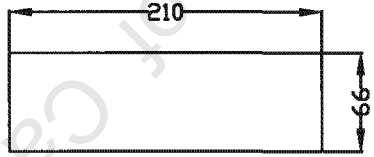

	SUPPORT		2
PART No.	DESCRIPTION	MATERIAL	No. OFF

	University of Cape Town Department of Mechanical Engineering		
	Title: Support		
Dimension in (mm)	Scale 1:3	Date: 24.02.2004	
Drawn By ODESH RAMBOCUS			

EXAMPLE: Fracture Toughness SENB fatigue on ESH.

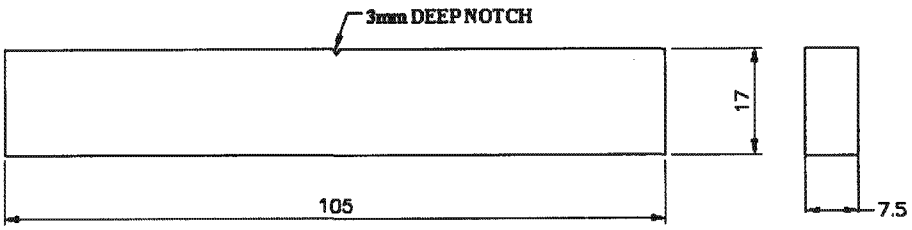

Specimen no.7 Al2030 T3

Date: 9th July 2004
Force P: 2.5kN
Mean: 1.375kN
Frequency: 10Hz
R- ratio: 0.1
Notch: 3mm
Condition: Room Temperature

Amplitude (kN)	No of Cycles	a (mm)	da/dN (mm/cycle)	Comments
1.097	1000	0.6		
1.022	3750	1.1	1.82E-04	crack initiate
	4181	1.2	2.32E-04	too fast
0.9	4921	1.5	4.05E-04	decrease amplitude
0.7	7191	1.7	8.81E-05	good
	9000	1.9	1.11E-04	good steady growth
	10000	2.1	2.00E-04	
0.65	12000	2.3	1.00E-04	
	14000	2.6	1.50E-04	crack taking a skew direction
	15000	2.9	3.00E-04	too fast
0.55	17000	3.1	1.00E-04	
	20000	3.5	1.33E-04	
	21000	3.6	1.00E-04	good in control
↓	↓	↓	↓	
0.425	34700	5.5	1.25E-04	Fatigue test terminated

Fracture toughness specimen (Example) AL 7075 T6				
Dial	**a**	**N**	**da/dN mm/cycles**	**Comments**
Load kN	**Crack length on graticule mm**	**No of cycles**	**Rate of crack growth**	
3.5 $\left(\frac{0.4}{3.45}\right)$	1.1	3000	Nil	Very small crack
	1.2	3300	3.3×10^{-4}	Fast
3.4 $\left(\frac{0.39}{3.35}\right)$	1.3	4000	1.4×10^{-4}	Good, carry on
	1.3	5000	nil	Carry on
	1.4	6860	0.5×10^{-4}	Slow
	1.5	7250	2.5×10^{-4}	Getting fast …
3.3 $\left(\frac{0.38}{3.25}\right)$	1.6	7800	1.8×10^{-4}	Under controlled
	1.75	8130	4.5×10^{-4}	Too fast. Reduce force!!
3.15 $\left(\frac{0.365}{3.10}\right)$	1.85	8410	3.57×10^{-4}	Still fast! Reduce more!
3.0 $\left(\frac{0.35}{2.95}\right)$				
	1.95	9000	1.69×10^{-4}	Good enough. …Carry on till approx. W/2.

Fracture Toughness (with 5% offset)

Specimen 1 Al2030 T3 (Graph is on a negaive scale due to compression as obtained from the ESH program.)

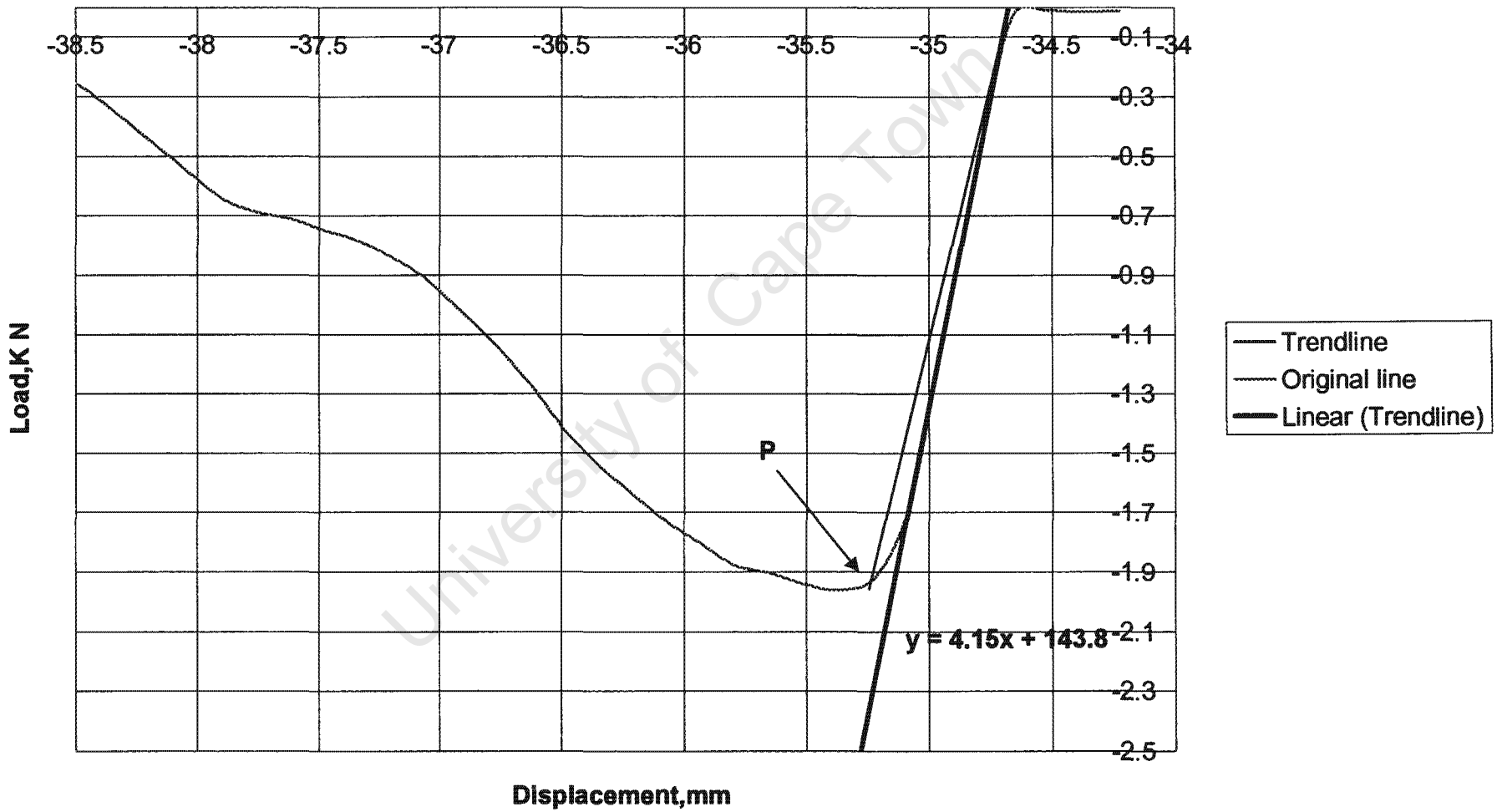

Fracture Toughness with 5% offset)

Specimen 2 Al2030 T3 (Graph is on a negative scale due to compression as obtained from the ESH program)

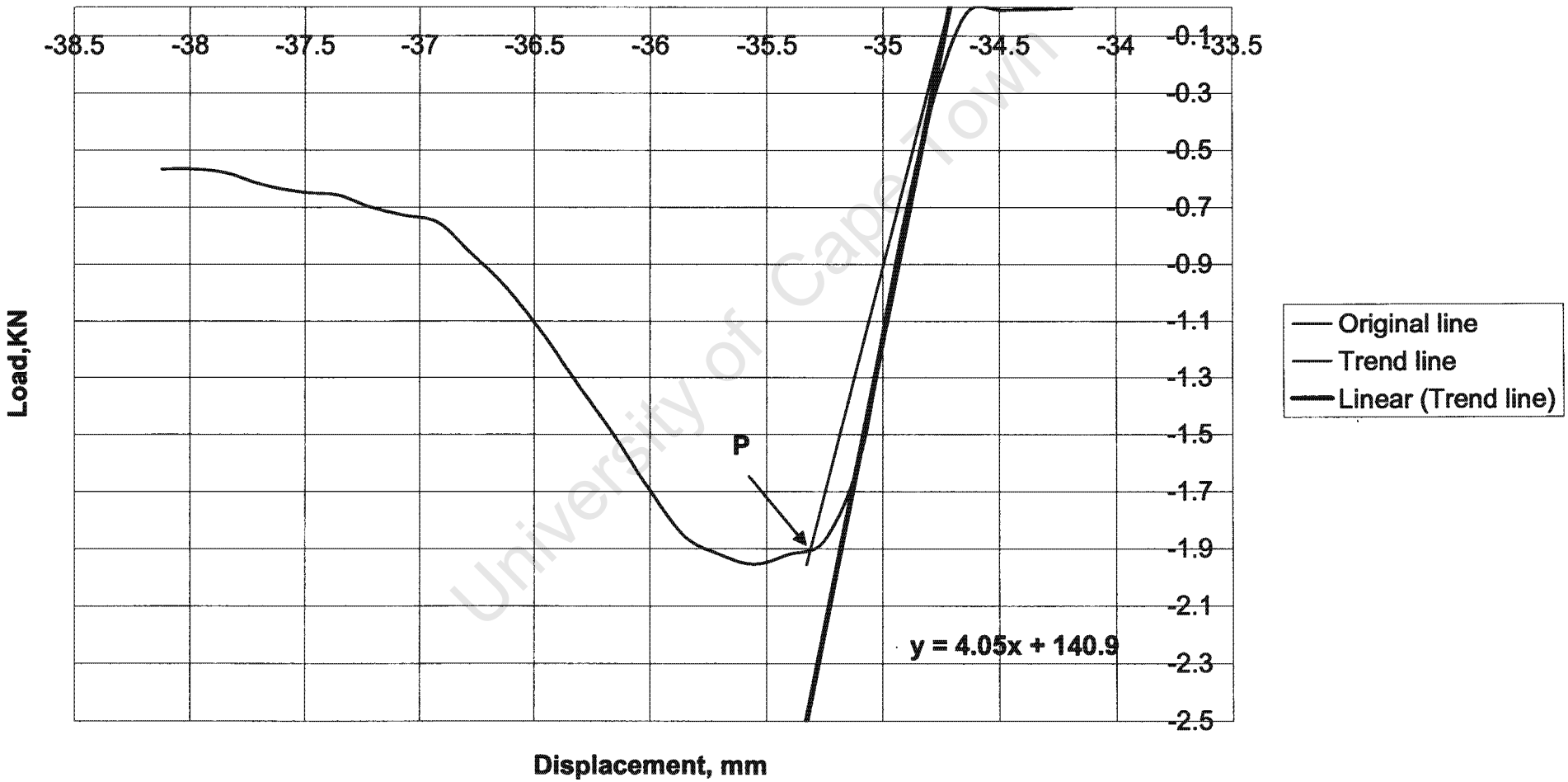

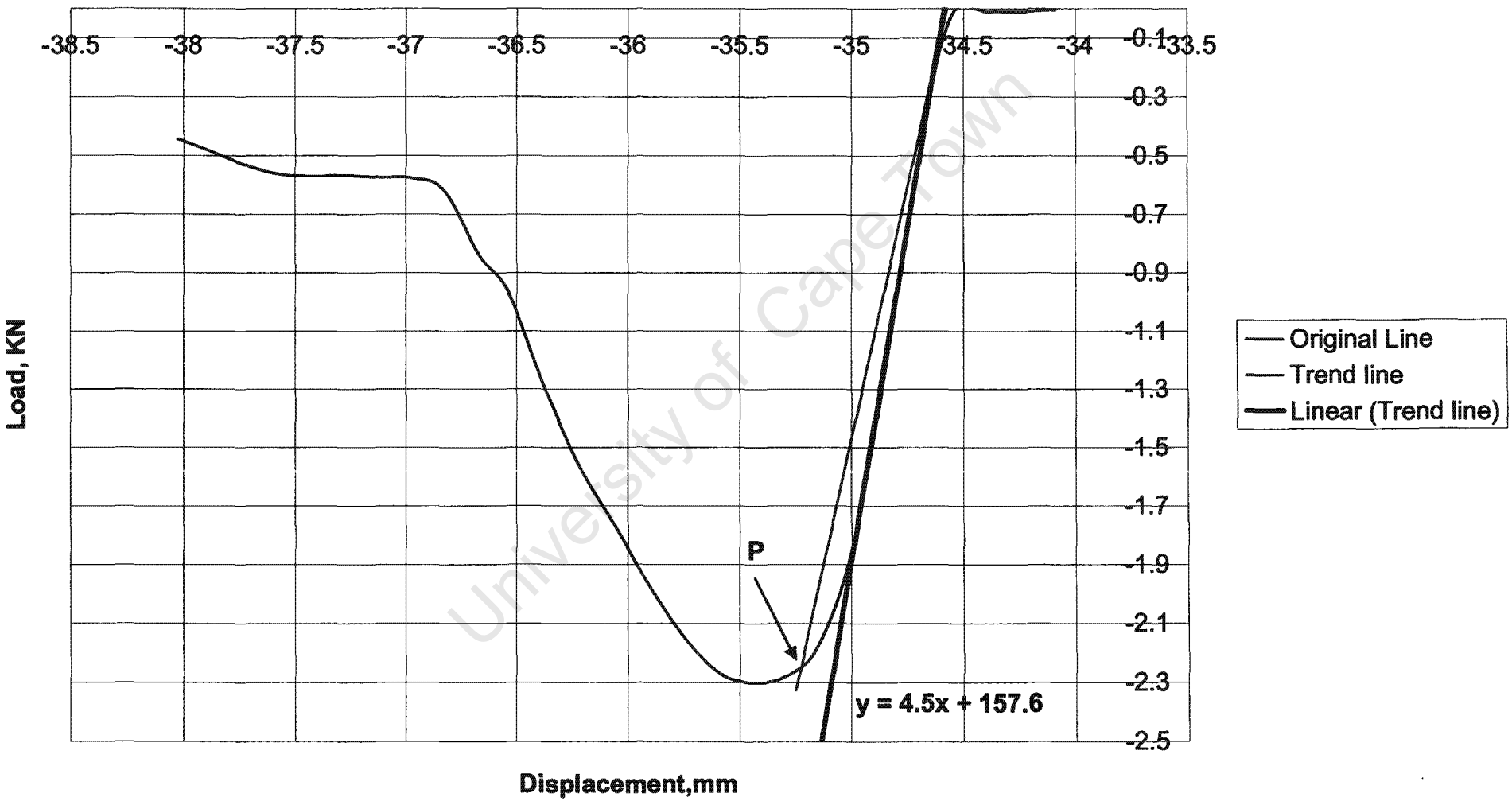
Specimen 3 Al2030 T3
-38.5
-38
-37.5
-37
-36.5
-36
-35.5
-35
-34.5
-34
-33.5
-0.1
-0.3
-0.5
-0.7
-0.9
-1.1
-1.3
-1.5
-1.7
-1.9
-2.1
-2.3
-2.5
Load, KN
Displacement,mm
P
y = 4.5x + 157.6
Original Line
Trend line
Linear (Trend line)
University of Cape Town

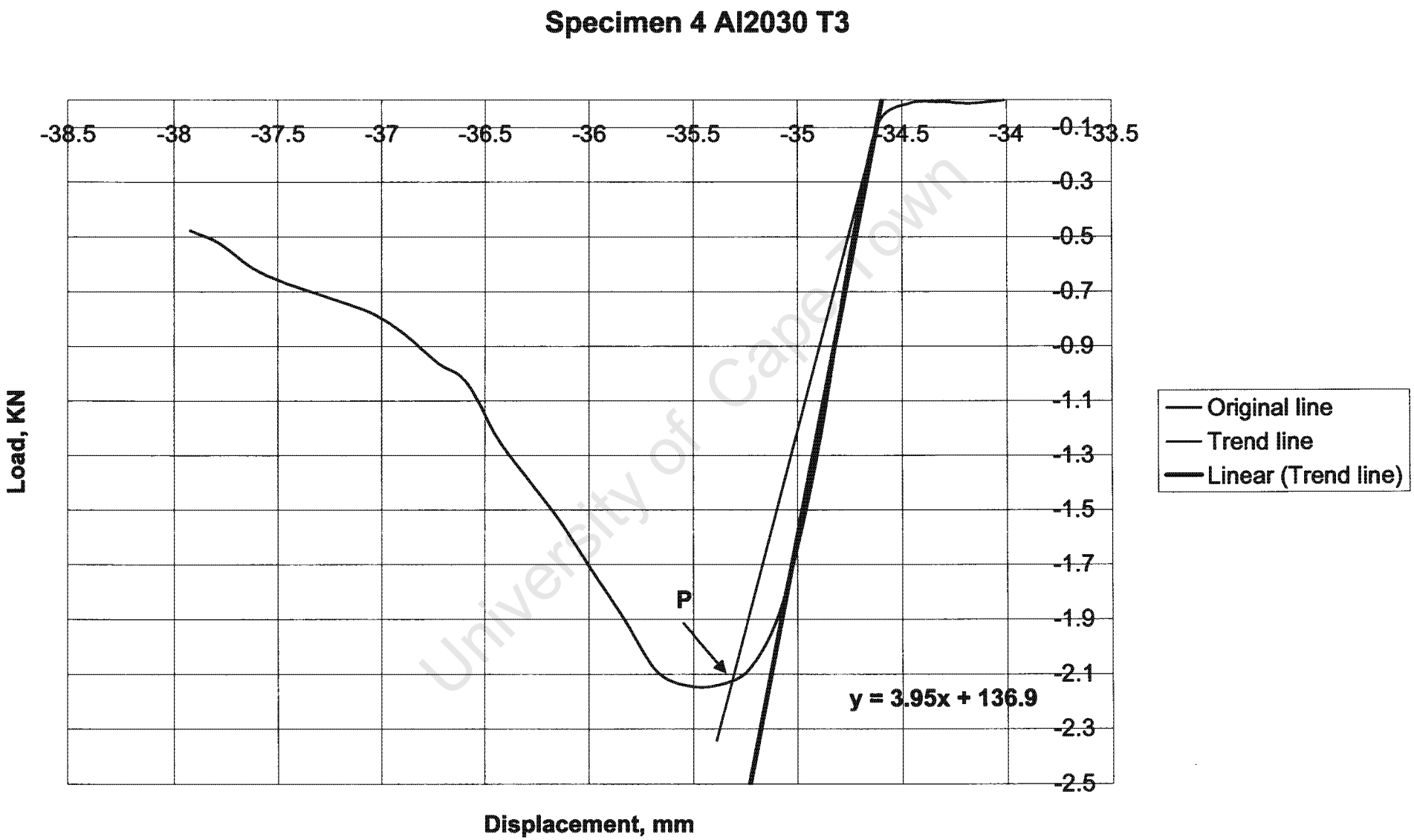
Specimen 4 Al2030 T3
-38.5
-38
-37.5
-37
-36.5
-36
-35.5
-35
-34.5
-34
-33.5
-0.1
-0.3
-0.5
-0.7
-0.9
-1.1
-1.3
-1.5
-1.7
-1.9
-2.1
-2.3
-2.5
Load, KN
Displacement, mm
P
y = 3.95x + 136.9
Original line
Trend line
Linear (Trend line)
University of Cape Town

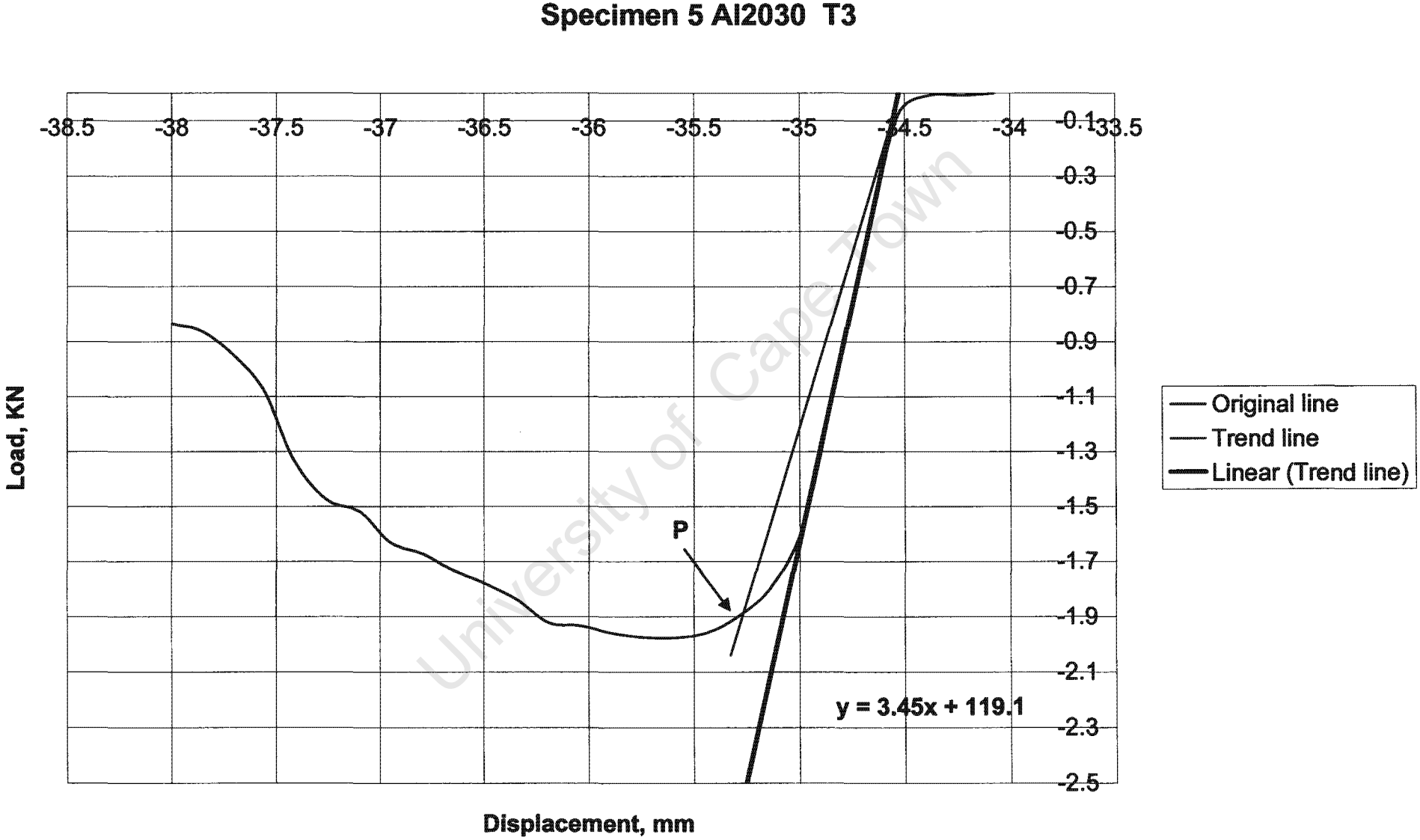
Specimen 5 Al2030 T3
-38.5
-38
-37.5
-37
-36.5
-36
-35.5
-35
-34.5
-34
-33.5
-0.1
-0.3
-0.5
-0.7
-0.9
-1.1
-1.3
-1.5
-1.7
-1.9
-2.1
-2.3
-2.5
Load, KN
Displacement, mm
P
y = 3.45x + 119.1
Original line
Trend line
Linear (Trend line)
University of Cape Town

Specimen 7 Al2030 T3

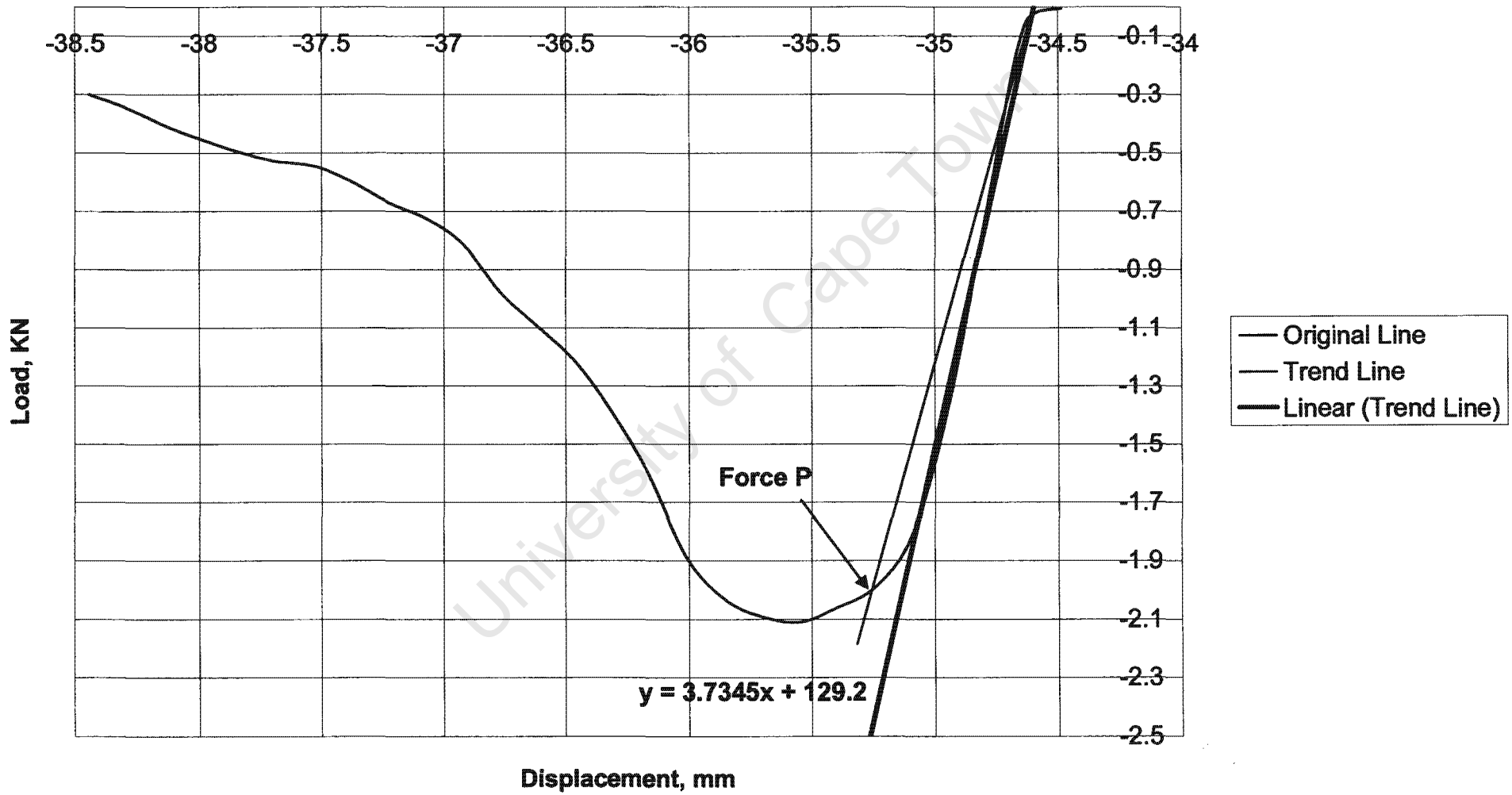

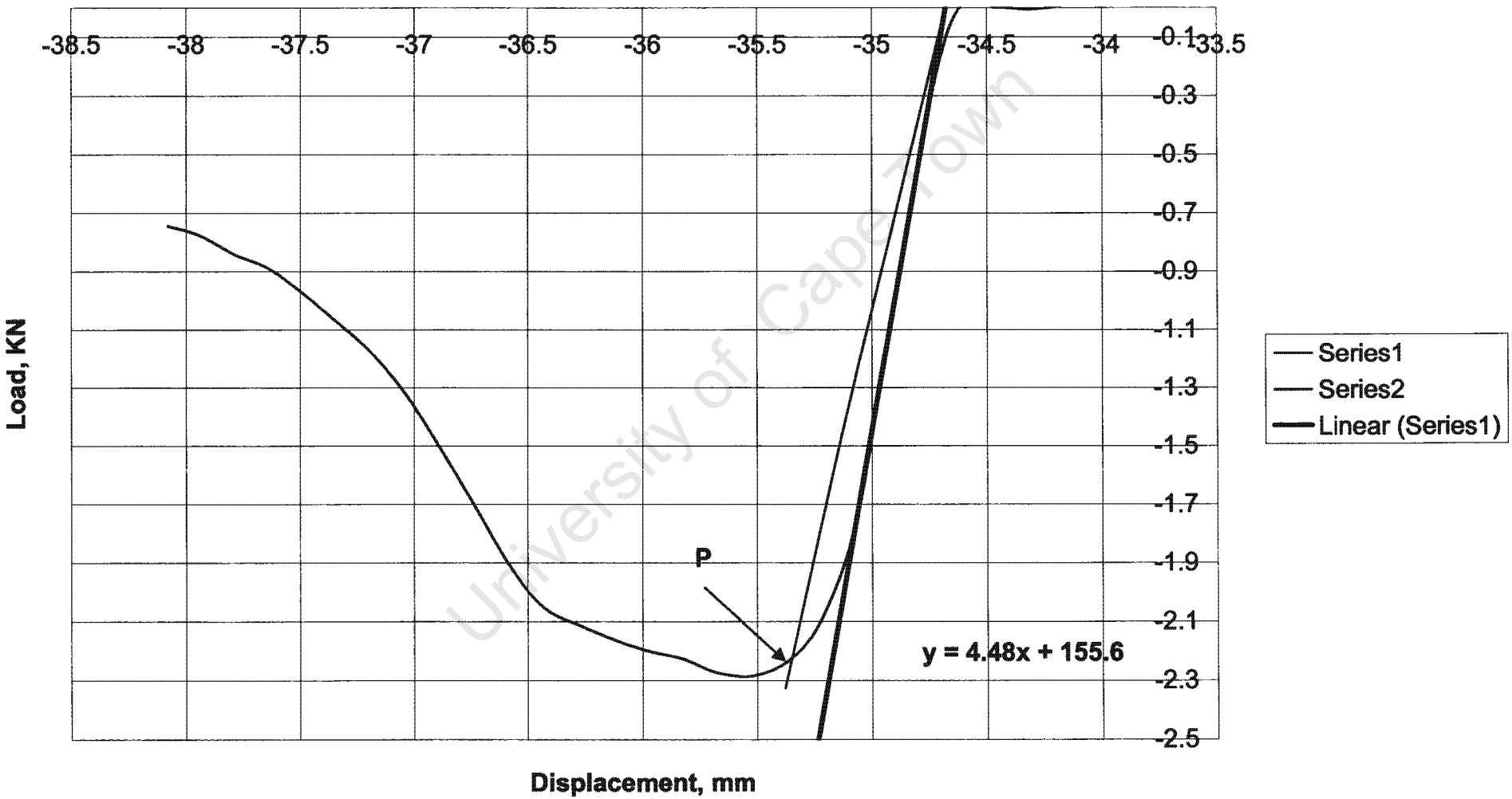

Average measurement of Crack in each specimen for Al2030 T3

	a0	a1/4	a1/2	a3/4	a5	a ave
	mm	mm	mm	mm	mm	mm
Spec1A	8.00	8.20	8.00	8.50	8.50	8.24
Spec2A	9.50	9.50	9.50	9.50	8.00	9.31
Spec3A	7.50	7.50	8.50	8.50	8.25	8.09
Spec4A	8.00	8.00	8.50	8.50	8.50	8.31
Spec5A	8.50	8.50	8.50	8.50	8.50	8.50
Spec6A						
Spec7A	8.50	9.20	9.20	9.20	9.20	9.11
Spec8A	8.50	8.50	8.50	8.50	8.50	8.50

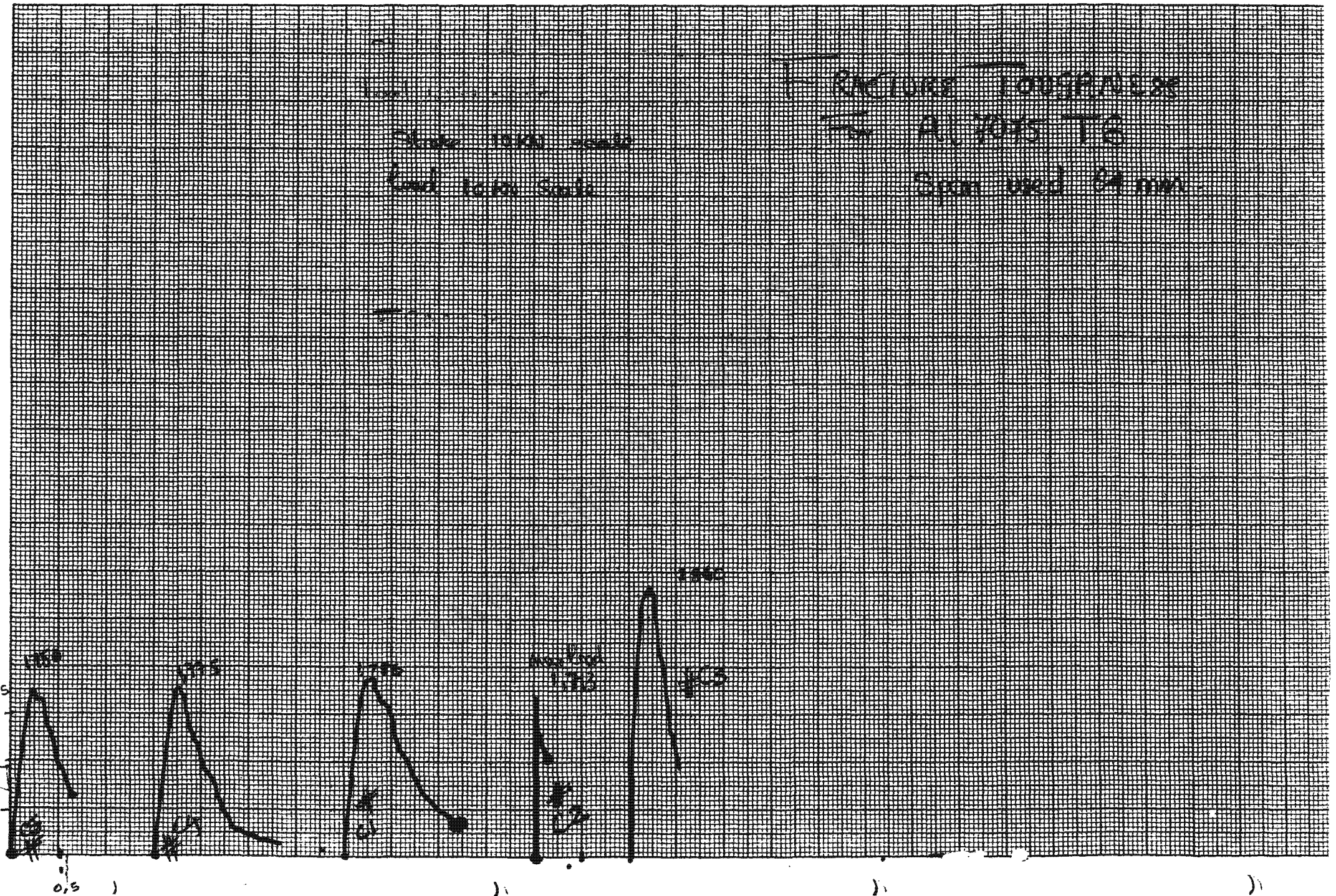
Stroke 10 kN scale
Load to be Scale
Span used 64 mm
1,75
1,5
1,0
0,5
kN
0,5

APPENDIX E:

- **Load versus Displacement for Thumbnail fatigue cracks**

Thumbnail specimen B2a (Example) Al 7075 T6				
Dial	**a**	**N**	**da/dN mm/cycles**	**Comments**
Load	**Crack length on graticule**	**No of cycles**	**Rate of crack growth**	
6.5 (0.7 / 6.45)		3510		Very small crack adjust microscope (focus)
6.25 (0.675 / 6.2)	2.25	5120		
	2.3	5310	2.63×10^{-4}	Getting fast
	2.4	5660	2.8×10^{-4}	Change load….
6.0 (0.65 / 5.95)	2.6	6800	1.7×10^{-4} Carry on…etc…… ……	

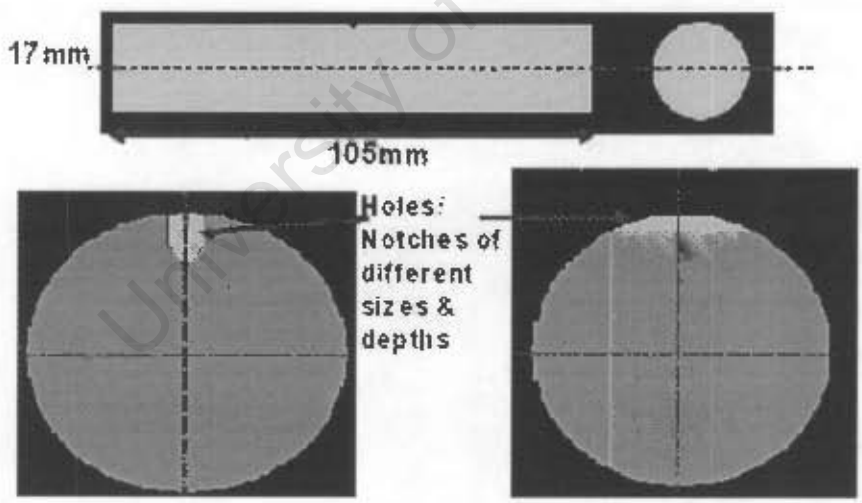

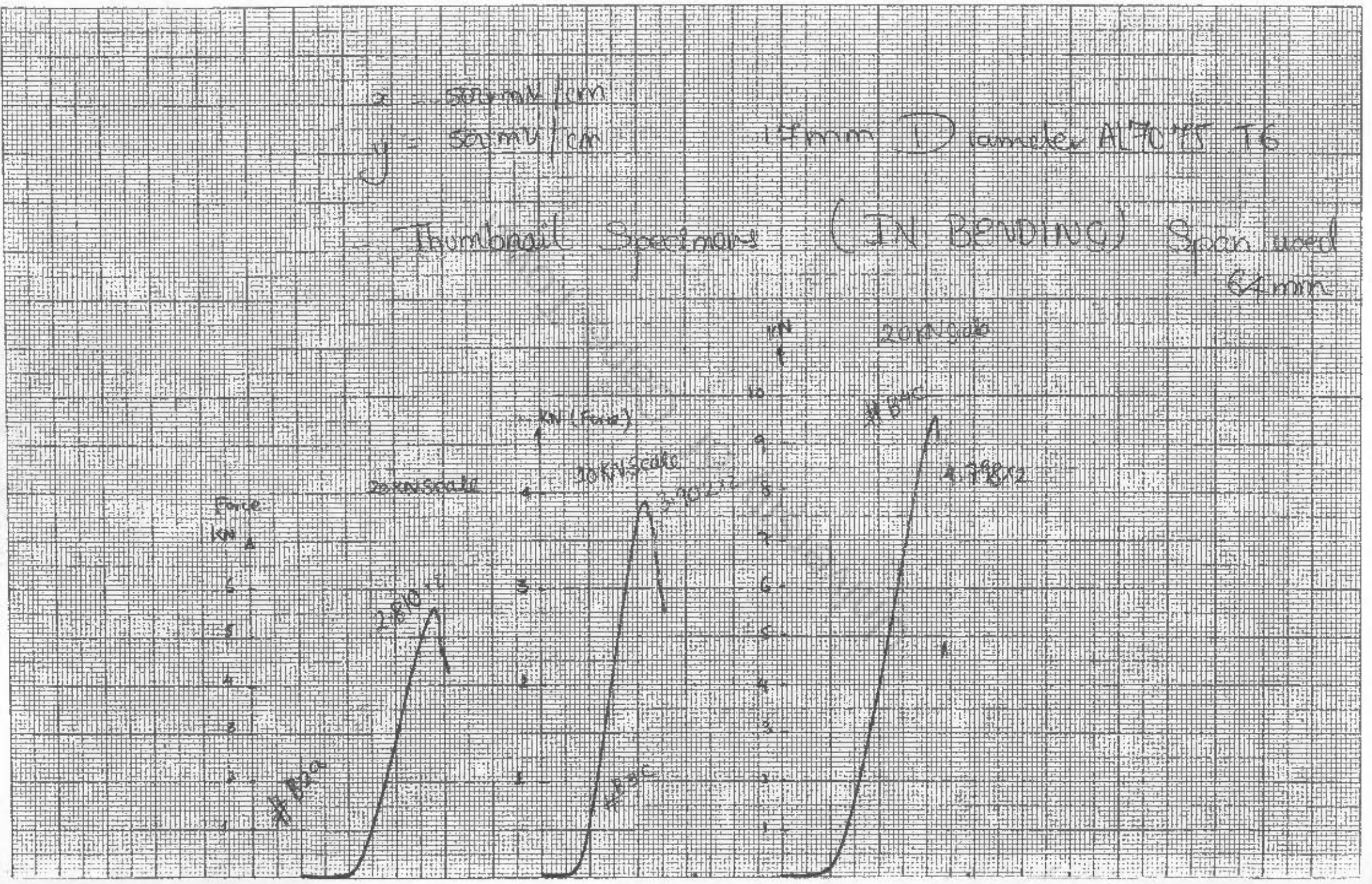
x - 500 mV / cm
y - 500 mV / cm
Thornbrail Specimen-2 (IN BENDING) Span used 64 mm
14 mm Ø Cannula AL 7075 T6
20 kN/cm
20 kN/cm
20 kN/cm
Force kN
kN (Force)
4.78 x 2

x = 500 mV/cm Load versus Displacement

y = 500 mV/cm

x = 500 mV/cm

y = 500 mV/cm

Smoothed 64 mm

THUMBNAIL SPECIMENS FOR ALL TESTS

(Bending)

A 20 KN Scale

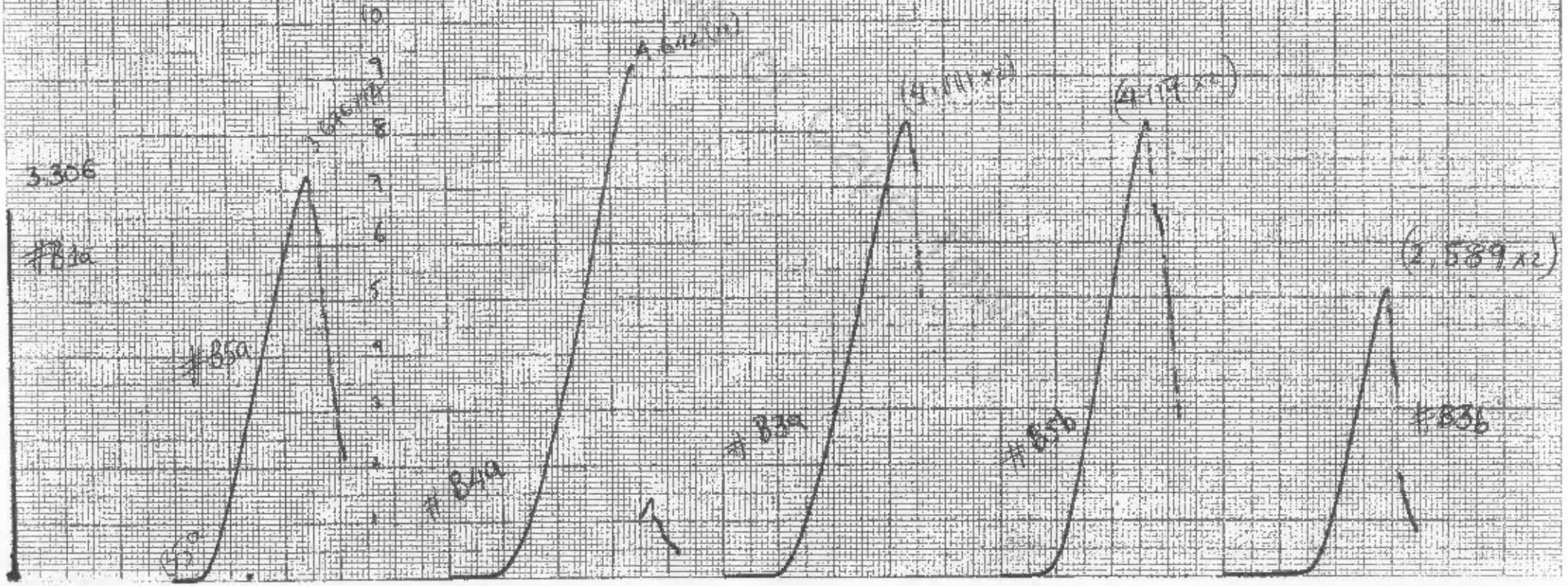

APPENDIX F:

- **Ramping of crescent moon Specimens Al7075 T6 (on the plotter) and Al2030 T3 (on the Zwick machine).**
- **Example of how readings were recorded during fatigue.**

Material Al7075 T6

Crescent moon Specimens (Step 20.3mm) A22 (14mm Diameter)				
Direction	**Cycles N**	**Crack length mm**	**da/dN mm/cycles**	**Comments**
Clockwise	20,100	7.25		Force 250N crack formed
Anti clockwise.	40,200	10.63	1.6×10^{-4}	Carry on! Not deep enough
Clockwise	60,200	17.158	3.26×10^{-4}	Still carry on,. Getting deeper.
Anti clockwise.	70,000	24.09	7×10^{-4}	Crack getting wider. On the way of breaking ($N > 5 \times 10^{-4}$) stop!!!

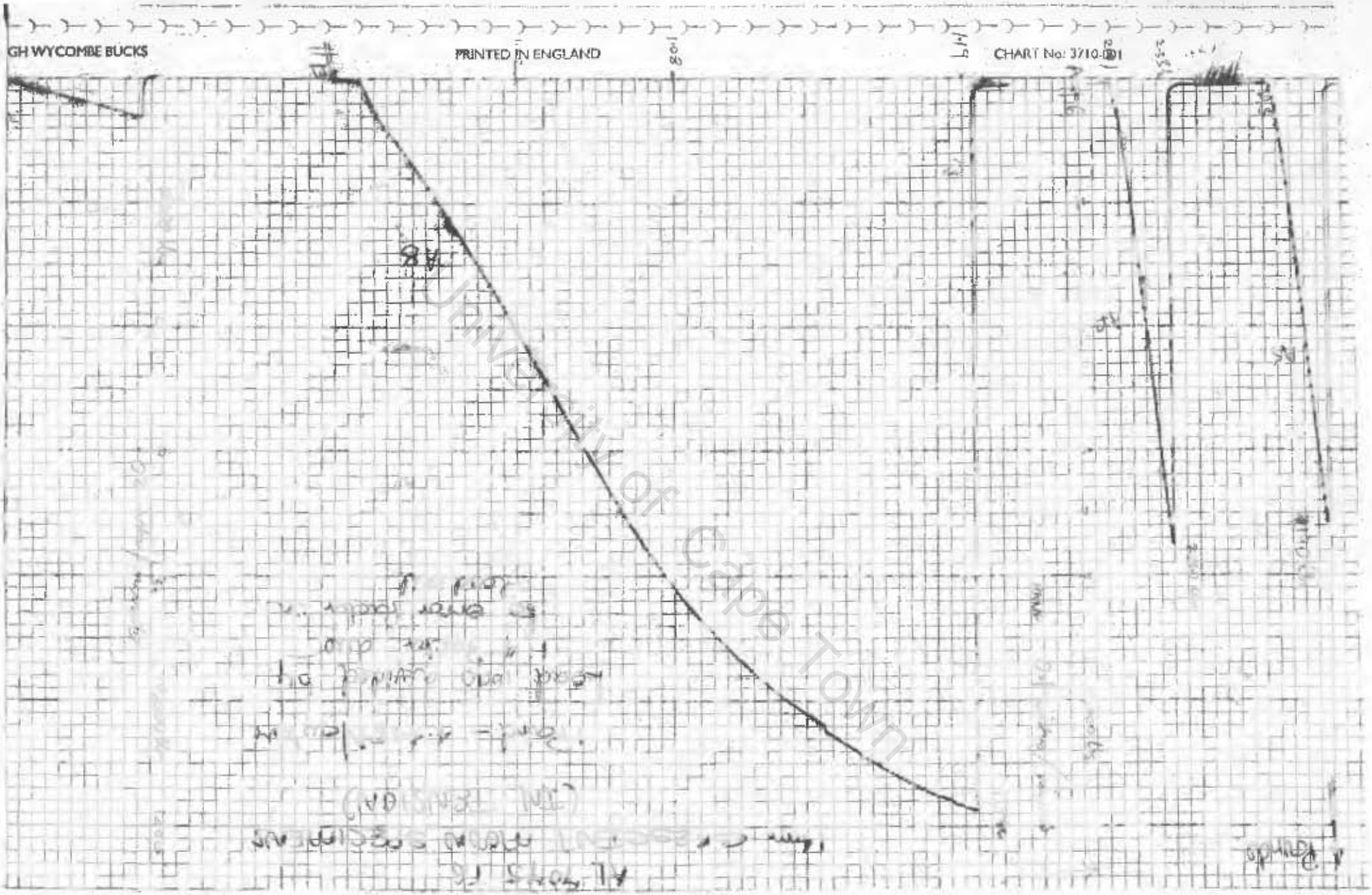

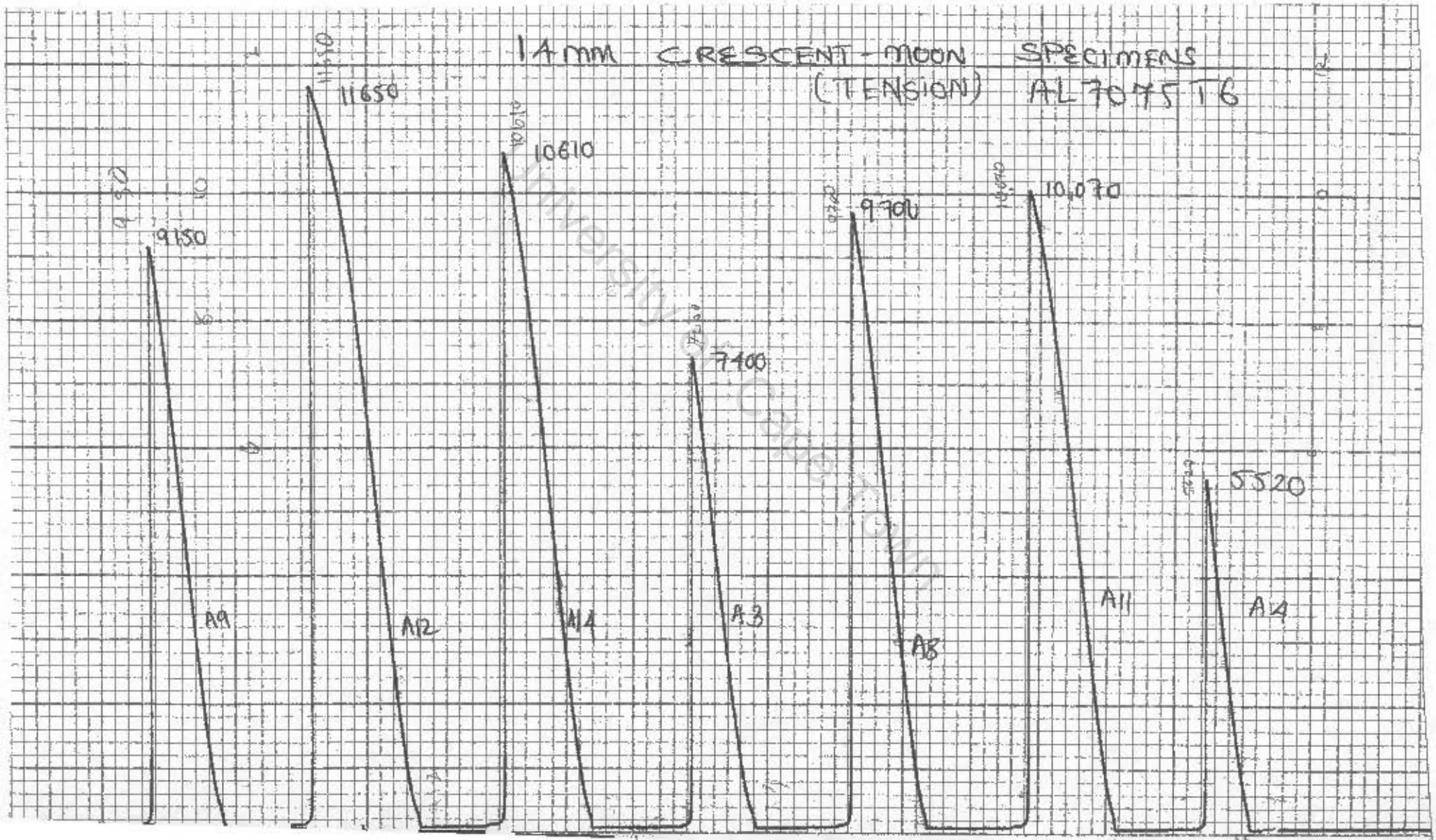
14mm CRESCENT-MOON SPECIMENS
(TENSION) AL 7075 T6
9150
A9
11650
A12
10610
A14
7400
A3
9700
A8
10,070
A11
5520
A4

INSTRON LTD HIGH WYCOMBE BUCKS PRINTED IN ENGLAND

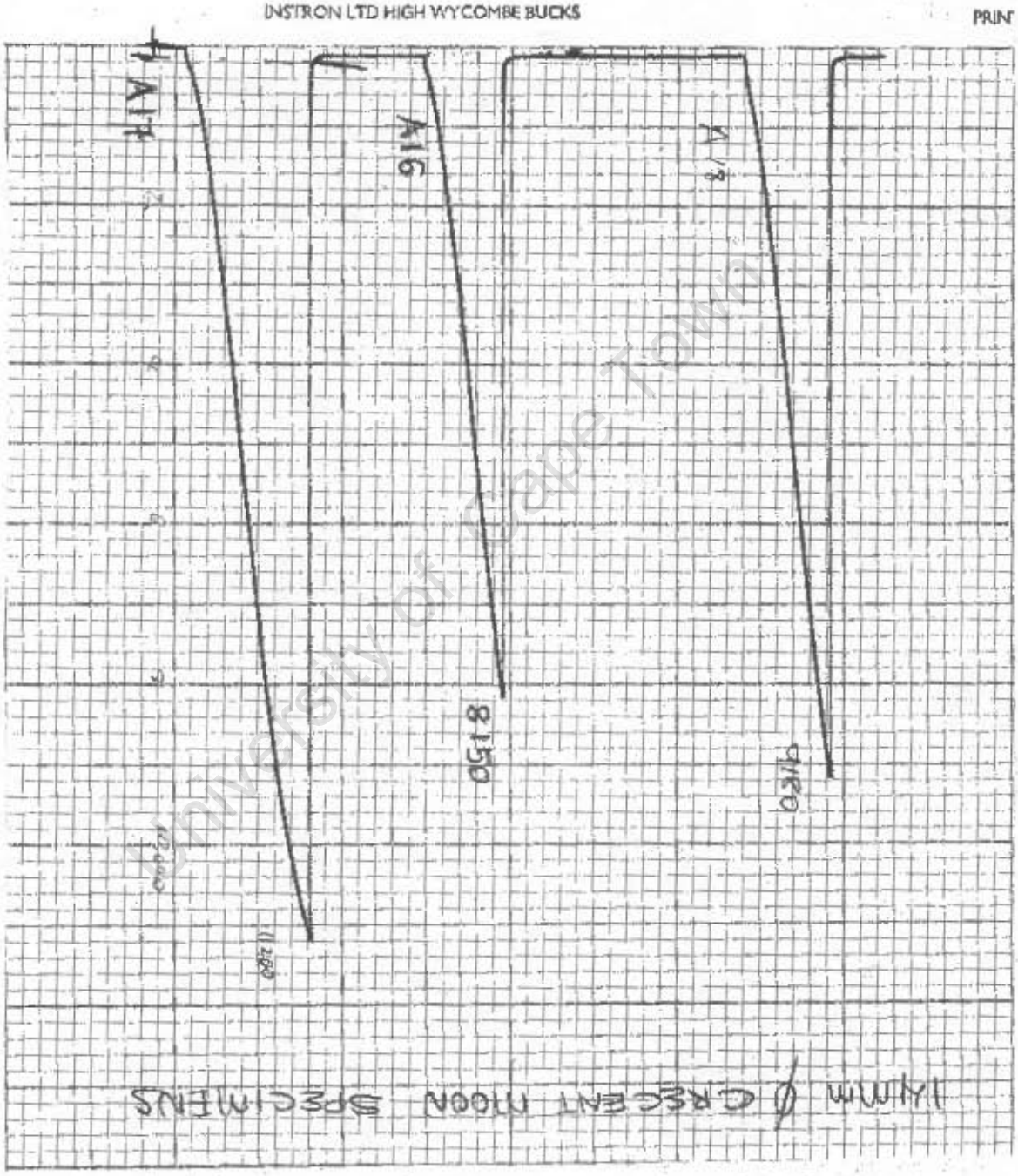
INSTRON LTD HIGH WYCOMBE BUCKS
PRINT
A14
A16
A18
A20
1/4MM @ CRESCENT MOON SPECIMENS

PRINTED IN ENGLAND

CHART No. 37

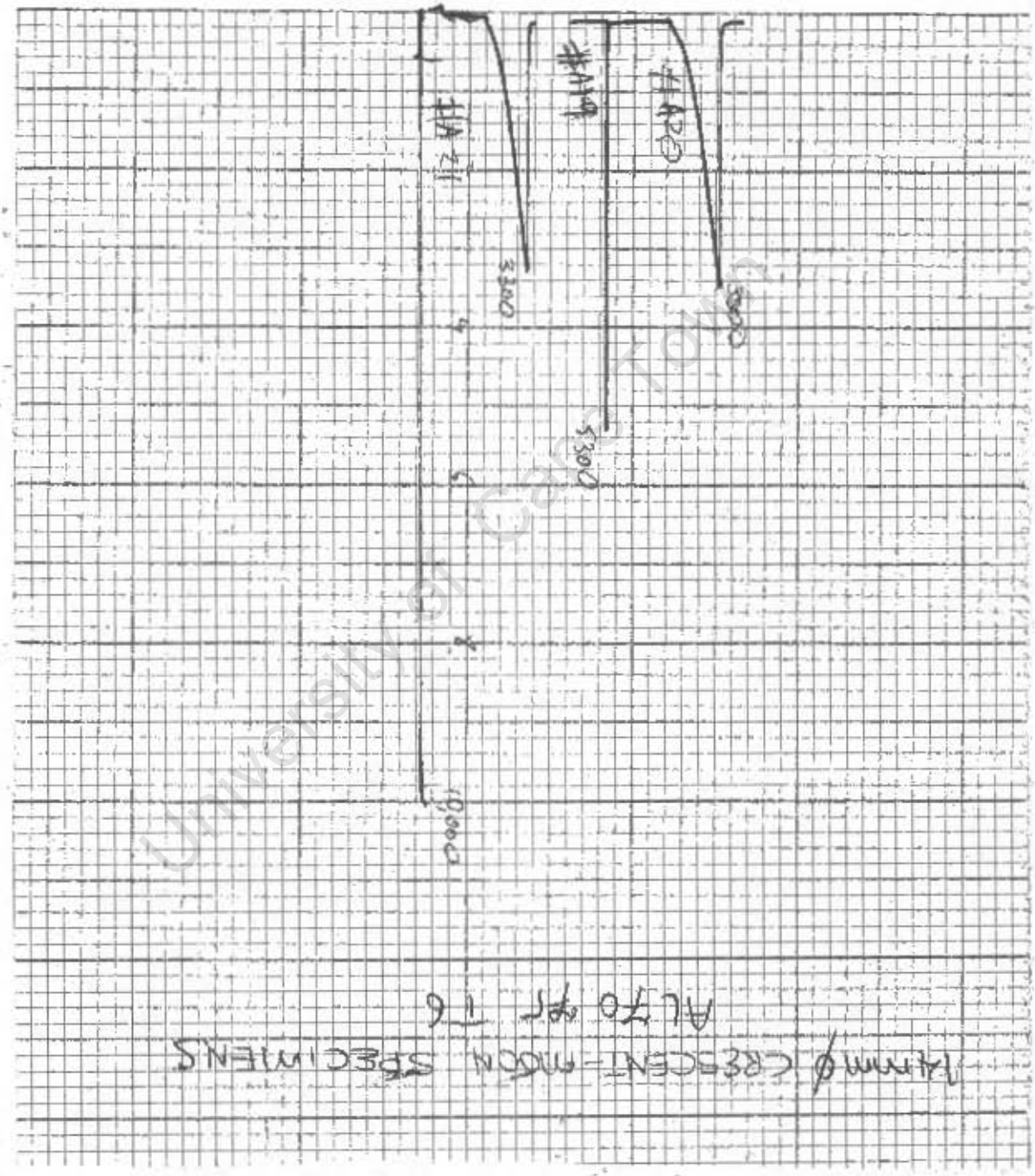

14mm ϕ CRESCENT-MOON SPECIMENS
AL 70 9T T6

Zwick / Roell **Standard test report** **29.04.2005**

Parameter table:

Customer	: Rambocus	Load cell	: 200kN
Tester	: rambo	Extensometer (path)	: Cross Head
Test standard	:	Specimen grips	:
Material	: Al2030T6	Machine data	:
Specimen ID	: 10mm ø		

Results:

Nr	ReH kN	Rm kN
1	-	20.34
2	27.00	27.00
3	-	36.26
4	-	35.45
5	36.33	36.33
6	-	36.33
7	55.45	55.45
8	60.91	60.91
10	40.15	40.15
9	-	53.29
13	-	40.38
↑12	-	0.14

Series graph:

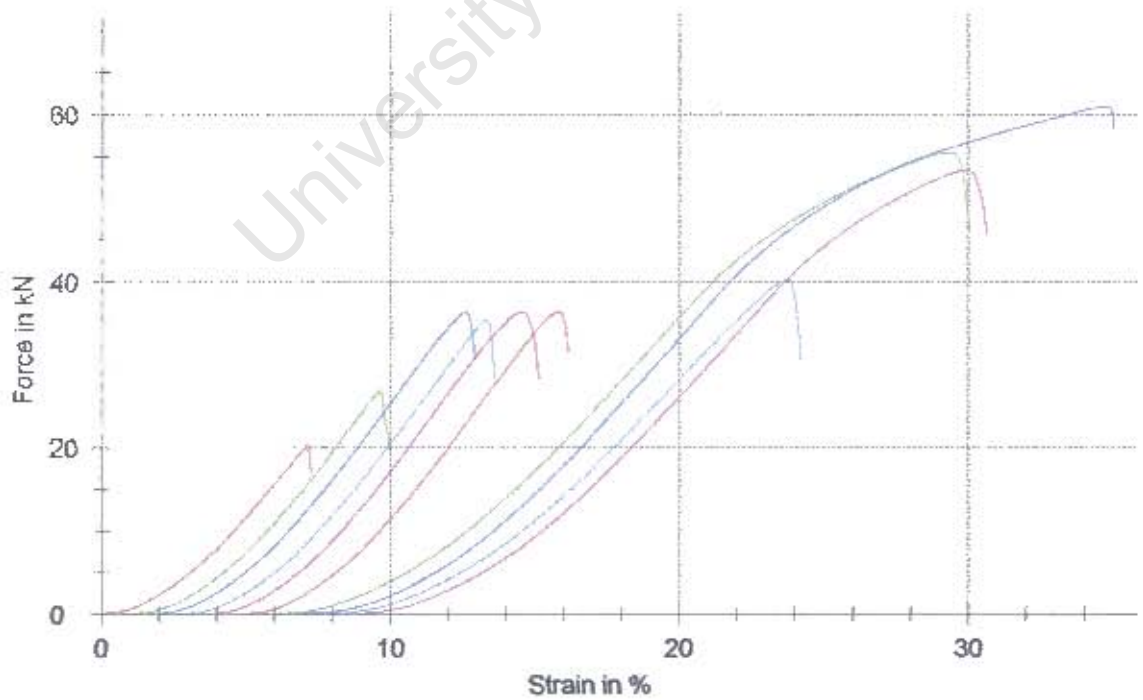

Parameter table:

Customer	: Rambocus	Load cell	: 200kN
Tester	: rambo	Extensometer (path)	: Cross Head
Test standard	:	Specimen grips	:
Material	: Al2030T6	Machine data	:
Specimen ID	: 17mmØ		

Results:

Nr	ReH kN	Rm kN
1	-	16.78
2	38.48	38.48
3	-	36.86
4	51.06	51.06
5	28.81	28.81
6	58.55	58.55
9	-	83.01
19	-	85.91
22	74.92	74.92
23	-	77.51
7	-	85.31

Nr	ReH kN	Rm kN
⌖8	-	-
⌖10	-	-
⌖11	-	-
⌖12	-	-
⌖13	-	-
⌖15	-	-
17	-	0.34
⌖16	-	37.39
18	-	0.30
⌖21	-	-

Series graph:

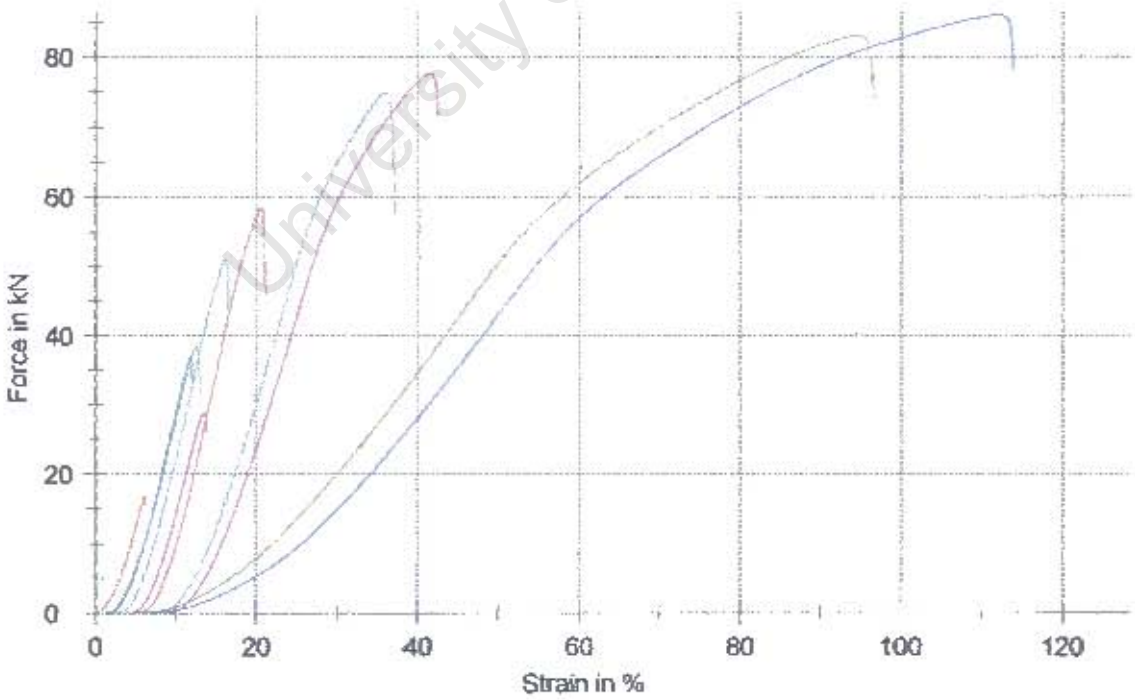

In tension

20mm ϕ Cement Mortar Specimen

Graph of Force (kN) versus Displacement (mm).

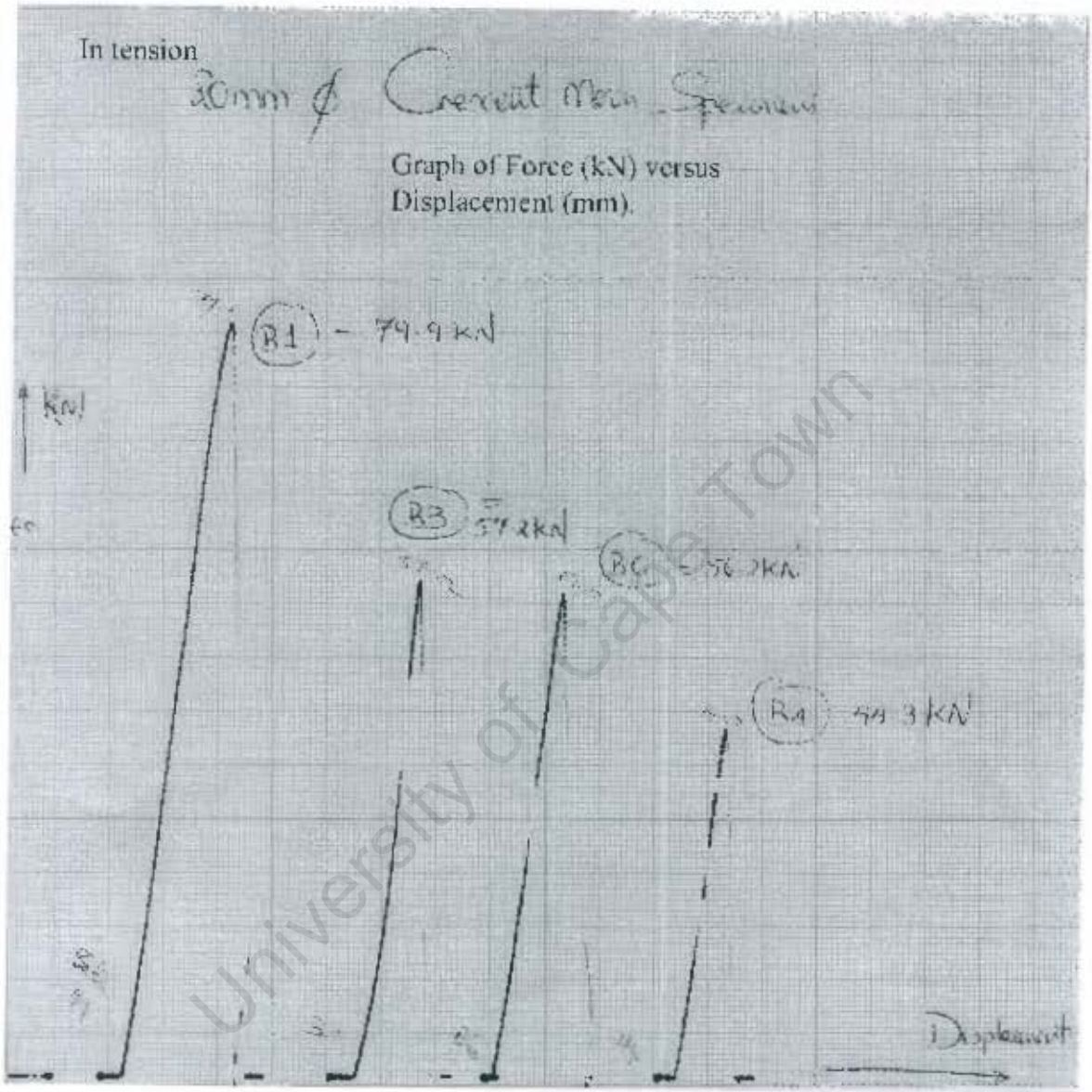

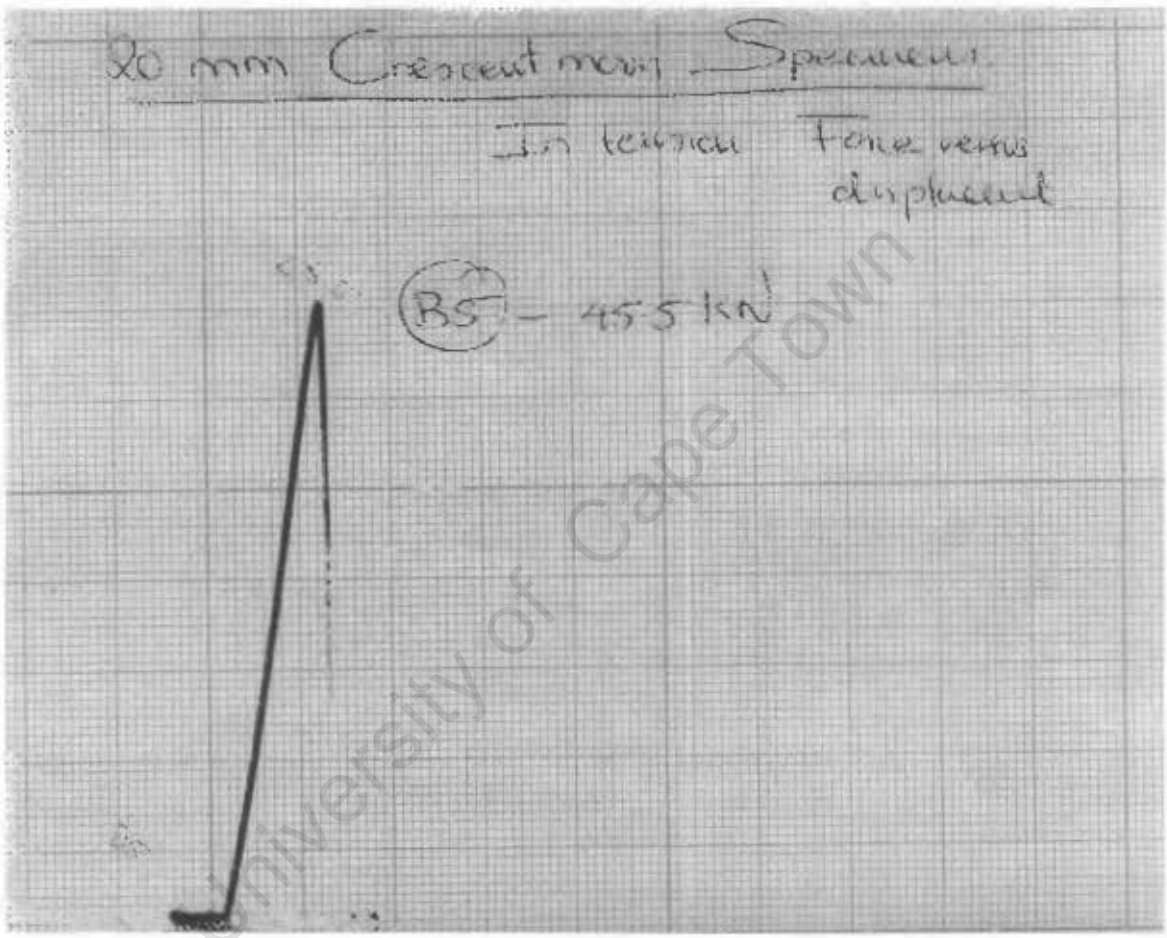

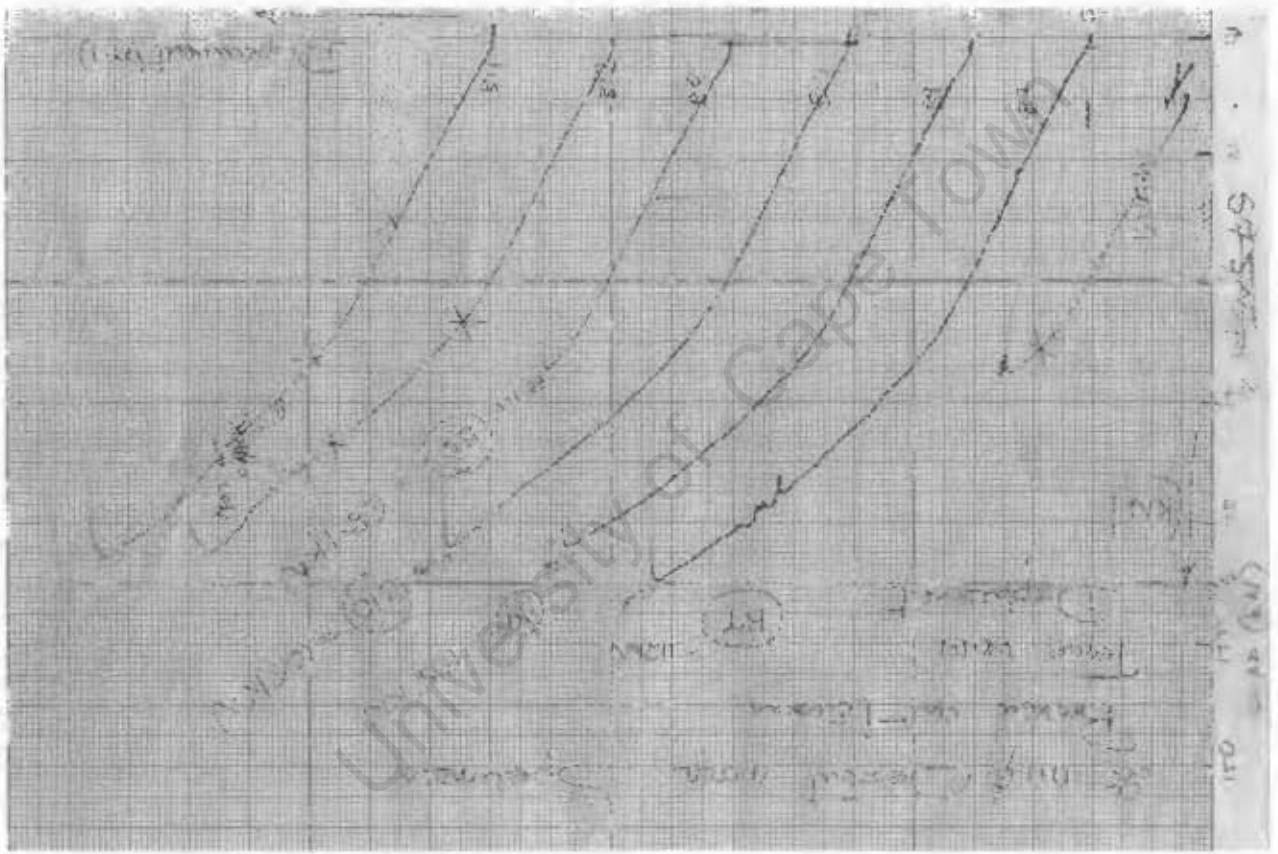

APPENDIX G:

- **Auto Cad Areas and Second moment of Areas for both thumbnail and crescent moon specimens.**

Thumbnail Fast Fractured Regions with New Second Moment Area

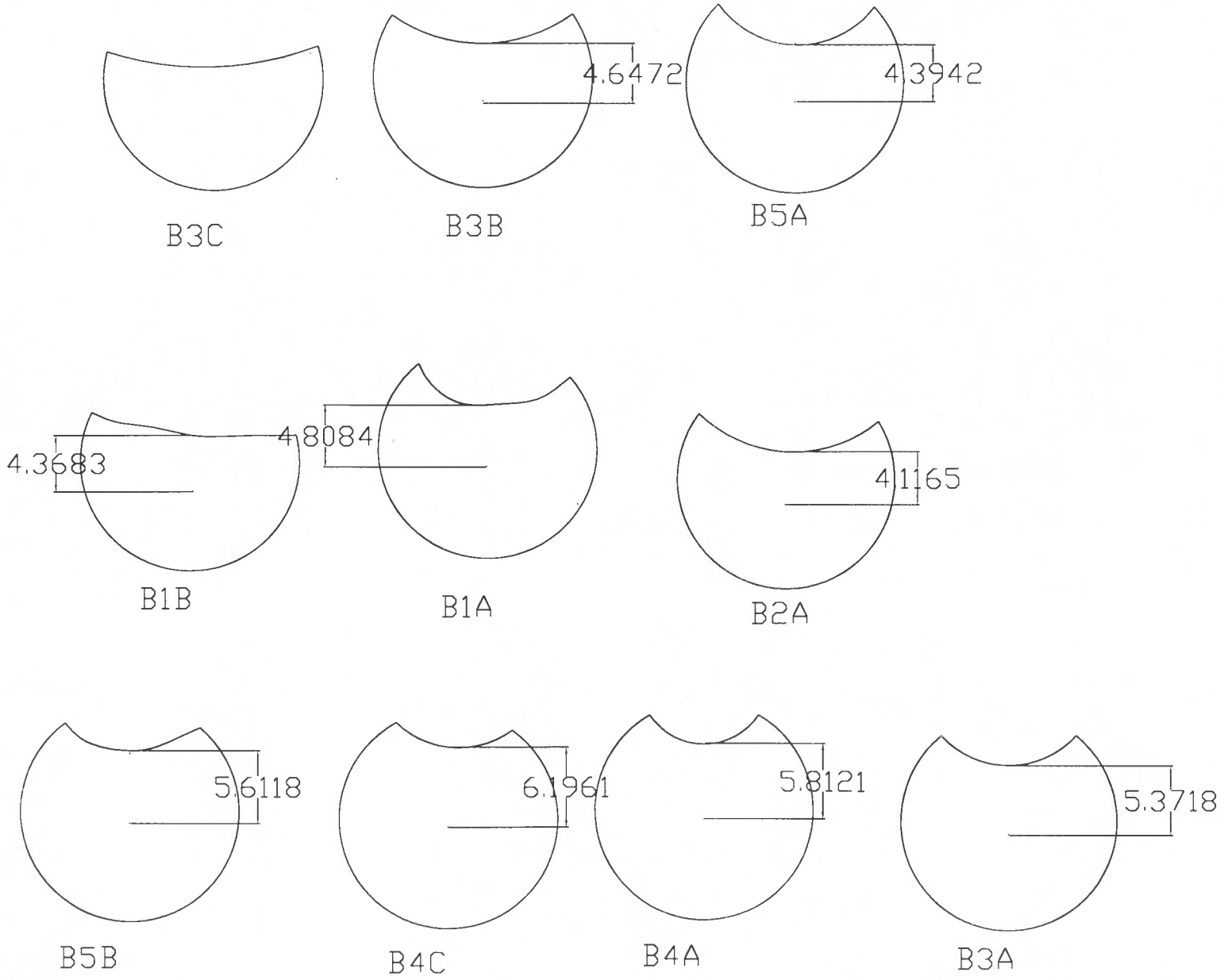

Autocad Results of Thumbnail Specimens

———— REGION B3C ————

Area: 138.0676
Perimeter: 48.1363
Bounding box: X: -80.4315 -- -63.4315
Y: 48.8093 -- 59.8979
Centroid: X: -71.8540
Y: 54.4845
Moments of inertia: X: 410831.7165
Y: 715620.2406
Product of inertia: XY: -540475.0013
Radii of gyration: X: 54.5489
Y: 71.9939
Principal moments and X-Y directions about centroid:
I: 968.9803 along [0.9996 0.0274]
J: 2778.6117 along [-0.0274 0.9996]

———— REGION B3B————

Area: 169.6958
Perimeter: 51.9028
Bounding box: X: -56.1462 -- -39.1462
Y: 49.0135 -- 62.3860
Centroid: X: -47.6356
Y: 55.6775
Moments of inertia: X: 527769.8494
Y: 388576.4372
Product of inertia: XY: -450061.8598
Radii of gyration: X: 55.7682
Y: 47.8523
Principal moments and X-Y directions about centroid:
I: 1715.2102 along [1.0000 0.0058]
J: 3511.7470 along [-0.0058 1.0000]

———— REGION B5A————

Area: 179.3954
Perimeter: 53.9402
Bounding box: X: -25.3074 -- -8.3074
Y: 48.6267 -- 63.1697
Centroid: X: -16.8371
Y: 55.6087
Moments of inertia: X: 556788.2635
Y: 54583.9912
Product of inertia: XY: -167998.7418
Radii of gyration: X: 55.7108
Y: 17.4432
Principal moments and X-Y directions about centroid:
I: 2039.0247 along [0.9998 -0.0196]
J: 3728.2997 along [0.0196 0.9998]

---------- REGION B1B----------

Area: 153.6440
Perimeter: 48.8078
Bounding box: X: -78.9129 -- -61.9129
Y: 19.3416 -- 31.6407
Centroid: X: -70.6433
Y: 25.5022
Moments of inertia: X: 101220.5745
Y: 769806.8259
Product of inertia: XY: -276973.2217
Radii of gyration: X: 25.6671
Y: 70.7837
Principal moments and X-Y directions about centroid:
I: 1279.2245 along [0.9952 -0.0981]
J: 3067.4141 along [0.0981 0.9952]

---------- REGION B1A----------

Area: 183.6669
Perimeter: 54.0915
Bounding box: X: -49.2293 -- -32.2293
Y: 20.3102 -- 35.4369
Centroid: X: -40.8186
Y: 27.4196
Moments of inertia: X: 140257.3749
Y: 309783.1127
Product of inertia: XY: -205672.6600
Radii of gyration: X: 27.6342
Y: 41.0689

Principal moments and X-Y directions about centroid:
I: 2162.6703 along [0.9978 -0.0666]
J: 3772.1974 along [0.0666 0.9978]

---------- REGION B2A----------

Area: 164.8258
Perimeter: 52.2495
Bounding box: X: -26.0044 -- -9.0044
Y: 26.0134 -- 39.6101
Centroid: X: -17.5897
Y: 32.5392
Moments of inertia: X: 176121.6939
Y: 54449.1519
Product of inertia: XY: -94418.8128
Radii of gyration: X: 32.6884
Y: 18.1754
Principal moments and X-Y directions about centroid:
I: 1601.0648 along [0.9991 -0.0432]
J: 3455.8056 along [0.0432 0.9991]

---------- REGION B5B----------

Area: 200.0768
Perimeter: 53.5828
Bounding box: X: -80.2804 -- -63.2804
Y: -2.5795 -- 12.7949
Centroid: X: -71.7872
Y: 5.0293
Moments of inertia: X: 7797.2295
Y: 1035024.8006
Product of inertia: XY: -72245.3281
Radii of gyration: X: 6.2427
Y: 71.9245
Principal moments and X-Y directions about centroid:
I: 2736.5244 along [1.0000 -0.0086]
J: 3949.1185 along [0.0086 1.0000]

---------- REGION B4C----------

Area: 208.8484
Perimeter: 53.6807
Bounding box: X: -52.2927 -- -35.2927
Y: -8.3558 -- 7.6131
Centroid: X: -43.8318
Y: -0.4673
Moments of inertia: X: 3158.4943
Y: 405265.7616
Product of inertia: XY: 4219.3209
Radii of gyration: X: 3.8889
Y: 44.0509
Principal moments and X-Y directions about centroid:
I: 3109.1516 along [0.9980 -0.0639]
J: 4023.6247 along [0.0639 0.9980]

---------- REGION B4A----------

Area: 207.0271
Perimeter: 54.5407
Bounding box: X: -32.4097 -- -15.4097
Y: -7.6473 -- 8.2226
Centroid: X: -23.9097
Y: 0.1885
Moments of inertia: X: 3054.3058
Y: 122376.7965
Product of inertia: XY: -932.8547
Radii of gyration: X: 3.8410
Y: 24.3129
Principal moments and X-Y directions about centroid:
I: 3046.9530 along [1.0000 0.0000]
J: 4024.6113 along [0.0000 1.0000]

---------- REGION B3A----------

Area: 196.4265
Perimeter: 53.8361
Bounding box: X: -8.5000 -- 8.5000
Y: -8.5000 -- 6.6323
Centroid: X: 0.0007
Y: -1.0026
Moments of inertia: X: 2799.2771
Y: 3920.4111
Product of inertia: XY: 0.7450
Radii of gyration: X: 3.7751

Y: 4.4675
Principal moments and X-Y directions about centroid:
I: 2601.8190 along [1.0000 0.0007]
J: 3920.4116 along [-0.0007 1.0000]

FAST FRACTURE REGION (for Crescent moon shapes) for Al7075 T6

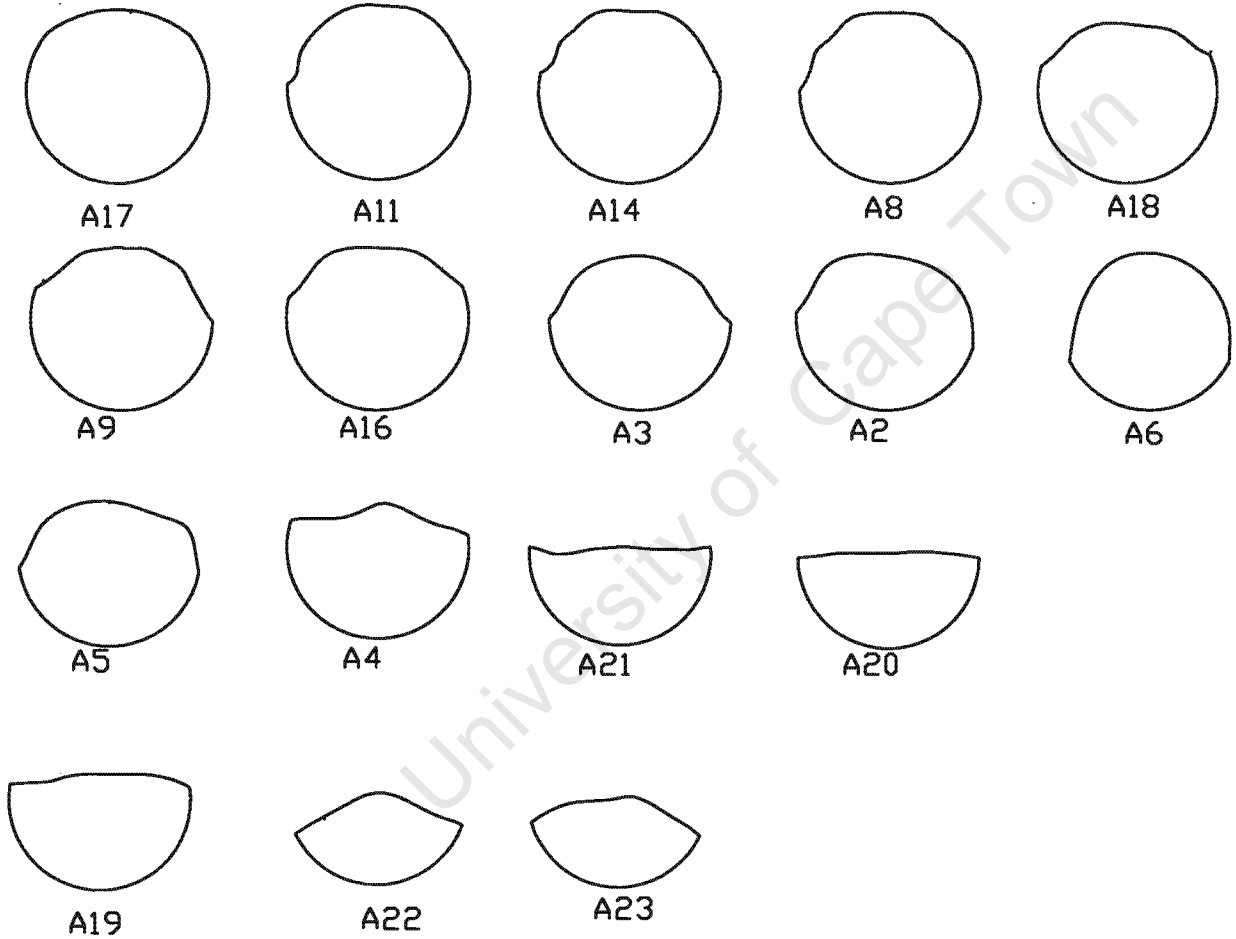

Area for the fast fracture surfaces for creeped mosaic specimens.

Selected object: A17	
Area:	147.8979 mm^2
Selected object: A11	
Area:	144.0131 mm^2
Selected object: A14	
Area:	143.6610 mm^2
Selected object: A8	
Area:	140.7748 mm^2
Selected object: A10	
Area:	134.8335 mm^2
Selected object: A9	
Area:	134.6134 mm^2
Selected object: A16	
Area:	138.6583 mm^2
Selected object: A3	
Area:	124.1393 mm^2
Selected object: A2	
Area:	126.5231 mm^2
Selected object: A6	
Area:	118.0415 mm^2
Selected object: A5	
Area:	117.6835 mm^2
Selected object: A4	
Area:	109.3982 mm^2
Selected object: A21	
Area:	81.5653 mm^2
Selected object: A20	
Area:	98.8965 mm^2
Selected object: A19	
Area:	109.1458 mm^2
Selected object : A23	
Area:	59.3 mm^2
Selected object : A22	
Area:	69.0 mm^2

Thumbnail Fast Fractured Regions with New Second Moment Area

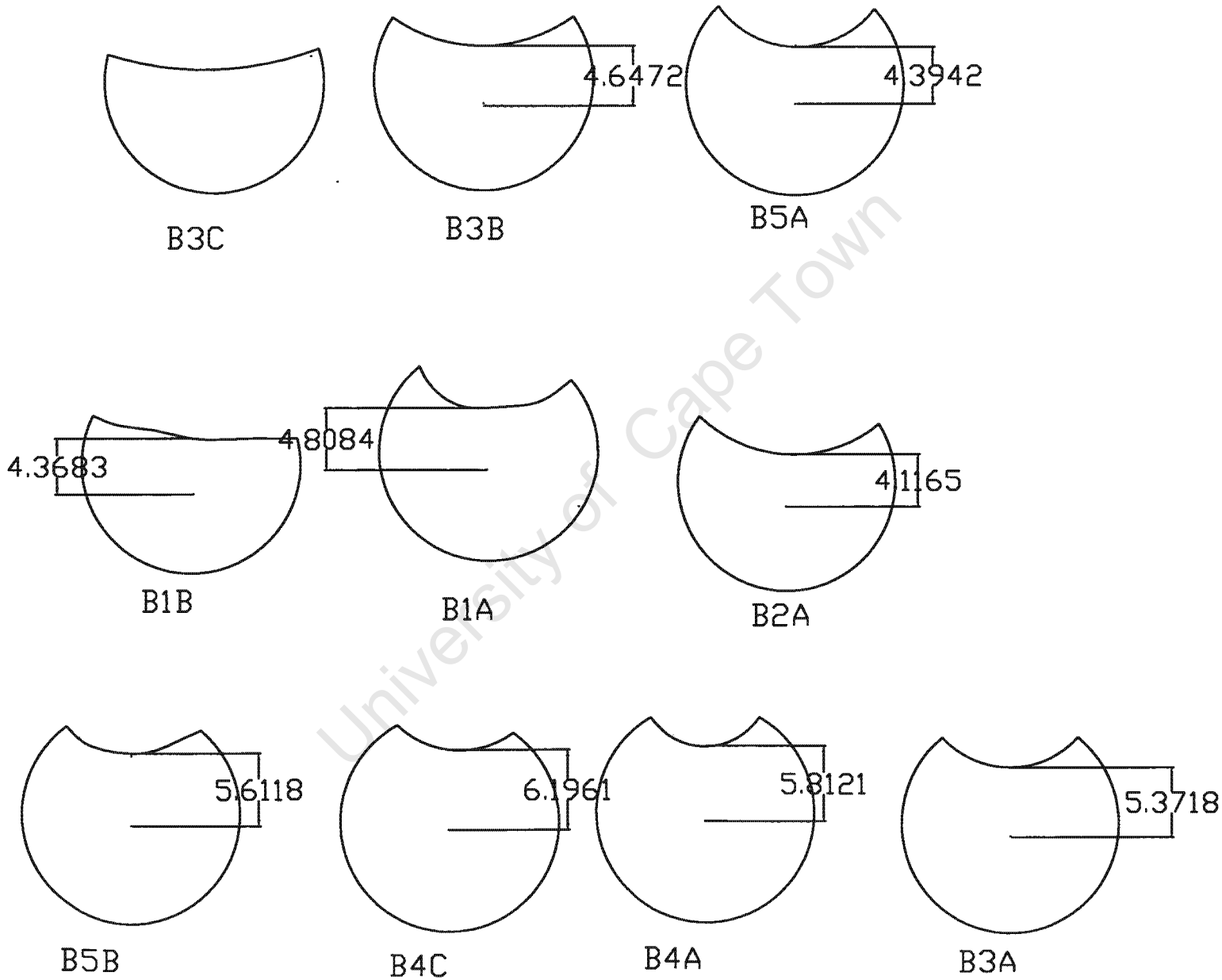

FAST FRACTURE REGION OF BROKEN SPECIMENS

20mm Diameter specimens

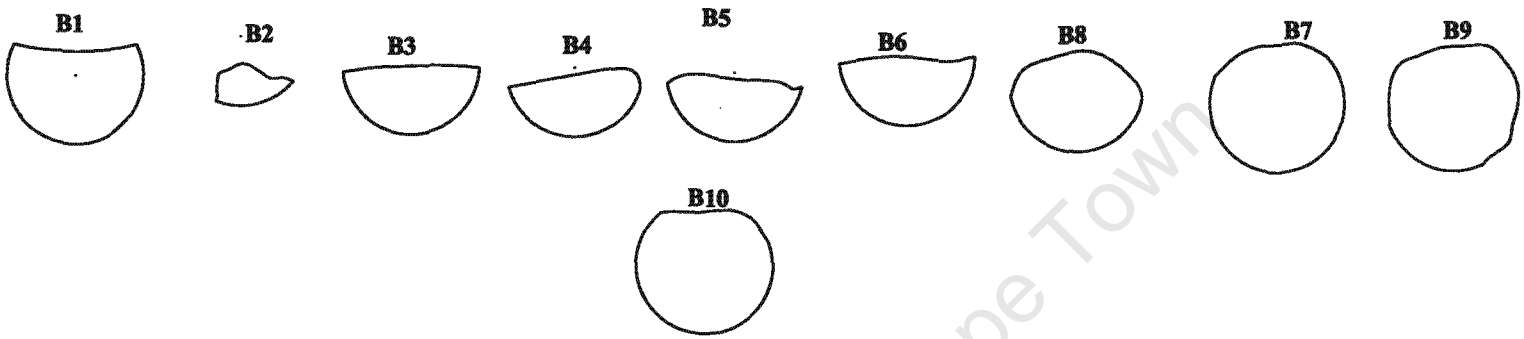

17mm Diameter specimens

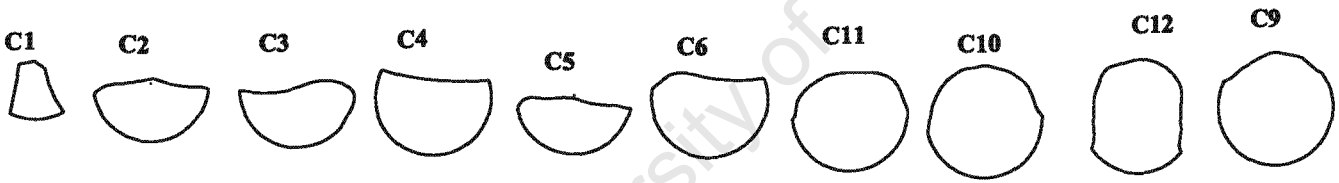

14mm Diameter specimens

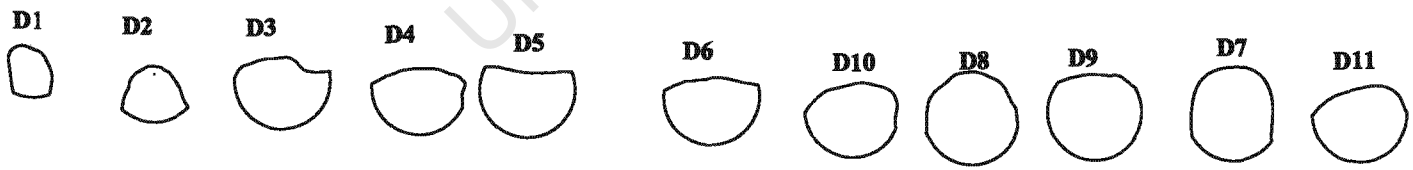

Some of the Physical Properties obtained from Auto-Cad of the Fast Fracture Region of each Crescent Moon Specimen.

For the 20mm Diameter Specimens

---------- **REGION B1** ----------

Area: **230.3527 mm^2**
Perimeter: 58.6569
Bounding box: X: 94.5566 -- 114.5566
Y: 277.5232 -- 292.0050
Centroid: X: 104.5409
Y: 285.2220
Moments of inertia: X: 18742612.2359
Y: 2523866.6912
Product of inertia: XY: 6868487.1595
Radii of gyration: X: 285.2452
Y: 104.6735
Principal moments and X-Y directions about centroid:
I: 3050.2105 along [1.0000 -0.0069]
J: 6389.0298 along [0.0069 1.0000]

---------- **REGION B2** ----------

Area: **45.0102 mm^2**
Perimeter: 28.3463
Bounding box: X: 125.1177 -- 136.3778
Y: 282.9641 -- 289.1994
Centroid: X: 129.7790
Y: 285.7621
Moments of inertia: X: 3675628.2613
Y: 758406.5111
Product of inertia: XY: 1669248.5906
Radii of gyration: X: 285.7657
Y: 129.8062
Principal moments and X-Y directions about centroid:
I: 92.2311 along [0.9999 0.0118]
J: 317.9353 along [-0.0118 0.9999]

---------- **REGION B3** ----------

Area: **152.0520 mm^2**
Perimeter: 50.0371
Bounding box: X: 143.5841 -- 163.5258
Y: 278.8385 -- 288.8255
Centroid: X: 153.6648
Y: 284.4625
Moments of inertia: X: 12304894.5777
Y: 3594031.3846
Product of inertia: XY: 6646557.6962
Radii of gyration: X: 284.4742
Y: 153.7428
Principal moments and X-Y directions about centroid:
I: 1012.3194 along [0.9995 0.0301]
J: 3647.9397 along [-0.0301 0.9995]

---------- **REGION B4** ----------

Area: **133.3993 mm^2**
Perimeter: 47.0223
Bounding box: X: 167.7916 -- 186.9957
Y: 278.4081 -- 289.1007
Centroid: X: 178.0214
Y: 283.5691
Moments of inertia: X: 10727600.5680
Y: 4230573.6218
Product of inertia: XY: 6734466.6422
Radii of gyration: X: 283.5793
Y: 178.0832
Principal moments and X-Y directions about centroid:
I: 736.7386 along [0.9915 0.1304]
J: 2972.5825 along [-0.1304 0.9915]

---------- **REGION B5** ----------

Area: **136.3068 mm^2**
Perimeter: 48.0481
Bounding box: X: 190.8852 -- 210.5330
Y: 277.7792 -- 287.6338
Centroid: X: 200.3545
Y: 282.9936
Moments of inertia: X: 10916973.9373
Y: 5474670.9552
Product of inertia: XY: 7728272.3183

Radii of gyration: X: 283.0039
Y: 200.4104
Principal moments and X-Y directions about centroid:
I: 772.8145 along [0.9964 -0.0849]
J: 3069.1289 along [0.0849 0.9964]

---------- **REGION B6** ----------

Area: **150.8121 mm^2**
Perimeter: 50.6882
Bounding box: X: 216.0167 -- 235.9783
Y: 280.0069 -- 290.6976
Centroid: X: 225.9962
Y: 285.5975
Moments of inertia: X: 12302127.5671
Y: 7706244.9001
Product of inertia: XY: 9734019.6926
Radii of gyration: X: 285.6091
Y: 226.0494
Principal moments and X-Y directions about centroid:
I: 994.1124 along [1.0000 0.0036]
J: 3625.1977 along [-0.0036 1.0000]

---------- **REGION B8** ----------

Area: **211.5585 mm^2**
Perimeter: 52.5852
Bounding box: X: 241.2224 -- 260.9917
Y: 276.2831 -- 291.8554
Centroid: X: 250.9168
Y: 283.6362
Moments of inertia: X: 17022487.4896
Y: 13324262.7830
Product of inertia: XY: 15056353.4757
Radii of gyration: X: 283.6588
Y: 250.9611
Principal moments and X-Y directions about centroid:
I: 2711.4756 along [0.9993 -0.0374]
J: 4698.1550 along [0.0374 0.9993]

---------- **REGION B7** ----------

Area: **296.8401 mm^2**
Perimeter: 61.3371
Bounding box: X: 270.6807 -- 290.6807
Y: 273.2649 -- 292.1731
Centroid: X: 280.7760
Y: 282.7754
Moments of inertia: X: 23742447.7504
Y: 23408978.9404
Product of inertia: XY: 23568279.0956
Radii of gyration: X: 282.8144
Y: 280.8212
Principal moments and X-Y directions about centroid:
I: 6501.2357 along [0.9817 0.1905]
J: 7586.3663 along [-0.1905 0.9817]

---------- **REGION B9** ----------

Area: **283.0698 mm^2**
Perimeter: 60.4933
Bounding box: X: 297.0703 -- 316.5808
Y: 273.4148 -- 292.1418
Centroid: X: 306.8115
Y: 282.7901
Moments of inertia: X: 22643202.2868
Y: 26653110.8825
Product of inertia: XY: 24560349.5883
Radii of gyration: X: 282.8278
Y: 306.8507
Principal moments and X-Y directions about centroid:
I: 5945.1432 along [0.9489 0.3157]
J: 6902.7442 along [-0.3157 0.9489]

---------- **REGION B10** ----------

Area: **294.2996 mm^2**
Perimeter: 61.5512
Bounding box: X: 186.3286 -- 206.3286
Y: 249.7620 -- 268.3716
Centroid: X: 196.2979
Y: 259.1891
Moments of inertia: X: 19777054.0899

Y: 11347819.2270
Product of inertia: XY: 14973402.3040
Radii of gyration: X: 259.2304
Y: 196.3638
Principal moments and X-Y directions about centroid:
I: 6304.5640 along [0.9992 -0.0397]
J: 7615.9382 along [0.0397 0.9992]

For the 17mm Diameter Specimens

SPECIMEN C1

Area: **43.7606 mm^2**
Perimeter: 26.7318
Bounding box: X: 142.1325 -- 150.0052
Y: 216.2135 -- 224.7135
Centroid: X: 145.6487
Y: 219.9050
Moments of inertia: X: 2116405.8763
Y: 928442.4045
Product of inertia: XY: 1401579.8867
Radii of gyration: X: 219.9166
Y: 145.6586
Principal moments and X-Y directions about centroid:
I: 120.2066 along [0.2145 -0.9767]
J: 227.6860 along [0.9767 0.2145]

SPECIMEN C2

Area: **111.0431 mm^2**

Perimeter: 41.7750
Bounding box: X: 154.5224 -- 171.3196
Y: 212.8702 -- 222.1205
Centroid: X: 162.8544
Y: 217.7030
Moments of inertia: X: 5263402.9773
Y: 2946863.0051
Product of inertia: XY: 3936904.9195
Radii of gyration: X: 217.7145
Y: 162.9049
Principal moments and X-Y directions about centroid:
I: 555.8520 along [1.0000 -0.0049]
J: 1827.8591 along [0.0049 1.0000]

SPECIMEN C3

Area: **116.5134 mm^2**

Perimeter: 43.3330
Bounding box: X: 175.8254 -- 194.1895
Y: 211.9769 -- 222.3718
Centroid: X: 184.5917
Y: 217.0257
Moments of inertia: X: 5488453.6234
Y: 3972105.0097
Product of inertia: XY: 4667803.9544
Radii of gyration: X: 217.0386
Y: 184.6386
Principal moments and X-Y directions about centroid:
I: 638.1513 along [0.9947 0.1028]
J: 2029.2200 along [-0.1028 0.9947]

SPECIMEN C4

Area: **159.7940 mm^2**

Perimeter: 49.3808
Bounding box: X: 195.6377 -- 212.6377
Y: 210.7778 -- 223.4029
Centroid: X: 203.9365
Y: 217.1268
Moments of inertia: X: 7534773.0915
Y: 6649040.6342
Product of inertia: XY: 7075525.7528
Radii of gyration: X: 217.1475
Y: 203.9855
Principal moments and X-Y directions about centroid:
I: 1424.2234 along [0.9956 -0.0933]
J: 3205.7500 along [0.0933 0.9956]

SPECIMEN C5

Area: **99.6711 mm^2**

Perimeter: 40.4878
Bounding box: X: 216.4590 -- 233.0077
Y: 210.9887 -- 219.6946
Centroid: X: 224.4020
Y: 215.4593
Moments of inertia: X: 4627430.6958

Y: 5020677.0569
Product of inertia: XY: 4818958.0231
Radii of gyration: X: 215.4692
Y: 224.4380
Principal moments and X-Y directions about centroid:
I: 417.3354 along [0.9969 -0.0782]
J: 1616.4826 along [0.0782 0.9969]

SPECIMEN C6

Area: 165.1382 mm^2

Perimeter: 48.5729
Bounding box: X: 236.0186 -- 253.0186
Y: 210.5100 -- 223.5680
Centroid: X: 244.4459
Y: 217.0227
Moments of inertia: X: 7779390.4106
Y: 9870811.1819
Product of inertia: XY: 8760562.0095
Radii of gyration: X: 217.0446
Y: 244.4853
Principal moments and X-Y directions about centroid:
I: 1569.9384 along [0.9991 -0.0419]
J: 3183.7128 along [0.0419 0.9991]

---------- **REGION C11** ----------

Area: 193.6853 mm^2
Perimeter: 49.8278
Bounding box: X: 213.7460 -- 230.6819
Y: 209.2271 -- 223.7374
Centroid: X: 222.3296
Y: 216.7025
Moments of inertia: X: 9098069.0568
Y: 9577395.9607
Product of inertia: XY: 9331772.1686
Radii of gyration: X: 216.7336
Y: 222.3696
Principal moments and X-Y directions about centroid:
I: 2589.0947 along [0.9884 0.1516]
J: 3459.5602 along [-0.1516 0.9884]

---------- **REGION C 10** ----------

Area: **211.3300mm^2**
Perimeter: 51.8274
Bounding box: X: 233.6789 -- 250.4630
Y: 208.2390 -- 224.8522
Centroid: X: 241.9992
Y: 216.3498
Moments of inertia: X: 9895305.8408
Y: 12379837.2761
Product of inertia: XY: 11064504.4452
Radii of gyration: X: 216.3884
Y: 242.0343
Principal moments and X-Y directions about centroid:
I: 3527.2865 along [0.9951 0.0989]
J: 3586.6225 along [-0.0989 0.9951]

---------- **REGION C12** ----------

Area: **188.0274mm^2**
Perimeter: 50.1972
Bounding box: X: 257.8167 -- 271.3904
Y: 208.9741 -- 225.8635
Centroid: X: 264.6199
Y: 217.1744
Moments of inertia: X: 8871758.8310
Y: 13168675.1959
Product of inertia: XY: 10805726.0388
Radii of gyration: X: 217.2172
Y: 264.6430
Principal moments and X-Y directions about centroid:
I: 2298.5339 along [0.0337 0.9994]
J: 3500.0566 along [-0.9994 0.0337]

---------- **REGION C9** ----------

Area: **215.8902mm^2**
Perimeter: 52.5117
Bounding box: X: 276.5746 -- 293.5746
Y: 210.1061 -- 226.7741
Centroid: X: 285.1666
Y: 218.2568
Moments of inertia: X: 10287695.2472
Y: 17560076.1940
Product of inertia: XY: 13437023.6050

Radii of gyration: X: 218.2944
Y: 285.1982
Principal moments and X-Y directions about centroid:
I: 3508.4229 along [0.9557 0.2943]
J: 3931.4797 along [-0.2943 0.9557]

For the 14mm Diameter Specimens

SPECIMEN D1
Area: 39.2789 mm^2

Perimeter: 23.2246
Bounding box: X: 140.5062 -- 147.0311
Y: 195.7199 -- 203.6903
Centroid: X: 143.6571
Y: 199.3375
Moments of inertia: X: 1560917.4579
Y: 810718.4767
Product of inertia: XY: 1124770.9474
Radii of gyration: X: 199.3473
Y: 143.6665
Principal moments and X-Y directions about centroid:
I: 92.6012 along [0.4265 -0.9045]
J: 167.1688 along [0.9045 0.4265]

SPECIMEN D2
Area: 56.5719 mm^2

Perimeter: 27.9124
Bounding box: X: 157.2796 -- 166.9942
Y: 192.0732 -- 200.3828
Centroid: X: 161.9276
Y: 195.8575
Moments of inertia: X: 2170348.0975
Y: 1483628.0063
Product of inertia: XY: 1794156.3952
Radii of gyration: X: 195.8684
Y: 161.9430
Principal moments and X-Y directions about centroid:
I: 239.6097 along [0.9894 -0.1454]
J: 283.2419 along [0.1454 0.9894]

SPECIMEN D3
Area: 109.7364 mm^2

Perimeter: 39.5629
Bounding box: X: 173.7703 -- 187.7703
Y: 191.0574 -- 201.5820
Centroid: X: 180.5727
Y: 196.3741
Moments of inertia: X: 4232456.9443
Y: 3579453.7855
Product of inertia: XY: 3891148.6538
Radii of gyration: X: 196.3907
Y: 180.6064
Principal moments and X-Y directions about centroid:
I: 706.5747 along [0.9918 -0.1278]
J: 1345.4903 along [0.1278 0.9918]

SPECIMEN D4
Area: 103.0600 mm^2

Perimeter: 37.7655
Bounding box: X: 193.8045 -- 207.8813
Y: 190.1676 -- 199.8667
Centroid: X: 200.7563
Y: 195.2547
Moments of inertia: X: 3929711.7301
Y: 4154835.4701
Product of inertia: XY: 4039818.0520
Radii of gyration: X: 195.2699
Y: 200.7853
Principal moments and X-Y directions about centroid:
I: 609.2037 along [0.9999 0.0140]
J: 1199.0717 along [-0.0140 0.9999]

SPECIMEN D5
Area: 114.0427 mm^2

Perimeter: 40.9042
Bounding box: X: 209.6302 -- 223.6302
Y: 189.7956 -- 200.1440
Centroid: X: 216.5193
Y: 195.2327
Moments of inertia: X: 4347587.3008
Y: 5347935.7056
Product of inertia: XY: 4820716.5181
Radii of gyration: X: 195.2497
Y: 216.5506

Principal moments and X-Y directions about centroid:
I: 753.7420 along [0.9975 -0.0707]
J: 1549.1075 along [0.0707 0.9975]

SPECIMEN D6

Area: 108.0048 mm^2

Perimeter: 38.9091
Bounding box: X: 236.5514 -- 250.5514
Y: 188.7209 -- 198.6477
Centroid: X: 243.5882
Y: 193.9365
Moments of inertia: X: 4062865.5890
Y: 6409842.8770
Product of inertia: XY: 5102229.6028
Radii of gyration: X: 193.9522
Y: 243.6140
Principal moments and X-Y directions about centroid:
I: 655.9954 along [0.9998 0.0195]
J: 1358.2952 along [-0.0195 0.9998]

---------- **REGION D10** ----------

Area: 114.8637 mm^2
Perimeter: 38.8985
Bounding box: X: 216.6978 -- 230.5982
Y: 163.5307 -- 174.4390
Centroid: X: 223.8319
Y: 169.0971
Moments of inertia: X: 3285238.5648
Y: 5756088.0562
Product of inertia: XY: 4347602.6171
Radii of gyration: X: 169.1188
Y: 223.8578
Principal moments and X-Y directions about centroid:
I: 829.5218 along [0.9850 0.1724]
J: 1347.6044 along [-0.1724 0.9850]

---------- **REGION D8** ----------

Area: 141.7281 mm^2
Perimeter: 42.5063
Bounding box: X: 234.4941 -- 247.9827
Y: 162.5541 -- 176.2600
Centroid: X: 241.1398
Y: 169.2089
Moments of inertia: X: 4059515.7295

Y: 8242862.5009
Product of inertia: XY: 5782937.3095
Radii of gyration: X: 169.2424
Y: 241.1632
Principal moments and X-Y directions about centroid:
I: 1593.7341 along [0.3018 0.9534]
J: 1607.3862 along [-0.9534 0.3018]

---------- **REGION D9** ----------

Area: **142.3888 mm^2**
Perimeter: 42.7382
Bounding box: X: 252.3325 -- 266.3325
Y: 163.2334 -- 175.8136
Centroid: X: 259.3338
Y: 169.7579
Moments of inertia: X: 4104775.0691
Y: 9578030.0297
Product of inertia: XY: 6268521.8960
Radii of gyration: X: 169.7879
Y: 259.3583
Principal moments and X-Y directions about centroid:
I: 1452.3975 along [1.0000 0.0074]
J: 1806.7851 along [-0.0074 1.0000]

---------- **REGION D7** ----------

Area: **138.5293 mm^2**
Perimeter: 42.1161
Bounding box: X: 273.6423 -- 285.8520
Y: 163.2334 -- 177.0160
Centroid: X: 279.8257
Y: 170.0500
Moments of inertia: X: 4007558.8599
Y: 10848550.2886
Product of inertia: XY: 6591833.2985
Radii of gyration: X: 170.0862
Y: 279.8434
Principal moments and X-Y directions about centroid:
I: 1372.3320 along [0.0233 0.9997]
J: 1709.4622 along [-0.9997 0.0233]

---------- **REGION D11** ----------

Area: **117.6828 mm^2**
Perimeter: 39.2445
Bounding box: X: 291.7020 -- 305.6995
Y: 162.9947 -- 174.4550
Centroid: X: 298.9300
Y: 168.6335
Moments of inertia: X: 3347461.6964
Y: 10517430.3473
Product of inertia: XY: 5932448.2636
Radii of gyration: X: 168.6558
Y: 298.9499
Principal moments and X-Y directions about centroid:
I: 865.6096 along [0.9810 0.1941]
J: 1419.6213 along [-0.1941 0.9810]